Breaking symmetries in ordered materials: spin polarized light transport in magnetized noncentrosymmetric 1D photonic crystals, and photonic gaps and fabrication of quasiperiodic structured materials from interference lithography.

by

Ion Bita

B.Sc. Chemical Engineering, B.Sc. Chemistry
Massachusetts Institute of Technology, 2000

Submitted to the Department of Materials Science and Engineering
in Partial Fulfillment of the Requirements for the Degree of

Doctor of Philosophy in Polymers

February 2006

Signature of Author: .....
Department of Materials Science and Engineering
February 6, 2006

Certified by: .....
Edwin L. Thomas
Morris Cohen Professor of Materials Science and Engineering
Thesis Advisor

Accepted by: .....
Samuel M. Allen
POSCO Professor of Physical Metallurgy
Chair, Departmental Committee on Graduate Students

Breaking symmetries in ordered materials: spin polarized light transport in magnetized noncentrosymmetric 1D photonic crystals, and photonic gaps and fabrication of quasiperiodic structured materials from interference lithography.

by
Ion Bita

Submitted to the Department of Materials Science and Engineering
on February 6, 2006 in Partial Fulfillment of the Requirements for the Degree of
Doctor of Philosophy in Polymers

Abstract:

Effects of breaking various symmetries on optical properties in ordered materials have been studied. Photonic crystals lacking space-inversion and time-reversal symmetries were shown to display nonreciprocal dispersion relations, and to exhibit a remarkable set of symmetry-related properties. Even in 1D, these materials are found to display indirect photonic band gaps, backward wave propagating modes (antiparallel phase and group velocities) which enable negative refraction at the air-crystal interface, ability to allow bending light with perpendicular magnetic fields, unidirectional superprism effects, etc. By calculating the complex photonic band structure, we show that the gap modes differ fundamentally from the commonly assumed evanescent modes with purely imaginary wave vectors - solely due to symmetry, we show that the gaps of nonreciprocal photonic crystals have complex wave vectors with both imaginary components and non-zero, frequency dependent real components. This basic finding is further studied in the context of tunneling dynamics, by considering the problem of tunneling time for nonreciprocal photonic band gap barriers (the tunneling wave packet has an energy in the middle of the gap). It was found that the classical Hartman effect (independence of tunneling time on barrier length, beyond a certain length), previously implied as universal, is forbidden solely due to symmetry. Instead of a classical zero group delay, we find that tunneling wave packets with opposite spins display non-zero group delays, with opposite signs. Due to analogies based on symmetry, these results directly impact the problem of spin-polarized electronic tunneling in magnetized noncentrosymmetric semiconductors, such as GaMnAs or carbon nanotubes with applied axial magnetic fields.

An interference lithography based fabrication process was developed to produce 2D and 3D quasiperiodically structured materials, which have long-range order but break translational symmetry. Multiple exposure interference lithography was used to fabricate 2D quasicrystals with feature sizes as small as 100nm. Replica molding was used to fabricate transparent and conformable 2D quasiperiodic phase masks, which subsequently allowed the fabrication of 3D structured materials with quasiperiodicity by coherent diffraction lithography. The effect of the higher point group symmetries of 2D quasicrystals on photonic band gap formation (TM polarized only) was studied by finite difference time domain calculations, and it was found that increasing the rotational symmetry does not always lead to wider gaps.

Thesis supervisor: Edwin L. Thomas
Title: Morris Cohen Professor of Materials Science and Engineering

Table of Contents

List of Figures

with thin lines, the darker ones for the real part of the wave vector, Re$\{k_z\}$, and the lighter lines for the imaginary part, Im$\{k_z\}$. **(a)** Transmission of plane waves propagating in the **+z** direction ($\gamma > 0$) through a finite piece of the RH photonic crystal, showing the total transmissivities of LCP waves ($T_{LL}+T_{LR}$) and stop-band for RCP waves ($T_{RR}+T_{RL}$). The polarization conversion contribution ($T_{LR}=T_{RL}$) is scaled by a factor of 200, for visibility on the same plot; **(c)** same as (a), but the magnetogyration vector is reversed ($\gamma < 0$), corresponding to an incident wave propagating in the **-z** direction.

Figure 3-4 - Isofrequency sections through numerically calculated dispersion surfaces, $\omega(k_x,k_y=0,k_z)$; **(a)** Effect of magnetooptic activity ($\gamma > 0$) on the isofrequency contours, when $\omega = 0.65\ [2\pi c/L]$ and the magnetogyration vector is parallel to the helical axis (**g**||**z**) ; **(b)** Isofrequency cuts at multiple frequencies, for constant magnetooptic activity ($\gamma = 0.1$, **g**||**z**).

Figure 3-5 - Isofrequency cut at $\omega = 0.67$ [$2\pi c/L$] through numerically calculated dispersion surfaces, $\omega(k_x,k_y=0,k_z)$, when **g**||**z** ($\gamma = 0.1$), showing the directions of the Poynting vectors of four eigenmodes that are phase matched to a particular value of the parallel wave vector, k_x.

Figure 3-6 - Isofrequency cuts through numerically calculated dispersion surfaces, $\omega(k_x,k_y=0,k_z)$; **(a)** Effect of magnetooptic activity ($\gamma > 0$) on the $\omega = 0.65\ [2\pi c/L]$ contours, when the magnetogyration vector is perpendicular to the helical axis (**g**||**x**) ; **(b)** Isofrequency cuts at multiple frequencies, for constant magnetooptic activity ($\gamma = 0.2$, to exaggerate this qualitative effect, **g**||**x**).

Figure 3-7 - Isofrequency cut at $\omega = 0.65\ [2\pi c/L]$ through numerically calculated dispersion surfaces, $\omega(k_x,k_y=0,k_z)$, showing three different regimes of transmission when **g**||**x** ($\gamma = 0.2$ to exaggerate the effect graphically); **(i)** and **(iii)** depict normal refraction at the air-photonic crystal interface; **(ii)** shows negative refraction at the air-photonic crystal interface.

Figure 4-1 - **(a)** dPBG at the anticrossing of bands with equal group velocities; **(b)** iPBG at the anticrossing of different v_g bands, as seen in nonreciprocal PCs. The original bands are shown with dashed lines, the coupled propagating modes with solid, black curves and the expected real part of the gap modes with a thicker solid gray line.

Figure 4-2 - **(a)** Reciprocal band structure with dPBG for a 1D PC breaking only T-R symmetry ($\varepsilon_F = 1.72$, $\gamma_F = 0.1$, $\varepsilon_c = 1.52$, $\xi_c = 0$ in Eqs. (2) and (3), see text); **(b)**, **(c)** and **(e)** Magnification of the first gap region showing the original bands and the real and imaginary parts of the complex k_{gap} solutions in the PBGs - note the vertical alignment at the edge of the first Brillouin zone.

Figure 4-3 - **(a)**, **(b)** Nonreciprocal band structure for a 1D PC breaking both S-I and T-R ($\varepsilon_F = 1.72$, $\gamma_F = 0.1$, $\varepsilon_c = 1.52$, $\xi_c = 0.02$ in Eqs. (2) and (3), see text). **(c)**, **(d)** and **(e)** show the gap mode solutions. Note the vertical (mirror) symmetry about $k = 0$ of Im$\{k_{gap}\}$ solutions and the different frequency dependence of the Re$\{k_{gap}\}$ solutions.

Figure 4-4 - Tunneling time for RCP and LCP pulses with narrow frequency bandwidths centered in the gaps of the LCP and RCP bands shown in Fig. 4-2 (dPBG) and Fig. 4-3 (iPBG). In both cases the

center frequencies are $\omega_{0,\,LCP} = 0.316\ [2\pi c/L_{period}]$ and $\omega_{0,\,RCP} = 0.311\ [2\pi c/L_{period}]$), with $L_{period} = 486nm$.

Figure 5-1 - Quasicrystalline structures. **(a)** HRTEM phase-contrast atomic-resolution image of Zn_6Mg_3Ho decagonal quasicrystal viewed along the 10-fold rotation axis [*www.jeol.com*] and a photograph of a macroscopic (mm scale) quasicrystal; **(b) and (c)** SEM pictures of photonic quasicrystal made by etching holes in a pattern given by a quasiperiodic tiling - Penrose in (b) (from [12]) and dodecagonal in (c) (from [13]); **(d) and (e)** calculated quasiperiodic light intensity patterns from interference of laser beams, showing 10-fold and 12-fold rotational symmetries (this work).

Figure 5-2 - Spatial distribution of the total light intensity, $I(x,y)$, pattern for **(a)** square crystal ($N = 2$ exposures); **(b)** octagonal ($N=4$), **(c)** decagonal ($N=5$) and **(d)** dodecagonal ($N=6$) quasicrystals. The axes units are normalized to the laser wavelength, and higher intensities are plotted as lighter pixels.

Figure 5-3 - Quasicrystalline structures with *18%* fraction of a given component (white pixels) for the investigated rotational symmetries; the (X-1) series corresponds to $I > I_{cut}$, while the (X-2) series to $I < I_{cut}$ (X = a, b, c); **(a)** octagonal quasicrystal with $I_{cut}/I_{maximum} = 67\%$ in (a-1) and *33%* in (a-2); **(b)** decagonal quasicrystal with $I_{cut}/I_{maximum} = 63\%$ in (b-1) and 34% in (b-2); **(c)** dodecagonal quasicrystal with $I_{cut}/I_{maximum} = 64\%$ in (c-1) and *35%* in (c-2).

Figure 5-4 - **(a)** Octagonal, **(b)** decagonal, and **(c)** dodecagonal patterns with varying volume fractions of the white region (where $I(x,y) > I_{cut}$), showing not only a continuous change of the size and shape of particular features, but also a discontinuous appearance of new structural features. Values of the corresponding I_{cut} are given in Table 5-1.

Figure 5-5 - Generation of a 1D quasicrystal by projection from a 2D square lattice. The key requirement is for the (e.g. 1D) axis $\boldsymbol{E}$ (onto which the projection is done) to be oriented at an irrational angle with respect to the translation vectors of the higher dimension (e.g. 2D) periodic structure. Adapted from [11].

Figure 5-6 - Examples of 2D quasicrystalline tilings. **(a)** octagonal quasicrystal; **(b)** decagonal quasicrystal and **(c)** dodecagonal quasicrystal. The patterns are centered with the high rotation axis at (5,5).

Figure 5-7 - 18% fill fraction 2D quasiperiodic structures based on mathematical quasicrystalline tilings (for comparison with interference lithography structures shown in Figure 5-3).

Figure 5-8 - Comparison between the location of the PBG via **(a)** photonic band structure (exact method), and **(b)** FDTD calculation of the LDOS at the center of a dielectric cylinder (approximate method) for a 2D triangular lattice with 10% dielectric rods with $\varepsilon = 6$ in air.

Figure 5-9 - Width of the 1st TM PBG in square and triangular 2D photonic crystals as a function of volume fraction, for dielectric **(a)** $\varepsilon = 4$, **(b)** $\varepsilon = 6$, **(c)** $\varepsilon = 8$, and **(d)** $\varepsilon = 11.4$ cylindrical rods surrounded by air. Each point on the plots represents an actual band structure calculation.

Figure 5-10 - Gap maps from assembling the LDOS curves calculated at the point (0,0) in each shown structure, for fill fractions f = 0.05-0.16 (steps of 0.01), and 0.18-0.30 (steps of 0.02) for **(a)**

octagonal, **(b)** decagonal, and **(c)** dodecagonal quasicrystals from interference, with an $\varepsilon = 6$ dielectric placed where $I > I_{cut}$. Small pieces of each PBG structure with 18% dielectric (white regions) are shown above each LDOS plot for emphasizing the structural differences between quasicrystals. Note that $a = \lambda_{interference}/2 = 1$.

Figure 5-11 - same as Figure 5-10, but with $\varepsilon = 8$ for the dielectric component (higher dielectric contrast).

Figure 5-12 - Gap maps from assembling the LDOS curves calculated at the highest point group symmetry location in each structure at various fill fractions for **(a)** 2D triangular photonic crystal, **(b)** octagonal PROJ- PQC and **(c)** octagonal IL-PQC, all with $\varepsilon = 4$ dielectric in air. Small pieces of each PBG structure with 18% dielectric (white regions) are shown above each LDOS plot for emphasizing the structural differences between quasicrystals.

Figure 5-13 - same as Figure 5-12, but for a dielectric with $\varepsilon = 6$.

Figure 5-14 - Gap maps from assembling the LDOS curves calculated at various fill fractions for **(a-1)** IL-style and **(a-2)** PROJ-style 2D decagonal quasicrystal, and **(b-1)** IL-style and **(b-2)** PROJ-style 2D dodecagonal quasicrystal, all with $\varepsilon = 6$ dielectric and air. Small pieces of each PQC with 18% dielectric (white regions) are shown next to each LDOS plot for emphasizing the structural differences between quasicrystals.

Figure 5-15 - Same as Figure 5-14, with $\varepsilon = 8$ dielectric and air.

Figure 5-16 - Effect of a shift of the projecting plane in high dimensions. The projected Penrose-family 2D quasicrystalline structural changes. **(a)** projection plane going the origin of the higher dimensional space, **(b)** shift with half a period in the hyperspace. See [11].

Figure 6-1 - IL with 5 beams arranged to produce a Penrose-like quasicrystal. **(a)** orientation of the **k** vectors corresponding to each beam; **(b)** orientation and relations between the difference vectors, $\Delta\mathbf{k}_{jl}$, that correspond to the pair-wise interference of any two of the 5 beams shown in (a).

Figure 6-2 - Perspective and top-down views of the 2D decagonal QC intensity distributions obtained from IL with **(a)** 5 exposures with 72° rotations and **(b)** 5 beams separated by 72°. In all cases, the axes are in units of the wavelength, $\lambda = 1$, and the polarizations are out-of-plane and in phase.

Figure 6-3 - 2D quasiperiodic pattern obtained from 3 exposures of line gratings with equal spatial periods ($P = \lambda/2 = 0.5$, see Eq. 6-1), but oriented as shown in the inset figure (at 0°, 36° and 90° measured from **x** towards **y**). **(a)** Total intensity pattern; **(b)** Binarized intensity pattern obtained by thresholding at $I_{threshold} = 75\%\ I_{max} = 9$; **(c)** horizontal profile at $y = 0$ for the total intensity pattern shown in (a); **(d)** horizontal profile at $y = 0$ for the binarized intensity pattern shown in (b). All dimensions are in units of λ.

Figure 6-4 - **(a)** A laser beam propagating in the *xyz* lab coordinate frame in an arbitrary direction **k**, with arbitrary amplitude and polarization given by $\mathbf{E}_1$ and $\mathbf{E}_2$; **(b)** Definition the $e_1e_2e_3$ coordinate system in relation with the *xyz* coordinate system.

Figure 6-5 - IL configuration for fabricating Penrose-like 2D PQC **(a)** interference of five laser beams converging to a central point from the corners of a regular pentagon (i.e. the projections of the five **k** vectors in the sample plane are separated by 72°); **(b)** Five exposures of line gratings formed by IL with 2 beams, where the sample substrate is rotated with 72° after each exposure.

Figure 6-6 - **(a)** Configuration of the Lloyd's mirror IL system built and shared by the MIT Nanostructures Laboratory; **(b)** Sample holder assembly, showing the rotation axis for changing the grating periodicity, and the axis around which the substrate is rotated during ME-IL; **(c)** Rotating the entire stage assembly changes the incidence angle and thus the periodicity of the recorded gratings. Adapted from [29].

Figure 6-7 - Dependence of volume fractions on the intensity cutoff level for 2D quasiperiodic patterns obtained from 4, 5, and 6 exposure IL. Representative pictures of the three types of 2D PQC structures at a few fill fractions are also shown in Figure 5.4.

Figure 6-8 - Tri-layer resist stack. An optically absorbing antireflection coating (ARC) placed on top of the substrate is used to eliminate the reflection R_2 from the bottom of the photoresist layer, such that only the interference between the T_1 rays is recorded. An optically thin interlayer (e.g. 20nm SiO_2) is placed between the photoresist and ARC layers for accurately capturing the photoresist pattern before transfer into the substrate.

Figure 6-9 - Process flow for using ME-IL to fabricate 2D PQC samples, with SEM images of actual samples produced in the case of line gratings (one exposure). **(a)** the initial tri-layer resist stack is composed of 200nm photoresist, 20nm SiO_2 and 200nm organic ARC material, on a 1.5μm thermal oxide coated silicon wafer substrate; **(b)** the developed photoresist structure; **(c)** the SiO_2 interlayer is etched with CHF_3 RIE using the photoresist as a mask; **(d)** the pattern is further transferred into ARC by etching with O_2 RIE using the thin SiO_2 caps as a mask; **(e)** the 2D quasiperiodic pattern is finally transferred to the SiO_2 substrate by CHF_3 etching using the ARC as a mask; **(f)** the final 2D PQC sample is obtained by stripping the ARC mask with O_2 plasma.

Figure 6-10 - **(a)** Tri-layer resist stack structure: (from the top) photoresist, SiO_2 interlayer, ARC layer and substrate (1.5μm thermal oxide on silicon); **(b)** Effect of varying the thickness of the ARC layer on the reflectivity R_2 from the bottom interface of the photoresist layer in the case of a 300nm period grating. The simulations used the refractive index data provided in Table 6-2.

Figure 6-11 - Scanning electron microscope images at 30k magnification of SiO_2 line gratings obtained from photoresist patterns produced using two IL approaches. In **(a)** and **(b)** a single exposure of 11.75min (115nW laser power delivered at the sample plane) is performed. The same total dose is delivered in **(c)** as 4 exposures and in **(d)** as 5 exposures, but additional 1min delays are introduced between each exposure. It can be seen that the resulting gratings are virtually identical within the error limit of the SEM measurement. Measured duty cycles are 43% in (a), and 41% in (b), 39% in (c), and 41% in (d).

Figure 6-12 - Top-down view SEM image of a Penrose-like decagonal 2D quasiperiodic pattern etched in SiO_2. Areas with local 5 and 10 fold rotational symmetries are emphasized, and a portion of a Penrose tiling pattern is overlayed on the sample image. The inset figure shows an edge-on SEM image of the same sample, where the height of the posts is 240nm. The structure was obtained by 5 exposures with 36° rotations of 300nm period line gratings.

Figure 6-13 - Top-down SEM images of 2D **(a)** octagonal, **(b)** decagonal, and **(c)** dodecagonal quasiperiodic structures in silica produced by ME-IL with N = 4, 5, and 6, respectively, exposures and rotations with 180°/N angles. Views of the central axis showing 8mm, 10mm, and 12mm point symmetry.

Figure 6-14 - Effect of exposure dose on the recorded photoresist pattern for the case of a 2D decagonal quasicrystal from ME-IL with 5 exposures and rotations with 36°. The fraction of substrate area covered with photoresist (gray areas in the figures) is 66% in **(a)**, 44% in **(b)**, and 30% in **(c)**.

Figure 6-15 - Comparison between SEM images of experimental photoresist patterns produced by ME-IL with **(a)** 5 exposures and 36° rotations, or **(c)** 6 exposures and 30° rotations, with computed intensity patterns approximating the experimental conditions, as **(b)** and **(d)**. 300nm period line gratings were recorded in each exposure.

Figure 6-16 - Large area, plan view SEM image of an octagonal 2D quasiperiodic silica structure obtained by 4 exposures of line gratings with 300nm periodicity, and subsequent rotations with 45°.

Figure 6-17 - Coherent diffraction lithography (also known as phase mask lithography). The schematic shows an implementation for creating 3D nanostructured polymeric templates by recording the near field intensity pattern generated by an elastomeric, transparent, 2D periodic diffraction grating into a photoresist. From [40].

Figure 6-18 - **(a)** Elastomeric replica in PDMS of an octagonal 2D quasiperiodic silica grating. The depth of the topographical features is 450nm; **(b)** the diffraction spectrum obtained for a 632nm HeNe laser - imaged by projection on a paper screen placed at 5.2cm away from the PDMS grating (digital photograph captured by Mr. Marcus Dahlem, MIT EECS).

Figure 6-19 - A sub-micron structured, 3D epoxy polymeric network with quasiperiodicy obtained by CDL with a transparent octagonal 2D quasiperiodic PDMS grating, exposed with the 361nm line of an Ar-ion laser. Representative local octagonally symmetric regions are indicated with green octagons.

Figure 6-20 - **(a)** Schematic of a diblock copolymer molecule, formed by two chemically distinct polymer chains joined covalently. Polystyrene-*b*-polyisoprene is shown as an examle; **(b)** Bulk morphologies obtained in diblock copolymers as the volume fraction of a component is increased from 0 to 50%.

Figure 6-21 - Block copolymer nanolithography. Formation of a nanopatterning mask after selectively removing a component from a self-assembled block copolymer thin film with either spherical or cylindrical morphology.

Figure 6-22 - Plan view SEM images of representative 2D quasiperiodic array of posts used as templates for BCP self-assembly studies **(a)** 2D dodecagonal QC; **(b)** 2D octagonal QC.

Figure 6-23 - SEM images of a monolayer of PS-PFS spherical morphology BCP, after O_2 RIE, self-assembled on 2D quasiperiodic topographically patterned substrates with **(a)** 12-fold rotationally symmetric QC and **(b)** 8-fold rotationally symmetric QC.

Figure 6-24 - MIT Nanoruler Project: 12" wafer patterned with 400nm period line gratings (*http://web.mit.edu/newsoffice/2004/nanoruler-0128.html*)

List of Tables

ACKNOWLEDGEMENTS

I am writing this section last, in the early morning hours of the day following my PhD defense. I am not sure I will be able to fully capture in words the gratitude I feel for the life enriching experiences I have enjoyed throughout the past nine years while here at MIT, as an undergraduate of Courses 10 and 5 between 1997-2000, and then as a graduate student in Course 3.

This section would not feel just without first acknowledging the mentorship of a few people from my undergraduate years, which have significantly shaped my later path at MIT. In particular, I am very thankful to Prof. Timothy Swager of the Chemistry Department for having offered me a place in his laboratory and my first real research job. Tim is an incredible scientist, and I feel fortunate for having been part of his lab. It was during the two years I spent working with him that my interest in the optical properties of materials has crystallized and ultimately led to my decision to join the PhD program of the DMSE at MIT. I am also very thankful to Prof. Robert Cohen of the ChemE Department, who was the first to teach me about polymer physics and offer genuine altruistic mentorship outside the classroom. I remember vividly the many conversations we had about graduate school and in particular about my desire to enroll in the ChemE Practice School. Bob is a wonderful individual, who cares deeply about the well being of his students. Last, but not least, I would like to acknowledge the late Dr. Michael Mohr, my undergraduate advisor. Mike remains to me the epitome of what a true Chemical Engineer is, and a reason for which I feel proud for still having some ChemE blood running through my veins. His passing away last year was a great loss for all of us that knew him.

Among all at MIT, I am most grateful to Prof. Edwin Thomas, my PhD advisor. From all my mentors, Ned has been by far the most influential contribution to my academic development. I feel very fortunate for having worked with, and learned from Ned on so many occasions, and am very thankful for his continued support throughout the past years as my research grew out of the initial mold it was supposed to fill. Ned's personal example remains to me the standard for an insatiable appetite for good science,

coupled with an outstanding intellectual bandwidth, and a sincere dedication for the success of his students. His unwavering support, and insightful feedback has allowed my research to truly bloom, and to reach boundaries that I could not have imagined when I joined his lab and the MIT DMSE.

I would also like to acknowledge the support of Prof. Henry Smith, who welcomed me in the Nanostructures Laboratory and made possible a significant portion of the research conducted in this thesis. Furthermore, I would like to thank my thesis committee, Profs. Caroline Ross, Moungi Bawendi and Rajeev Ram for their help and feedback on my research. In particular, I am thankful to Rajeev for being one of the best teachers I have ever had.

I have been fortunate over the past years to call myself the colleague and friend of numerous people at MIT. Apologizing in advance to those that may not have been remembered at this early morning hour, I would like to acknowledge Vance Williams, Jinsang Kim, Chinedum Osuji, Chaitanya Ullal, Augustine Urbas, JongSeung Yoon, Sam Ha, Taeyi Choi, JiWoong Park, Taras Gorishnyy, Rafal Mickiewicz, Joe Walish, Michael Walsh, Tim Savas, Joel Yang, Brian Cord, Jim Daley, Joy Cheng, Mihai Ibanescu, Marcus Dahlem, Joe Tracy, Dmitry Dinega. I thank you all.

Among all, I am most thankful to my family. I thank my parents and brother for their continued love and support. I thank my wife Cristina for her love, patience and for believing in me, despite the long hours MIT took from our time spent together. I am most fortunate for having her besides me, and carry the deepest admiration for her inner strength and beauty. I am thankful to her for having given me a most beautiful present four months ago, our first-born son.

I dedicate this thesis to you, Cristina, my dear love.

Chapter 1.
Thesis overview

The central theme of this thesis has been the study of photonic band gap materials where certain symmetries are broken by design. The first half of the thesis focuses on a theoretical analysis of the basic features of light propagation and tunneling dynamics in 1D photonic crystals simultaneously lacking time-reversal and space-inversion symmetries, the photonic analogs of noncentrosymmetric magnetic semiconductors. In the second part of the thesis, both theoretical and experimental results are reported for 2D photonic quasicrystals, a novel class of materials where translational symmetry is broken.

Chapter 2 serves as an introduction to photonic crystals (PC), structured materials with a periodic spatial variation of the refractive index on the scale of the wavelength of light [1]. Since the first part of the thesis deals with fairly advanced theoretical problems in PC physics, we set out to provide in this chapter an overview of the basic concepts and tools used to understand the optical properties of PC. The material science perspective is first adopted, and pictorial examples of real PC materials are shown. We then adopt a physics view, and by considering the case of a 1D photonic crystal, we introduce Maxwell's equations and their solutions in periodic media. A strong emphasis is placed on the fundamental connections between PC physics and the physics of electronic wave propagation in atomic crystals. Dispersion relations and photonic band diagrams are introduced semiquantitatively, and their use for predicting PC properties is described.

Chapter 3 is the first of two chapters presenting the results of our theoretical investigations of light propagation in 1D periodic PC simultaneously lacking space-inversion (S-I) and time-reversal (T-R) symmetries. S-I symmetry is absent, for example, in PC having a noncentrosymmetric arrangement of their material constituents (e.g. helical, or spiral dielectric structures, the case investigated in Chapter 3), or in PC comprised of noncentrosymmetric material components (i.e. optically active materials, see Chapter 4). Similarly, including magneto-optically active material components in the unit cell can break T-R symmetry if the light propagation direction is not perpendicular to the material magnetization. The representative material systems that were studied are a 1D periodic, dielectric helical medium with magnetooptic activity in Chapter 3, and a 1D periodic photonic crystal comprised of alternating layers with optical activity and with magnetooptic activity in Chapter 4.

The initial motivation for this work has been our interest in understanding the physics of PC with nonreciprocal dispersion relations, $\omega(\mathbf{k}) \neq \omega(-\mathbf{k})$. While the vast majority of PC literature focuses on reciprocal systems, a 2001 publication by Figotin and Vitebsky [2] were first to report that nonreciprocal PC exhibit properties that significantly deviate from known optical properties. Figotin discussed the design of a 1D nonreciprocal PC that allows "freezing" light in one direction, while allowing free propagation in the opposite direction (an optical diode-like behavior enabled by introducing a mode with zero group velocity and zero group velocity dispersion at a frequency for which the opposite propagation direction displays a normal propagating mode). In Chapter 3 we present a first comprehensive study of the optical properties of 1D nonreciprocal PC, where we show that this class of PC exhibits in fact many more

remarkable PC properties as a sole consequence of symmetries, properties which are thus independent of the choice of materials, magnitudes of their optical constants, etc.. We introduced the concept of indirect photonic band gaps (edges not aligned in k-space even in 1D, formed at the anticrossing of bands with different group velocities), and showed for the first time that 1D nonreciprocal PC will always display propagating eigenmodes with a negative group velocity in select frequency intervals (which is found to also allow for negative refraction at the air-PC interface). Furthermore, we show that the path of light inside such PC can be bent with perpendicular magnetic fields, similarly to the photonic Hall effect observed in uniform (i.e. non-periodic) materials with similar symmetries [3], and point out the presence of unidirectional superprism effects (large variations of the refraction angle for small changes of the incident angle or of the wavelength, but only for one direction, while normal refractive properties are displayed if the propagation direction or the material magnetization are reversed). These results are remarkable, since they arise as a consequence of symmetry, and because they extend our knowledge of optical properties and phenomena enabled by PC through the careful choice of material components and their arrangement inside the unit cell.

During our studies of 1D PC breaking both S-I and T-R symmetries, we became increasingly aware of, and very interested in the consequences of the fact that optical properties arising solely from symmetry constraints should also apply in the electronic case, where the material periodicity is at the atomic scale. The electronic analog to our photonic crystal system is a noncentrosymmetric periodic atomic system containing, for example, magnetic atoms. Two prominent examples that fit this description are semiconductors with zinc-blende crystal structure (GaAs, CdTe, etc.) doped with

magnetic atoms (Mn in most cases) [4], and chiral carbon nanotubes in the presence of magnetic fields applied axially [5]. Both these types of materials are subjects of intense investigation in the fields of spin electronics (spintronics) [6]. Thus, by using this photonic-electronic crystal analogy, we were able to bring to light some unique insights into the basic tunneling electronic properties of two very important classes of materials.

Chapter 4 presents results from our investigations of the tunneling time problem in the case of spin-polarized particles traversing a barrier region lacking both S-I and T-R symmetries. The basic analysis of tunneling dynamics is conducted in the context of wave packets propagating across a barrier, which is used to describe both electronic and photonic tunneling due to analogies between Schrodinger's and Maxwell's equations [7, 8]. Even though tunneling is a classical problem that has been investigated for many decades, it remains presently an active subject for investigation, and a source of controversy (related primarily to explaining predicted and experimentally measured superluminal group delays). While studying the band structures of our nonreciprocal 1D PC systems, it became clear to us that the classical features of tunneling dynamics cannot be exhibited in the absence of the two inversion symmetries. We find that the non-propagating, complex eigenmodes in the first photonic band gap are circularly polarized (analogous to spin-polarized electronic states), and that the gap eigenmodes are not described by the expected evanescent solutions (purely imaginary wave vector). Due to symmetry, the gap modes are shown to have complex wave vectors, with frequency dependent and non-zero real components. This allowed us to show for the first time that symmetries alone forbid the universally assumed Hartman effect (independence of tunneling time on barrier length beyond a certain length) [7, 9]. Instead, we find that, as

the barrier length is increased beyond a threshold, the tunneling time becomes linearly dependent on barrier length, and, moreover, that the sign of the group delay changes with the spin of the tunneling particle (i.e. the tunneling time can decrease with increasing barrier length). As will be discussed in Chapter 4, this unusual prediction of a negative group delay has been recently confirmed by an independent study of electronic tunneling in barriers of noncentrosymmetric semiconductors with out-of-plane magnetization ($Zn_{1-x}Mn_xSe$ and $Cd_{1-x}Mn_xTe$), which are electronic analogs to the 1D photonic cyrstal system studied by us [4].

In the second half of the thesis, we shift focus and examine the case of photonic quasicrystals (PQC), which are ordered materials without translational symmetry [10]. This class of photonic band gap (PBG) materials has only recently been introduced [11], and to this date it remains vastly unexplored by comparison with PC, both experimentally and theoretically [12].

The theoretical development of PQC is significantly affected by the fact that the absence of translational periodicity does not allow one to employ the same theoretical tools as those developed for photonic crystals. As an example, since one cannot assume Bloch waves as solutions to Maxwell's equations, describing the propagation of light through PQC is a very poorly understood problem, with no easy solutions. The PBG properties of PQC PBG are somewhat easier to investigate, but these studies still place a very high demand on computational resources as a result of having to model large structures (since no representative small unit cell can be defined). The current interest in PQC lays in their promise for superior PBG properties compared to PC, arising from their intrinsic higher rotational symmetries which are known to lead to rounder dispersion

surfaces and thus to a potential increase of the PBG widths at a given refractive index contrast (or a reduction of the contrast required for a certain PBG width). Furthermore, the theoretical studies of PQC are also affected by a poor understanding of the choices for PQC structures - consider that in 2D, while all crystals can be classified as belonging to five Bravais lattices, an arbitrarily large number of N-fold rotationally symmetric PQC lattices could be defined. Adding to the complexity of the problem, current investigations of PQC properties are affected by the essential lack of systematic studies of any the problems presented above, which could guide current research in this young research field.

In order to develop some basic understanding of the main factors affecting PBG properties in 2D PQC, in Chapter 5 we explore PBG properties in two types of 2D PQC while varying the symmetry of the lattice and the choice of structural features (related to fabrication method, similar to the choice of a basis given a crystalline lattice). In particular, we studied the formation of 2D complete TM PBG in two families of 2D quasicrystals with 8mm, 10mm, and 12mm point group symmetries (local rotational symmetries N = 8, 10, 12), and used as a basis of comparison corresponding 2D PC (4mm and 6mm point group symmetries). For each of the three noncrystallographic point group symmetries, we examined the corresponding 2D PQC structures obtained from interference lithography by multiple exposures, and 2D PQC structures obtained by placing dielectric rods at the vertices of 2D quasiperiodic tiling patterns having the same three noncrystallographic point groups. While the few existing studies of the properties of 2D PQC focus on the latter type of PQC, no study to date attempts to systematically compare the various point group symmetries. Furthermore, currently there is only one

investigation of the properties of PQC from interference lithography (in [13] the propagation of TM waves through 12-fold rotationally symmetric 2D PQC was used as indirect way to determine PBG properties).

Due to computational power restrictions, we have focused our PBG studies on the calculation of the local density of states (LDOS) for TM polarized modes at a center of high rotational symmetry for the two families of 2D PQC, for each of the three point group symmetries, 8mm, 10mm, and 12mm. We have varied both the dielectric contrast and the fill fractions to construct PBG maps. To gain more insight into the importance of point group symmetry, we first compared the 2D square (4mm) and hexagonal (6mm) lattice PC by using exact band structure calculations. While larger PBG are expected for more symmetric PC when keeping the same structural features constant (e.g. dielectric rods on square vs. triangular 2D lattices), we quantitatively showed that symmetry has to be considered in the context of the contrast (and vice-versa): the higher the refractive index contrast, the smaller the increase of the PBG width with increasing symmetry. It was found that complete 2D TM gaps form for all the considered quasicrystals, and that they have widths comparable to those found for 2D PC with 4mm and 6mm symmetries. Increasing the rotational symmetry at the LDOS monitor point in the investigated 2D PQC systems was not found to correlate necessarily with wider PBG. However, as a consistent trend across the range of parameters explored, the simulations showed that the 2D quasiperiodic arrays of dielectric cylinders tend to display wider TM PBG than their interference lithography (IL) counterparts having the same point group symmetries but structures consisting of ensembles of various shapes and sizes of dielectric domains. The

decagonal IL-PQC was found to have significantly inferior complete 2D TM PBG than the octagonal and dodecagonal IL-PQC.

The actual fabrication of PQC is another difficulty affecting the progress in this field. The few existing experimental studies of PQC optical properties have employed samples fabricated via electron beam lithography [14-16]. However, the interference of properly arranged laser beams is known to also produce quasiperiodic light intensity patterns [17, 18], and, to date, was reported on three occasions to allow fabrication of quasiperiodically structured patterns. In 2003, Wang *et al.* [19] interfered five beams of light to produce Penrose-like photoresist structures, followed in 2004 by Gauthier and Ivanov [20] who used two beam IL to expose multiple line gratings on a rotatable substrate, producing 8-, 10-, and 12-fold rotationally symmetric quasiperiodic structures with features sizes of a few microns. In 2005, Gorkhali *et al.* [21] used again five beam IL to record a Penrose-like structure in a liquid crystal containing photopolymer. These three reports are the first to experimentally confirm the expectation that IL can be used to produce quasiperiodically structured materials.

In Chapter 6, we first present a theoretical analysis of the 2D quasiperiodic structures that are produced via either multiple beam IL (MB-IL) [19] or via multiple exposure IL (ME-IL) [20], and quantitatively show that, while having the same rotational symmetries, the resulting quasicrystalline structures are physically different. MB-IL is found to produce intensity patterns that are equivalent to the superposition of a certain number of 2D quasiperiodic patterns similar to those produced by ME-IL. For example, the superposition of five laser beams in MB-IL produces a total intensity pattern that is equivalent to the sum of two incommensurate quasiperiodic intensity patterns of the type

obtained from ME-IL, where each of the latter patterns is a sum of five rotated line gratings. The actual fabrication of 8-, 10-, and 12-fold rotationally symmetric samples via ME-IL was thus pursued next. We describe a practical implementation that has allowed us to fabricate 2D quasicrystalline samples uniformly over ultra large areas (square centimeters, but our approach can be scaled up to entire silicon wafer sizes), and with feature sizes as small as 100nm, a ~10x smaller size compared to the only two existing literature reports on using IL to fabricate quasicrystals [19, 20]. This reduction in size is significant, given the difficulties expected from the low contrast of the intensity patterns resulting from ME-IL. These results have been enabled by using an ultra-stable lithographic interferometer based on the Lloyd's mirror design (only one laser beam is present in the system), in conjunction with using an antireflection layer inside the photoresist stack, properly designed to maximize the fidelity with which the quasiperiodic pattern is recorded in the top photoresist layer. These experimental results prove for the first time that IL can produce 2D PQC with feature sizes and quality similar to those obtained from electron beam lithography, but in a much more economic fashion and with sample sizes that allow for a wider potential for practical impact.

Towards the end of Chapter 6, we report on two projects enabled by our success in fabricating large area, high quality 2D quasiperiodic structures with sub-micron features. First, we designed and implemented a coherent diffraction lithography based process for the fabrication of novel 3D sub-micron structured quasiperiodic structures, by recording the near field intensity pattern produced by transparent 2D quasiperiodic diffraction gratings illuminated from the opposite side in a thick photoresist layer. The 2D gratings that were used in this study were fabricated by replica molding

polydimethylsiloxane (PDMS) in 2D quasiperiodic topographically patterned silica substrates. PDMS is a material particularly advantageous for this fabrication method due to its low surface energy and ability to conform well over large areas of photoresist coated substrates. Second, preliminary results for the self-assembly of block copolymers with spherical monolayer morphology in thin films on 2D quasiperiodic topographically patterned substrates are presented. This study was initiated with the goal of gaining novel insight into the competition between crystalline and quasicrystalline structure formation in materials, and at this time remains a work in progress.

In conclusion, this thesis has shown that a wide variety of opportunities exist for exploiting symmetries to enable useful and novel optical properties in photonic band gap materials. Thus, one the one hand, *decreasing symmetry* in 1D systems (i.e. breaking time-reversal and space-inversion symmetries) enabled a remarkable set of optical properties arising solely from symmetry reasons - indirect photonic band gaps containing nonpropagating modes with both real and imaginary wave vector components that were shown to forbid the classically assumed Hartman effect in tunneling, and lead to an opposite dependence of the photonic tunneling time on barrier length for the two opposite circular polarizations (or spins). The propagating eigenmodes of these 1D periodic systems are also remarkable, as solely due to symmetry, a number of properties (that were not previously reported) were identified: backward wave propagation (opposite group and phase velocities, similar to negative refractive index materials), negative refraction at the air - 1D PC interface, and unidirectional superprism effects (previously only known in 2D and 3D systems). On the other hand, *increasing symmetry* in 2D systems (i.e. noncrystallographic higher rotational/reflection point group symmetry)

opened a window for the rational design of PBG structures with potentially improved band gap properties. A first systematic analysis of PBG properties in three quasiperiodic 2D lattices was performed (8mm, 10mm, and 12mm point group symmetries), with a focus on those structures produced by IL. Comparisons of PBG properties as obtained from FDTD calculations of LDOS at the center of high rotational symmetry suggest that 2D quasicrystals with dielectric cylinders placed at the vertices of quasiperiodic tilings lead to more robust band gaps than their IL counterparts, and that, among IL quasicrystals, octagonal symmetry leads to the largest gaps at small volume fractions ($f < 0.1$) and dodecagonal symmetry leads to the largest gaps at larger volume fractions ($f > 0.2$). Although these results are preliminary and more detailed examinations are in progress, due to the lack of previous work in the literature they offer useful guidance for future investigations of PBG properties of quasicrystals. We have also used this insight to guide our experimental investigations, which resulted in the fabrication for the first time of 2D PQC from IL with feature sizes comparable to those of 2D PQC produced by electron beam lithography, but with significantly larger areas.

Ion Bita

Massachusetts Institute of Technology
Cambridge, Massachusetts, USA
ibita@alum.mit.edu

January 2006

References:

1. J.D. Joannopoulos, R.D. Meade, and J.N. Winn, *Photonic Crystals: Molding the Flow of Light.* 1995, Princeton, N.J.: Princeton University Press. ix, 137 p.

2. A. Figotin and I. Vitebsky, *Nonreciprocal Magnetic Photonic Crystals.* Physical Review E, 2001. **63**: p. 066609.

3. G.L.J.A. Rikken, A. Sparenberg, and B.A. Van Tiggelen, *Photonic Magneto-Transport.* Physica B, 1998. **246-247**: p. 188-194.

4. Y. Guo, C.-E. Shang, and X.-Y. Chen, *Spin-Dependent Delay Time and the Hartman Effect in Tunneling through Diluted-Magnetic-Semiconductor/Semiconductor Heterostructures.* Physical Review B, 2005. **72**: p. 045356.

5. H. Mehrez, *et al.*, *Carbon Nanotube Based Magnetic Tunnel Junctions.* Physical Review Letters, 2000. **84**(12): p. 2682-2685.

6. I. Zutic, J. Fabian, and S. Das Sarma, *Spintronics: Fundamentals and Applications.* Reviews of Modern Physics, 2004. **76**(2): p. 323-410.

7. R.Y. Chiao and A.M. Steinberg, *Tunnelling Times and Superluminality.* Progress in Optics, Vol. 37, 1997. **37**: p. 345-405.

8. N.W. Ashcroft and N.D. Mermin, *Solid State Physics.* 1976, Philadelphia: Saunders College. xxi, 826 p.

9. T.E. Hartman, *Tunneling of a Wave Packet.* Journal of Applied Physics, 1962. **33**(12): p. 3427-3433.

10. C. Janot, *Quasicrystals: A Primer.* 2nd Edition ed. Monographs on the Physics and Chemistry of Materials; 50. 1994, New York: Clarendon Press. xvi, 409 p.

11. Y.S. Chan, C.T. Chan, and Z.Y. Liu, *Photonic Band Gaps in Two Dimensional Photonic Quasicrystals.* Physical Review Letters, 1998. **80**(5): p. 956-959.

12. W.N. Man, *et al.*, *Experimental Measurement of the Photonic Properties of Icosahedral Quasicrystals.* Nature, 2005. **436**(7053): p. 993-996.

13. R.C. Gauthier and K. Mnaymneh, *Photonic Band Gap Properties of 12-Fold Quasi-Crystal Determined through Fdtd Analysis.* Optics Express, 2005. **13**(6): p. 1985-1998.

14. K. Nozaki and T. Baba, *Quasiperiodic Photonic Crystal Microcavity Lasers.* Applied Physics Letters, 2004. **84**(24): p. 4875-4877.

15. M. Notomi, *et al.*, *Lasing Action Due to the Two-Dimensional Quasiperiodicity of Photonic Quasicrystals with a Penrose Lattice.* Physical Review Letters, 2004. **92**(12): p. -.

16. M.E. Zoorob, *et al.*, *Complete Photonic Bandgaps in 12-Fold Symmetric Quasicrystals.* Nature, 2000. **404**(6779): p. 740-743.

17. F.M. Deespinosa, *et al.*, *Acoustic Quasi-Crystals.* Europhysics Letters, 1993. **21**(9): p. 915-920.

18. M.M. Burns, J.M. Fournier, and J.A. Golovchenko, *Optical Matter - Crystallization and Binding in Intense Optical-Fields.* Science, 1990. **249**(4970): p. 749-754.

19. X. Wang, *et al.*, *Large-Area Two-Dimensional Mesoscale Quasi-Crystals.* Advanced Materials, 2003. **15**(18): p. 1526.

20. R.C. Gauthier and A. Ivanov, *Production of Quasi-Crystal Template Patterns Using a Dual Beam Multiple Exposure Technique.* Optics Express, 2004. **12**(6): p. 990-1003.

21. S.P. Gorkhali, J. Qi, and G.P. Crawford, *Electrically Switchable Mesoscale Penrose Quasicrystal Structure.* Applied Physics Letters, 2005. **86**(1): p. 011110.

Chapter 2.
Introduction to photonic crystals

Photonic crystals are structured materials having a spatial distribution of the refractive index that is translationally periodic with a unit cell comparable in size with the wavelength of light.

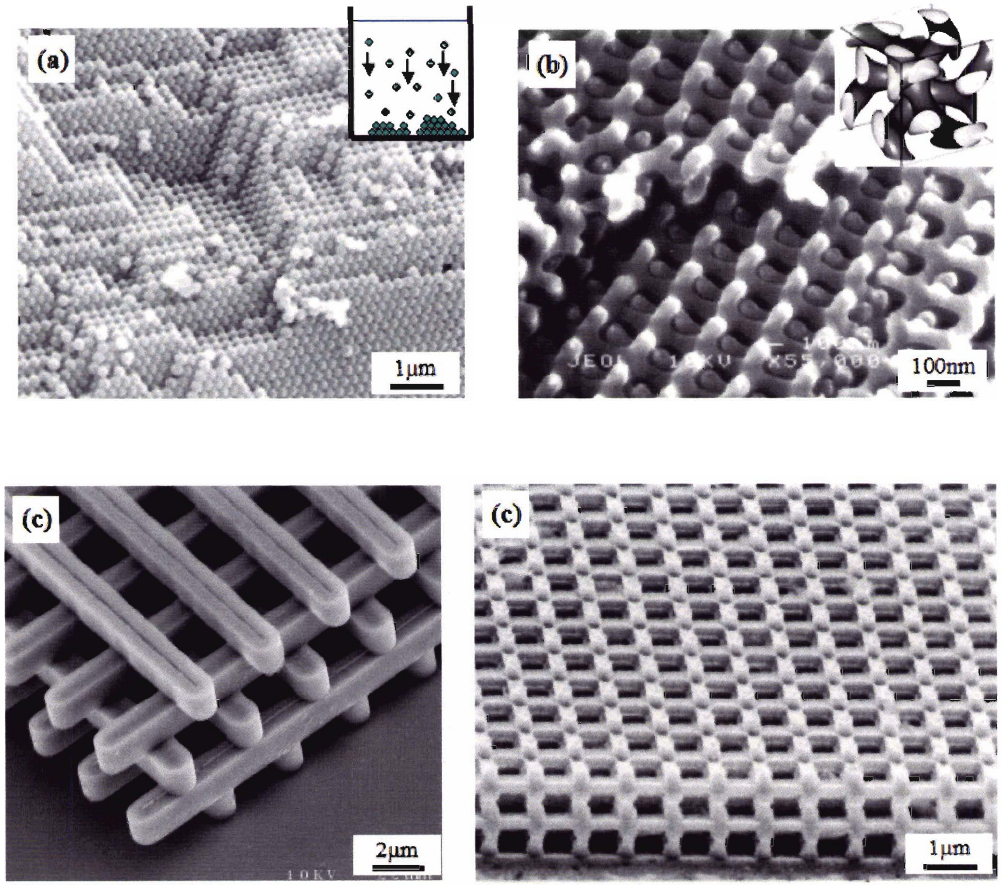

Figure 2-1 - Examples of 3D photonic crystals. **(a)** Face centered cubic crystals obtained by sedimentation of colloidal silica particles [1]; **(b)** Self-assembled double gyroid crystal from a polystyrene-polyisoprene diblock copolymer after the isoprene phase was selectively removed [2]; **(c)** "Woodpile" photonic crystal fabricated in silicon [3]; **(d)** Simple cubic lattice photonic crystal made in silicon [4].

Figure 2-1 depicts a few examples of 3D periodic material structures. As will be explained in this chapter, as deceptively simple some of these structures may appear at first sight, they hold the key for a revolutionary control over light-matter interactions, because photonic crystals display optical properties fundamentally different than those of their individual components.

The beginning of photonic crystals as a research field is typically considered to coincide with two seminal publications from 1987 [5]. Eli Yablonovitch [6] pointed out the possibility of obtaining photonic band gaps and localized electromagnetic modes in 3D structured materials, and of inhibiting spontaneous light emission for optoelectronic applications. In the same year, Sajeev John [7] independently discussed the strong localization of electromagnetic waves in disordered 3D photonic crystals with a high refractive index contrast. However, a much less acknowledged contribution to the development of photonic crystals is the outstanding work on wave propagation in periodic media from early in the 20th century. To not only emphasize the importance of this theoretical foundation, but also to pay tribute to somebody whose vision and impact on science are truly remarkable, I would like to cite two paragraphs from the preface of a book written in 1946.

> "Some readers may be surprised or even disturbed at the mixture of problems assembled in this book. These problems actually extend from electrical engineering to electromagnetism and wave mechanics of the spinning electron, but the link connecting this variety of problems will soon be discovered in their common mathematical background. [...]
>
> All problems discussed deal with periodic structures of various kinds, and they all lead to similar results: these structures, be they electric lines or crystal lattices, behave like band-pass filters. If energy dissipation is omitted, there is a sharp distinction between frequency bands exhibiting wave propagation without attenuation (passing bands) and those showing attenuation and no propagation (stopping bands).

> These general properties are defined for an infinite unbounded medium, but they bear a very close relation to *selective reflections* shown by a bounded medium. A wave striking from outside may be partly reflected from the surface, if the second medium is able to transmit the corresponding frequency. The amount of reflection depends upon how well the media are matched at their common boundary. But when the frequency falls inside a stopping band of the reflecting medium, there is no longer any matching problem; the wave cannot be transmitted, and hence it must be totally reflected. This same explanation applies to electric filters, rest rays, anomalous optical reflections, and selective reflections of X rays or electrons from a crystal." [8]

The author of the above text is Léon Brillouin, who was introducing his book on wave propagation in periodic structures, published in 1946 [8]. In the case of the reader familiar with photonic crystals (PC) but not with the extent of Brillouin's contributions, the above citation may come as a pleasant surprise. It is remarkable to be able to learn from a book written so early about the essence of the definition, basic physics and even of a few applications of PC. For example, consider the concept of a photonic band gap and its consequences on light propagation. Brillouin teaches us that "infinite unbounded [...] periodic structures" can forbid the propagation of certain waves, if their energies fall in a range called "stopping band." These waves are explained to couple to evanescent modes ("those showing attenuation and no propagation"). Brillouin also goes on to explain how this property affects finite (real) crystals: waves with frequencies in the gap are completely reflected, while those outside the gap will be able to propagate after incurring a partial reflection at the interface with the incidence medium, depending on the phase matching at the interface. Furthermore, in another book [9], Brillouin teaches us about the importance and impact of structural periodicity on the phase, group and signal velocities of waves. Many of the features of these velocities described by Brillouin in [9] were recently rediscovered in the case of photonic band structures, and viewed with great

excitement as examples of the special properties of photonic crystals - slowing down the velocity of light with frequencies at band gap edges, superluminal group velocities (*i.e.* greater than velocity of light in vacuum), negative group velocities, etc.

It should be clear by now that photonic crystals represent another facet of solid state physics, where the fundamental problems of wave propagation in crystals (extensively studied in the context of electronic waves and semiconductors [10]), are revisited in the context of electromagnetic waves propagating in the appropriate periodic materials, called photonic crystals.

Since the first half of the thesis deals with fairly advanced theoretical problems in photonic crystals, we now provide a self-contained introduction to the theory of light propagation in photonic crystals. This introduction is complementary to existing texts on photonic crystals [5, 11], which tend to require a more advanced physics background than that of the average material scientist.

2.1. The basics

We start with a brief introduction to light as an electromagnetic wave, and then to quantitatively connect material properties to the propagation of light in the case of a homogeneous medium. This theoretical basis is used in the following section, where light propagation in photonic crystals is studied.

Just as fundamental as Newton's law or the second law of thermodynamics, the laws of electricity and magnetism established by James Clark Maxwell in 1873 [12]

describe the propagation of electromagnetic waves in any material, anywhere in the universe. Using vector notation, Maxwell's equations take the following form

$$\begin{aligned} \textit{Ampere's law} \quad & \nabla \times \mathbf{H}(\mathbf{r},t) = \frac{\partial}{\partial t}\mathbf{D}(\mathbf{r},t) + \mathbf{J}(\mathbf{r},t) \\ \textit{Faraday's law} \quad & \nabla \times \mathbf{E}(\mathbf{r},t) = -\frac{\partial}{\partial t}\mathbf{B}(\mathbf{r},t) \\ \textit{Coulomb's law} \quad & \nabla \cdot \mathbf{D}(\mathbf{r},t) = \rho(\mathbf{r},t) \\ \textit{Gauss' law} \quad & \nabla \cdot \mathbf{B}(\mathbf{r},t) = 0 \end{aligned} \tag{2-1}$$

where the contribution of Maxwell was to add the displacement term $\partial \mathbf{D}(\mathbf{r},t)/\partial t$ to Ampere's law [12]. The space- and time-dependent quantities that appear in these equations are the electric field strength (**E**), magnetic flux density (**B**), magnetic field strength (**H**), electric displacement (**D**), electric current density (**J**) and electric charge density (ρ).

Together with constitutive relations (which describe the electromagnetic material properties), Maxwell's equations describe light propagation in any material system. In the simplest case of propagation in a homogeneous dielectric material with linear properties, the constitutive relations are

$$\begin{aligned} \mathbf{D} &= \varepsilon \mathbf{E} \\ \mathbf{B} &= \mu \mathbf{H} \end{aligned} \tag{2-2}$$

where ε and μ are, respectively, the permittivity (or dielectric constant) and permeability. Isotropic materials are characterized by scalar ε and μ, while anisotropic materials can be described by tensorial quantities.

The six equations comprised of Maxwell's equations, Eq. (2-1), and the above constitutive relations, Eq. (2-2), show all the electromagnetic quantities (e.g. **J**, **E**, **D**, **H**,

or **B**) are interdependent. That is why, for simple materials, it is possible to combine all these relationships into a single equation, formulated for a particular field of interest. The result for the electric field is known as the Helmholtz equation (or simply, the wave equation):

$$\nabla^2\mathbf{E}(\mathbf{r},t) - \mu\varepsilon\frac{\partial^2}{\partial t^2}\mathbf{E}(\mathbf{r},t) = 0 \tag{2-3}$$

A similar equation can be derived for the magnetic field strength vector

$$\nabla\times\left(\frac{1}{\mu\varepsilon}\nabla\times\mathbf{H}(\mathbf{r},t)\right) = \frac{\partial^2}{\partial t^2}\mathbf{H}(\mathbf{r},t) \tag{2-4}$$

The above equation will be shown in the next section to be similar to Schrödinger's equation, and to thus allow a quantitative analogy between the propagation of light in photonic crystals, and the case of electronic wave propagation in atomic crystals [11].

Solutions to these differential equations are well understood from mathematics to be periodic, and that is why, given the context, we refer to them as electromagnetic waves. In the simplest case of a wave propagating in the z direction and polarized along the x direction, the electric field can be written as:

$$\mathbf{E}(\mathbf{r},t) = \mathbf{x}E_x(z,t) \tag{2-5}$$

Thus, the Helmholtz wave equation, Eq. (2-3), takes the form

$$\frac{\partial^2}{\partial z^2}E_x(z,t) - \mu\varepsilon\frac{\partial^2}{\partial t^2}E_x(z,t) = 0 \tag{2-6}$$

From mathematics, the solution to the above differential equation is a wave, a function periodic in both space and time. As an example, consider a cosine function

$$E_x(z,t) = E_0 \cos(kz - \omega t) \tag{2-7}$$

where the minus sign was chosen in order to describe a wave propagating towards +**z** as time increases, as discussed below. The constant ω is called angular frequency, and it is related to the temporal frequency (or simply, frequency) f of this wave

$$\omega = 2\pi f \tag{2-8}$$

Similarly, the constant k is called spatial frequency, and it is related to the wavelength λ (i.e. spatial period) of the considered wave

$$k = \frac{2\pi}{\lambda} \tag{2-9}$$

Thus, by using the general wave solution from Eq. (2-7) with the wave equation Eq. (2-6), we obtain a very important relation between the two frequencies, k and ω

$$\omega = \frac{k}{\sqrt{\mu\varepsilon}} \tag{2-10}$$

The above result is called the dispersion relation, and it is extremely important for understanding how a wave propagates in a given material. This includes photonic crystals, even though in their case the relationship between ω and k has to be often obtained numerically since explicit, analytic forms are inaccessible. Due to energy conservation, the frequency of an electromagnetic wave is almost always conserved

(except in nonlinear processes). Thus, by analogy with energy diagrams, $E(k)$, in atomic crystals, the dispersion relation is typically written as $\omega(k)$, rather than $k(\omega)$.

To showcase the importance of this relation, we end this section by presenting the rigorous definition of the refractive index of material. This is one of the most basic optical properties of materials, and it is typically described as the ratio between the velocity of propagation of a wave in vacuum, c, and the velocity of the wave inside the material, v

$$n = \frac{c}{v} \tag{2-11}$$

However, one may be surprised that the refractive index does not appear in Maxwell's equations at all, and wonder how is it quantitatively affecting the propagation of light. The answer is that, in fact, the refractive index is a derived quantity, one that we prefer to use because of convenience. As shown before, the fundamental material properties that enter Maxwell's equations are only the permittivity and permeability.

The refractive index is more exactly defined as the ratio of the *phase* velocity, v_p, of light propagating in vacuum and that in a particular material. The phase velocity is the velocity with which the constant phase fronts of a wave move in space. For the wave solution in Eq. (2-7), the velocity of a particular phase front (kz - ωt = *constant*) is

$$v_p = \frac{dz}{dt} = \frac{\omega}{k} \tag{2-12}$$

The result in Eq. (2-12) is very general, and it is a first example of the great importance of the dispersion relation. Using the $\omega(k)$ solution derived for a homogeneous material in Eq. (2-10), we obtain that

$$v_p = \frac{1}{\sqrt{\mu \varepsilon}} \tag{2-13}$$

We can now use the definition of refractive index based on the ratio of phase velocity in vacuum and that inside the material to find that

$$n = \frac{c}{v_p} = \frac{1/\sqrt{\mu_0 \varepsilon_0}}{1/\sqrt{\mu \varepsilon}} = \sqrt{\varepsilon_r \mu_r} \tag{2-14}$$

where the relative permittivity and permeability are defined as $\varepsilon_r = \varepsilon/\varepsilon_0$, and $\mu_r = \mu/\mu_0$.

Although seemingly basic, this section has introduced very important concepts. Light propagation in any material is quantitatively described by Maxwell's equations in conjunction with the constitutive relations. Mathematically, the solution to the resulting system of differential equations is a wave, a function periodic in both space and time. The spatial and temporal frequencies, $k = 2\pi/\lambda$ and $f = \omega/2\pi$, of the wave solution are related by the so-called dispersion relation, which couples k and ω to material properties. Using this relation, the velocity with which phase fronts advance in a homogenous material was derived (phase velocity), and the definition of the refractive index was introduced. Thus, going back to the definition of a photonic crystal at the very beginning of the chapter, it is now clear that periodicity of the refractive index means a periodic arrangement of either of, or of both ε and μ.

2.2. Photonic crystals as semiconductors for light

Photonic crystals are sometimes called semiconductors for light, because of the analogies between the physics of electromagnetic wave propagation in photonic crystals and the physics of electronic wave propagation in atomic crystals. As discussed in the first few pages of this chapter, these analogies are possible because of the underlying and more general problem of wave propagation in periodic media. In this section we introduce the optical properties of PC by employing a quantitative analogy with semiconductors. Just as in the previous section, the path towards the solution will start with a definition of the material system, followed by stating the equations that describe wave propagation in space-time. Then, appropriate guesses for the wave solutions are made, and the propagation equations are solved to yield, for example, the dispersion relation for the photonic crystal.

As shown in Figure 2-2(a), both atomic and photonic crystals are periodic structures, however with the typical unit cells of interest differing in size by 3-4 orders of magnitude. Hence, while atomic crystals are known to Bragg scatter (i.e. reflect) X-rays (wavelength $\lambda \sim 10^{-10}$m), photonic crystals interact strongly with much longer wavelengths, most typically in the visible and infrared regions of the electromagnetic spectrum ($\lambda \sim 10^{-7}$-10^{-5}m).

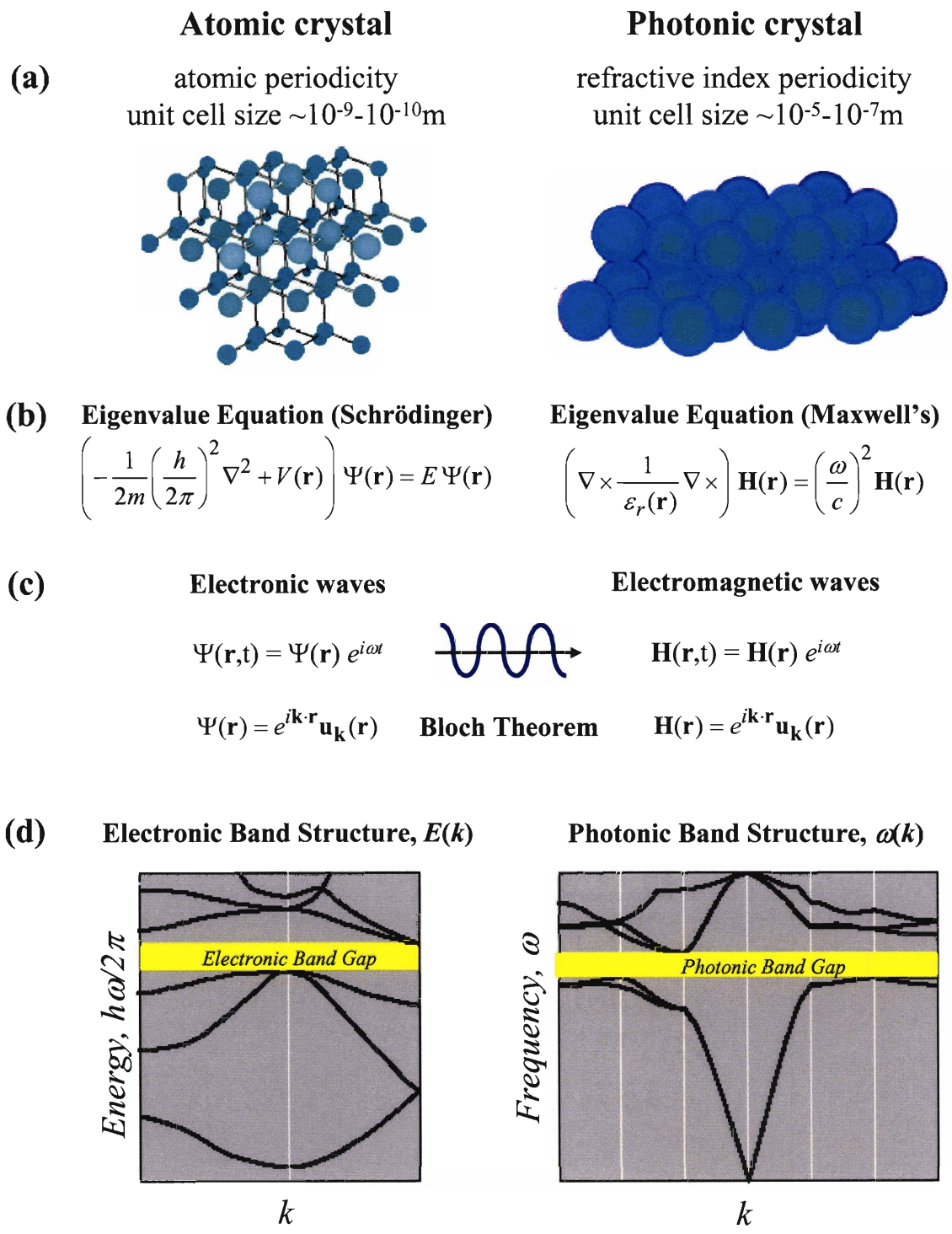

Figure 2-2 - Analogies between atomic crystals and photonic crystals. Adapted from [11]. See text.

The equations that govern electronic and electromagnetic wave propagation are shown in Figure 2-2(b). In order to enable an analogy with the quantum mechanical

treatment of electronic wave propagation based on the Schrödinger equation, it was shown that casting Maxwell's equations in terms of the magnetic field strength vector, $\mathbf{H}(\mathbf{r},t)$, leads to an analogous eigenvalue equation [11] (all the other fields, **E**, **D**, **B**, etc. can be derived using Eq. 2-1). The equation shown in Figure 2-2(b) is obtained from Eq. (2-4) assuming a time dependent $\exp(-i\omega t)$ harmonic fields and nonmagnetic materials, i.e. $\mu_r = 1$. It is important to remember that, while Maxwell's equations are fundamental and involve no approximations, solving the Schrödinger equation in a real, multi-electron system always involves approximations due to the fact that electrons interact with each other, have mass, and are affected by a variety of potentials (electric, magnetic, etc.). Rigorously keeping track of all these interactions leads to a many-body problem that is unsolvable given current computing resources, hence the approximations mentioned. Such approximations are not typically needed for describing light propagation, since photons to not interact with each other in most materials (the exceptions are related to nonlinear optical processes [13]).

The effect of the atomic crystal structure on the propagation of electronic waves is captured in the Schrödinger equation by the periodic atomic potential, $V(\mathbf{r})$, see Figure 2-2(b). For electromagnetic waves, the role of the atomic potential is taken by the inverse of the spatially varying dielectric constant, i.e. the $1/\varepsilon(\mathbf{r})$ term.

Due to particle-wave duality, electrons in atomic crystals are described as electronic waves, where a special quantity called electron wavefunction, $\Psi(\mathbf{r},t)$ (a complex scalar field) is varying in both space and time (remember that this wavefunction is the central quantity in quantum mechanics [10]). As discussed above and shown in Figure 2-2(c), the magnetic field strength vector, $\mathbf{H}(\mathbf{r},t)$, is used to describe wave

propagation in photonic crystals, and both $\Psi(\mathbf{r},t)$ and $\mathbf{H}(\mathbf{r},t)$ are assumed to be time harmonic functions.

$$\begin{aligned}\Psi(\mathbf{r},t) &= \Psi(\mathbf{r})e^{i\omega t} \\ \mathbf{H}(\mathbf{r},t) &= \mathbf{H}(\mathbf{r})e^{i\omega t}\end{aligned} \tag{2-15}$$

The last piece of the puzzle before the actual solution to these equations is related to making an assumption for the spatial variation of the wave solutions in Eq. (2-15). Due to the translational periodicity of $V(\mathbf{r})$ and $\varepsilon(\mathbf{r})$ in the two eigenvalue equations, the wave solutions obey the Bloch-Floquet theorem [10, 14, 15]. As shown in Figure 2-2(c), in the photonic crystal case, the $\mathbf{H}(\mathbf{r})$ solutions take the following form

$$\mathbf{H}(\mathbf{r}) = e^{i\mathbf{k}\cdot\mathbf{r}}\mathbf{u}_{\mathbf{k}}(\mathbf{r}) \tag{2-16}$$

where the wave vector $\mathbf{k}$ is a linear combination of the reciprocal lattice vectors of the periodic structure and $\mathbf{u}_{\mathbf{k}}(\mathbf{r})$ is a periodic function in real space. More details about the reciprocal space of a periodic structure, and about the Bloch-Floquet theorem can be found in classic texts on solid state physics [10].

At this point, both propagation equations can be solved. The actual solutions are not easy to obtain analytically for most cases, and in general the eigenvalue equations are solved numerically for each $\mathbf{k}$ vector [10, 11, 16]. It should be mentioned that it is also possible to implement a solution by starting from the wave frequency, and then by solving for the allowed $\mathbf{k}$ vectors (this method will be used in Chapter 3 to study 1D photonic crystals) [17, 18]. In both cases, what is obtained is a dispersion relation, $\omega(\mathbf{k})$, which in graphical form is referred to as a band structure. Representative photonic and

electronic band structures are shown in Figure 2-2(d), using solid lines to denote propagating bands and highlighting the band gap regions with yellow.

It is clear by now that the study of photonic crystals heavily benefits from a fundamental connection with solid state physics, by sharing a common foundation - wave propagation in periodic media.

2.3. Optical properties of photonic crystals

As described in the previous section, in order to best understand the optical properties of photonic crystals one needs to think outside the typical boundaries of electromagnetic wave theory, and to try and adapt known results for the general problem of wave propagation in periodic media, extensively explored in the context of electronic wave propagation in crystals.

Most (but not all!) of the information about the optical properties of photonic crystals is contained in the dispersion relation, $\omega(\mathbf{k})$, or the so-called photonic band structure. For example, given a frequency ω, the dispersion relation can be solved to find out the wave vectors of the allowed propagating modes (real $\mathbf{k}$) - i.e. in what directions is light allowed to propagate, and with what spatial frequencies (remember that this should also produce the effective refractive index displayed by the photonic crystal along this particular direction, by calculating the corresponding phase velocity). Both positive and negative $\mathbf{k}$ solutions are expected, since both forward and backward propagation should be possible at any frequency. However, what the dispersion relation does not tell us are the polarizations of these propagating modes - whether they are linear, circular, or have a general, elliptical polarization. This should not be surprising, since the dispersion

relation is the solution to an eigenvalue problem, while the polarizations of the propagating wave solutions are described by the corresponding eigenvectors.

To better explain the importance and the information provided by the dispersion relation, consider the case of a 1D PC composed of two alternating layers with thickness, d_i, and dielectric constants ε_i, $i = 1,2$.

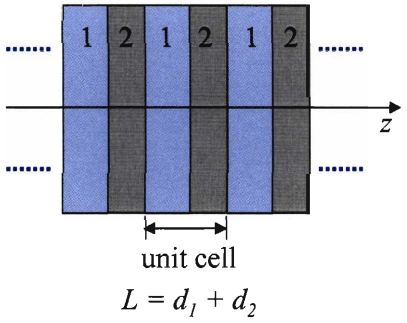

Figure 2-3 - 1D photonic crystal with a bilayer unit cell.

The propagation of light waves along the periodicity direction, z in Figure 2-3, is described by a dispersion relation of the form $\omega(k_z)$. While analytic results for $\omega(k_z)$ can be obtained in particular cases [19], we adopt here a more revealing, graphical approach in order to explain the main properties of a 1D PC (which can be then generalized to higher dimensions).

If the two dielectric constants are equal, the PC shown in Figure 2-3 becomes essentially a homogeneous material, and thus, in the limit of zero dielectric contrast ($\Delta\varepsilon = \varepsilon_1 - \varepsilon_2$), $\omega(k_z)$ should also reduce to the solution for a homogeneous material, shown in Eq. (2-10). However, if $\Delta\varepsilon \neq 0$, it is guaranteed that a photonic band gap of width $\Delta\omega$ will open up in the 1D photonic band structure [11]. Note that the larger $\Delta\varepsilon$, the larger the $\Delta\omega$ as well. Moreover, note that the photonic band gap forms at the edges of the reduced Brillouin zone, the region $-\pi/L \leq k_z \leq \pi/L$, and that it holds for both propagation

directions - a wave with a frequency that falls inside the gap will not be able to propagate inside the crystal regardless of direction (+**z** or -**z**).

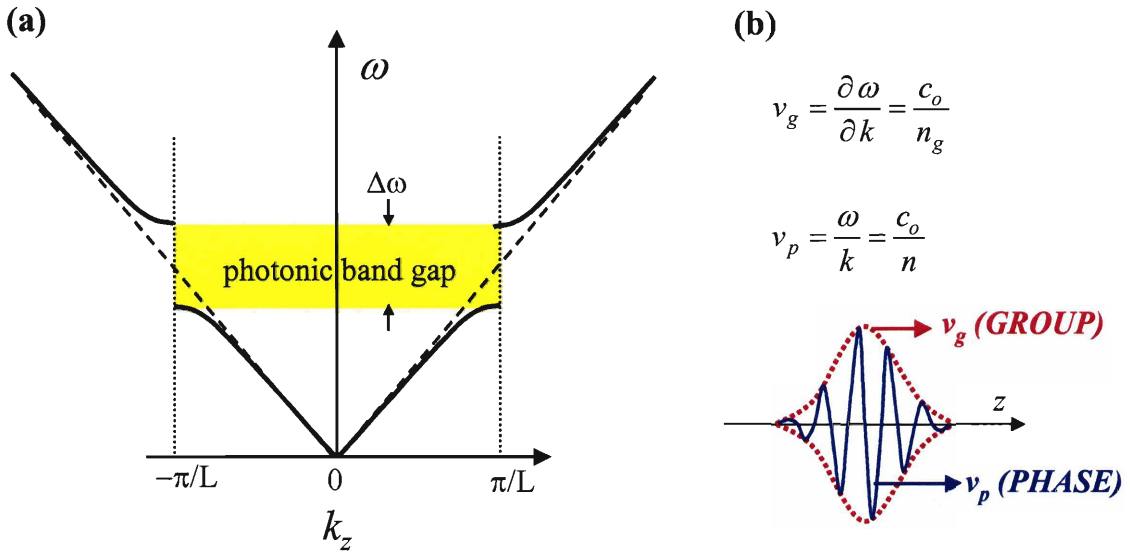

Figure 2-4 - (a) Dispersion relation in a 1D photonic crystal showing formation of the first band gap and propagating modes in the photonic crystal (solid lines). Dashed lines represent the solutions in the case of a homogeneous material, the limit of equal dielectric constants in the two layers of the photonic crystal unit cell. **(b)** Definitions of the phase and group velocities. A wave packet (or pulse) is shown in order to emphasize that the phase velocity corresponds to the motion of phase fronts, while the group velocity gives the signal velocity, the velocity with which the pulse envelope propagates in space.

As shown in the above figure with dashed lines, the $\omega(k_z)$ solutions for a homogeneous material are straight lines with slopes equal to c/n_p, see Eqs. (2-12)-(2-14). Note that we use a subscript p to emphasize that n_p is the *phase* index (i.e. the refractive index). Besides the *phase velocity* (v_p), which is related to the motion of constant phase fronts, a *group velocity* (v_g) can also be derived from the dispersion relation. As shown in Figure 2-4(b), and discussed at length by Brillouin [9], the latter deals with the velocity of signal (pulse) propagation, and can be shown to also equal the velocity of energy flow inside the crystal [10]. The phase and group velocities are defined as

$$\mathbf{v_p} \equiv \frac{\omega}{\mathbf{k}} = \frac{c}{n_p}$$
$$\mathbf{v_g} \equiv \frac{\partial \omega}{\partial \mathbf{k}} = \frac{c}{n_g} \tag{2-17}$$

where n_g is called the group index, by analogy with n_p, the phase (refractive) index.

As shown in Figure 2-4(a), the impact of periodicity on the propagation of light is largest at frequencies adjacent to the photonic band gap because of the nonlinearity of the bands in these regions. Thus, unlike a homogeneous material, the combination of two materials in a PC has the ability to affect the velocity of light propagation as function of the light frequency, structural period, and refractive indices of the respective materials. The most dramatic example of this concept is provided by the group velocity, which becomes zero at the band edges (v_g is the local slope of the tangent to the photonic band). This reduction of the velocity with which energy flows through the material greatly enhances light-matter interactions such as optical gain, absorption, nonlinearities, etc. [11].

One of the consequences of structural periodicity and of the use of the Bloch theorem is that the dispersion relation solution should also be periodic. Using the fact that the reciprocal lattice vector in the 1D photonic crystal shown in Figure 2-3 is equal to $2\pi/L$, we have

$$\omega(k_z) = \omega(k_z \pm N * 2\pi / L) \tag{2-18}$$

where N is an integer number.

Graphically, this means that the V-shaped diagram plotted in Figure 2-4(a) should be repeated at every reciprocal lattice vector, $2\pi/L$, along the k_z axis.

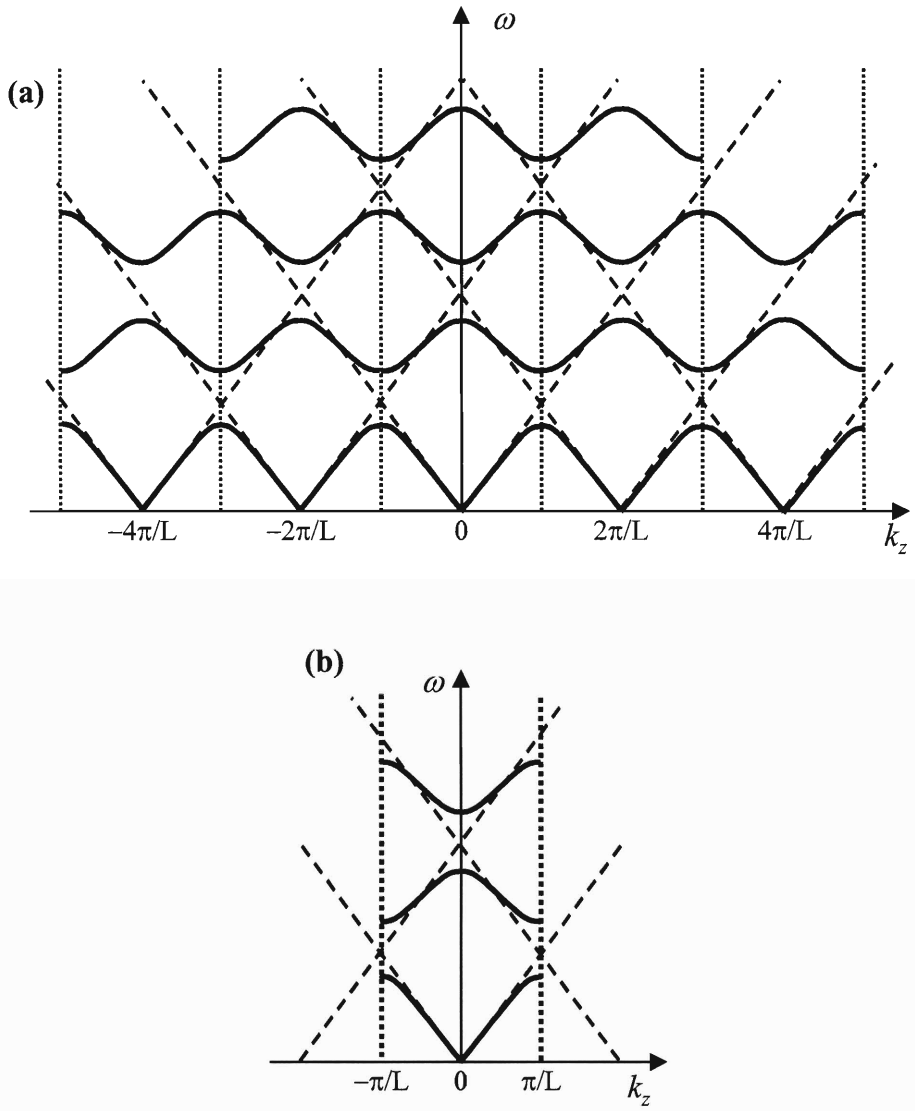

Figure 2-5 - (a) Periodic dispersion relation solution for a 1D photonic crystal. The gray area indicates the reduced Brillouin zone. **(b)** Band structure of a 1D photonic crystal obtained either by folding the $\omega(k_z)$ solution belonging to $k_z=0$ into the reduced Brillouin zone, or by generating the upper bands using the periodicity of the dispersion relation, as shown in (a).

As shown in Figure 2-5(a), the periodicity of the system leads to periodic $\omega(k_z)$ solutions having the same period as the reciprocal lattice vector of the photonic crystal, $2\pi/L$. However, as it can immediately be seen, this periodicity also allows a great simplification of the resulting fairly complicated band structure: only the region between $-\pi/L$ and π/L needs to be considered, because the rest of the diagram can be generated by

translating this special area along the k_z axis with integer multiples of the corresponding reciprocal lattice vector. This special region is called the reduced Brillouin zone, in honor of the same Brillouin cited early in the chapter. Using this simplification, we arrive at the typical form of a photonic diagram, shown in Figure 2-5(b). Note that the bands and band gaps in the reduced Brillouin zone are typically numbered from low to high frequency, for more conveniently referencing particular band structure features (e.g. a first photonic band gap forms between the first and the second band).

A limitation of the conceptual photonic band structure shown in Figure 2-5 is that it assumed that photonic band gaps form at all the intersections between photonic bands. In reality that is not true, because some intersections do not produce gaps due to symmetry reasons (the photonic bands become degenerate at the intersection point). As an example, we calculated [17, 18] the photonic band structure of a real 1D photonic crystal composed of two layers with refractive indices 1.5 and 2.2, and show the results below.

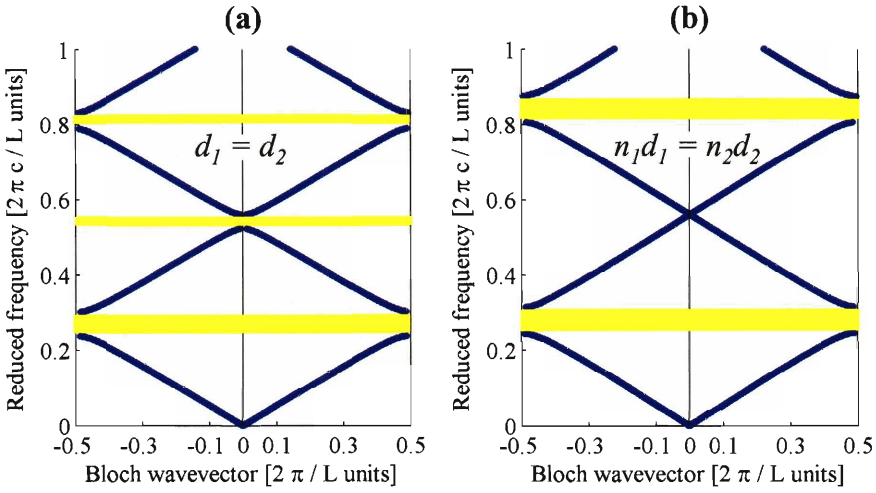

Figure 2-6 - Calculated photonic band structures for 1D photonic crystals with bilayer unit cells and n_1 = 1.5, and n_2 = 2.2. **(a)** Photonic gaps form at all band crossing points in the case when the layers have the same thickness, $d_1 = d_2$, similar to the conceptual diagram shown in **Figure 2-6**; **(b)** In the special case when the optical thickness of each layer is a constant (also called quarter-wave case) certain photonic bands remain degenerate instead of forming gaps.

Figure 2-6 shows that, for a given material system (i.e. n_1 and n_2), the choice of layer thicknesses (i.e. composition, or fill fraction) in the photonic crystal unit cell may significantly affect the photonic band structure. The comparison in Figure 2-6 contrasts the cases of equal physical thickness and of equal optical thickness (also called quarter wave stack, $n_i d_i = \lambda_0/4$, where λ_0 is a constant wavelength). Due to the more symmetric nature of the quarter wave stack, the second and the third band become degenerate at $k_z = 0$. Lastly, note that it is customary to use normalized units for the vertical (reduced frequency, $2\pi c/L$ units) and horizontal axes (reduced wave vector, $2\pi/L$ units), such that the resulting photonic band structure becomes length independent (i.e. if the photonic crystal unit cell is doubled in length, keeping everything else constant, the plotted band structures will not change).

In conclusion, this section demonstrates that most of the optical properties of photonic crystals can be obtained from the study of the dispersion relations. As an

example, the propagation characteristics of the allowed modes at a certain frequency can be described by using the phase and group velocity concepts, which are quantitatively related to $\omega(\mathbf{k})$. The photonic band structure was introduced for a 1D photonic crystal as the graphical representation of the periodic $\omega(k_z)$ solutions, and translational periodicity was used to explain the band structures in the reduced Brillouin zone. The formation of photonic band gaps at band intersections was described, and emphasized to depend on the symmetry of the structure. It was also explained that the $\omega(k_z)$ relation does not give a complete picture of how light propagates in photonic crystals - the polarizations of these eigenmodes have to be obtained separately, by calculating the eigenvectors corresponding to the eigenvalues (ω or k_z, depending on how Maxwell's equations are solved).

2.4. Conclusions

This chapter attempted to provide a brief introduction to photonic crystals, formulated in a way that would allow a reader new to the field to understand the remaining chapters of the thesis.

The key to understanding the great potential of photonic crystals to control the generation and propagation of light in materials in revolutionary new ways was explained to lie in the deep connections with solid state physics, and with the even more basic and older problem of wave propagation in periodic media. Using a 1D example, dispersion relations and photonic band structures were introduced as important tools in the study of the optical properties of photonic crystals.

2.5. References

1. Vlasov, Y. A. *Nature*, **414**, 289 (2001).

2. Urbas, A. M. *Block copolymer photonic crystals*, Ph.D. thesis, Department of Materials Science and Engineering, Massachusetts Institute of Technology (Cambridge, MA, 2003).

3. Lin, S. Y. *Nature*, **394**, 251 (1998).

4. Lin, S. Y. *Journal of the Optical Society of America B-Optical Physics*, **18**, 32 (2001).

5. Sakoda, K. *Optical properties of photonic crystals*, Springer (Berlin, 2001).

6. Yablonovitch, E. "Inhibited Spontaneous Emission in Solid-State Physics and Electronics," *Physical Review Letters*, **58**, 2059 (1987).

7. John, S. "Strong Localization of Photons in Certain Disordered Dielectric Superlattices," *Physical Review Letters*, **58**, 2486 (1987).

8. Brillouin, L. *Wave propagation in periodic structures*, 2nd Edition, Dover Publications, Inc. (New York, 1953).

9. Brillouin, L. *Wave propagation and group velocity*, Academic Press (New York, 1960).

10. Ashcroft, N. W., and Mermin, N. D. *Solid state physics*, Saunders College (Philadelphia, 1976).

11. Joannopoulos, J. D., Meade, R. D., and Winn, J. N. *Photonic crystals: molding the flow of light*, Princeton University Press (Princeton, N.J., 1995).

12. Kong, J. A. *Electromagnetic wave theory*, EMW Publishing (Cambridge, Mass., 2000).

13. Bloembergen, N. *Nonlinear optics*, W.A. Benjamin (New York, 1965).

14. Floquet, G. "Sur les équations différentielles linéaries à coefficients périodiques," *Ann. École Norm. Sup.*, **12**, 47 (1883).

15. Bloch, F. "Über die quantenmechanik der electronen in kristallgittern," *Z. Physik*, **52**, 555 (1928).

16. Johnson, S. G., and Joannopoulos, J. D. "Block-iterative frequency-domain methods for Maxwell's equations in a planewave basis," *Optics Express*, **8**, 173 (2001).

17. Yeh, P. *Optical waves in layered media*, Wiley (New York, 1988).

18. Berreman, D. W. "Optics in Stratified and Anisotropic Media: 4x4-Matrix Formulation," *Journal of the Optical Society of America B-Optical Physics*, **62**, 502 (1972).

19. Fink, Y., Winn, J. N., Fan, S., Chen, C., Michel, J., Joannopoulos, J. D., and Thomas, E. L. "A dielectric omnidirectional reflector," *Science*, **282**, 1679 (1998).

Chapter 3.
Light propagation in photonic crystals breaking space-inversion and time-reversal symmetries

In this chapter we present the results of a theoretical investigation of the general properties of photonic crystals without time-reversal and space-inversion symmetries by examining the case of 1D periodic, lossless dielectric helical media with magnetooptic activity (MO-HM). We show that photonic band gap formation in the absence of these two symmetry elements leads to a remarkable set of properties: indirect photonic band gaps (edges not aligned in k-space), backward wave propagating eigenmodes (which allow for negative refraction), very unusual non-propagating modes in the gap (their complex valued wave vectors have frequency dependent, non-zero real parts, which do not change sign for opposite decay directions), anomalous propagation and group velocity based superprism effects. Particular properties of MO-HM are discussed in detail.

3.1. Introduction

While the theoretical foundation of photonic crystals (PCs) was developed as early as the 1930s, as evidenced by Brillouin's fundamental work on wave propagation in periodic media [1], it was only in 1987 when Yablonovitch [2] and John [3] first

suggested that PCs represent a revolutionary new framework for designing materials that can exert an exceptional control over the generation and propagation of electromagnetic (EM) waves. These special properties of PCs arise from the constraints on EM wave propagation imposed by a periodic spatial variation of at least one constitutive EM parameter (e.g. dielectric permittivity $\underline{\underline{\varepsilon}}$, magnetic permeability $\underline{\underline{\mu}}$, etc.) throughout the structured matter embodying the PC. These constraints are most fundamentally related to the symmetry of the PC material structure, and also to the magnitude of the refractive index modulation [4].

In this article, we investigate the optical properties of structurally chiral, 1D periodic photonic crystals that exhibit magnetooptic activity in the presence of an external static magnetic field. Well known examples of structurally chiral, 1D periodic lattices are cholesteric liquid crystals [5] (CLCs) and so-called chiral sculptured thin films [6, 7] (CSTFs), typically fabricated by vapor deposition at a glancing angle on a catalyst coated substrate that is rotated. More recently, interference lithography has been used to fabricate similarly structured polymeric templates [8]. These materials, also called dielectric helical media [9] (HM), are inhomogeneous and periodic along their helical axis. They are chiral due to their structural rotation around the helical axis, along which a locally constant dielectric tensor is continuously rotated in the plane perpendicular to this axis (see Fig. 1). Also, it is known that the application of an external static magnetic field will induce magnetooptic activity, generally much stronger in ferromagnetic than in paramagnetic or diamagnetic materials [10]. Thus, one practical example of the material system theoretically investigated here can be fabricated by using a magnetooptical material precursor as the physical vapor deposition source in the

fabrication [7] of CSFTs, or by infiltrating a chiral structured polymeric template [8] with a sol-gel precursor for magnetooptic materials such as doped yttrium iron garnets, or various ferrites. For the purpose of our analysis, the material choice is less important, since we focus primarily on understanding the symmetry related consequences on photonic band structures, as both space-inversion and time-reversal symmetry are absent. A quantitative description of the dielectric helical medium with magnetooptic activity (MO-HM) considered in out study follows in Section 3.2, where the underlying electromagnetic constitutive relations are presented.

The propagation of light in 1D periodic, MO-HM photonic crystals has been of increased interest over the past five years. Koerdt [11], Eritsyan [12] and Gevorgyan [13] have studied the case when the static magnetic field is applied along the helical axis, and all three found evidence for nonreciprocal optical properties. More exactly, it was described that these periodic media produce different intensities of Bragg scattering (or transmission intensity) if either the propagation direction or the direction of the magnetic field is reversed. Lakhtakia [14] and Pickett [15] have theoretically studied wave propagation along the helical axis with a static magnetic field applied perpendicular to it, and found evidence for anomalous propagation and enhanced optical rotation arising from the cooperative action of magnetooptic activity and structural chirality. However, all of these existing studies focus on particular problems, without providing a clear picture of the general optical properties of this class of photonic crystals that break both space-inversion and time-reversal symmetries.

Thus, in this chapter, we present our results of a comprehensive study of the optical properties of 1D periodic MO-HM photonic crystals. We employ both analytic

and numerical tools to determine the dispersion relation, $\omega(\mathbf{k})$, and the corresponding photonic band structure, as a way to gain insight into the optical properties of this periodic medium. We are able to validate that the dispersion relation can indeed be nonreciprocal, $\omega(\mathbf{k}) \neq \omega(-\mathbf{k})$, and find that this holds for as long as the propagation direction is not perpendicular to either the helical axis or the static magnetic field. Moreover, by investigating the dispersion surfaces, we find optical properties that have not been previously reported. We show that the application of an external magnetic field leads to propagating eigenmodes with opposite phase and group velocities ($\mathbf{v_p}$, $\mathbf{v_g}$) along the direction of the magnetic field. Waves with antiparallel phase and group velocities are called backward waves, and have been long known in the microwave literature [16] and more recently investigated in the context of left-handed materials [17]. We further show that, just as in the case of left-handed materials, the presence of backward waves can lead to the negative refraction of waves incident at the air - photonic crystal interface, when the helical axis of the MO-HM photonic crystal and the magnetic field have nonzero components along the interface in the incidence plane. Moreover, we find inflection points in the isofrequency contours that are uncharacteristic of 1D periodic HM without magnetooptic activity. These inflection points are the source of the previously reported anomalous propagation [14] and in practice can give rise to photon focusing caustics [18], or self-collimation phenomena [19]. Moreover, being inside the reduced Brillouin zone, the eigenmodes around these inflection points are propagating freely and display large changes of their group velocity directions for only small changes of the wave vector or frequency, similar to the previously reported superprism effect [20] in PC.

However, perhaps the most peculiar finding is that this class of photonic crystals can display indirect photonic band gaps, by analogy with electronic counterparts (here, band anticrossing leads to band edges that are not aligned in k-space). In this case, the band edges move away from $\mathbf{k} = 0$ in the reduced Brillouin zone, so that the non-propagating eigenmodes in the band gap (with complex wave vectors) do not fit anymore the definition of evanescent modes ($\mathrm{Re}\{\mathbf{k}\}=0$, $\mathrm{Im}\{\mathbf{k}\}\neq 0$). Even though we show that these modes still do not allow for a net power transport, besides an imaginary part, their wave vectors also have a *frequency dependent* nonzero real part, a peculiar fact since our material system is lossless. Furthermore, in one of the directions of "non-propagation," these band gap modes share a similarity with backward waves, as their $\mathrm{Re}\{\mathbf{k}\}$ points oppositely to the direction of exponential decay (given by the sign of $\mathrm{Im}\{\mathbf{k}\}$). Thus, we finally make the argument that all of these findings represent universal optical properties of the general class of photonic crystals lacking space-inversion and time-reversal symmetries.

This chapter is organized as follows. In Section 3.2, we present the constitutive relations that define the 1D periodic MO-HM photonic crystal. For clarity and perspective, we review in Section 3.3 the optical properties of homogeneous media that break space-inversion and time-reversal symmetries. In Section 3.4, we analytically examine the problem of wave propagation along the helical axis, and show the fundamental importance of the relative orientations of the static magnetic field inducing magnetooptic activity, the structural chirality axis and the wave vector direction. In Section 3.5, we describe the numerical approach we employed to calculate the photonic band structure for arbitrary propagation directions and magnetic field orientations, and to

calculate the transmission properties of finite portions of the crystal. Finally, we present in Section 3.6 a detailed analysis of the resulting photonic band structures and isofrequency contours for the different situations mentioned above. A note about notation in this chapter: vectors are in bold-face, second-rank tensors and matrices are in bold-face with two underlines, and we use the compact dyadic notation [21] to describe the elements of tensors and matrices.

3.2. Constitutive Relations

In this section we will present the constitutive relations that define 1D periodic, helical media with magnetooptic activity (MO-HM). Since we are interested in the symmetry-induced effects on the photonic band structure as both the space-inversion (S-I) and time-reversal (T-R) symmetries are broken, we make a few simplifying assumptions that, while not reducing the generality of the results, make the analysis more clear. First, we consider a dielectric helical medium, thus only the dielectric permittivity tensor ($\underline{\underline{\boldsymbol{\varepsilon}}}$) is varying in space, while $\mu_r = 1$. Second, we assume that the application of an external static magnetic field breaks T-R symmetry through magnetooptic effects, thus affecting the off-diagonal elements of the dielectric permittivity tensor. Similar considerations can apply to the magnetic permeability tensor ($\underline{\underline{\boldsymbol{\mu}}}$), particularly as a function of the frequency of the electromagnetic waves of interest. However, it is known [22] that analogous results are obtained if working in either $\underline{\underline{\boldsymbol{\varepsilon}}}$ or $\underline{\underline{\boldsymbol{\mu}}}$ frameworks, therefore we develop our analysis around $\underline{\underline{\boldsymbol{\varepsilon}}}$ without sacrificing the generality of the

results. Lastly, we consider a lossless material system, thus neglecting the effects of linear and circular dichroism.

Therefore, the electromagnetic constitutive relations of the linear, dielectric helical medium with magnetooptic activity analyzed in this chapter can be written as:

$$\begin{aligned} \mathbf{D}(\mathbf{r}) &= \varepsilon_0 \cdot \underline{\underline{\boldsymbol{\varepsilon}}}_{xyz}(\mathbf{r}) \cdot \mathbf{E}(\mathbf{r}) \\ \mathbf{B}(\mathbf{r}) &= \mu_0 \cdot \mathbf{H}(\mathbf{r}) \end{aligned} \tag{3-1}$$

In the above expression, $\underline{\underline{\boldsymbol{\varepsilon}}}_{xyz}(\mathbf{r})$ represents the spatially periodic dielectric permittivity tensor in the *xyz* laboratory coordinate frame. Choosing the periodicity direction along **z** (same as the helical axis), the dielectric tensor can be written in compact dyadic notation:

$$\begin{aligned} \underline{\underline{\boldsymbol{\varepsilon}}}_{xyz}(z) &= \underline{\underline{\mathbf{S}}}_z(z) \cdot \underline{\underline{\boldsymbol{\varepsilon}}}_{ref} \cdot \underline{\underline{\mathbf{S}}}_z^{-1}(z) + \varepsilon_g \, \mathbf{gg} + i\gamma \, \mathbf{g} \times \underline{\underline{\mathbf{I}}} \\ \underline{\underline{\boldsymbol{\varepsilon}}}_{ref} &= \varepsilon_{11} \, \mathbf{xx} + \varepsilon_{22} \, \mathbf{yy} + \varepsilon_{33} \, \mathbf{zz} \\ \underline{\underline{\mathbf{S}}}_z(z) &= (\mathbf{xx} + \mathbf{yy})\cos(\phi(z)) + (\mathbf{yx} - \mathbf{xy})\sin(\phi(z)) + \mathbf{zz} \\ \mathbf{g} &= \mathbf{x}\cos(\theta_g) + \mathbf{z}\sin(\theta_g) \\ \underline{\underline{\mathbf{I}}} &= \mathbf{xx} + \mathbf{yy} + \mathbf{zz} \end{aligned} \tag{3-2}$$

where $\underline{\underline{\boldsymbol{\varepsilon}}}_{ref}$ is the dielectric tensor in the reference material coordinate frame (assumed biaxial above, for generality), $\underline{\underline{\mathbf{S}}}_z(z)$ is a rotation matrix, and **g** is the magnetogyration vector [10]. This unit vector corresponds to the direction along which circular birefringence (or magnetooptic activity) is induced, and for most materials it points along the external static magnetic field. Without loosing generality, we chose to constrain **g** to lie in the **x-z** plane, with an orientation defined by a polar angle θ_g measured from x, $0 \le \theta_g \le 2\pi$ (see Eq. 2). As a reminder [21], the dyadic product of two vectors **uv** is equal to a square matrix with elements given by the scalar product $u_i v_j$.

As written in Eq. 2, the $\underline{\underline{\boldsymbol{\varepsilon}}}_{xyz}$ tensor shows that magnetooptic activity ($|\mathbf{g}| \neq 0$) causes the locally biaxial, rotating $\underline{\underline{\boldsymbol{\varepsilon}}}_{ref}$ tensor to acquire anti-symmetric off-diagonal terms ($i\gamma \mathbf{g} \times \underline{\underline{\mathbf{I}}}$, responsible for magnetooptic rotation), and to have its diagonal elements modified by a constant ε_g (usually [10] much smaller than ε_{ii}, $i = 1, 2, 3$).

Finally, the structural rotation is quantified by the matrix $\underline{\underline{\mathbf{S}}}_z(z)$, whose elements shown in Eq. 2 are defined in terms of the azimuthal rotation angle $\phi(z)$ (see Figure 3-1), which is assumed here [23] to vary linearly with z:

$$\begin{aligned} \phi(z) &= q\,z \\ q &= q_0(2\pi / L) \end{aligned} \tag{3-3}$$

where $q_0 = \pm 1$ is a parameter used to describe the right (+1) or left (-1) handedness of the HM. We will also employ a vector $\mathbf{q}$, of magnitude q shown above, to describe the handedness of the structural rotation according to the right-hand rule (thus, for $q_0 = +1$, $\mathbf{q}$ points along $+\mathbf{z}$).

The structural rotation is conceptually depicted in Fig. 1, where the orientation of an arbitrary vector in the material coordinate frame is traced along the periodicity axis, $\mathbf{z}$. Note that we define the spatial period of this 1D photonic crystal as the length L along the $\mathbf{z}$ axis for which the dielectric tensor $\underline{\underline{\boldsymbol{\varepsilon}}}_{xyz}$ is rotated with a full angle of 2π, since $\phi(z+L)=\phi(z) + 2\pi q_0$ (see Eq. 3-3).

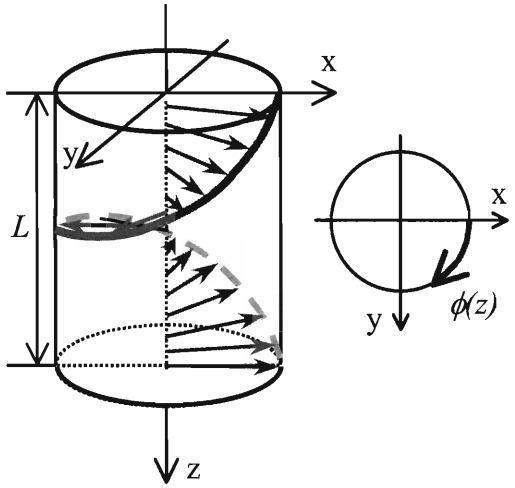

Figure 3-1 - Conceptual representation of the structural rotation throughout the unit cell of a 1D chiral photonic crystal showing the periodic, right-handed (RH) continuous twist along the **z** axis of an arbitrary vector with fixed orientation in the local material coordinate system. The spatial period L is defined for a full 2π rotation, $\phi(z+L) = \phi(z) + 2\pi$.

3.3. Electrodynamics of homogeneous media without time-reversal and time-inversion symmetries

In this section, we review the main results of previous studies of EM wave propagation in homogeneous media that break space-inversion and time-reversal symmetry (or display both reciprocal and non-reciprocal chirality features). The purpose of this section is to identify those optical properties that are sufficiently general to allow analogies based on symmetry considerations with those of our system, 1D periodic MO-HM photonic crystals.

A first category of studies revolves around the magnetochiral effect, related to the change of the optical properties of natural optically active media on the application of an external static magnetic field. More of a curiosity in physical chemistry with "no apparent practical use," as discussed in a recent review by Wagnière [24], the magnetochiral effect is manifested as a very small, but measurable [25, 26] change of the

refractive index of a chiral molecular medium when a static magnetic field is applied along the propagation direction of an incident wave. As expected from the Kramers-Kronig relations [27], the magnetochiral effect was predicted [28-30] and later experimentally shown to also manifest in both the absorption [31] and emission [32] of EM radiation. From a quantitative electrodynamics point of view, the optical properties of these non-magnetic materials in the presence of the static magnetic field are described [33] by the following constitutive equation:

$$\begin{aligned} \mathbf{D}(\mathbf{r}) &= \varepsilon_0 \, \underline{\underline{\varepsilon}} \, \mathbf{E}(\mathbf{r}) \\ \underline{\underline{\varepsilon}}(\omega, \mathbf{k}, \mathbf{B_0}) &= \varepsilon(\omega)\underline{\underline{\mathbf{I}}} + i\alpha(\omega)\left(\mathbf{k} \times \underline{\underline{\mathbf{I}}}\right) + i\beta(\omega)\left(\mathbf{B_0} \times \underline{\underline{\mathbf{I}}}\right) + \gamma(\omega)\left(\mathbf{k} \bullet \mathbf{B_0}\right) \end{aligned} \tag{3-4}$$

where ω is the angular frequency of light, $\mathbf{B_0}$ is the external static magnetic field, and the frequency dependent parameters α, β, and γ describe, in order, natural optical activity, magnetooptical activity and magnetochiral activity in homogeneous and isotropic media.

A second set of investigations, comes from the microwave community's interest in the so-called "Faraday chiral media" [34]. Also called gyrotropic-gyrochiral [35], these are described as homogeneous materials (or homogenized composites) with both Faraday rotation and natural optical activity, as embodied by chiroferrites and chiroplasmas. Although conceptually similar to the above-described magnetochiral molecular materials, and, as we will describe later, with quite similar properties, electrodynamics in Faraday chiral media employs constitutive relations that are nonequivalent to those of Eq. (3-4). While the detailed form of the constitutive tensors is subject of discussions [36], the generally accepted constitutive relations for gyrotropic-gyrochiral media are of the following form:

$$\begin{aligned}
\mathbf{D} &= \varepsilon_0 \underline{\underline{\boldsymbol{\varepsilon}}}\,\mathbf{E} + i\sqrt{\varepsilon_0\mu_o}\,\xi^c\mathbf{H} \\
\mathbf{B} &= -i\sqrt{\varepsilon_0\mu_o}\,\xi^c\,\mathbf{E} + \mu_0\,\underline{\underline{\boldsymbol{\mu}}}\,\mathbf{H} \\
\underline{\underline{\boldsymbol{\varepsilon}}} &= \varepsilon_a\underline{\underline{\mathbf{I}}} + \varepsilon_b\,\mathbf{gg} + i\varepsilon_g\,\mathbf{g}\times\underline{\underline{\mathbf{I}}} \\
\underline{\underline{\boldsymbol{\mu}}} &= \mu_a\underline{\underline{\mathbf{I}}} + \mu_b\,\mathbf{gg} + i\mu_g\,\mathbf{g}\times\underline{\underline{\mathbf{I}}}
\end{aligned} \tag{3-5}$$

where ξ^c is the isotropic optical activity parameter (or a second-rank tensor [36] for a fully bianisotropic medium), and the vector $\mathbf{g}$ is the magnetogyration vector (see Section 3.2). Note that chiroplasmas are defined as having $\underline{\underline{\boldsymbol{\mu}}} = \mu\underline{\underline{\mathbf{I}}}$, while chiroferrites have $\underline{\underline{\boldsymbol{\varepsilon}}} = \varepsilon\underline{\underline{\mathbf{I}}}$, instead of the corresponding gyrotropic tensors shown above.

It is very interesting to observe the similarities between the results from the two above-introduced research directions and the findings of the theoretical and experimental studies of inhomogeneous, periodic media [11-15]. Leaving aside the differences arising from specific properties of the material systems (e.g. plasma frequency for chiroplasmas), from a qualitative point of view it seems that EM propagation in all of these types of materials has the same general features. Most prominently, in all cases it is reported that the optical properties are different if the propagation direction is reversed, i.e. the dispersion relation is nonreciprocal, $\omega(\mathbf{k})\neq\omega(-\mathbf{k})$. This is experimentally proven in the case of magnetochiral molecular media beyond doubt, where the observed differences in the refraction [26], absorption [31] and emission [32] of waves in opposite directions along an external static magnetic field are intuitive consequences of the differences in the phase ($\mathbf{v_p}$) and group ($\mathbf{v_g}$) velocities for opposite propagation directions, since:

$$\begin{aligned}
\mathbf{v_p} &= \omega(\mathbf{k})/\mathbf{k} \\
\mathbf{v_g} &= \partial\omega(\mathbf{k})/\partial\mathbf{k}
\end{aligned} \tag{3-6}$$

Thus, the nonreciprocal dispersion relation fundamentally leads to a set of optical properties regardless of the specific details of the material system, be it a homogeneous or an inhomogeneous periodic material. It might seem surprisingly simple, but this important relation allows one to qualitatively predict all the above-cited differences in the refraction, absorption, emission, optical rotation etc. of waves traveling in opposite directions.

A particularly interesting observation was made by Engheta *et al* [34], who theoretically studied EM wave propagation in Faraday chiral media. The autors reported that, in chiroplasmas, certain circularly polarized propagating eigenmodes are backward waves, having phase velocities pointing opposite of the group velocity. This intriguing property is attributed by the authors to the competition between the gyration induced by the external magnetic field on the electrons of the plasma and the gyration induced by counter-rotating circularly polarized eigenmode. To the best of our knowledge, no other investigation of media that break both time and space inversion symmetry mentions this property. The work of Engeta *et al.* is very interesting because we find that backward waves are also possible in 1D periodic, MO-HM photonic crystals, as we show in Section 3.6, which suggesting that, overall, the presence of backward waves is another symmetry-related property of this class of materials.

3.4. Axial wave propagation: analytic dispersion relation.

In this section we derive an analytic expression for the dispersion relation that describes wave propagation along the helical axis of a 1D periodic, MO-HM. Although analytic solutions of Maxwell's equations are very difficult to obtain for most periodically

inhomogeneous media, by limiting the wave propagation to only $\mathbf{k}=\mathbf{z}k_z$ (axial propagation, since $\mathbf{q}\|\mathbf{z}$, see Eq. 3), and the magnetogyration vector to also point along the helical axis, $\mathbf{g}\|\mathbf{z}$, it is possible to reach an analytic solution for $\omega(k_z)$ as shown below. We follow the usual solution employed for uniformly rotating, 1D periodic media, treated in the most general case by Lakhtakia for helical bianisotropic media [9].

In a source-free space region, assuming $\exp(-i\omega t)$ time harmonic EM fields, Maxwell's equations can be reduced to:

$$\nabla \times \nabla \times \mathbf{E}(\mathbf{r},t) = \omega^2 \mu_0 \mathbf{D}(\mathbf{r},t) \tag{3-7}$$

With the assumption of axial propagation, $\mathbf{k}=\mathbf{z}k_z$, Eq. (3-7) further leads to:

$$\nabla \times \nabla \times \mathbf{E}(\mathbf{r},t) = \omega^2 \mu_0 \mathbf{D}(\mathbf{r},t) \tag{3-8}$$

where ∂_{zz}^2 denotes the second derivative with respect to z, and c is the speed of light in vacuum.

Following the classic approach of deVries [37], we rewrite Eq. (3-8) in a coordinate frame that rotates with respect to the Cartesian lab coordinate frame, such that the transformed dielectric tensor becomes a constant (this coordinate transformation is known as the Oseen transformation [38]). Naturally, the rotating frame corresponds to the local material coordinate system, where the dielectric tensor is just:

$$\underline{\underline{\boldsymbol{\varepsilon}}}' = \underline{\underline{\boldsymbol{\varepsilon}}}_{ref} + i\gamma\, \mathbf{z} \times \underline{\underline{\mathbf{I}}} \tag{3-9}$$

Note that the above expression is derived from Eq. (3-2), taking $\mathbf{g}\|\mathbf{z}$ and neglecting the effect of magnetooptic activity on the diagonal tensor elements, since it is known [10] that $\varepsilon_g << \varepsilon_{ref,ii}$. This assumption is additionally justified because the small

contribution of ε_g to the anisotropy of the material is already captured in the model by using of a biaxial $\underline{\underline{\boldsymbol{\varepsilon}}}_{ref}$.

The coordinate transformation for the electric field can be written as:

$$\mathbf{E}(z) = \underline{\underline{\mathbf{S}}}_z(z)\mathbf{E}'(z) \tag{3-10}$$

where $\mathbf{E}' = (E_1', E_2', E_3')$ is the electric vector in the rotating coordinate frame.

Noting that for axial propagation $E_3' = 0$, after the coordinate transformation to the rotating frame, Eq. (3-8) leads to:

$$\begin{pmatrix} \partial_{zz}^2 - (\partial_z\phi)^2 & -(\partial_{zz}^2\phi) - 2(\partial_z\phi) \\ (\partial_{zz}^2\phi) + 2(\partial_z\phi) & \partial_{zz}^2 - (\partial_z\phi)^2 \end{pmatrix} \begin{pmatrix} E_1' \\ E_2' \end{pmatrix} = -\frac{\omega^2}{c^2}\underline{\underline{\boldsymbol{\varepsilon}}}' \begin{pmatrix} E_1' \\ E_2' \end{pmatrix} \tag{3-11}$$

where ∂_z denotes the first derivative with respect to z. Note that the above result is general, and applies to any distribution of the structural rotation, $\phi(z)$.

Substituting in Eq. (3-11) the linearly varying $\phi(z)$ from Eq. (3-3), we obtain:

$$\begin{pmatrix} \frac{\omega^2}{c^2}\varepsilon_{11} - k_z^2 - q^2 & \frac{\omega^2}{c^2}\varepsilon_{12} - 2iqk_z \\ \frac{\omega^2}{c^2}\varepsilon_{21} + 2iqk_z & \frac{\omega^2}{c^2}\varepsilon_{22} - k_z^2 - q^2 \end{pmatrix} \begin{pmatrix} E_1' \\ E_2' \end{pmatrix} = 0 \tag{3-12}$$

where ε_{ij} is the (i,j) component of the permittivity tensor $\underline{\underline{\boldsymbol{\varepsilon}}}_{ref}$ (note that $\varepsilon_{12} = -i\gamma = -\varepsilon_{21}$ if $|\mathbf{g}| \neq 0$, see Eq. 3-9).

Finally, solving Eq. (3-12) for nontrivial solutions yields the dispersion relation $\omega(k_z)$, very similar in form to that obtained by Eritsyan [12] for the case of cholesteric liquid crystals in the presence of an axial magnetic field:

$$\frac{\omega^4}{c^4}\left(\varepsilon_{11}\varepsilon_{22}-\gamma^2\right)-\frac{\omega^2}{c^2}\left((\varepsilon_{11}+\varepsilon_{22})(k_z^2+q^2)-4\gamma k_z q\right)+\left(k_z^2-q^2\right)^2=0 \qquad (3\text{-}13)$$

The above equation is a very important result. The odd-powered product $\gamma k_z q$ represents the origin of the expected nonreciprocal optical properties. Even though in an implicit form, Eq. (3-13) shows that the frequency solutions $\omega(k_z)$ are affected by a sign change of any one of γ, k_z or q. This entails, for example, that electromagnetic waves will be subject to different dispersion relations as the propagation direction is reversed from +**z** to -**z**, i.e. $\omega(k_z) \neq \omega(-k_z)$, or that changing the sign of two of the three quantities, e.g. $\omega(\gamma, k_z) = \omega(-\gamma, -k_z)$, will result in the same dispersion relation, and thus the same optical properties displayed by the material. Similarly, changing the handedness of the structural chirality (±**q**), or the direction of the magnetogyration vector direction (±**g**, equivalent to $\pm\gamma$), will also affect the $\omega(k_z)$ solutions. It can already be guessed that the presence of this $\gamma k_z q$ term captures most of the optical properties reviewed in the previous section, but we postpone the detailed discussion of these issues to Section 3.6.

3.5. Arbitrary wave propagation: numerical modeling with the transfer matrix method

The analytic solution for the dispersion relation, outlined in the previous section, becomes hard to obtain for arbitrary wave propagation (**k** = **x**k_x + **z**k_z) and/or arbitrary orientation of the magnetogyration vector (see Eq. 2). For example, when **g**||**x** (an external magnetic field pointing along **x** and inducing magnetooptic activity), the elements of the dielectric tensor in the rotating coordinate frame, $\underline{\underline{\varepsilon}}'$, are not constant

anymore, so the system of differential equations in Eq. (3-11) becomes very difficult to solve analytically.

A practical numerical approach for studying the optical properties of such 1D periodic photonic crystals is the transfer matrix method [39]. The strength of this method lies in allowing full characterization of the optical properties of both finite and infinite structures, in a relatively simple to implement mathematical framework. In the following sections we describe how this method was used to calculate the photonic band structures (propagating and evanescent eigenmodes in infinite crystals), and the reflection and transmission of waves from finite 1D periodic, helical media with magnetooptic activity.

3.5.1. Bloch Solutions in Infinite 1D Periodic MO-HM Photonic Crystals

In order to find the Bloch eigenmodes describing wave propagation in infinite, 1D periodic chiral photonic crystals with magnetooptic activity, we need to first derive the transfer matrix relating the electromagnetic field components across a translation unit cell, along the propagation direction.

We begin by discretizing the spatially varying dielectric tensor $\underline{\underline{\boldsymbol{\varepsilon}}}_{xyz}(z)$ along the **z** axis, and approximate it locally, in a particular interval (z_j, z_j+h_j), by a constant $\underline{\underline{\boldsymbol{\varepsilon}}}_j \equiv \underline{\underline{\boldsymbol{\varepsilon}}}_{xyz}(z_j)$. The local value of the dielectric tensor is evaluated by using the definitions in Eq. (3-2), where the rotation angle is the discretized quantity, $\phi(z_j)$ given by Eq. (3-3). The propagation of a wave of frequency ω, restricted in the (x, z) plane (**k** = $\mathbf{x}k_x + \mathbf{z}k_z$), can be then conveniently described by Maxwell's equations written in matrix form [39, 40]

$$\partial_z \boldsymbol{\Psi}(z) = i\omega \underline{\underline{\underline{\underline{\mathbf{M}}}}}(\omega, \underline{\underline{\boldsymbol{\varepsilon}}}, \mathbf{k})\, \boldsymbol{\Psi}(z) \tag{3-14}$$

where $\mathbf{\Psi}(z) = [E_x(z), E_y(z), H_x(z), H_y(z)]^{\mathrm{T}}$. Note that Eq. (3-14) represents a system of only four differential equations, because the choice of restricting the wave propagation in the (**x**, **z**) plane leads to algebraic (instead of differential) equations for the E_z and H_z field components.

The elements of the matrix $\underline{\underline{\mathbf{M}}}(\omega, \underline{\underline{\boldsymbol{\varepsilon}}}, \mathbf{k})$ were calculated following the popular 4x4 transfer matrix approach [39], and will not be reproduced here due to their complexity. The system of differential equations in Eq. (3-14), having constant coefficients, leads to the simple solution:

$$\mathbf{\Psi}(z + h_j) = \underline{\underline{\mathbf{P}}}_j \, \mathbf{\Psi}(z) \tag{3-15}$$

Equation (3-15) represents the essence of the transfer matrix method, in which the vectors of the electromagnetic fields at two distinct positions along the propagation axis (here z and $z+h_j$) are related by a square matrix. In our case, h_j is the spatial discretization step for the rotating dielectric tensor. Thus, the matrix $\underline{\underline{\mathbf{P}}}_j$ is:

$$\underline{\underline{\mathbf{P}}}_j = \exp\left(i\,\omega h_j \, \underline{\underline{\mathbf{M}}}(\omega, \underline{\underline{\boldsymbol{\varepsilon}}}_j, \mathbf{k})\right) \tag{3-16}$$

We note that Eq. (3-16) was numerically evaluated by employing the third method of the many reviewed by Moler [41], as implemented by the matrix exponential function in MATLAB ®.

By discretizing the spatial period L in N intervals of thickness $h_j = L/N$, and recalling [22] that the boundary conditions for **E** and **H** fields require the vector $\mathbf{\Psi}(z)$ to be continuous across the boundaries of each of these N intervals, we obtain:

$$\mathbf{\Psi}(z+L) = \left(\prod_{j=N}^{1} \underline{\underline{\mathbf{P}}}_j \right) \mathbf{\Psi}(z) = \underline{\underline{\mathbf{P}}}\, \mathbf{\Psi}(z) \tag{3-17}$$

where $\underline{\underline{\mathbf{P}}}$ is the transfer matrix relating the EM fields $\mathbf{\Psi}$ across an entire unit cell.

Finally, the Bloch wave vectors can be obtained by solving:

$$\det\left[\underline{\underline{\mathbf{P}}} - \exp(ik_z L)\right] = 0 \tag{3-18}$$

Solutions of the above equation typically yield four k_z eigenvalues, which represent propagating eigenmodes in the PC if real-valued, or evanescent (exponentially decaying modes) if complex-valued. In the case of the usual *reciprocal* photonic crystals, the four eigenvalues are in fact two pairs of wave vectors with equal magnitudes, i.e. $k_{z,1} = -k_{z,3}$ and $k_{z,2} = -k_{z,4}$, which lead to identical dispersion relations regardless of the direction of propagation along a given axis, $\omega(\mathbf{k}) = \omega(-\mathbf{k})$. However, in light of the predictions of the analytic model for the materials considered here as described in Section 3.4, we expect that Eq. (3-18) will yield four different k_z solutions, numerically proving the case of nonreciprocal dispersion relations.

It should be pointed out that the accuracy of the $\omega(k_z)$ solutions using this method based on a discrete representation of the structure improves with increasing the number of steps, N, used to approximate the real, continuously rotating structure. In our numerical studies, we chose a value of $N = 90$, which if further increased did not result in a noticeable change of the $\omega(k_z)$ curves or of the eigenmodes' polarization states (both amplitudes and phase differences were examined).

3.5.2. Reflection and Transmission Coefficients of a Finite Thickness 1D Periodic MO-HM Photonic Crystal

The propagation of plane waves through finite size 1D photonic crystals can be easily described by building on the result for the transfer matrix of the unit cell, shown in Eq. (3-17). For a stack composed of $N_{periods}$, the electromagnetic fields at the incidence and transmission interfaces of the finite stack are related by:

$$\Psi_t = \left(\prod_{m=N_{periods}}^{1} \underline{\underline{\mathbf{P}}}_m \right) (\Psi_i + \Psi_r) = \underline{\underline{\mathbf{P}}}_{total} (\Psi_i + \Psi_r) \tag{3-19}$$

where Ψ_i, Ψ_r and Ψ_t describe the incident, reflected and transmitted fields, and $\underline{\underline{\mathbf{P}}}_{total}$ is the transfer matrix for the entire finite crystal.

Assuming linearly polarized incident waves, it is easy to derive [39] the transmission coefficients (and reflection coefficients, by analogy) as:

$$\begin{pmatrix} E_{t,p} \\ E_{t,s} \end{pmatrix} = \begin{pmatrix} t_{pp} & t_{ps} \\ t_{sp} & t_{ss} \end{pmatrix} \begin{pmatrix} E_{i,p} \\ E_{i,s} \end{pmatrix} \tag{3-20}$$

where the subscripts s and p represent the two orthogonal linear polarizations, and i and t denote the incident and transmitted fields.

A similar approach can be used to study the propagation in a circularly polarized eigenmode basis, by replacing the linear polarized fields in Eq. (3-20) with the equivalent [15] linear combination of right-hand (R) and left-hand (L) circularly polarized eigenmodes. For axial propagation, $\mathbf{k}=\mathbf{z}k_z$, the two sets of eigenmodes are related by:

$$\begin{pmatrix} E_x \\ E_y \end{pmatrix} = \begin{pmatrix} 1 & 1 \\ i & -i \end{pmatrix} \begin{pmatrix} E_R \\ E_L \end{pmatrix} \tag{3-21}$$

Thus, the reflection and transmission coefficients in the circularly polarized eigenmode basis can be derived by using the field transformation from Eq. (3-21) to replace the **x** and **y** components of the vectors Ψ in the transfer matrix equation (Eq. 3-19). The resulting matrix equation can be solved to yield similar coefficient matrices:

$$\begin{pmatrix} E_{t,L} \\ E_{t,R} \end{pmatrix} = \begin{pmatrix} t_{LL} & t_{LR} \\ t_{RL} & t_{RR} \end{pmatrix} \begin{pmatrix} E_{i,L} \\ E_{i,R} \end{pmatrix} \tag{3-22}$$

where t_{LR}, for example, is the transmission coefficient for a left-hand circularly polarized transmitted wave originating from a right-hand circularly polarized incident wave.

Note that, regardless of the polarization framework chosen to describe the wave propagation through these non-dissipative photonic crystals, power conservation is always satisfied:

$$|r_{ii}|^2 + |r_{ji}|^2 + |t_{ii}|^2 + |t_{ji}|^2 = 1 \tag{3-23}$$

where the subscripts i and j can be either *s* or *p* (see Eq. 3-20), or, in the case of circularly polarized waves, either *R* or *L* (see Eq. 3-22).

3.6. Effect of magnetooptic activity on the photonic band structure of 1D periodic helical media

In this section, we investigate the photonic band structure of 1D periodic, chiral photonic crystals in the presence of magnetooptic activity. We examine the effects of the magnetooptic activity strength (**g** in Eq. 3-2) and of the orientation of the magnetogyration vector (γ in Eq. 3-2) with respect to the propagation direction (**k**). We

begin by presenting the photonic band structure, $\omega(k_z)$, for axial propagation ($\mathbf{k} \parallel \mathbf{q} = q\mathbf{z}$), and follow with an analysis of the isofrequency contours for understanding the optical response for arbitrary wave propagation ($\mathbf{k} = \mathbf{x}k_x + \mathbf{z}k_z$).

The computational tools we use in this section are numerically-obtained photonic band structures and isofrequency sections through the corresponding dispersion surface $\omega(k_x, k_z)$. We also calculate the transmission spectra for finite pieces of the photonic crystal (see Section 3.5).

3.6.1. Photonic Band Structure of 1D Periodic MO-HM with g||q.

The analytic model presented in Section 3.4 has already shown that waves propagating parallel to both the chirality axis and magnetogyration vector are subject to nonreciprocal dispersion relations, $\omega(\mathbf{k}) \neq \omega(-\mathbf{k})$. This situation is depicted in Figure 3-2, where we show numerically calculated photonic band structures for the two main orientations of the static magnetic field, while keeping the propagation along the helical axis ($\mathbf{k}||\mathbf{q}||\mathbf{z}$). The black and thin curves correspond to a perpendicular magnetogyration vector ($\mathbf{k} \perp \mathbf{g}$, $\mathbf{g}||\mathbf{x}$), while the thicker and gray curves represent the $\mathbf{k}||\mathbf{g}$ case. The first observation we make is that the photonic band structure for the $\mathbf{k} \perp \mathbf{g}$ case looks essentially identical to the band structure of a simple 1D periodic helical medium without magnetooptic activity ($\gamma = 0$ in Eq. 3-2). Although we will discuss the subtle differences in Section 3.6.2, for now we also use this band structure as a reference for the $\gamma = 0$ case.

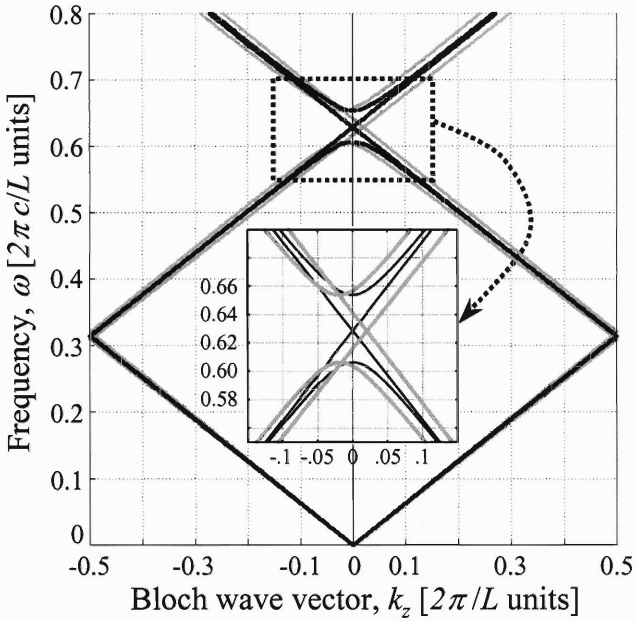

Figure 3-2 - Numerically calculated photonic band structure for axial propagation, $\omega(k_z, k_x=k_y=0)$, at two orientations of the magnetogyration vector, **g**||**z** (gray curves), and **g**||**x** (black curves). Inset shows a magnification of the photonic band structure near the bandgap. Note that the **g**||**x** band structure is also valid for the case when no magnetooptic activity is present, describing a simple dielectric helical medium.

It is clear from Figure 3-2 that the presence of magnetooptic activity leads to nonreciprocal dispersion relations when **k**||**g**||**q**, because the band structure is not symmetric with regard to the center of the reduced Brillouin zone (k_z = 0 vertical axis). To explain the effect of magnetooptic activity, it is worth to first analyze the photonic band structure of a simple dielectric helical medium (corresponding to $\gamma = 0$ in the current analysis). It is known that the eigenmodes of a lossless 1D periodic helical medium are left- and right-hand circularly polarized (LCP and RCP) [37]. As magnified in the inset in Figure 3-2, only one polarization develops a photonic band gap. This is the origin of the circular Bragg scattering [37], when a circularly polarized wave of appropriate wavelength and with the same handedness as the structural rotation of the HM is completely reflected along the helical axis. To the contrary, all the counter-

rotating eigenmodes propagate freely through the photonic crystal, experiencing no scattering.

Returning now to the case of MO-HM ($\gamma \neq 0$), we find that, unlike the band structure, the eigenmode polarizations are not affected by magnetooptic activity - they are still circularly polarized away from the band gap, and linearly polarized at the gap edges. One example of the effects of magnetooptic activity on the band structure is that, for $\mathbf{g}\|\mathbf{k}\|\mathbf{q}$, visually, a horizontal translation of the band gap edges occurs opposite to that of the degeneracy point at the intersection of the bands without a gap (modes with opposite CP than the handedness of the HM). A more physical explanation for how the nonreciprocal band structure forms can be presented by on the basis of the observation that applying a static magnetic field along the helical axis affects the HM's circularly polarized eigenmodes in opposite ways. As it can be seen from the inset of Figure 3-2, the presence of magnetooptic activity causes the group velocity (v_g, see Eq. 3-6) of the eigenmodes to either increase or decrease (the slope of a photonic band gets either steeper or shallower), depending on the particular modes' polarization handedness and direction of propagation. Importantly, these changes of band slopes (or v_g) are reversed for when reversing the direction of the magnetic field ($\pm\mathbf{g}$), the propagation direction ($\pm\mathbf{k}$), or the structural handedness ($\pm\mathbf{q}$), just as one would expect from Eq. (3-13). This is the qualitative reason for which the degeneracy point's horizontal shift is opposite to that of the band gap edges, since these two features belong to eigenmodes with different handedness.

A more quantitative insight into the effect of magnetooptic activity when $\mathbf{g}\|\mathbf{k}\|\mathbf{q}$ can be obtained from the implicit dispersion relation derived in Section 3.4 (see Eq. 3-

13). It is useful to first recast this equation in terms of the normalized quantities used in Figure 3-2:

$$\tilde{\omega}^4\left(\varepsilon_{11}\varepsilon_{22}-\gamma^2\right)-\tilde{\omega}^2\left((\varepsilon_{11}+\varepsilon_{22})(\tilde{k}_z^2+1)-4\gamma\tilde{k}_z q_0\right)+\left(\tilde{k}_z^2-1\right)^2=0 \qquad (3\text{-}24)$$

where $\tilde{\omega}=\omega/(2\pi c/L)$ and $\tilde{k}_z=k_z/(2\pi/L)$ are the normalized angular frequency and wave vector.

Since $\tilde{k}_z$ represents Bloch wave vector solutions, its numerical value is bound between $-0.5\le\tilde{k}_z\le 0.5$ while spanning the entire reduced 1D Brillouin zone. Thus, by neglecting fourth order terms, Eq. (3-24) can be solved [12] for the frequencies ($\tilde{\omega}_1$ and $\tilde{\omega}_2$) and wave vectors ($\tilde{k}_{z,1}$ and $\tilde{k}_{z,2}$) of the band edges (extremum points, $\partial\tilde{\omega}/\partial\tilde{k}_z=0$), yielding the following approximate solutions:

$$\tilde{\omega}_i\cong\frac{1}{\sqrt{\varepsilon_{ii}}}\left(1+\frac{\gamma^2}{2\varepsilon_{ii}(3\varepsilon_{ii}+\varepsilon_{jj})}\right)$$
$$\tilde{k}_{z,i}\cong q_0\frac{\gamma}{3\varepsilon_{ii}+\varepsilon_{jj}} \qquad (3\text{-}25)$$

where the two band edges correspond to ($i=1,\ j=2$) and ($i=2,\ j=1$), with $q_0\equiv\pm 1$ (helix handedness), and ε_{ii} and ε_{jj} are elements of the dielectric tensor written in the rotating material coordinate frame ($\underline{\underline{\varepsilon}}_{ref}$ in Eq. 3-2).

First, note that, in the absence of magnetooptic activity ($\gamma = 0$), Eq. (3-25) predicts exactly the band gap features of simple helical media (e.g. cholesteric liquid crystals). The gap has the right width and position [37, 42], and it is located at $\tilde{k}_z=0$ (a consequence of reciprocity, in fact). Secondly, we remark that the results of Eq. (3-25)

agree very well with our numerically obtained band structures. It is now clear why the band edges appear to translate "horizontally": since $(\gamma/\varepsilon_{ii})^2 << 1$, the vertical component of the shift of the band edge frequencies is not easily perceived visually from a plot like the one shown in Figure 3-2. This effectively horizontal translation scales linearly with the magnetooptic strength, in agreement with our numerical simulations.

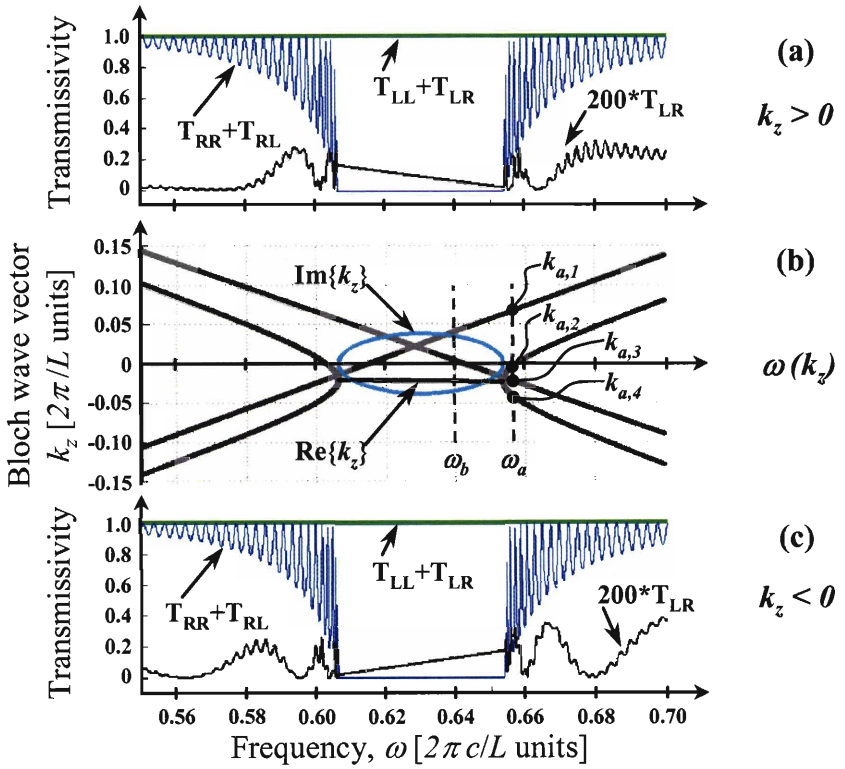

Figure 3-3 - (b) Numerically calculated photonic band structure for axial propagation, $\omega(k_z, k_x=k_y=0)$, when **g**||**z**. The thick lines correspond to propagating eigenmodes. The evanescent modes are shown with thin lines, the darker ones for the real part of the wave vector, Re$\{k_z\}$, and the lighter lines for the imaginary part, Im$\{k_z\}$. **(a)** Transmission of plane waves propagating in the **+z** direction ($\gamma > 0$) through a finite piece of the RH photonic crystal, showing the total transmissivities of LCP waves ($T_{LL}+T_{LR}$) and stop-band for RCP waves ($T_{RR}+T_{RL}$). The polarization conversion contribution ($T_{LR}=T_{RL}$) is scaled by a factor of 200, for visibility on the same plot; **(c)** same as (a), but the magnetogyration vector is reversed ($\gamma < 0$), corresponding to an incident wave propagating in the **-z** direction.

To further interpret the photonic band structure in the **k**||**g**||**q** case we compare in Figure 3-3 the optical properties of this infinitely periodic photonic crystal structure with those of a corresponding finite structure. Note first that we show in Figure 3-3(b) both

the propagating eigenmodes (thick dark gray curves) and the decaying modes from the band gap (thin black line for the real part of the wave vector, $\mathrm{Re}\{k_z\}$, and thin light gray for $\mathrm{Im}\{k_z\}$). At first sight, the band structure shown Figure 3-3(b) (similar to the inset of Figure 3-2, only with transposed axes) might suggest that in the frequency interval $0.62 < \tilde{\omega} < 0.64$ there are no propagating eigenmodes in the **-z** direction.

By employing the numerical transfer matrix model from Section 3.5, we have calculated the transmission curves of a corresponding finite MO-HM ($N_{periods} = 100$, $\varepsilon_{11} = 2.7225$, $\varepsilon_{22} = 2.3409$, $\gamma = 0.1$, incidence and transmission media with $\varepsilon = \sqrt{\varepsilon_{11}\varepsilon_{22}}$). We show in Figure 3-3(a) and (c) the frequency dependence of the total transmission of left-hand circularly polarized (LCP) waves ($T_{LL} + T_{LR} = |t_{LL}|^2 + |t_{LR}|^2$, see Eq. 3-22), and of the total transmission of RCP waves ($T_{RR} + T_{RL}$) for the two propagation directions (simulated by reversing the sign of γ, per Eq. 3-13). It is evident from these two plots that the stop gap has the same width regardless of propagation direction, thus the supposition that there are no propagating modes in the **-z** direction for $0.62 < \tilde{\omega} < 0.64$ has to be wrong. In fact, this apparent issue can be reconciled solely on the basis of the band structure shown in Figure 3-3(b) by realizing that, even if there is no propagating mode with $k_z < 0$, one of the two modes still has a group velocity in the **-z** direction (e.g. see ω_b). Related to this issue is also the fact at other frequencies, such as ω_a, there are three modes with $k_z < 0$ versus only one with $k_z > 0$. This should obviously not be taken as an argument for an unphysical situation when three distinct (orthogonal) eigenmodes exist for propagation along **-z**. As before, one of the three modes at ω_a with phase velocity along **-z** has an opposite group velocity, pointing along **+z**: $v_p < 0$ and $v_g > 0$ at the point labelled $k_{a,2}$ in Figure 3-3(b). Waves with antiparallel group and phase

velocities have been long known in the microwave literature [16] as backward waves, but have recently become of great interest in the area of negative refractive index materials [17, 43], also called left-handed materials [44]. Although these type of waves have not been reported in previous investigations of helical media with magnetooptic activity, the present situation can be argued to be qualitatively similar to the backward waves found by Engheta *et al* in chiroplasmas [34], which, instead of a gap originating from band anticrossing, have a pseudo - band edge at the cut-off frequency (see Section 3.3). Engeta *et al.* argued that the competition of left-hand circular polarization with the right-hand induced current due to the applied magnetic field caused the phase velocity of these eigenmodes to change sign as the strength of the magnetooptic activity increases, while their corresponding group velocities did not change direction. The resemblance of this result to our observations, where structural chirality replaces molecular optical activity and a periodic dielectric constant leads to photonic band gaps, invites the conjecture that all media that break time-reversal and space-inversion symmetries with a mechanism for band gap formation will display backward waves in select frequency intervals.

However, photonic crystals lacking space-inversion and time-reversal symmetries have additional special properties. To the best of our knowledge a new concept for photonic crystals, we find that, as long as these two symmetries are broken along the light propagation direction, a periodic dielectric contrast leads to the formation of *indirect photonic band gaps*, by analogy with electronic band gaps. Fundamentally, this could be qualitatively predicted from the fact that band anticrossing occurs at the intersection of photonic bands with *different* group velocities, thus having to yield band edges that are not aligned in k-space. Although a bit hard to see on the plotting scale used in **Figure**

3-2 and Figure 3-3(b), this fact is proved quantitatively by our numerical results and by the approximate analytical solutions in Eq. (3-25).

The presence of indirect photonic band gaps has quite intriguing consequences. We discuss here the potentially most interesting feature of this class of photonic crystals from a theoretical standpoint, arising from the subtler problem of non-propagating modes inside the indirect photonic band gap. A common assumption is that the eigenmodes in the gap represent evanescent waves [22], defined as waves with complex wave numbers having zero real parts and non-zero imaginary parts (in 1-D, $\mathrm{Re}\{k_z\}=0$ and $\mathrm{Im}\{k_z\}\neq 0$). However, as shown in Figure 3-3(b), we find that in the case of MO-HM the $\mathrm{Re}\{k_z\}$ of these non-propagating eigenmodes is not only non-zero, but also frequency dependent. This is very peculiar due to the fact that the material system is lossless (see Eq. (3-2), easy to show that the lossless condition [22] is satisfied at any value of z, $\underline{\underline{\boldsymbol{\varepsilon}}}_{xyz} = (\underline{\underline{\boldsymbol{\varepsilon}}}_{xyz})^{+}$, where the superscript $^{+}$ denotes transpose and complex conjugate). Fortunately, the transmission spectra simulations in Figure 3-3(a) and Figure 3-3(c) sustain the physically expected fact that these non-propagating modes do not transport power, temporarily solving this apparent contradiction. Referring to Figure 3-3(b), it is also evident that at any frequency in the photonic band gap, e.g. ω_b, there will be two non-propagating modes decaying in either **+z** or in the **-z** directions (given by the sign of their $\mathrm{Im}\{k_z\}$). However, the interesting aspect is that one of these two modes has an exponential decay direction that is opposite from that of the phase front movement, just like backward *propagating* waves (here the mode decaying in the **+z** direction has $\mathrm{Im}\{k_z\} > 0$ and $\mathrm{Re}\{k_z\} < 0$). Lastly, we remark that on top to being non-zero, the real parts of the Bloch wave vectors in the gap are also frequency dependent, to the best of our knowledge a

novel concept with regard to the features of the non-propagating modes of photonic band gaps. Although the frequency dependence in our case is very small, in practice its existence might still be probed by photon tunneling experiments at frequencies from the gap of these photonic crystals. This rich problem of the non-propagating eigenmodes in indirect photonic band gaps is addressed in the next chapter, but it should be clear by now that photonic crystals without time-reversal and space-inversion symmetries display very unusual *general* properties (arising solely from having translational periodicity, refractive index contrast, and an absence of the two inversion symmetry elements).

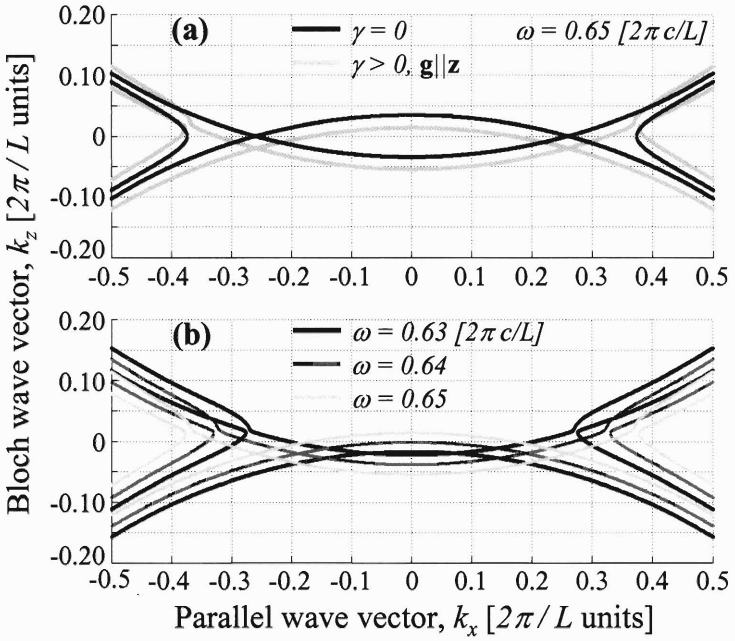

Figure 3-4 - Isofrequency sections through numerically calculated dispersion surfaces, $\omega(k_x,k_y=0,k_z)$; **(a)** Effect of magnetooptic activity ($\gamma > 0$) on the isofrequency contours, when $\omega = 0.65\ [2\pi\ c/L]$ and the magnetogyration vector is parallel to the helical axis (**g**||**z**) ; **(b)** Isofrequency cuts at multiple frequencies, for constant magnetooptic activity ($\gamma = 0.1$, **g**||**z**).

Having described the case of axial propagation with **k**||**g**||**q**, we now address the problem of non-axial propagation with arbitrary propagation in the **x**-**z** plane (**k** = **x**k_x + **z**k_z), keeping **g**||**q**||**z**. The complete dispersion surface $\omega(k_x, k_y=0, k_z)$ that corresponds to

the band structure $\omega(k_x=0,\ k_y=0,\ k_z)$ of Figure 3-2 is shown as isofrequency contours (sections through the 3D surface at particular frequencies) Figure 3-4. It can be seen in Figure 3-4(a) that magnetooptic activity with $\mathbf{g}\|\mathbf{z}$ causes the contours to shift along $\mathbf{z}$ as compared to those for $\gamma = 0$ (a simple HM). As in the case of axial propagation (Figure 3-2), this $\mathbf{z}$-translation is opposite for left- and right-handed circularly polarized eigenmodes. As shown in both Figure 3-4(a) and Figure 3-4(b), this translation leads to formation of band anticrossing at the intersection of contours corresponding to eigenmodes with opposite handedness (note that, for $k_x \neq 0$, the eigenmodes become elliptically polarized). There, the resulting isofrequency contours have an inflection point and are highly nonlinear. This large nonlinearity allows for significant changes of the direction of the group velocity for small changes of the frequency or of the wave vector of a wave propagating through this MO-HM ($\mathbf{v_g}$ points along the normal to the $\omega(\mathbf{k})$ contour, Eq. 3-6). The large sensitivity of $\mathbf{v_g}$ for small variations of either $\mathbf{k}$ or ω has been previously described in other photonic crystals and represents the basis of the so-called photonic crystal superprism effect [20], which allows the fabrication of highly dispersive optical devices on the tens of microns length scale and thus a potential for important uses in microphotonic devices.

As already described earlier in this section, in certain frequency intervals, waves propagating along the helical axis could be described as backward waves, having oppositely pointing group and phase velocities. We find that this remains true even for non-axial propagation as long as $\mathbf{k}$ is not perpendicular to both the helical axis and magnetogyration vector. We show in Figure 3-5 the isofrequency section at $\tilde{\omega} = 0.67$ through the same dispersion surface analyzed above ($\mathbf{g}\|\mathbf{q}\|\mathbf{z}$), and the group velocities of

the eigenmodes phase matched to a particular value of the parallel wavevector k_x. As shown on the graph, there are four propagating modes, (a)-(d). The three eigenmodes (a), (b) and (d) all have $\mathbf{v_g} \cdot \mathbf{v_p} > 0$ (i.e. they are normal waves, where the energy flows in the same general direction as **k**). However, eigenmode (c) has the features of a backward wave ($v_{g,z} * v_{p,z} < 0$). The general conclusion that can be drawn from these observations is that magnetooptic activity causes MO-HM to exhibit propagating eigenmodes that have opposite phase and group velocities *along the direction of the magnetogyration vector.*

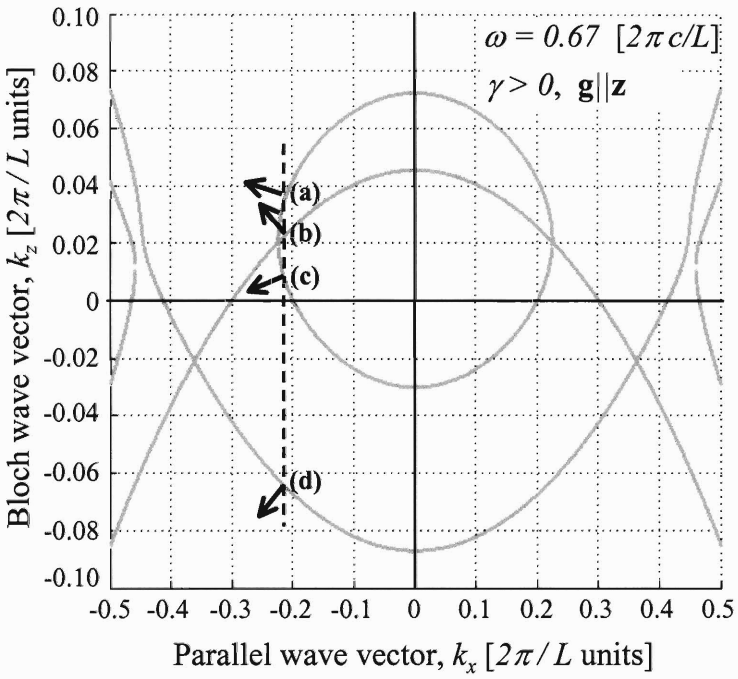

Figure 3-5 - Isofrequency cut at $\omega = 0.67$ [$2\pi c/L$] through numerically calculated dispersion surfaces, $\omega(k_x,k_y=0,k_z)$, when **g**||**z** ($\gamma = 0.1$), showing the directions of the Poynting vectors of four eigenmodes that are phase matched to a particular value of the parallel wave vector, k_x.

3.6.2. Photonic Band Structure of 1D Periodic MO-HM with g⊥q.

Having analyzed in the previous section the case when time-reversal and space-inversion symmetries are broken simultaneously in a MO-HM having its helical axis (**q**) parallel to the magnetogyration vector (**g**, describing magnetooptic activity), we now examine the consequences of having **g**⊥**q**.

In the case of axial propagation (**k**||**q**), one would qualitatively predict a reciprocal photonic band structure, since only space-inversion symmetry is broken along the propagation direction. The same prediction can be made by examining the analytic solution for the dispersion relation when **k**||**q**||**z** (see Section 3.4). In this case, Eq. (3-12) shows that only the ε_{ij} elements ($i, j = 1, 2$) of the dielectric tensor affect the $\omega(k_z)$ solution. When **g**⊥**z**, magnetooptic activity involves off-diagonal tensor elements that couple the **z** components of the EM fields with their **x** and/or **y** components, depending on the direction of **g** (see Eq. 3-2). Thus, when **g**⊥**z**, the ε_{ij} terms in Eq. (3-12) will not be affected by magnetooptic activity. Indeed, as shown in Figure 3-2, the numerically calculated photonic band structure of a MO-HM with **g**⊥**q** is reciprocal, and it is in fact identical to that of the corresponding HM ($\gamma = 0$), just as predicted. Note that we used this numerical approach since the analytic procedure presented in Section 3.4 fails due to the fact that the vector **g**, while static in the *xyz* coordinate frame, becomes a rotating vector after the Oseen transformation, and introduces to *z*-dependent dielectric tensor elements in the system of differential equations shown in Eq. (3-11). Although with no effect on $\omega(k_z)$, magnetooptic activity does affect the propagating eigenmodes by altering their polarization, which is no longer circular.

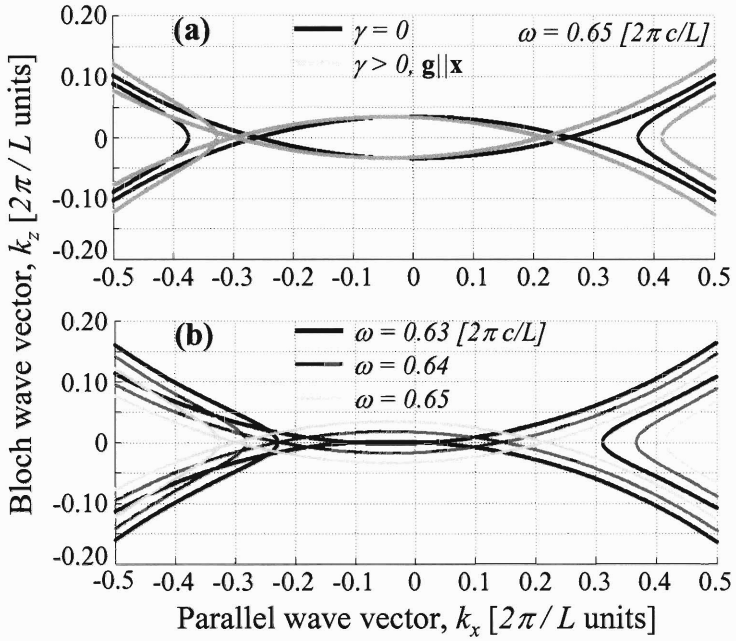

Figure 3-6 - Isofrequency cuts through numerically calculated dispersion surfaces, $\omega(k_x,k_y=0,k_z)$; **(a)** Effect of magnetooptic activity ($\gamma > 0$) on the $\omega = 0.65$ [$2\pi c/L$] contours, when the magnetogyration vector is perpendicular to the helical axis (**g**||**x**) ; **(b)** Isofrequency cuts at multiple frequencies, for constant magnetooptic activity ($\gamma = 0.2$, to exaggerate this qualitative effect, **g**||**x**).

In order to learn more about the optical properties of the MO-HM with **g**⊥**q**, we have calculated the full dispersion surface $\omega(k_x, k_y = 0, k_z)$ for **g**||**x** and **q**||**z**, and show in Figure 3-6 representative isofrequency cuts. As depicted in Figure 3-6(a), magnetooptic activity ($\gamma > 0$) causes again a translation of the contours along the magnetogyration vector direction. As observed before, this translation is opposite for the two types of propagating eigenmodes (with different polarization handedness). Furthermore, as observed in the previous section for **g**||**q**, we find again that magnetooptic activity causes the MO-HM to display propagating eigenmodes with opposite group and phase velocities along the magnetogyration vector (**g**||**x** in this case). To better understand the consequences of this fact, we show in Figure 3-7 a single isofrequency contour ($\tilde{\omega} = 0.65$). The region labeled (ii) represents eigenmodes with the property that $v_{g,x} \cdot v_{p,x} < 0$. This is quite remarkable, since it predicts that a wave incident from air will couple

into a MO-HM photonic crystal on the same side of the surface normal, assuming that the surface is perpendicular to the helical axis, **q**. This is very similar to the negative refraction predicted at the interface between air and left-handed media [17, 43, 44] or certain types of photonic crystals [20], in contrast to the usual situation when the refraction occurs on the opposite side of the normal (see (i) and (iii) in Figure 3-7).

Lastly, another interesting consequence of the fact that the isofrequency contours shift along the **x**-direction as the strength of the magnetooptic activity increases is given by the fact that the directions of the group velocities are deflected towards the direction of the magnetic field. For example, it can be seen from Figure 3-6(a) or Figure 3-7 that a wave (here with $\tilde{\omega} = 0.65$) propagating along the helical axis (**k**||**q**, $k_x = 0$) will have $\mathbf{v_g}||\mathbf{z}$ for $\gamma = 0$, shown in Figure 3-6(a), but in the presence of magnetooptic activity with **g**||**x**, while still having **k**||**z**, its group velocity will be deflected towards the **x** axis (and away from the phase velocity direction, obviously). Essentially, this result bears a resemblance to the electronic Hall effect, where a magnetic field applied perpendicular to the propagation direction results in a lateral deviation (in the case of electrons, this deflection is due to the Lorentz force, $\mathbf{F} = q\mathbf{v}\times\mathbf{B}$).

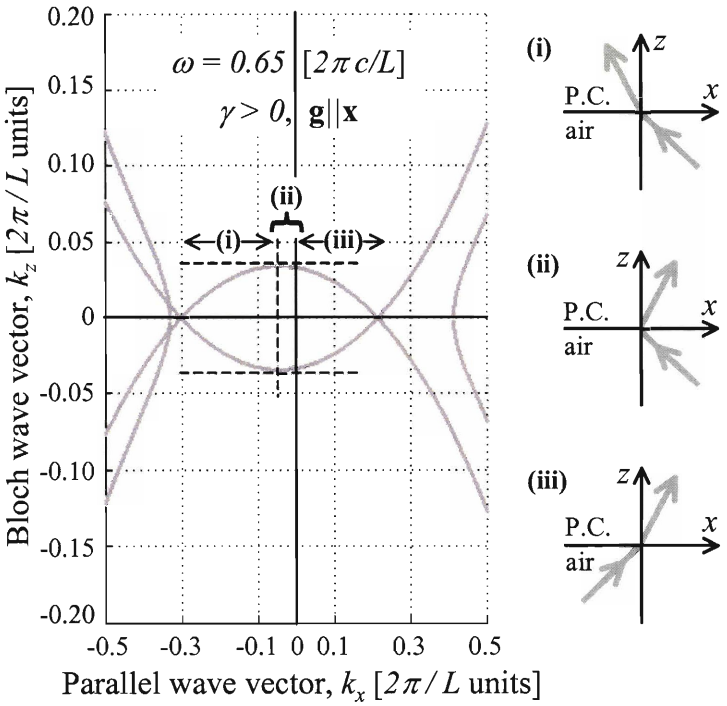

Figure 3-7 - Isofrequency cut at $\omega = 0.65\ [2\pi c/L]$ through numerically calculated dispersion surfaces, $\omega(k_x,k_y=0,k_z)$, showing three different regimes of transmission when $\mathbf{g}\|\mathbf{x}$ ($\gamma = 0.2$ to exaggerate the effect graphically); **(i)** and **(iii)** depict normal refraction at the air-photonic crystal interface; **(ii)** shows negative refraction at the air-photonic crystal interface.

3.7. Conclusions

In this chapter we attempted to provide a unifying view of the general optical properties of photonic crystals that simultaneously break time-reversal and space-inversion symmetries. We studied the representative case of a 1D periodic, dielectric helical medium with magnetooptic activity. Space-inversion symmetry is broken due to the structural chirality of this photonic crystal. Similarly, time-reversal symmetry is broken by the presence of magnetooptic activity (spontaneous, or induced by an external magnetic field) for any propagation direction that is not perpendicular to the magnetogyration vector that describes the MO activity.

We have analyzed the analytic dispersion relation for propagation along the helical axis, and numerically-derived photonic band structures and their isofrequency sections in representative cases for the magnetogyration vector orientation with arbitrary light propagation directions. We confirmed that the dispersion relationship becomes nonreciprocal, $\omega(\mathbf{k}) \neq \omega(-\mathbf{k})$, if the time-reversal and space-inversion symmetries are simultaneously broken along the wave vector direction. Due to the existence of a photonic band gap, the nonreciprocal band structure exhibits a set of interesting and intriguing features, which have not been reported in the previous investigations of similar periodically inhomogeneous materials. For example, immediate consequences of a nonreciprocal dispersion relation include presence of backward wave eigenmodes (opposite phase and group velocity, here only along the magnetogyration vector direction), and indirect photonic band gaps, by analogy to electronic band gaps in atomic crystals. We find that the presence of backward waves can allow for negative refraction, when the corresponding waves are incident from a normal, right-handed material on the interface with the photonic crystal. Furthermore, the variation of the magnetooptic strength causes a shift of the dispersion surfaces along the field direction and a deflection of the propagating modes' group velocity directions towards the same axis.

A fascinating consequence of indirect photonic band gaps is that the non-propagating modes in the gap have wave vectors with frequency dependent non-zero real parts, while the material components are lossless and they still do not not transport any power, thus having to be categorized for now as a pseudo-evanescent type. Furthermore, regardless of the frequency inside the band gap, one of the two decaying modes always has $\mathrm{Re}\{\mathbf{k}\}\cdot\mathrm{Im}\{\mathbf{k}\} < 0$, which resembles backward waves since the phase change is

opposite to the direction of energy flow. This problem will be further explored in the next chapter, and, as it will be shown there, it will open an extremely valuable window into understanding the propagation of electrons in the atomic crystals that are analogous to the photonic crystal system investigated here - e.g., a magnetically-doped (or magnetized) noncentrosymmetric atomic crystal, such as gallium arsenide based materials (e.g. with manganese dopants), or chiral carbon nanotubes with applied axial magnetic fields.

Since the properties outlined above were found to arise solely due to symmetry reasons, the absence of time-reversal and space-inversion symmetries, we conjectured that these properties will be displayed by any photonic crystal as long as these symmetries are broken simultaneously (thus for a given chiral photonic crystal, inducing magnetooptic activity will always lead to these effects, i.e. their magnitude will be material dependent, but their existence is guaranteed).

In terms of the optical properties specific to 1D periodic helical media with magnetooptic activity, we have also found evidence for anomalous wave propagation and superprism effects, due to the large variation of the direction of the group velocity around inflection points introduced upon anticrossing of certain photonic bands.

3.8. References

1. Brillouin, L. *Wave propagation in periodic structures*, 2nd Edition, Dover Publications, Inc. (New York, 1953).

2. Yablonovitch, E. "Inhibited Spontaneous Emission in Solid-State Physics and Electronics," *Physical Review Letters*, **58**, 2059 (1987).

3. John, S. "Strong Localization of Photons in Certain Disordered Dielectric Superlattices," *Physical Review Letters*, **58**, 2486 (1987).

4. Joannopoulos, J. D., Meade, R. D., and Winn, J. N. *Photonic crystals: molding the flow of light*, Princeton University Press (Princeton, N.J., 1995).

5. Warner, M., and Terentjev, E. M. *Liquid crystal elastomers*, Oxford University Press (Oxford, 2003).

6. Lakhtakia, A. "Sculptured thin films: accomplishments and emerging uses," *Materials Science & Engineering C-Biomimetic and Supramolecular Systems*, **19**, 427 (2002).

7. Robbie, K., Brett, M. J., and Lakhtakia, A. "Chiral sculptured thin films," *Nature*, **384**, 616 (1996).

8. Pang, Y. K., Lee, J. C. W., Lee, H. F., Tam, W. Y., Chan, C. T., and Sheng, P. "Chiral microstructures (spirals) fabrication by holographic lithography," *Optics Express*, **13**, 7615 (2005).

9. Lakhtakia, A., and Weiglhofer, W. S. "On Light-Propagation in Helicoidal Bianisotropic Media," *Proceedings of the Royal Society of London Series a-Mathematical and Physical Sciences*, **448**, 419 (1995).

10. Zvezdin, A. K., and Kotov, V. A. *Modern magnetooptics and magnetooptical materials*, Institute of Physics Pub. (Philadelphia, PA, 1997).

11. Koerdt, C., Duchs, G., and Rikken, G. L. J. A. "Magnetochiral anisotropy in Bragg scattering," *Physical Review Letters*, **91**, (2003).

12. Eritsyan, O. S. "Diffraction reflection of light in a cholesteric liquid crystal in the presence of wave irreversibility and bragg formula for media with nonidentical forward and return wavelengths," *Journal of Experimental and Theoretical Physics*, **90**, 102 (2000).

13. Gevorgyan, A. H. "Magneto-optics of a thin film layer with helical structure and enormous anisotropy," *Molecular Crystals and Liquid Crystals*, **382**, 1 (2002).

14. Lakhtakia, A. "Anomalous axial propagation in a gyrotropic, locally uniaxial, dielectric, helicoidally nonhomogeneous medium," *Aeu-International Journal of Electronics and Communications*, **53**, 45 (1999).

15. Pickett, M. D., and Lakhtakia, A. "On gyrotropic chiral sculptured thin films for magneto-optics," *Optik*, **113**, 367 (2002).

16. Collin, R. E. *Foundations for microwave engineering*, McGraw-Hill (New York, 1966).

17. Veselago, V. G. "Electrodynamics of materials with negative index of refraction," *Physics-Uspekhi*, **46**, 764 (2003).

18. Chigrin, D. N., and Torres, C. M. S. "Periodic thin-film interference filters as one-dimensional photonic crystals," *Optics and Spectroscopy*, **91**, 484 (2001).

19. Kosaka, H., Kawashima, T., Tomita, A., Notomi, M., Tamamura, T., Sato, T., and Kawakami, S. "Self-collimating phenomena in photonic crystals," *Applied Physics Letters*, **74**, 1212 (1999).

20. Kosaka, H., Kawashima, T., Tomita, A., Notomi, M., Tamamura, T., Sato, T., and Kawakami, S. "Superprism phenomena in photonic crystals," *Physical Review B*, **58**, 10096 (1998).

21. Chen, H. C. *Theory of electromagnetic waves: a coordinate-free approach*, McGraw-Hill Book Co. (New York, 1983).

22. Kong, J. A. *Electromagnetic wave theory*, EMW Publishing (Cambridge, Mass., 2000).

23. I. Bita, E.L. Thomas - in preparation`; manuscript describing the effects of further reducing the symmetry of the repeat unit, for example by departing from the lineasr rotation in Eq. 3

24. Wagniere, G. H. "The magnetochiral effect and related optical phenomena," *Chemical Physics*, **245**, 165 (1999).

25. Kleindienst, P., and Wagniere, G. H. "Interferometric detection of magnetochiral birefringence," *Chemical Physics Letters*, **288**, 89 (1998).

26. Vallet, M., Ghosh, R., Le Floch, A., Ruchon, T., Bretenaker, F., and Thepot, J. Y. "Observation of magnetochiral birefringence," *Physical Review Letters*, **87**, 183003 (2001).

27. Landau, L. D., Lifshitz, E. M., and Pitaevskii, L. P. *Electrodynamics of continuous media*, 2nd, Pergamon (New York, 1984).

28. Barron, L. D., and Vrbancich, J. "Magneto-Chiral Birefringence and Dichroism," *Molecular Physics*, **51**, 715 (1984).

29. Wagniere, G. "Magnetochiral Dichroism in Emission - Photoselection and the Polarization of Transitions," *Chemical Physics Letters*, **110**, 546 (1984).

30. Wagniere, G., and Meier, A. "The Influence of a Static Magnetic-Field on the Absorption-Coefficient of a Chiral Molecule," *Chemical Physics Letters*, **93**, 78 (1982).

31. Rikken, G. L. J. A., and Raupach, E. "Pure and cascaded magnetochiral anisotropy in optical absorption," *Physical Review E*, **58**, 5081 (1998).

32. Rikken, G. L. J. A., and Raupach, E. "Observation of magneto-chiral dichroism," *Nature*, **390**, 493 (1997).

33. Pinheiro, F. A., and van Tiggelen, B. A. "Magnetochiral scattering of light: Optical manifestation of chirality," *Physical Review E*, **66**, (2002).

34. Engheta, N., Jaggard, D. L., and Kowarz, M. W. "Electromagnetic-Waves in Faraday Chiral Media," *Ieee Transactions on Antennas and Propagation*, **40**, 367 (1992).

35. Taouk, H. "Optical wave propagation in active media: Gyrotropic-gyrochiral media," *Journal of the Optical Society of America a-Optics Image Science and Vision*, **14**, 2006 (1997).

36. Weiglhofer, W. S., Lakhtakia, A., and Michel, B. "On the constitutive parameters of a chiroferrite composite medium," *Microwave and Optical Technology Letters*, **18**, 342 (1998).

37. deVries, H. L. "Rotatory power and other optical properties of certain liquid crystals," *Acta Crystallographica*, **4**, 219 (1951).

38. Oseen, C. W. "The theory of liquid crystals," *Journal of the Chemical Society, Faraday Transactions II: Molecular and Chemical Physics*, **29**, 882 (1933).

39. Yeh, P. *Optical waves in layered media*, Wiley (New York, 1988).

40. Berreman, D. W. "Optics in Stratified and Anisotropic Media: 4x4-Matrix Formulation," *Journal of the Optical Society of America B-Optical Physics*, **62**, 502 (1972).

41. Moler, C., and Van Loan, C. "Nineteen dubious ways to compute the exponential of a matrix, twenty-five years later," *Siam Review*, **45**, 3 (2003).

42. Kopp, V. I., Zhang, Z. Q., and Genack, A. Z. "Lasing in chiral photonic structures," *Progress in Quantum Electronics*, **27**, 369 (2003).

43. Pendry, J. B. "Negative refraction makes a perfect lens," *Physical Review Letters*, **85**, 3966 (2000).

44. Smith, D. R., and Kroll, N. "Negative refractive index in left-handed materials," *Physical Review Letters*, **85**, 2933 (2000).

Chapter 4.
Tunneling time for barriers lacking space-inversion and time-reversal symmetries

As it was discussed in the previous chapter, photonic crystals that simultaneously lack space-inversion and time-reversal symmetries display many remarkable properties. One of the interesting observations made in Chapter 3 was related to the characteristics of the nonpropagating eigenmodes in the photonic band gap of such a photonic crystal system. This problem is further explored in the current chapter, because the nature of these modes is intimately related to a very important problem in physics, tunneling - the traversal by a particle (photon, electron, etc.) of a region of physical space where the particle is not allowed to propagate in the first place. This corresponds to an electron tunneling across an insulating gap between two metallic electrodes, or to light traversing a finite region of space filled with a photonic crystal displaying a band gap at the frequency of the incoming light waves.

A particularly important motivation for this study is the analogy between atomic and photonic crystals, described in more detail in Chapter 2. By studying the tunneling of a photon through such a photonic crystal, we gain insight into the analogous problem of an electron tunneling in an appropriate atomic crystal barrier. Since we find that, in the absence of the two inversion symmetries, the eigenmodes of the photonic crystal are circularly polarized, the corresponding electronic case is embodied by spin-polarized

electronic tunneling in a semiconductor that is both noncentrosymmetric (no space-inversion symmetry) and magnetized (no time-reversal symmetry). Immediate examples that come to mind are manganese-doped gallium arsenide (i.e. the zinc-blende crystal structure is noncentrosymmetric), or chiral carbon nanotubes with an applied axial magnetic field. These two types of material systems are, incidentally, subjects of significant research activities in the present, such as for spin electronics (spintronics) and nanoelectronics. Thus, the results of our theoretical study offer an original and insightful view into a research problem of great importance presently.

We find that breaking space-inversion and time-reversal symmetries along the tunneling axis causes the tunneling (phase) time to become dependent on both the length of the barrier, and on the spin of the tunneling wave packet. For photons, corresponding photonic crystal barriers exhibit circularly-polarized eigenmodes and indirect photonic band gaps (iPBG), inside which the complex, non-propagating solutions (k_{gap}) have frequency dependent nonzero real parts - remarkably different from the usually assumed evanescent solutions, which are purely imaginary (i.e. of the form $k_{gap}=ik$). The tunneling (phase) time in finite barriers is found to correlate with the group-like velocity, $1/v_g = \mathrm{dRe}\{k_{gap}\}/d\omega$, of the iPBG modes in the photonic crystal. The sign of the group delay is found to change with the spin of the tunneling particle.

4.1. Introduction

The estimation of the time required for tunneling across a barrier is of practical importance because it provides an upper limit for the operating speed of tunneling-based devices. Although old, this problem remains today controversial due to an insufficient understanding of tunneling dynamics. Theoretical predictions and experimental evidence show that, for example, tunneling is superluminal (group velocity exceeds that of light in vacuum, c), yet without violating Einstein's causality [1-4]. The superluminality is caused by the fact that as the length of a tunnel barrier is increased beyond a certain point, the tunneling time remains constant and thus the corresponding velocity quickly exceeds c. This phenomenon is often called the Hartman effect [5], and has been shown first in a microwave experiment [6] and in the same year confirmed with laser pulses [7]. Today, the Hartman effect is widely accepted as one of the most fundamental features of the tunneling dynamics for both waves and particles [1-4] to the point that even a universal tunneling time has been introduced [2]. The only known deviations from this behavior arise when particular frequency-dependent factors are introduced, such as material absorption [8] and dispersion, or tunneling of wave packets with large momentum spreads [9].

In this chapter we study the problem of tunneling time in 1D barriers that break simultaneously space-inversion (S-I) and time-reversal (T-R) symmetries, and show that solely due to symmetry reasons the tunneling dynamics deviates fundamentally from the expected behavior. Particularly, the Hartman effect is forbidden, which is remarkable since the absence of the two inversion symmetries is a frequency independent factor - the

tunneling time not only becomes dependent on barrier length, but also on the spin of the tunneling wave packet. By studying an appropriate photonic tunneling case, we further show that one of the spins will always tunnel with a negative time delay, because for this spin the barrier supports pseudo-evanescent photonic band gap modes with a negative group-like velocity (thus, the longer the barrier the shorter the tunneling time).

This study sheds light on issues not only of scientific importance (i.e. effects of inversion symmetries on tunneling dynamics), but also of practical relevance. In the electronic case, spin-polarized tunneling is currently a very important area of spintronics [10]. Our results thus give new valuable insight into the operation of those magnetotunneling junctions that break both S-I (e.g. due to a noncentrosymmetric barrier material) and T-R symmetries (e.g. external magnetic field, or intrinsic material magnetization) along the tunneling axis. A prominent example of such a spintronic device is a junction with a noncentrosymmetric barrier material that may also be magnetically doped, such as manganese-doped gallium arsenide (GaAs), the "model" magnetic semiconductor. With one exception, previous investigations of the spin-dependent tunneling time in GaAs-related systems take into account the absence of S-I, however T-R is not broken due to the magnetization being perpendicular to the tunneling axis (in-plane magnetization of the electrodes with out of plane tunneling) or due to absence of magnetism entirely [11, 12]. A few months ago, after we submitted for review and publication a manuscript with the results reported in this chapter [13], Guo *et al.* [14] reported on a study of electronic tunneling in magnetic semiconductor heterostructures (based on $Cd_{1-x}Mn_xTe$ and $Zn_{1-x}Mn_xSe$) with magnetic fields applied along the tunneling direction, which independently confirmed some of our observations

in the photonic case. Another relevant example is that of carbon nanotube based magnetic tunnel junctions [15] with an external magnetic field applied axially.

4.2. Gap states in nonreciprocal photonic crystals

In order to study the effects of the absence of the two inversion symmetries, we focused on photonic tunneling through a 1D photonic crystal (PC) excited in the center of its first photonic band gap. We showed in Chapter 3 that 1D PCs lacking both S-I and T-R develop *indirect* photonic band gaps (iPBG) due to their nonreciprocal dispersion relations, $\omega(k) \neq \omega(-k)$, and support propagation and tunneling via spin-polarized eigenmodes (i.e. circularly polarized, CP) [16]. One of our initial goals was to understand the fundamental differences between tunneling in PC barriers with iPBGs and in those with *direct* photonic band gaps (dPBG), the latter being to the best of our knowledge the case analyzed in virtually all published studies of photon tunneling dynamics [1-4]. Any such difference will have to stem from the nature of the non-propagating gap modes - this is because the tunneling time has been shown to be directly related to the phase change experienced by photons while traversing the barrier [2, 5], which in turn is connected to the real part of the tunneling mode's k-vector. The propagation of the peak of a pulse is described by the group velocity, which generally may be defined as:

$$\frac{1}{v_g} = \frac{d\,\mathrm{Re}\{k\}}{d\,\omega} = \frac{1}{L_{barrier}} \frac{d\,\phi_t}{d\omega} \tag{4-1}$$

where ω is the angular frequency, k is the spatial frequency, and ϕ_t is the phase change upon transmission through a barrier of length $L_{barrier}$ ($\phi_t = \mathrm{Re}\{k\}\ L_{barrier}$).

The main difference between dPBG and iPBG is qualitatively illustrated in Figure 4-1. At the anticrossing of bands with equal and opposite group velocities it can be argued that the real parts of the k-vectors of the resulting dPBG gap modes, $\mathrm{Re}\{k_{gap}\}$, fall on a vertical line joining the two band edges, which for purely evanescent modes should further be identical to zero. Based on Eq. (4-1), this argument is an agreement with the classical view that tunneling is "instantaneous" (with no phase change) because in this case tunneling takes place with infinite group velocity. However, as shown in Figure 4-1(b), the nonreciprocal group velocities of media with $\omega(k) \neq \omega(-k)$, arising from the simultaneous absence of S-I and T-R, result in an iPBG as the band anticrossing lead to band edges that are not aligned vertically in k-space. Unlike dPBG, then the $\mathrm{Re}\{k_{gap}\}$ solutions of iPBG become frequency dependent (end points have to match the band edges). Note that this qualitative argument is supported by numerical photonic band structure calculations of real systems as described below. Thus, at this point we will only mention an inviting conjecture based on Figure 4-1(b): in the case of iPBG, tunneling cannot become "instantaneous" (i.e. $v_g \rightarrow \infty$) as in the Hartman effect [5].

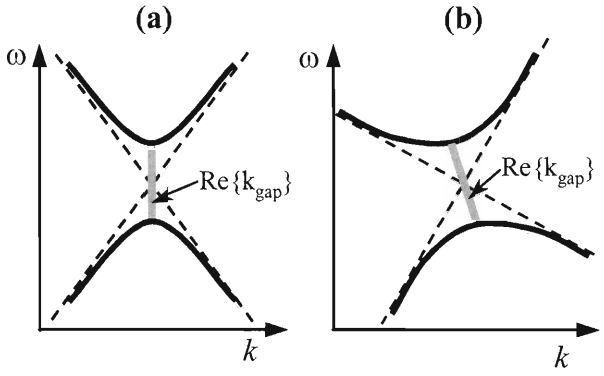

Figure 4-1 - **(a)** dPBG at the anticrossing of bands with equal group velocities; **(b)** iPBG at the anticrossing of different v_g bands, as seen in nonreciprocal PCs. The original bands are shown with dashed lines, the coupled propagating modes with solid, black curves and the expected real part of the gap modes with a thicker solid gray line.

4.3. Tunneling phase time in nonreciprocal photonic barriers

The model PC investigated in this chapter is a lossless 1D PC composed of alternating optically active (chiral) and Faraday active (magnetooptic) layers, lacking both S-I and T-R symmetries for propagation along the periodicity direction. The constitutive relations of an optically active material are:

$$\begin{aligned} \mathbf{D} &= \varepsilon_0 \varepsilon_c \mathbf{E} + i\xi_c \sqrt{\varepsilon_0 \mu_0}\, \mathbf{H} \\ \mathbf{B} &= -i\xi_c \sqrt{\varepsilon_0 \mu_0}\, \mathbf{E} + \mu_0 \mathbf{H} \end{aligned} \tag{4-2}$$

where ε_c is the isotropic dielectric constant, and ξ_c is the isotropic chirality admittance (or optical activity parameter) responsible for absence of S-I [17].

The Faraday active layer is described by the following constitutive relations:

$$\begin{aligned} \mathbf{D} &= \varepsilon_0 \underline{\underline{\varepsilon}}_F \mathbf{E} = \varepsilon_0 \begin{pmatrix} \varepsilon_F & i\gamma_F & 0 \\ -i\gamma_F & \varepsilon_F & 0 \\ 0 & 0 & \varepsilon_F \end{pmatrix} \mathbf{E} \\ \mathbf{B} &= \mu_0 \mathbf{H} \end{aligned} \tag{4-3}$$

where γ_F is the Faraday activity parameter, responsible for the absence of T-R. This is a purely magnetooptic (or gyroelectric) material with a magnetization along the **z** axis, where the usually small effect of the magnetization on the (3,3) element of $\underline{\underline{\varepsilon}}_F$ is neglected. For convenience, we use quarter-wave-like layer thicknesses, $d_i = \lambda_0 / \left(4\sqrt{\varepsilon_i}\right)$, $i = F, c$. Note that the choice of λ_0 is not important, as in our numerical studies we use normalized frequencies (ω in $2\pi c/L$ units) and wavevectors (k in $2\pi/L$ units), where L is the PC period ($L = d_F + d_c$).

In order to estimate the tunneling time through the 1D PC barrier, we use the group-delay (or phase time) formalism because of its acceptance following from both photonic experiments [1] and theoretical results for the more general quantum mechanical tunneling problem [2], including spin-polarized electronic tunneling [11]. Although other models for the tunneling time are available, under our assumptions of a photonic crystal with lossless and non-dispersive components, the tunneling phase time is known to be equal to the tunneling time calculated from more complex models, such as the Green function approach [18], and thus a perfectly valid choice. Furthermore, we used the 4x4 transfer matrix method [19] (also described in more detail in Chapter 3, Section 3.5), because it allows the study of both finite and infinite structures - we can thus solve for the properties of a finite, multilayer photonic barrier, and also for the eigenmodes of the photonic crystal, in order to understand what states are available at the frequencies of the tunneling wave packet. In the latter case, both propagating and non-propagating eigenmodes can be obtained by solving for the *complex band structure*.

For the estimation of the spin-polarized tunneling time we first calculate the complex transmission coefficients in a finite multilayer photonic barrier for right-hand

(R) and left-hand (L) CP waves, t_{RR} and t_{LL}, where e.g. t_{RR} describes RCP transmission with spin conservation (see Section 3.5.2 in Chapter 3, or [16] and references therein). We then use in Eq (4-1) the corresponding frequency-dependent transmission phase change, $\phi_t(\omega) = \arg(t(\omega))$, and obtain the tunneling phase time, τ, for waves tuned to the mid-gap frequency (ω_0) for each spin

$$\tau = \left. \frac{d\phi_t(\omega)}{d\omega} \right|_{\omega_0} \tag{4-4}$$

4.4. Results

To emphasize the effects of the simultaneous absence of the two inversion symmetries and of the differences between dPBG and iPBG, we first present the case of a 1D PC lacking only T-R symmetry. More exactly, we examine the 1D PC introduced above where the chiral layer is replaced by a dielectric isotropic layer (Eq. 4-2 with $\xi_c = 0$ and $\varepsilon_c \neq \varepsilon_F$). This case is also related to the Larmor clock approach to tunneling time [20]. From the start, we expect reciprocal dispersion relations since only T-R is absent.

For propagation along the **z** axis, the eigenmodes are LCP and RCP, as shown in Figure 4-2(a), where the bands are labeled according to the phase difference between the x and y components of their electric field eigenvectors ($\phi_{Ex} - \phi_{Ey} = \pm 90°$). Please note the expected reciprocity, $\omega(k) = \omega(-k)$, even if Faraday nonreciprocity is present (this describes the change of polarization handedness upon reversal of the propagation direction, while phase and group velocities remain unchanged). We also show in Figure 4-2(b) that the two band gaps are direct and aligned at the edge of the Brillouin zone.

The non-propagating complex solutions inside the gaps are also CP, and their corresponding real and imaginary parts, $\mathrm{Re}\{k_{gap}\}$ and $\mathrm{Im}\{k_{gap}\}$, are plotted in Figure 4-2(c) and (d). Note that these numerical results support very well the qualitative argument illustrated in Figure 4-1(a).

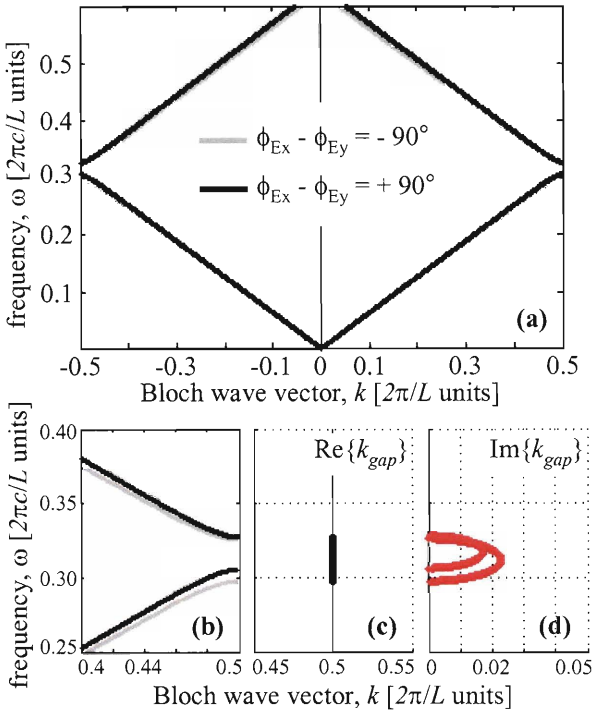

Figure 4-2 - **(a)** Reciprocal band structure with dPBG for a 1D PC breaking only T-R symmetry ($\varepsilon_F = 1.72$, $\gamma_F = 0.1$, $\varepsilon_c = 1.52$, $\xi_c = 0$ in Eqs. (2) and (3), see text); **(b)**, **(c)** and **(e)** Magnification of the first gap region showing the original bands and the real and imaginary parts of the complex k_{gap} solutions in the PBGs - note the vertical alignment at the edge of the first Brillouin zone.

We now present the case of a PC with iPBGs, the 1D periodic structure introduced earlier, with a bilayer period formed by a magnetooptic layer and an optically active layer. The first band gap region for propagation perpendicular to the interfaces (**z** axis) is shown in Figure 4-3(a) and (b): the nonreciprocity of the $\omega(k)$ solutions is evident. At a particular frequency, reversing the propagation direction leads to

eigenmodes with different phase and group velocities, even though their polarization remains circular.

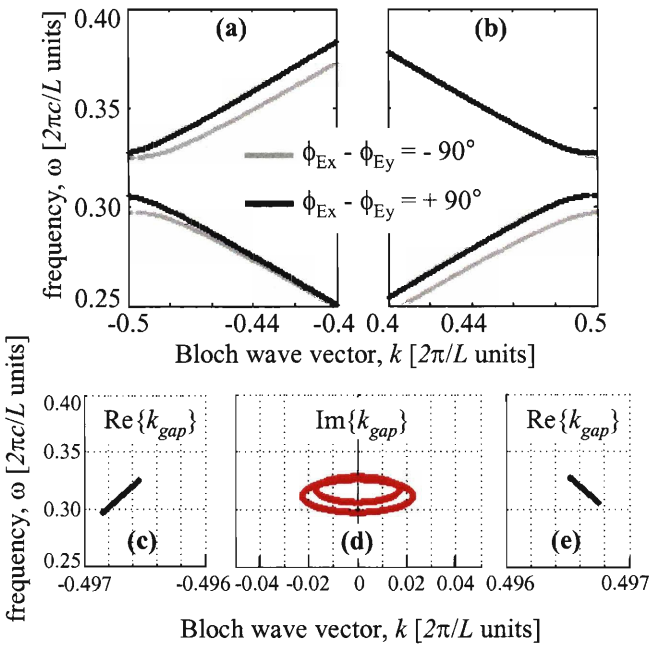

Figure 4-3 - **(a)**, **(b)** Nonreciprocal band structure for a 1D PC breaking both S-I and T-R ($\varepsilon_F = 1.72$, $\gamma_F = 0.1$, $\varepsilon_c = 1.52$, $\xi_c = 0.02$ in Eqs. (2) and (3), see text). **(c)**, **(d)** and **(e)** show the gap mode solutions. Note the vertical (mirror) symmetry about $k = 0$ of Im$\{k_{gap}\}$ solutions and the different frequency dependence of the Re$\{k_{gap}\}$ solutions.

Being interested in tunneling, we now proceed to examine the non-propagating solutions in the iPBGs. The real and imaginary parts of the gap solutions, Re$\{k_{gap}\}$ and Im$\{k_{gap}\}$, are plotted separately in Figure 4-3(c), (d), and (e). As it was qualitatively predicted in Figure 4-1(b), note that Re$\{k_{gap}\}$ solutions are indeed frequency dispersive and nonzero. Furthermore, for each gap, the two k_{gap} solutions are pseudo-evanescent, being complex conjugate with Re$\{k_{gap}\} \neq 0$. This can be seen in Figure 4-3(c) and (e), where the Re$\{k_{gap}\}$ solutions are doubly degenerate, while Figure 4-3(d) shows that, for each gap, the Im$\{k_{gap}\}$ curves are symmetric with respect to the $k = 0$ axis. It is

important to point that such complex gap modes do not carry a net average power flux, fact confirmed by our numerical TMM calculations of RCP and LCP reflectivities that are found to approach 100% inside their respective band gaps [16] (also shown in Chapter 3, Figure 3-3, for the case of a nonreciprocal 1D periodic, magnetooptic helical medium).

To study the effect of the type of photonic band gap (dPBG vs iPBG) on the tunneling time, we consider the normal-incidence case and calculate the complex CP transmission coefficients and the corresponding phase changes, $\phi_{t,RCP} = \arg(t_{RR})$ and $\phi_{t,LCP} = \arg(t_{LL})$, for finite 1D stacks of varying numbers of periods, $N_{periods}$. To reduce the effect of resonances due to the incidence and transmission interfaces, we also assume that the dielectric constants of the incidence and transmission media are equal to the geometric average of the dielectric constants of the two layers in the photonic crystal $\varepsilon_i = \varepsilon_t = \sqrt{\varepsilon_F \varepsilon_c}$.

We show in Figure 4-4 the calculated tunneling time for waves with RCP and LCP polarizations tunneling through finite barriers of varying length. Note that each circularly polarized wave is chosen to have a frequency centered in the middle of its corresponding photonic band gap ($\omega_{0,\,RCP} = 0.311\ [2\pi c/L]$ and $\omega_{0,\,LCP} = 0.316\ [2\pi c/L]$), which numerically happen to be the same for both the dPBG ($\xi_c = 0$, $\gamma_F \neq 0$) and iPBG ($\xi_c \neq 0$, $\gamma_F \neq 0$) cases considered here.

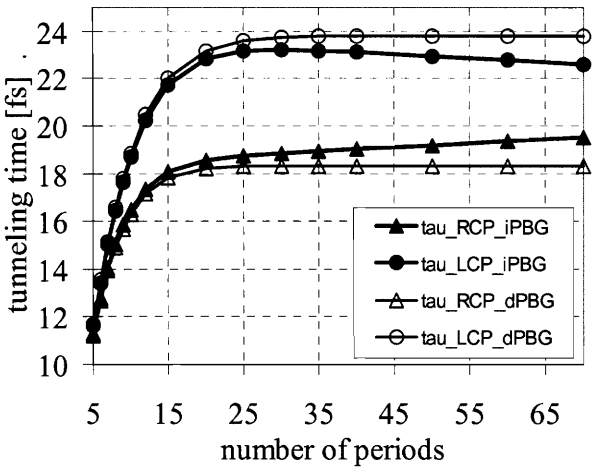

Figure 4-4 - Tunneling time for RCP and LCP pulses with narrow frequency bandwidths centered in the gaps of the LCP and RCP bands shown in Fig. 4-2 (dPBG) and Fig. 4-3 (iPBG). In both cases the center frequencies are $\omega_{0,\,LCP} = 0.316\,[2\pi c/L_{period}]$ and $\omega_{0,\,RCP} = 0.311\,[2\pi c/L_{period}]$), with $L_{period} = 486nm$.

Examining the above figure, it can be seen that, in the dPBG case without T-R, the Hartman effect applies for both circular polarizations (or spins), just as expected by analogy with the Larmor clock approach to tunneling time [16] (estimation of the tunneling time by introducing Faraday activity artificially in a tunneling barrier). However, in the case of iPBGs the Hartman effect does not seem to apply anymore. It can be seen in Figure 4-4 that the tunneling time becomes dependent on the barrier length in a specific way for each CP handedness. The tunneling time for RCP modes (solid triangles in Figure 4-4) increases with barrier length, while the result for the LCP band gap is counterintuitive: the longer the barrier, the shorter the tunneling time (solid circles in Figure 4-4). As unexpected as this observation might seem, it is in perfect accordance with the predictions of the photonic band structure calculations. It can be seen in Figure 4-3(d) that for k > 0 (+**z** propagation) there are two gaps, for each CP band. However, while there are two decay constants, $\mathrm{Im}\{k_{gap}\}$, as expected in the $k > 0$ region, see Figure 4-3(d), the slopes of the corresponding real parts of the k_{gap} solutions have opposite signs.

The wider gap, corresponding to RCP modes and centered at $\omega_0 = 0.311$, has its $\mathrm{Re}\{k_{gap}\}$ solutions in the $k < 0$ region and a positive slope, while the narrower gap, corresponding to LCP and with $\omega_0 = 0.316$, has $\mathrm{Re}\{k_{gap}\}$ solutions in the $k > 0$ region and a negative slope. Thus, tunneling inside the RCP gap proceeds with a positive group-like velocity, $v_g > 0$, while in the case of the LCP gap $v_g < 0$. This is why we believe that the LCP tunneling time decreases with increasing barrier length in Figure 4-4. Supporting this claim, we also numerically observe that the slopes $\mathrm{dRe}\{k_{gap}\}/\mathrm{d}\omega$ in Figure 4-3(c) and (e), corresponding to the case of an infinite PC, predict very well the saturation values of $\mathrm{d}\tau/\mathrm{d}L_{barrier}$ for both the LCP and RCP curves (e.g. at $N_{periods} > 30$), calculated for finite structures (which are still superluminal). This suggests that tunneling takes places via well defined modes having group-like velocities of the form given in Eq. (4-1).

4.5. Conclusions

In conclusion, we have shown that tunneling of spin-polarized wave packets in barriers that lack space-inversion and time-reversal symmetries differs significantly from the expected behavior. Particularly, the Hartman effect is forbidden, as the tunneling time not only depends now on barrier length but also on the spin of the tunneling particle.

In the case of a "model" 1D photonic crystal barrier, the origin of this behavior is found to be the indirect nature of the photonic band gaps, because the gap modes are now pseudo-evanescent with frequency dispersive, nonzero real parts of their complex wave vectors. We find that the tunneling phase time for finite structures correlates with the group-like velocity of the gap modes, $1/v_g = \mathrm{dRe}\{k_{gap}\}/\mathrm{d}\omega$. While one of the spins tunnels with an expected positive group delay, the other spin will exhibit a negative

group delay by tunneling with a group-like velocity opposite to the exponential decay direction ($\mathrm{Im}\{k_{gap}\}*\mathrm{d}\omega/\mathrm{dRe}\{k_{gap}\} < 0$) that corresponds to the tunneling direction.

These results also offer useful insight for practical applications relying on discriminating between opposite spins during tunneling, by showing that the choice of a barrier length does not only affect tunneling probabilities, as well known [21], but may also affect the balance between spin-polarized tunneling fluxes due to an opposite dependence of tunneling time on the barrier length for the two spins.

Electronic analogs of the photonic case studied in this chapter include a number of tunneling-based spintronic devices under active investigation currently, such as magnetotunneling junctions with magnetized noncentrosymmetric barrier materials (e.g. $Ga_{1-x}Mn_xAs$, or other magnetically doped semiconductors with a zinc-blende crystal structure), or semiconducting chiral carbon nanotubes with applied axial magnetic fields.

4.6. References

1. Chiao, R. Y., and Steinberg, A. M. "Tunnelling times and superluminality," *Progress in Optics, Vol. 37*, **37**, 345 (1997).

2. Nimtz, G. "On superluminal tunneling," *Progress in Quantum Electronics*, **27**, 417 (2003).

3. Nimtz, G., and Heitmann, W. "Superluminal photonic tunneling and quantum electronics," *Progress in Quantum Electronics*, **21**, 81 (1997).

4. Olkhovsky, V. S., Recami, E., and Jakiel, J. "Unified time analysis of photon and particle tunnelling," *Physics Reports-Review Section of Physics Letters*, **398**, 133 (2004).

5. Hartman, T. E. "Tunneling of a Wave Packet," *Journal of Applied Physics*, **33**, 3427 (1962).

6. Enders, A., and Nimtz, G. "Evanescent-Mode Propagation and Quantum Tunneling," *Physical Review E*, **48**, 632 (1993).

7. Spielmann, C., Szipocs, R., Stingl, A., and Krausz, F. "Tunneling of Optical Pulses through Photonic Band-Gaps," *Physical Review Letters*, **73**, 2308 (1994).

8. Nimtz, G., Spieker, H., and Brodowsky, H. M. "Tunneling with Dissipation," *Journal De Physique I*, **4**, 1379 (1994).

9. Olkhovsky, V. S., Petrillo, V., and Zaichenko, A. K. "Decrease of the tunneling time and violation of the Hartman effect for large barriers," *Physical Review A*, **70**, (2004).

10. Zutic, I., Fabian, J., and Das Sarma, S. "Spintronics: Fundamentals and applications," *Reviews of Modern Physics*, **76**, 323 (2004).

11. Voskoboynikov, O., Liu, S. S., and Lee, C. P. "Spin-dependent delay time in electronic resonant tunneling at zero magnetic field," *Solid State Communications*, **115**, 477 (2000).

12. Wu, H.-C., Guo, Y., Chen, X.-Y., and Gu, B.-L. "Rashba spin-orbit effect on traversal time in ferromagnetic/semiconductor/ferromagnetic heterojunction," *Journal of Applied Physics*, **93**, 5316 (2003).

13. Bita, I., and Thomas, E. L. "Tunneling time for barriers lacking space-inversion and time-reversal symmetries," *submitted to the Physical Review Letters on January 2005. Currently in review*, (January 2006).

14. Guo, Y., Shang, C.-E., and Chen, X.-Y. "Spin-dependent delay time and the Hartman effect in tunneling through diluted-magnetic-semiconductor/semiconductor heterostructures," *Physical Review B*, **72**, 045356 (2005).

15. Mehrez, H., Taylor, J., Guo, H., Wang, J., and Roland, C. "Carbon nanotube based magnetic tunnel junctions," *Physical Review Letters*, **84**, 2682 (2000).

16. Bita, I., and Thomas, E. L. "Structurally chiral photonic crystals with magneto-optic activity: indirect photonic bandgaps, negative refraction, and superprism effects," *Journal of the Optical Society of America B-Optical Physics*, **22**, 1199 (2005).

17. Kong, J. A. *Electromagnetic wave theory*, EMW Publishing (Cambridge, Mass., 2000).

18. D'Aguanno, G. D., Mattiuci, N., Scalora, M., Bloemer, M. J., and Zheltikov, A. M. "Density of modes and tunneling times in finite one-dimensional photonic crystals: A comprehensive analysis," *Physical Review E*, **70**, 016612 (2004).

19. Yeh, P. *Optical waves in layered media*, Wiley (New York, 1988).

20. Buttiker, M. "Larmor Precession and the Traversal Time for Tunneling," *Physical Review B*, **27**, 6178 (1983).

21. Ashcroft, N. W., and Mermin, N. D. *Solid state physics*, Saunders College (Philadelphia, 1976).

Chapter 5.
Photonic band gaps in 2D quasicrystals

This chapter marks a shift in the focus of the thesis towards materials with quasiperiodic structures, which break translational symmetry. In the current chapter we explore the optical properties of 2D photonic quasicrystals (PQC), a class of photonic band gap (PBG) materials that has been introduced only seven years ago. The current interest in PQC is related to their intrinsic high rotational symmetries, which are known to lead to rounder dispersion surfaces and thus to offer a potential for obtaining larger complete PBG at a given refractive index contrast (or to lower the contrast required for a certain PBG width). However, while promising, the PQC field remains largely undeveloped by comparison with photonic crystals (PC). As discussed in the next section, very few experimental papers have been published, and the few existing theoretical studies address the optical properties of various choices of PQC structures. To better understand the difficult problem related to the choice amongst quasiperiodic structures, consider that, while 2D crystals can be classified in only five distinct Bravais lattices, an infinite number of 2D quasicrystalline structures can be theoretically defined (e.g. consider only the case of N-fold rotationally symmetric structures, where N can be arbitrarily large). Thus, while a few PQC lattices have been the subjects of preliminary studies, much remains to be done. Particularly important at this early stage in the field of PQC seem to be systematic studies that would identify the more promising quasiperiodic

structures, those with a combination of both desired optical properties and also suitability for efficient fabrication.

In this chapter, we explore two basic but key problems that provide insight into the potential usefulness of PQC: the effects of systematically varying the point group symmetry (related to the maximum local rotational symmetry displayed by the 2D PQC, 8-, 10-, and 12-fold in this work), and the effects of choosing different types of PQC structures for each of these point group symmetries (related to the method of fabrication, dielectric cylinders placed on a quasiperiodic tiling pattern, or dielectrics patterned by interference lithography). These are important questions because, in practice, one has a choice of fabricating a wide variety of quasiperiodic structures and currently there are no published guidelines as to which structures have better photonic band gap properties, if at all. In particular, we try to understand the properties of quasiperiodically structured materials made with interference lithography (IL), because this fabrication platform allows efficient large area patterning of structures with readily tunable symmetries, and thus offers a great potential for practical applications (2D PQC based on quasiperiodic tilings have been made with electron-beam lithography, which severely limits the experimentally achievable sample sizes).

Next, in Chapter 6, we present an experimental study on the actual fabrication of large-area, 2D quasiperiodically structured materials using interference lithography, and the design of, and preliminary results for the fabrication at the sub-micron level of 3D quasiperiodic structured material using coherence diffraction lithography. The small feature size enables these structures to be potentially used as photonic band gap materials, and for novel microstructured composite materials with improved mechanical properties

arising from the combination of high rotational symmetries and the absence of crystal (fracture) planes in quasicrystals.

5.1. Introduction

By definition, quasicrystals break translational periodicity while maintaining a well-defined and long-range ordered structure, as evident from their diffraction spectra consisting of sharp peaks [1]. As a class of materials, quasicrystals have only been known since 1984, remarkably the year of both the first experimental observation of quasicrystalline atomic order by Shechtman *et al.* [2] working on metal alloys, and of the independent theoretical report of Levine and Steinhardt [3] that introduced quasicrystals as a new class of ideal atomic structures. The discovery of these materials sent waves through a number of fields, particularly in crystallography where the notion of a crystalline state being evidenced by the presence of sharp peaks in the diffraction pattern (reciprocal space) had to be fundamentally altered. Just three years later in 1987, photonic band gap (PBG) materials were taking stage as a new branch of solid state physics, due to the seminal works of Yablonovitch [4] and John [5], which announced profound opportunities for engineering light-matter interactions in this new class of artificial optical materials. Although photonic crystals (PC) are typically described as analogs of atomic crystals (where the atomic periodicity is replaced by the periodicity of the refractive index on length scales comparable with the wavelength of light) it was only in 1998 when the photonic analog of a particular atomic quasicrystalline arrangement was first reported. Chan *et al.* [6, 7] studied a 2D octagonal quasiperiodic structure and were first to show that photonic quasicrystals (PQC) can also display photonic band gaps. The

formation of band gaps in the absence of translational periodicity did not come as a surprise, since both electronic and photonic band gaps were known to exist even in amorphous materials, due to short-range order [8]. However, the main importance of Chan's report is, arguably, the fact that the quasicrystalline order was introduced as an alternative approach for enabling PBG in structures with well defined geometries and thus with a clear path towards the optimization of their properties through systematic variation of structure.

The current interest in PQC lies in their ability to exhibit local rotational symmetries higher than those of crystals. A higher rotational symmetry is associated with rounder dispersion surfaces [9], which has the potential to enable larger photonic band gaps at a given refractive index contrast, or to lower the refractive index contrast required for a particular width of the photonic band gap. Due to their translational symmetry, crystals (2D and 3D) can *only* exhibit 1-, 2-, 3-, 4- and 6-fold rotation axes (2π, π, $2\pi/3$, $\pi/2$, and $\pi/3$ angles) [10]. Quasicrystals, on the other hand, can exhibit much higher rotational symmetries: 8-, 10-, and 12-fold rotation axes have been observed in atomic quasicrystals [1], and even higher rotations are possible in mathematical quasicrystalline tilings [11] (theoretically up to infinite rotational symmetry in the 2D pinwheel tiling).

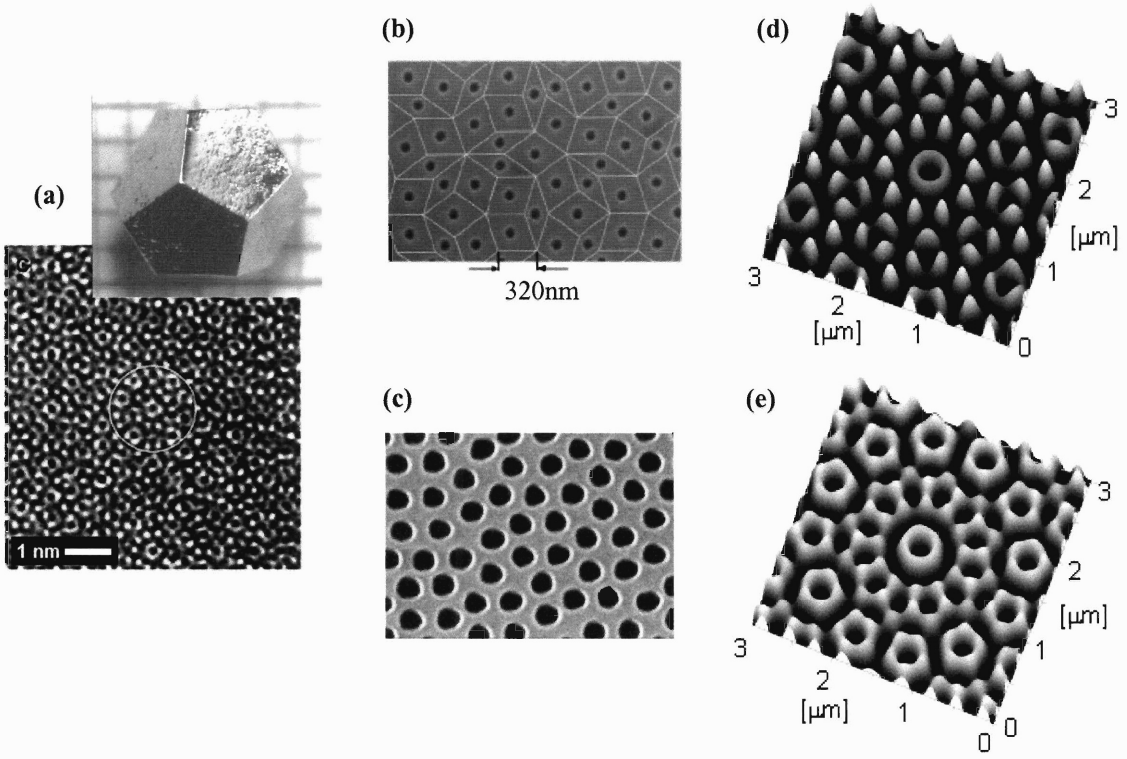

Figure 5-1 - Quasicrystalline structures. **(a)** HRTEM phase-contrast atomic-resolution image of Zn_6Mg_3Ho decagonal quasicrystal viewed along the 10-fold rotation axis [*www.jeol.com*] and a photograph of a macroscopic (mm scale) quasicrystal; **(b) and (c)** SEM pictures of photonic quasicrystal made by etching holes in a pattern given by a quasiperiodic tiling - Penrose in (b) (from [12]) and dodecagonal in (c) (from [13]); **(d) and (e)** calculated quasiperiodic light intensity patterns from interference of laser beams, showing 10-fold and 12-fold rotational symmetries (this work).

Figure 5-1(b-e) shows some types of quasiperiodic structures, including those currently being investigated as potential PBG materials. The few existing theoretical and experimental studies to date have focused on the case of mathematical quasiperiodic tilings. The first PQC paper by Chan *et al.* in [6] examined 2D octagonal tilings. Figure 5-1(b) shows the case of a 2D decagonal (Penrose) tiling from the work of Notomi *et al.* [12], and Figure 5-1(c) shows the case of a 2D dodecagonal PQC from the work of Zoorob *et al.* [13]. Finally, in Figure 5-1(d) and (e) we show predicted structures from the interference of laser beams designed to produce the same rotational symmetries as the two shown quasiperiodic tilings but with very different detailed geometries. In the case of PQC from interference lithography, there is only one publication in 2005 by Gauthier

and Mnaymneh, where the propagation of TM polarized waves through finite portions of dodecagonal 2D PQC made via interference lithography was computationally investigated in order to understand PBG formation [14]. This study is particularly important for this chapter, since as described below, we are going to investigate in much greater detail the same family of PQC (including the system studied in [14])

As presented in the next chapter, our main interest is with the fabrication and properties of quasiperiodically structured materials made with interference lithography (IL), because this fabrication platform allows efficient large area patterning and thus offers a great potential for practical applications (PQC based on quasiperiodic tilings require electron-beam lithography for practical implementations, an expensive and very slow process, thus greatly limiting possible applications). Due to the large number of quasiperiodic structures that can be fabricated by IL, and the lack of prior investigations of their corresponding PBG properties, in the present chapter we identify and theoretically study a number of important and previously unanswered basic problems related to PBG formation in 2D quasicrystals.

First, we study the effects of point group symmetry on PBG formation by examining in particular 8-, 10-, and 12-fold rotationally symmetric 2D PQC from IL (8mm, 10mm, and 12mm symmetries). In two dimensions, point group symmetries are limited to rotation axes and reflections (mirror lines). For crystals, there are 10 point groups (1, m, 2, 2mm, 3, 3m, 4, 4mm, 6, 6mm). For quasicrystals, the number of point groups is infinite, consisting of rotation axes of degree N and mirror lines passing through the point of the rotation axes (N, Nm, Nmm types). The point group symmetry of the structure influences the resultant physical properties. For example, Von Neumann's

principle states that the symmetry of any physical property of a crystal (as signified by the tensor representing that physical property) must be at least as high as the point group symmetry of the crystal. In PC and PQC, the key characteristic for band gaps is the the "roundness" of dispersion surfaces in reciprocal space and thus the formation of complete gaps for a given refractive index contrast [9]. Examples for the importance of symmetry on the formation of PBG include reports of larger TM gaps in 2D hexagonal lattice PC (6mm point group symmetry) compared to 2D square lattice PC (4mm symmetry) [15], and recently the report of complete 2D PBG in a dodecagonal 2D PQC (12mm symmetry) that exceed the gap widths of known 2D PC [13]. However, while able to exhibit arbitrary higher rotational symmetries, PQC lattices are yet to be investigated systematically in order to establish the importance of these symmetries in the context of the absence of translational periodicity. Thus, we set out to investigate PBG formation in quasiperiodic structures with 8-, 10-, 12-fold rotational symmetries (point groups 8mm, 10mm, and 12mm), focusing primarily on the those produced by IL due to our practical interest in large area fabrication (see Figure 5-1). Our investigation not only impacts the theoretical understating of symmetry effects on PBG formation, but, equally important, also offers a first guide for understanding the potential properties of 2D PQC made with IL, given that only one previous investigation exists in this area (which examined transmission spectra for TM propagation in a 12-fold rotationally symmetric 2D quasicrystal [14]).

The second problem studied in this chapter is related to the choice between types of quasicrystal structures available for a given symmetry. As shown in Figure 5-1(b) and (c), one way a PQC can be obtained from mathematical quasiperiodic tilings is by placing

cylindrical rods with a given radius at the vertices of the tiling. A second type of quasicrystal that we study is obtained from IL, as shown in Figure 5-1(d) and (e). While the two kinds of quasiperiodic lattices display similar rotational symmetries, their structural features differ greatly and thus they are expected to display different PBG properties.

The next subsections present in the IL model we used to generate the 2D PQC structures that were investigated, and the finite-difference time domain (FDTD) computational electrodynamics approach used to study PBG formation.

5.2. Quasiperiodic structures in 2D

In order to computationally study PBG properties in 2D quasicrystals, methods need to be first developed for the numerical generation and representation of the structures of interest, as well as for the realization of such structures in actual material systems.

5.2.1. Quasiperiodic 2D structures from interference lithography (IL)

For the purpose of PBG formation studies, the numerical representation of PQC structures is achieved by starting with a model for predicting the 2D spatial distribution of light intensity, $I(x,y)$, that is obtained during the interference of laser beams arranged properly in space. The restriction of the analysis to the 2D case is mainly for clarity, as it is easy to generalize the interference to 3D space [16]. As further presented in the next chapter, two different approaches for obtaining quasiperiodic interference patterns exist - either interference of multiple beams (e.g. 5, 8 or 12 beams for deca-, octa- or

dodecagonal quasicrystals) [17, 18], or multiple exposures of line patterns from 2-beam interference, with sample rotations after each exposure (e.g. $N = 4$, 5 or 6 rotations with π/N angles for octa-, deca-, and dodecagonal quasicrystals) [19]. Although the resulting structures obtained from these two approaches have the same point group symmetry, as shown quantitatively in Chapter 6, Section 6.2.1, the structures are significantly different. The reason for this is because multiple beams IL (MB-IL) results in a superposition of multiple 2D quasiperiodic patterns with more than one value of fringe spacing. For the purpose of the studies presented in this chapter, we choose to focus on the multiple exposure structures, because they are the simplest structures that capture all the symmetry and structural features of IL PQC.

The model used for calculating the corresponding spatial distribution of the light intensity, $I(x,y)$, in the sample plane is easily derived considering the intensity pattern obtained from interference of two TE polarized laser beams is [16]

$$I_2(\mathbf{r}) = 2I_0^2\left(1+\cos(\Delta\mathbf{k}\cdot\mathbf{r}+\Delta\phi)\right) \tag{5-1}$$

where the two beams are assumed to have the same intensity, I_0, and $\Delta\mathbf{k} = \mathbf{k_2} - \mathbf{k_1}$ and $\Delta\phi$ are the difference of their wave vectors and phases. To focus on understanding the structural features of quasicrystals made via the multiple exposure of line gratings approach, we further assume the two interfering beams in Eq. (5-1) are counterpropagating in the (x,y) plane, in-phase, polarized out-of-plane ($\mathbf{E}||\mathbf{z}$), and that the total intensity pattern is just the sum of the set of latent intensity patterns that would be recorded experimentally in a photoresist layer. Assuming $I_0 = 1$ and N exposures, the total light intensity distribution becomes

$$I(x,y) = \sum_{j=1}^{N} \left(2 + 2\cos(2\,x\,k_0 \cos\theta_j + 2\,y\,k_0 \sin\theta_j)\right) \tag{5-2}$$

where $k_0 = 2\pi/\lambda$, and λ = wavelength of the laser. The orientation of each exposed line grating is described by the polar angle θ_j as measured from **x** towards **y**, assuming a common origin. Note that we assumed $\theta_j = (j\text{-}1)*\pi/N$.

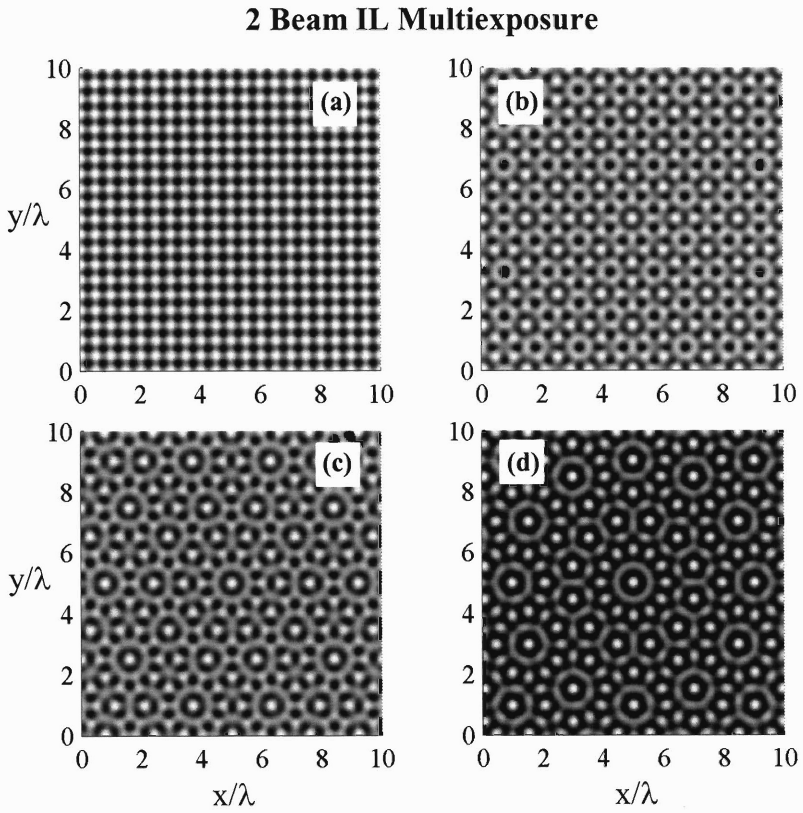

Figure 5-2 - Spatial distribution of the total light intensity, *I(x,y)*, pattern for **(a)** square crystal *(N = 2* exposures*)*; **(b)** octagonal *(N=4)*, **(c)** decagonal *(N=5)* and **(d)** dodecagonal *(N=6)* quasicrystals. The axes units are normalized to the laser wavelength, and higher intensities are plotted as lighter pixels.

The resulting intensity distributions *I(x,y)* for *N = 2, 4, 5* and *6* exposures with π/N rotations are shown in Figure 5-2, where the lighter pixels represent higher intensity values. When *N=2*, the resulting structure is simply a translationally periodic, square lattice with *λ/2* period. The evident higher rotational symmetries of the octagonal *(N=4)*,

decagonal ($N=5$), and dodecagonal ($N=6$) quasiperiodic patterns imply the lack of translational periodicity. It is important to realize that these $I(x,y)$ patterns do not yet represent the actual quasiperiodic structures generated in interference lithography. If a positive (negative) photoresist is used, the high intensity regions will increase (decrease) the solubility of the resist in the developer solution. Thus, a positive photoresist will adopt the structure obtained by cutting the $I(x,y)$ landscape at a particular intensity value (level set), I_{cut} (which corresponds to the experimental exposure dose), and keeping only the regions where the light intensity was smaller than this threshold, $I(x,y) < I_{cut}$. Thus, by varying the parameter I_{cut}, we can numerically represent structures with different fill fractions that can be generated from a particular interference lithography configuration by varying the exposure dose.

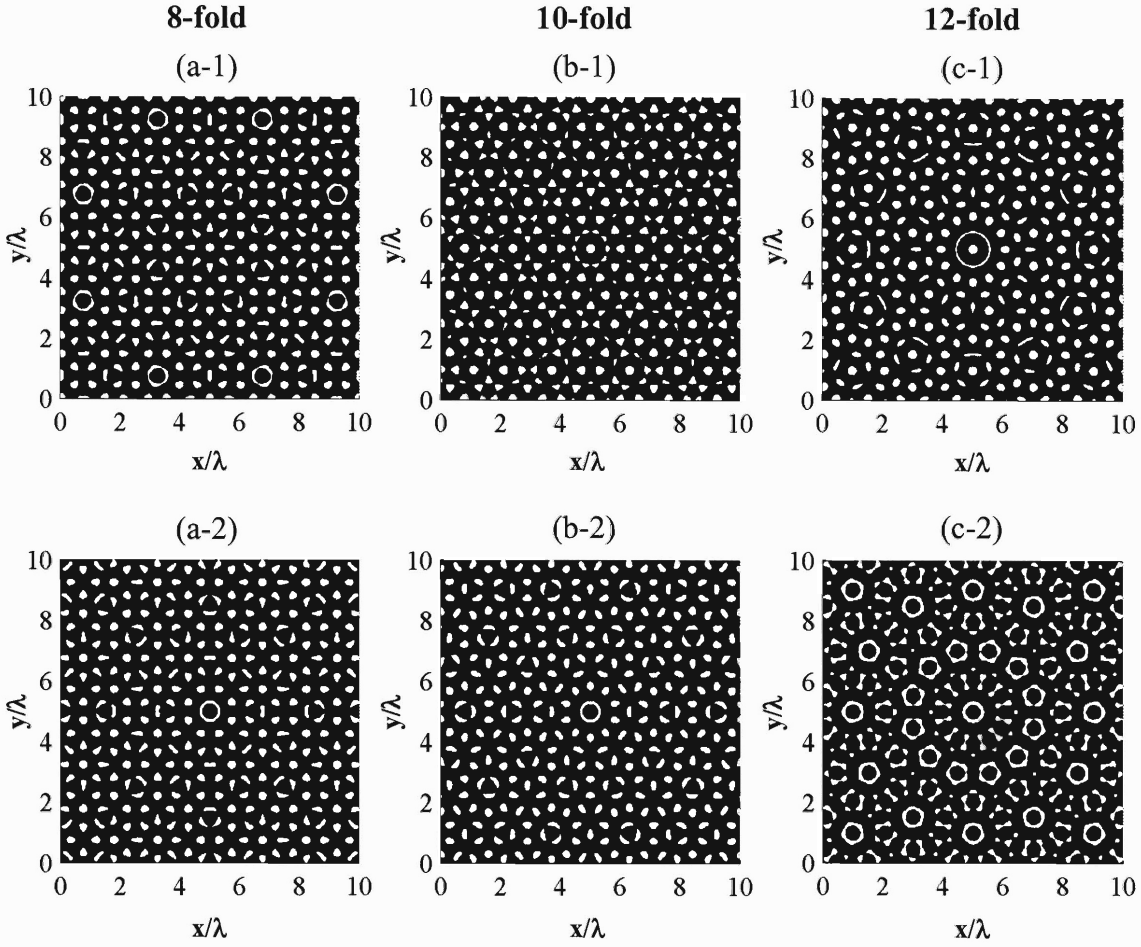

Figure 5-3 - Quasicrystalline structures with *18%* fraction of a given component (white pixels) for the investigated rotational symmetries; the (X-1) series corresponds to $I > I_{cut}$, while the (X-2) series to $I < I_{cut}$ (X = a, b, c); **(a)** octagonal quasicrystal with $I_{cut}/I_{maximum}$ = *67%* in (a-1) and *33%* in (a-2); **(b)** decagonal quasicrystal with $I_{cut}/I_{maximum}$ = *63%* in (b-1) and 34% in (b-2); **(c)** dodecagonal quasicrystal with $I_{cut}/I_{maximum}$ = *64%* in (c-1) and *35%* in (c-2).

It is important to notice the differences between quasicrystal structures with a given volume (area) fraction (18%), as presented in Figure 5-3. In order to obtain a given volume fraction, one could place the dielectric material in the regions with $I(x,y) > I_{cut}$ at high values of I_{cut}, shown in Figure 5-3(a,b,c-1), or place the dielectric in the regions $I(x,y) < I_{cut}$ with low values of I_{cut}, shown in Figure 5-3(a,b,c-2). While the octagonal structure seems very similar in both of these situations, the decagonal and dodecagonal

structures exhibit different structural features depending on whether they are generated at intensity values higher or lower than the I_{cut} that leads to the desired volume fraction.

While exploring the effects of varying the threshold intensity, it became clear that besides the expected change in volume fractions, these quasiperiodic patterns displayed significant changes of their structures. By contrast, in the case of a 2D square lattice such as that in Figure 5-2(a) changing I_{cut} leads to a continuous change in the diameter of the holes (rods), without e.g. changing the number of rods (holes). For quasiperiodic patterns, we observe that variations of I_{cut} lead to not only a change in the size of existing structural features, but also to significant changes of their shape and, most importantly, to the appearance or disappearance of certain structural features (and a more "fragmented" overall appearance). Connectivity of the dielectric material is important for maximizing PBG as a result of a tradeoff. TM polarized gaps are favored by arrays of individual (disconnected) dielectric domains, while TE PBG tend to become wider in more connected structures [9]. In our studies we focus on TM PBG, and thus the concern with the structural features observed in 2D PQC from IL is not as much related to having a "fragmented" appearance (which may favor wider gaps), but with the effect of the size distribution of these structural features.

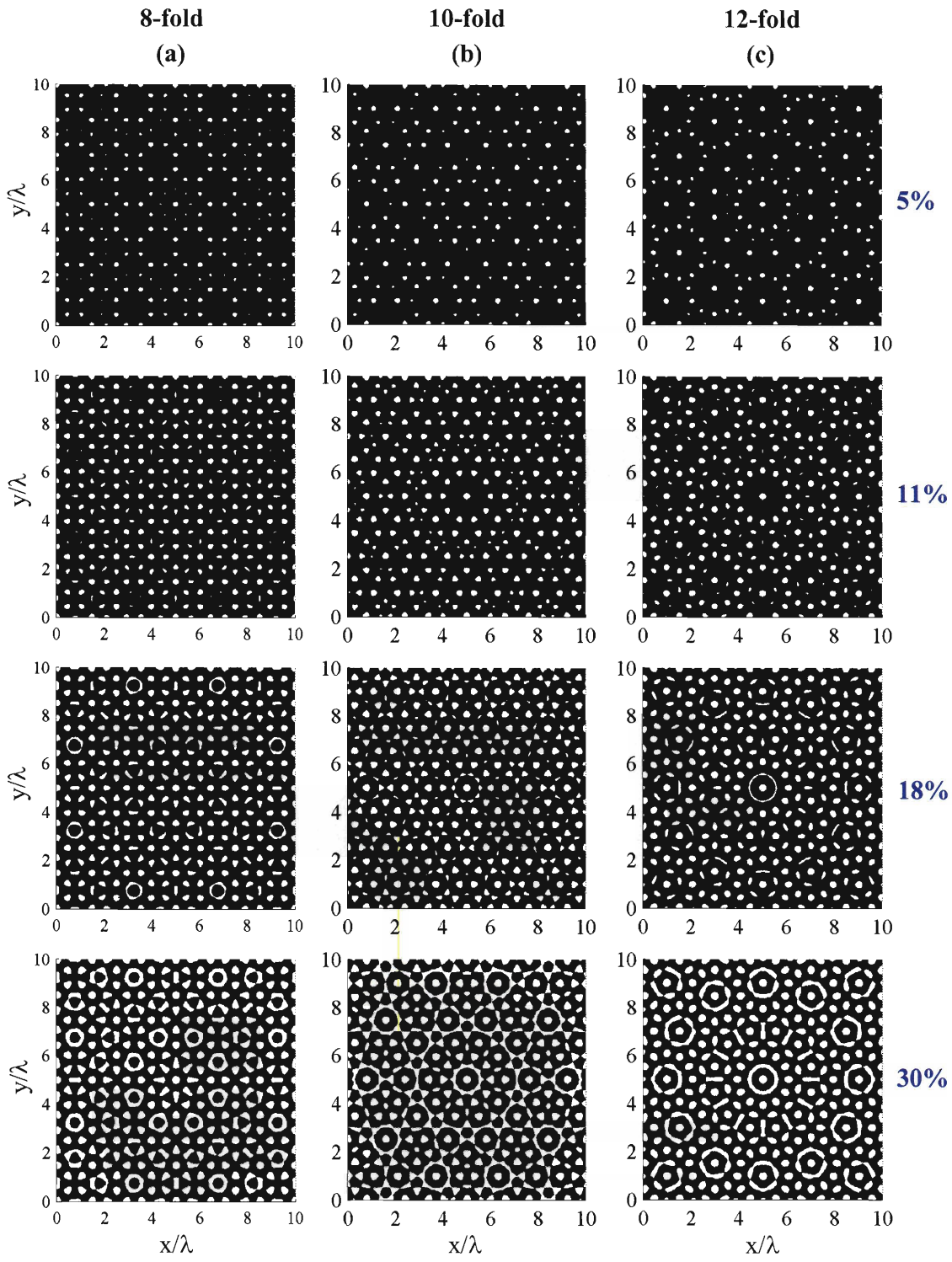

Figure 5-4 - **(a)** Octagonal, **(b)** decagonal, and **(c)** dodecagonal patterns with varying volume fractions of the white region (where $I(x,y) > I_{cut}$), showing not only a continuous change of the size and shape of particular features, but also a discontinuous appearance of new structural features. Values of the corresponding I_{cut} are given in Table 5-1.

Table 5-1 - Values of I_{cut} and corresponding dielectric volume fractions of 2D quasicrystals from IL where dielectric material is generated in regions with $I(x,y) > I_{cut}$, see Figure 5-4.

f	I_{cut} / $I_{maximum}$		
(area fraction)	OCTAGONAL	DECAGONAL	DODECAGONAL
5%	79.3%	76.0%	76.7%
11	72.0%	67.8%	68.7%
18	66.8%	63.4%	63.7%
30	59.5%	59.0%	57.6%

Figure 5-4 shows structures with four distinct area fractions between *5* to *30%* for each type of quasicrystal of interest - octagonal, decagonal and dodecagonal (their corresponding I_{cut} values are listed in Table 5-1). The purpose of this figure is to show the important property that varying the area fraction in a quasicrystal made by interference lithography is accompanied by significant changes of the pattern structure. The consequences of this fact will become important later in this chapter, when the formation of PBG in PQC is quantitatively investigated.

Lastly, we note that the type of quasicrystals described in this section will be referred to as IL-PQC, to emphasize that their structure is produced by interference lithography, and to distinguish from PQC obtained by placing cylinders on the vertices of tiles in quasiperiodic tilings (labeled PROJ-PQC, see next section). This nomenclature allows us to more clearly distinguish between the different types of 2D PQC throughout this chapter.

5.2.2. Quasiperiodic 2D structures from quasiperiodic tilings

Existing theoretical and experimental work in the area of PQC focuses on quasicrystals obtained by placing dielectric rods or air holes at the nodes of a mathematical quasiperiodic tiling [6, 12, 13, 20]. It is interesting to note that, although

the most famous quasicrystalline tiling is the Penrose type, the first 2D PQC paper examined the case of a tiling with octagonal symmetry [6].

Our interest in the formation of PBG in PQC based on tilings was motivated by an interest to directly compare quasicrystals from interference lithography to them, and to thus learn about the importance of the choice of quasiperiodic structure for the formation and extent of PBG. Thus, in this section we outline the computational method used for generating 2D quasiperiodic tilings with point group symmetries similar to those described in the previous section.

Although it is beyond the scope of the current thesis to explore in great detail the mathematical representation of 2D quasicrystals, we note that studying quasiperiodicity involves rather complex and quite intellectually stimulating problems. Consider that the typical 2D quasicrystalline tilings (e.g. with local 8-, 10- and 12-fold rotation axes) can be obtained by projecting a translationally periodic lattice from a higher dimensional space (typically a simple cubic lattice) onto a physical 2D or 3D space. For example, Penrose tilings can be generated by projecting a 5D cubic lattice onto a plane, and 12-fold rotationally symmetric (dodecagonal) tilings can be generated by a similar projection, but now from 6D [11]. This projection approach can be more easily understood, if described in the case of generating a 1D quasicrystal from a 2D square lattice.

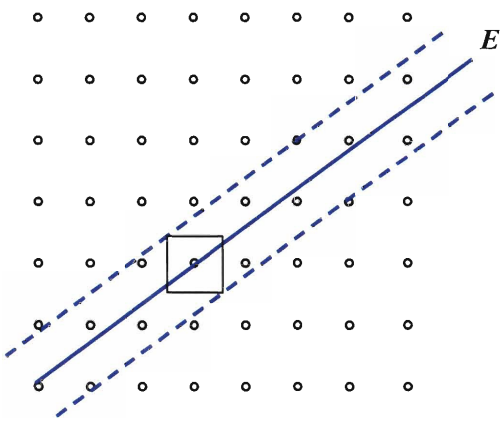

Figure 5-5 - Generation of a 1D quasicrystal by projection from a 2D square lattice. The key requirement is for the (e.g. 1D) axis ***E*** (onto which the projection is done) to be oriented at an irrational angle with respect to the translation vectors of the higher dimension (e.g. 2D) periodic structure. Adapted from [11].

To obtain a 1D quasiperiodic lattice, the projection method requires starting from a higher dimensional space, here just 2D. Quasiperiodicity requires the orientation of the axis onto which the projection is done (***E*** in Figure 5-5) to be at an irrational angle from the translation vectors of the 2D lattice. Also, only the lattice points contained in a finite thickness "shell" around the considered axis (shown with dashed lines in Figure 5-5) are projected. As an example, the Fibonacci sequence can be generated with this method, if the slope of the line ***E*** is related to the golden mean, $\tau = (1+\sqrt{5})/2$.

While it is more difficult to graphically describe the method of projecting a lattice from high dimensional spaces onto a 2D physical space, it is essentially similar to the 1D quasicrystal example presented above. For the purpose of this thesis, a computer code provided by Dr. Mihai Ibanescu from the research group of Prof. John Joannopoulos from the MIT Physics department was used to generate a text file containing the coordinates of the vertices in quasiperiodic lattices with desired rotational symmetries (vertices shown as circular dots in Figure 5-6). The code uses the same projection algorithm as described in Chapter 5 of [11].

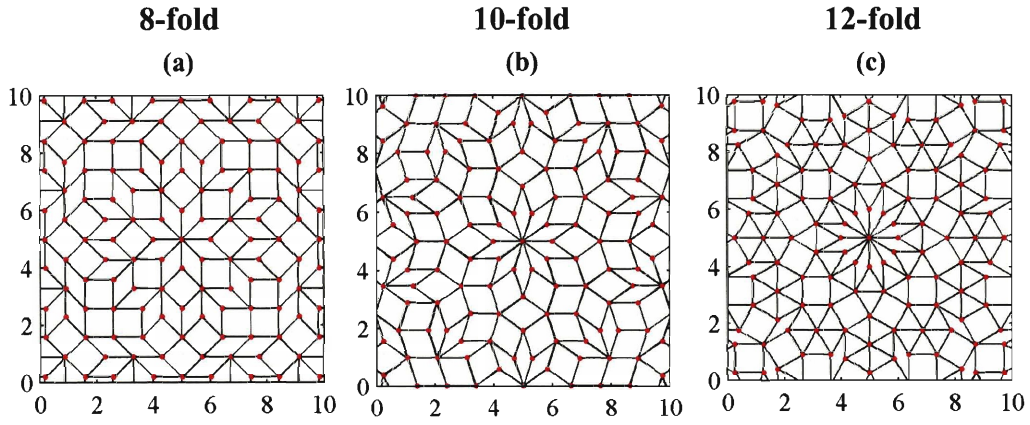

Figure 5-6 - Examples of 2D quasicrystalline tilings. **(a)** octagonal quasicrystal; **(b)** decagonal quasicrystal and **(c)** dodecagonal quasicrystal. The patterns are centered with the high rotation axis at (5,5).

Typical results of the projection method are shown in Figure 5-6, where the high rotational symmetry axis for each type of quasicrystal is located at the center of the plots. Note that a tiling pattern is obtained by joining the vertices of the quasiperiodic tiling patterns, just as expected. For 8- and 10-fold rotational symmetry, quasiperiodic tilings are formed from two unique tiles, while for the case of 12-fold rotational symmetry at least three tiles are needed [21]. Below we show the corresponding quasiperiodic structures obtained by placing dielectric rods at the vertices of these three quasi-lattices, where the rod diameter has been chosen to give 18% fill fraction, to allow direct comparison with the corresponding IL-PQC structures shown in Figure 5-3.

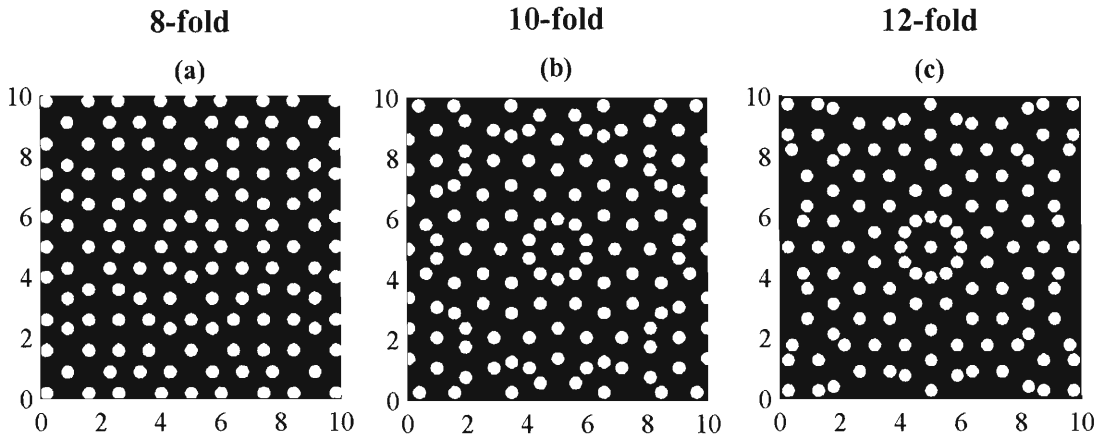

Figure 5-7 - 18% fill fraction 2D quasiperiodic structures based on mathematical quasicrystalline tilings (for comparison with interference lithography structures shown in Figure 5-3).

To complement the data in Table 5-1, we show next the effect of the dielectric cylinder radius on the volume fraction of 2D PQC from quasiperiodic tilings.

Table 5-2 - Effect of dielectric cylinder radius on volume fraction in 2D PQC obtained from 2D quasiperiodic tilings as shown in Figure 5-7, calculated for a square sample of side 21*a* discretized with 32points/*a* (*a* = *1*, same sizes as used in the PBG simulations discussed in Section 5.3). For each symmetry, we also include the total number of cylinders contained in the 21x21*a* computational box.

f	r / a		
(area fraction)	OCTAGONAL (513 cylinders)	DECAGONAL (521 cylinders)	DODECAGONAL (541 cylinders)
5%	0.1159	0.1163	0.1143
11	0.1735	0.1723	0.1694
18	0.2217	0.2208	0.2160
30	0.2858	0.2847	0.2810

Lastly, we note that the type of quasicrystals described in this section will be referred to as PROJ-PQC, given that their structure is obtained by the projection method.

5.3. FDTD for computing photonic band gap frequencies

The absence of translational periodicity in photonic quasicrystals makes the theoretical prediction of their optical properties much more difficult than in the case of photonic crystals. Translational periodicity in PC enables the use of Bloch's theorem,

and allows optical properties to be derived by examining a small portion of the crystal, typically the translational unit cell of the structure using periodic boundary conditions, or the reduced Brillouin zone in the reciprocal space [9, 22]. In PQC, by definition, there is no translational unit cell and thus computational investigations of optical properties have to approximate the properties of the entire structure based on examining finite but larger size pieces of the quasicrystal.

The finite difference time domain (FDTD) approach to solving Maxwell's equations is particularly well suited for investigating PBG formation in quasicrystals, because it allows modeling of the optical properties of materials with arbitrary size, shape, and composition. The essence of this numerical method is the discretization of both spatial and temporal derivatives in Maxwell's equations, followed by the evaluation of the resulting algebraic equations [23]. To illustrate this concept, consider a wave propagating along the **z** axis in a material with dielectric constant ε, and polarized along **x**. For this case, the propagation is described by the following differential equation

$$\frac{\partial E_x(z,t)}{\partial t} = -\frac{1}{\varepsilon}\frac{\partial H_y(z,t)}{\partial z} \tag{5-3}$$

In FDTD, the above equation is numerically evaluated by employing a finite difference approximation for both the spatial and temporal derivatives, which in its most simple form reduces to

$$\frac{E_x(z,t+\Delta t)-E_x(z,t)}{\Delta t} = -\frac{1}{\varepsilon}\frac{H_y(z+\Delta z,t)-H_y(z,t)}{\Delta z} \tag{5-4}$$

While the above equation illustrates the concept behind FDTD, it is important to keep in mind that more sophisticated finite difference formulas can be used in practice,

and that the algorithm for stepping in time can be quite complicated when solving Maxwell's equations [23]. In all cases, the accuracy of the FDTD solution ultimately relies on the choice of the temporal and spatial steps, Δt and Δz. The smaller these two parameters are, the more accurately the material structure and time varying electromagnetic fields are represented, and the better the final solution. Accuracy in FDTD is thus obtained at the expense of a larger size and of a longer duration of the numerical simulation.

In our studies, we have used the MIT Electromagnetic Equation Propagation (MEEP) FDTD simulation engine developed in the research group of Prof. John Joannopoulos from the Physics Department at MIT by Dr. David Roundy and Dr. Mihai Ibanescu, both of whom we acknowledge for their help and access to this software. Currently, the development of MEEP is continued at MIT by Prof. Steven Johnson. MEEP was also recently released as freely available software [24].

Since the goals of our investigation revolve around developing a basic understanding of the effects of symmetry and quasicrystal type on PBG formation, we choose to focus on PBGs for TM polarization. The FDTD approach we use is similar to that used by Chan *et al.* in their study of octagonal PQC [6, 7], except that due to computational constraints and the large problem space that will be explored, we have restricted the calculations to the local density of states (LDOS) at the center of high rotational symmetry of the 2D quasicrystals introduced above. A superior approach is to average LDOS at many locations in the 2D PQC structure of interest, but doing so requires very large computational resources. By integrating over a unit cell in a PC, the total density of states (DOS) can be obtained [22] - of course, PQC do not have a unit

cell, and thus a much larger area would need to be surveyed in order to obtain the total 2D DOS. Nevertheless, as previous studies of gap formation in amorphous semiconductors have shown, LDOS calculations can have the similar predictive power as total DOS calculations if only the gap formation is of interest. For amorphous silicon, Allan and Joannopoulos [25] have shown that LDOS at arbitrary choices of atoms in the amorphous lattice differ only in the number of the propagating modes, while the gaps remain of similar magnitudes and, in fact, comparable to those in crystalline silicon. Similar observations were also made in the case of amorphous compound semiconductors, where at least two different atoms are present in the lattice. Yndurain and Joannopoulos [26] have calculated the LDOS in amorphous III-V semiconductors, and their results show that LDOS curves at either Ga or As atom locations display the same gaps. The effects of a different local environment in amorphous semiconductors on the gaps predicted from LDOS are understood to include possible appearance of defect states in the gaps at certain energies - the gap edges, on the other hand, remain essentially unchanged (e.g. see Figure 6 in [26]).

Since, with one exception [14], no previous studies exist for IL-PQC, we have decided to base our current survey on gap formation as predicted by LDOS at the point of high rotational symmetry to gain insight into the general effects of point group symmetry (8mm, 10mm, and 12mm) and quasicrystal type (IL- and PROJ-PBG) at various dielectric contrasts ($\varepsilon = 4$, 6, 8, and 10 dielectric in air) for a range of fill fractions (0 to 30%). Besides the analogy with LDOS in amorphous semiconductors, discussed above, our choice was also motivated by other previous studies of photonic quasicrystals. Della Vila *et al.* also employed LDOS calculations at a central point, in a Penrose-type 2D

PQC, and discussed that the observed PBG properties were not affected by the location of the monitor point [20]. Wang *et al.* [27] examined DOS and LDOS in 2D PROJ-PQC and found that, for frequencies in the PBG, the LDOS was zero across the entire PQC structure, which suggests again that the location of the monitor point may not significantly affect the location of photonic gaps in 2D PQC as numerically determined by FDTD. Furthermore, as shown below, we employed the same FDTD computational method used for our PQC studies to obtain the LDOS at a center of high rotational symmetry in 2D triangular (6mm) and square (4mm) PC, and confirmed that the predicted PBGs agree very well with the exact predictions based on band structure calculations. The intuition derived from these results offers a useful guide for future investigations, where particular structures of interest would be characterized in more detail (not only LDOS averaging to obtain the total DOS and to understand propagating properties as well, but also investigating TE gaps for example, to search for complete 2D PBG).

Thus, the numerical representations of the quasiperiodic structures of interest for our studies introduced in Section 5.2 were first implemented as C++ routines. The structure generating functions are then passed to the MEEP FDTD engine, where a random magnitude, out-of-plane electric field component ($\mathbf{E}\|\mathbf{z}$ for TM polarization) is first initialized across the entire structure, using perfectly reflecting boundary conditions. The choice of initializing a random magnitude electric field was made in order to excite all the possible modes of propagation in 2D, so that any PBG that will be observed will in fact be a complete TM PBG (for any propagation direction in 2D from the chosen point) [6, 7]. The simulation is then performed for a long enough duration, and the electric field

is monitored at a point of high rotational symmetry in the structure, which is positioned in the computational box such that dielectric resides in the center of structures such as those shown in Figure 5-4 and Figure 5-7, where LDOS will be calculated (this offers a basis for comparing among various 2D PQC). By taking the Fourier transform of this time-varying electric field trace, we finally obtain a numerical approximation to the local density of states (LDOS) at this particular location, which allows us to determine the location of the photonic gaps.

In order to increase the accuracy of the FDTD simulations and to capture the fine structural details of IL-PQC (see Figure 5-4), we chose a small spatial discretization step, $\Delta x = \Delta y = a/32$, where a is a parameter equal to 1 (this parameter is used for normalization purposes, such that the units of both structural dimensions and electromagnetic wave frequencies are described as function of a). The temporal step, Δt, is not independent, but in FDTD is set for numerical stability purposes using the Courant condition [23]

$$\Delta t = \frac{\Delta x}{2 \cdot c} \tag{5-5}$$

where c is the speed of light in vacuum. Thus, in our simulations $\Delta t = (1/64)*(a/c)$.

To gain an understanding of the effect of symmetries on PBG formation, we chose to calculate the LDOS at a monitor point located at a center of high rotational symmetry, using a FDTD simulation with size, resolution and duration similar to those employed in previous publications [6, 7, 20]. Thus, for 2D IL-PQC we investigate structures similar to those shown in Figure 5-3(a-1), (b-1) and (c-1), and for 2D PROJ-PQC we focus on the case of dielectric rods placed at the vertices of the quasi-lattice, as

shown in Figure 5-6 and Figure 5-7. The size of the array and duration of FDTD simulations were increased until the observed gaps in the LDOS curves were not affected anymore. For all the results reported in this chapter we have used 512,000 time steps, which corresponds to a total simulation time of 8000(a/c). Similarly, the computational box was a square with a side equal to 21a (more than twice the size of the structures shown in Figure 5-3 and Figure 5-7, and slightly larger than in [6, 7]), .

To verify the ability of the FDTD LDOS calculations to predict PBG formation, we have first examined 2D photonic crystal structures, since in this case the location of PBGs can be independently obtained from photonic band structure calculations. For this purpose, we have used the "MIT Photonic Bands" (MPB) software [28], also developed by the group of Prof. Joannopoulos at MIT. We find that for both triangular and square lattice 2D PC, the FDTD simulations with MEEP predict PBG locations that are essentially the same as those predicted by MPB. In Figure 5-8 we show a direct comparison between the TM photonic band structure and the TM 2D-LDOS calculated with FDTD for a 2D triangular lattice of dielectric rods with $\varepsilon = 6$ embedded in air.

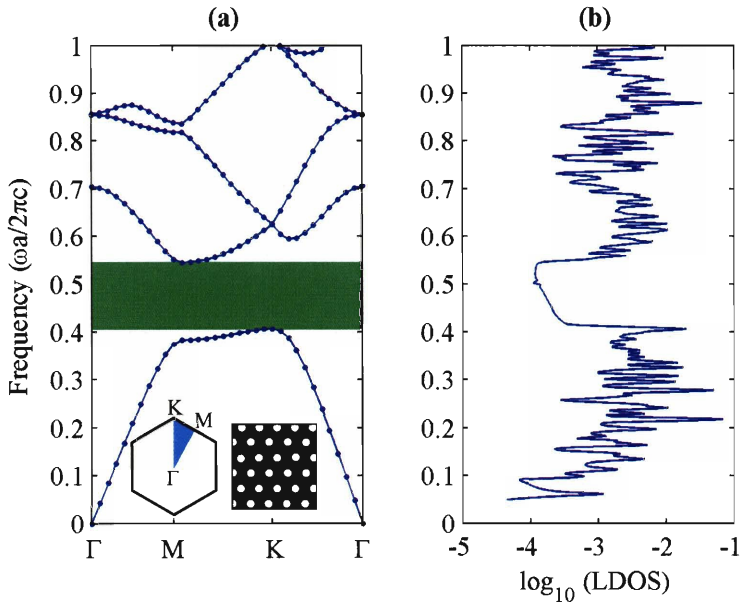

Figure 5-8 - Comparison between the location of the PBG via **(a)** photonic band structure (exact method), and **(b)** FDTD calculation of the LDOS at the center of a dielectric cylinder (approximate method) for a 2D triangular lattice with 10% dielectric rods with $\varepsilon = 6$ in air.

The size of the square computational box chosen for the above FDTD simulation results, and for all the other results reported in this chapter, was $21a$. In the case of 2D photonic crystals, a is chosen to be equal to the period of the structure. For the IL-PQC shown in Figure 5-4, we choose a to be equal to the spatial period of each grating written in the multiple exposure method (since $a = 1$ in the computer code, this amounts to using $\lambda = 2$ in Eq. 5-2, since the period of a line grating obtained from interference of two laser beams is $\lambda/2$). Lastly, for the PROJ-PQC shown in Figure 5-7, a was chosen to equal the length of the side of the tiles forming a 2D quasiperiodic pattern. Thus, for example, the distance between the center of high rotational symmetry to the nearest set of rods is taken to be $a = 1$. Varying the volume fraction of the 2D PQC structures is achieved by changing I_{cut} for IL-PQC (see representative data in Table 5-1) and the normalized radius of the cylinders for PROJ-PQC (r/a, see representative data in Table 5-2).

In summary, an FDTD approach for studying PBG formation was implemented similarly to a previous studies [6, 7, 20], using the MIT MEEP FDTD engine. The FDTD predictions were tested against exact results from photonic band structure calculations for 2D square and triangular PC, and a set of optimum simulation parameters were identified. These include a spatial discretization step $\Delta x = \Delta y = (1/32)*a$, temporal step $\Delta t = (1/64)*(a/c)$, box size with $L_x = L_y = 21a$, and a total simulation time equal to $8000a/c$ (512,000 time steps), where $a = 1$ and c is the speed of light in vacuum.

5.4. Effect of point group symmetry on PBG formation in IL-PQC

It is known that crystals with higher rotational symmetries have rounder dispersion surfaces in reciprocal space [8]. Furthermore, in photonic crystals, rounder dispersion surfaces are also associated with lager complete photonic band gaps [9]. That is why the higher rotational symmetries characteristic of quasicrystals have sparked an immediate interest in these structures for PBG applications. The first report of a PQC examined a 2D octagonal quasicrystal [6] and theoretically showed that a complete TM PBG can be formed. Two years later, in 2000, Zoorob *et al.* [13] reporting on a combined theoretical and experimental investigation predicted formation of a complete PBG (both TM and TE polarizations) for a 2D dodecagonal quasicrystal. The investigated 2D PROJ-PQC were fabricated with electron-beam lithography.

Only a few months ago, a first article investigating the optical properties of IL-PQC was published, where Gauthier *et al.* [14] computationally showed that TM PBG can also form in 2D dodecagonal quasicrystals made by interference lithography. Thus, while IL-PQC have a clear potential for higher impact in applications due to their low

fabrication cost and access to ultra-large device areas (e.g. entire 12" silicon wafers), there is currently no study directed towards developing a basic understanding of the effect of point group symmetry and dielectric volume fraction on PBG formation that would allow the experimental efforts to focus only on the most promising material structures. Furthermore, another important and yet absent study is a direct comparison of the PBG properties of IL-PQC to those of PROJ-PQC, given the structural differences that were presented in Section 5.2.

In the current section we will thus focus on investigating symmetry effects on the formation of TM PBG in 2D quasicrystals made by interference lithography, and continue in the next section with a comparison of the importance of quasicrystal type on PBG formation, for each of the investigated point group symmetries. In all studies, we assumed structures composed of a dielectric material and air, where the dielectric fill fraction and contrast were varied in order to construct TM photonic gap maps [9].

5.4.1. Effect of symmetry on 2D TM PBG formation in 2D PC

To better understand the importance of point group symmetries, we first examine the case of 2D photonic crystals because their PBG properties can be efficiently obtained from band structure calculations. We have thus used the MPB software [28] to study the formation of the lowest order TM PBG in 2D square (4mm point group) and triangular (6mm point group) photonic crystals consisting of dielectric rods in air. Note that the structures of both PC can be obtained by similar IL-based techniques as described for IL-PQC in Section 5.2.1, when $N = 2$ (square PC) and $N = 3$ (triangular PC). Both the radius and the dielectric constant of the cylinders have been varied, and by calculating the band structure for each case we tracked the evolution of the first TM PBG in both crystals.

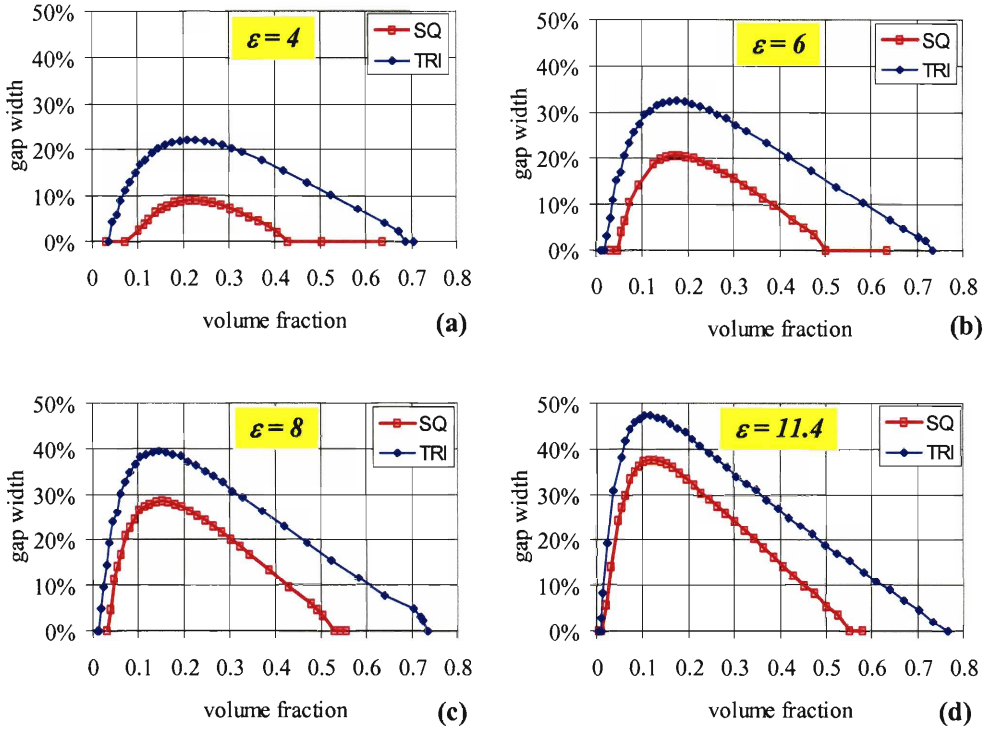

Figure 5-9 - Width of the 1st TM PBG in square and triangular 2D photonic crystals as a function of volume fraction, for dielectric **(a)** $\varepsilon = 4$, **(b)** $\varepsilon = 6$, **(c)** $\varepsilon = 8$, and **(d)** $\varepsilon = 11.4$ cylindrical rods surrounded by air. Each point on the plots represents an actual band structure calculation.

The effects of the dielectric contrast and fill fraction on the first TM PBG for both 2D PC are shown in Figure 5-9. The quantity that is plotted is the gap width, defined as

$$gap\ width = \frac{\Delta\omega}{\omega_{center}} = \frac{\omega_{upper} - \omega_{lower}}{(\omega_{upper} + \omega_{lower})/2} \tag{5-6}$$

where ω_{center} is the frequency in the center of the gap, and ω_{upper} and ω_{lower} are the frequencies of the upper and lower gap edges.

The results in Figure 5-9 quantitatively show that a higher point group symmetry leads indeed to larger PBG. The plots also show that the importance of rotational symmetry diminishes with increasing dielectric contrast, and that the maximum gap widths are obtained for the two families of PC at very similar fill fractions for a given

dielectric contrast. For dielectric rods with $\varepsilon = 4$ in air, a maximum gap width of 9% is obtained in a 2D square lattice PC with fill fraction of 0.21 (corresponding cylinder radius is $r/a = 0.26$) - however, using the same contrast and fill fraction, a 2D triangular lattice ($r/a = 0.25$) allows a maximum gap width of 22%, more than twice that of the square lattice. For comparison, consider now the high dielectric contrast case shown in Figure 5-9(d): for $\varepsilon = 11.4$, the gaps are much wider and they still appear at similar fill fractions - however, changing from a square lattice to a triangular one leads to an increase of the gap width from 38% to only 47%, a much smaller increase than the more than 2x factor observed for $\varepsilon = 4$. Villeneuve and Piché [15] studied PBG in PC with air cylinders on square and triangular lattices at a particular refractive index contrast, and also found that the triangular lattice led to larger PBG than the square lattice. These quantitative results agrees with a qualitative speculation that, a higher dielectric contrast leads to a higher repulsion of dispersion surfaces near band edges in reciprocal space (i.e. origin of larger gaps in the first place), which results in rounder (more spherical in 3D, or circular in 2D) dispersion surfaces. Therefore, qualitatively one would expect that the impact of rotational symmetry is diminished if the dispersion surfaces are already somewhat rounded off as a consequence of a high dielectric contrast in the PBG structure.

The results of this case study of 2D photonic crystals provide useful insight towards understanding the effect of point group symmetry in the formation of PBG. Importantly, the results suggest that quasicrystals can become a very important class of materials for enabling PBGs in practical applications, since most optically transparent materials that are commonly available do not typically have very large refractive indices -

it is exactly in this regime of lower dielectric contrast where increasing rotational symmetry was found to lead to the largest improvement of 2D TM complete PBG widths in photonic crystals.

5.4.2. Effect of symmetry on 2D TM PBG formation in 2D IL-PQC

We now proceed to investigate PBG formation in IL-PQC with 8-, 10- and 12-fold rotational symmetries. These structures were introduced in Section 5.2.1, and are also shown in Figure 5-4 at various fill fractions. PBG formation is studied again for the case of TM polarized modes, and, instead of band structure calculations, we now employ the FDTD approach discussed in the previous section for calculating the LDOS at a center of high point group symmetry. Both dielectric contrast and fill fractions were varied, using similar values as those used in the 4-fold and 6-fold dielectric cylinder PC study. Typical results are shown in Figure 5-10, where each plot is constructed from individual LDOS traces calculated at the central point of the IL-PQC, for 19 values of the fill fraction (f = 0.05-0.16 in steps of 0.01, and f = 0.18-0.30 in steps of 0.02).

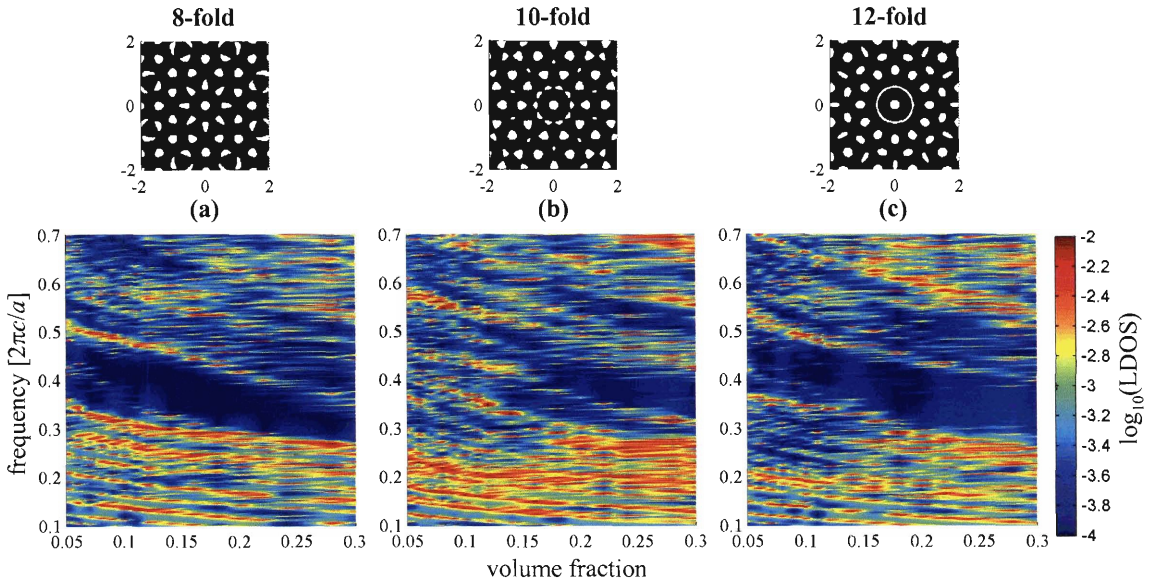

Figure 5-10 - Gap maps from assembling the LDOS curves calculated at the point (0,0) in each shown structure, for fill fractions f = 0.05-0.16 (steps of 0.01), and 0.18-0.30 (steps of 0.02) for **(a)** octagonal, **(b)** decagonal, and **(c)** dodecagonal quasicrystals from interference, with an $\boldsymbol{\varepsilon = 6}$ dielectric placed where $I > I_{cut}$. Small pieces of each PBG structure with 18% dielectric (white regions) are shown above each LDOS plot for emphasizing the structural differences between quasicrystals. Note that $a = \lambda_{interference}/2 = 1$.

The results shown in Figure 5-10 correspond to 8mm, 10mm, and 12mm point group symmetry IL-PQC at a relatively low dielectric contrast of $\varepsilon = 6$ versus air, where the 2D LDOS curves calculated at various volume fractions have been plotted on the same graph in 3D, with color indicating the value of the LDOS. Note that the frequencies are normalized to the parameter a, assumed here to be equal to the spatial period of the line gratings obtained if only two laser beams would be interfering ($a = \lambda/2 = 1$ in the FDTD code; also see Eq. 5-2). It is clear from this figure that complete 2D PBG for TM polarizations also form in the cases of octagonal and decagonal quasicrystals, in addition to dodecagonal PQC. For the latter PQC, the recent report of Gauthier and Mnaymneh [14] already predicted TM PBG formation based on a study of TM wave propagation through finite 2D PQC, but, unfortunately, we cannot compare our results to those in [14] because the authors used absolute wavelengths and finite size PQC and omitted to

include the wavelength used to generate the IL-PQC (thus it is not possible to normalize the location of their observed spectral gaps for comparison purposes). The most striking result in Figure 5-10 is that decagonal symmetry does not (by far) seem to lead to as good PBG properties as the other two quasicrystals.

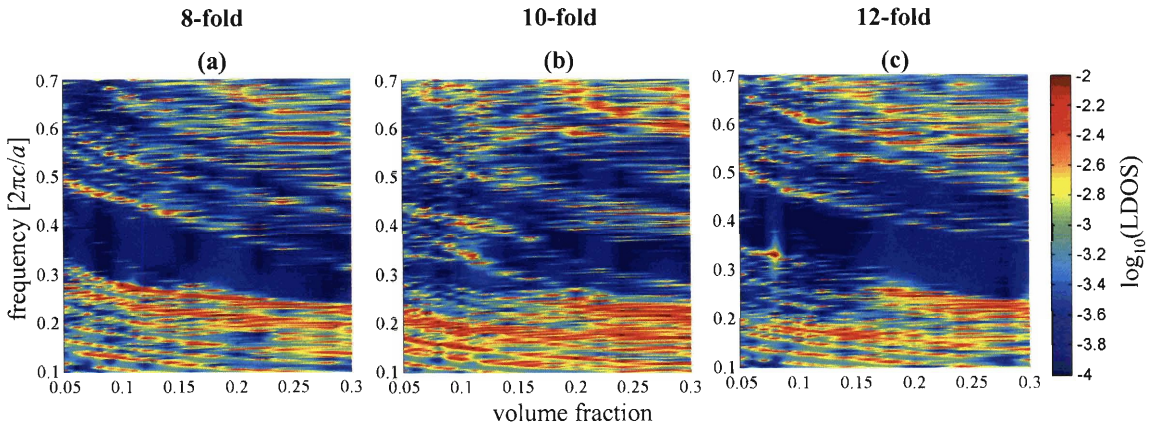

Figure 5-11 - same as Figure 5-10, but with $\varepsilon = 8$ for the dielectric component (higher dielectric contrast).

A higher dielectric contrast is investigated in Figure 5-11 ($\varepsilon = 8$ dielectric in air). As before, the 10-fold rotational symmetry seems to not be conducive to large TM 2D PBG in IL-PQC. While at lower fill fractions ($f < 0.1$) the octagonal symmetry provides the largest complete TM PBG, at larger fill fractions ($f > 0.2$) the dodecagonal IL-PQC exhibits the largest gaps. Furthermore, both octagonal and dodecagonal IL-PQC display larger PBG at small fill fractions than the square and triangular 2D PC investigated in Figure 5-9 (for $f = 0.05$ and $\varepsilon = 6$, quasicrystals have a 2D complete TM gap with widths $\Delta\omega/\omega_{center} \approx$ 20-25%, while the square lattice PC has $\Delta\omega/\omega_{center} \approx 4\%$ and the 2D triangular PC has $\Delta\omega/\omega_{center} \approx 16\%$).

These results indicate that increasing the point group symmetry in 2D IL-PQC does not lead to a clear trend in terms of the width of the observed 2D complete TM

PBG, as was the case in 2D photonic crystals. Thus, in practice, one may need to check all rotational symmetries to find the quasiperiodic structure that offers the best properties for a particular set of material parameters preferred in the application (dielectric contrast, fill fraction, etc.), instead of directly targeting e.g. the highest rotational symmetry structure.

A possible explanation for the absence of a clear trend for the effect of increasing the point group symmetry on PBG width can be obtained from studies of electron propagation in atomic quasicrystals. Understanding the conduction properties of all quasicrystals is a nontrivial problem because in the absence of translational periodicity one cannot use the Bloch wave formalism, which allowed the definition of conduction states as extended modes with well defined group velocities (or electronic effective masses). In atomic quasicrystals, electron conduction is described on the basis of wavefunctions that are partially localized, but which contribute to conduction by a tunneling-like transport between regions in the quasicrystal structure that are locally similar [1]. To better understand this concept, consider Figure 5-2 - there, the high rotation axis is centered in the image for the three quasicrystals. Note that the cluster structure found around this high symmetry point can be found at other locations, arranged around the center of the image with the same local (but not global) rotational symmetry. It can be observed in Figure 5-2 that, while the same laser wavelength was used to produce all structures (λ = 2), the distance between these local rotational symmetry clusters changes among the three quasicrystalline patterns. Thus, a possible explanation for the observed poor PBG properties of the decagonal structure compared to octagonal and dodecagonal IL-PQC may be an unfavorable combination of the decagonal cluster

size and inter-cluster distance that is more conducive of photonic transport rather than localizing these TM polarized modes.

In conclusion, we have shown that 8mm, 10mm and 12mm point group symmetry IL-PQC also allow for 2D complete PBG for TM polarized modes, based on LDOS FDTD calculations at a center of high rotational symmetry in each quasiperiodic structure. The study of TM band structures in 2D PC with 4mm and 6mm symmetries has confirmed that increasing rotational symmetry indeed leads to wider PBG, and showed quantitatively that this effect diminishes if the dielectric contrast is increased. However, further increasing the rotational symmetry in IL-PQC was found to not lead to a clear trend: 10-fold rotational symmetry had significantly inferior PBG forming properties when compared to both 8mm and 12mm point group cases. Both octagonal and dodecagonal IL-PQC displayed a larger first TM PBG than square and triangular PC at small dielectric fill fractions ($f < 0.10$), with the octagonal quasicrystal overall providing a slightly wider PBG than the dodecagonal IL-PQC. At larger fill fractions, $f > 0.20$, the largest TM PBG was obtained for the dodecagonal IL-PQC. Unlike PC, the observed differences of PBG formation amongst IL-PQC were not significantly large even for low dielectric contrasts where rotational symmetry is expected to matter most.

These results are useful because they show that, in practice, for maximizing TM photonic band gaps the experimentalist may focus on the octagonal structure rather than IL-PQC with tempting higher rotational symmetries. This is especially useful, since as it will be described in the next chapter of the thesis, octagonal quasicrystals also have fabrication advantages stemming from an increased contrast of the interference pattern, and robustness in interference lithography when compared to the other two investigated

IL quasicrystals. Nevertheless, it should be noted that these results are preliminary, as it would be desirable to average LDOS over a multitude of points in the PQC structure and obtain a quantity similar to a total density of states. Comparing the total DOS of the various IL-PQC may be the most definitive way to assess the importance of the point group symmetries in PQC.

5.5. Comparison of PBG formation in IL-PQC and PROJ-PQC

Having found in the previous section that 8mm and 10mm quasicrystals fabricated by interference lithography can also display sizeable complete 2D TM photonic gaps, we shift our attention now to the broader problem of the importance of the choice of quasicrystal type on PBG formation. In particular, we are interested in comparing the IL-PQC structures presented in the previous section to quasiperiodic tilings (PROJ-PQC) chosen such that they have the same three point group symmetries. The goal is to understand the effect the detailed quasicrystalline structure has on the PBG formation at a given symmetry. Besides the natural scientific interest, this is an important problem to consider also from practical reasons. While IL-PQC offer significant cost advantages over PROJ-PQC, for applications requiring small area devices (e.g. in integrated photonics) both types of PQC could be fabricated with minimal cost differences, and performance would then be the main distinguishing element.

As in the previous section, due to computational constraints, we focus the analysis on TM photonic band gaps. Since these gaps are known to be maximized in PC by using an array of dielectric cylinders, we examine 2D quasiperiodic structures with dielectric material in the center of high rotational symmetry, as shown in Figure 5-4 for IL-PQC

and in Figure 5-7 for PROJ-PQC. PBG formation is explored by calculating the LDOS at this center of high point group symmetry using the FDTD approach discussed in Section 5.3. Since PROJ-PQC consist of dielectric rods placed at the vertices of a quasiperiodic tiling, the case of the 2D triangular lattice photonic crystal with dielectric rods was included in this study to allow for a more relevant direct comparison between PBG formation in photonic crystals and quasicrystals. Frequencies in the LDOS spectra are in $2\pi c/a$ units, where, for proper comparison, a in the PC is equal to the lattice period, in the PROJ-PQC is taken to correspond to the distance between the center rod and the first set of 8, 10, or 12 nearest neighbors (i.e. equal to the side of a tile in the quasiperiodic lattice). In the case of IL-PQC, a is equal to the spatial period of a line grating that would be obtained from two interfering beams with the same wavelength used to create the quasicrystals ($a = \lambda/2 = 1$).

The first case we discuss is that of 8mm point group symmetry. Figure 5-12 shows a direct comparison of the 2D LDOS calculated at various fill fractions for the cases of a 2D triangular lattice PC, and octagonal PROJ-PQC and IL-PQC, all using a dielectric material with $\varepsilon = 4$ embedded in air.

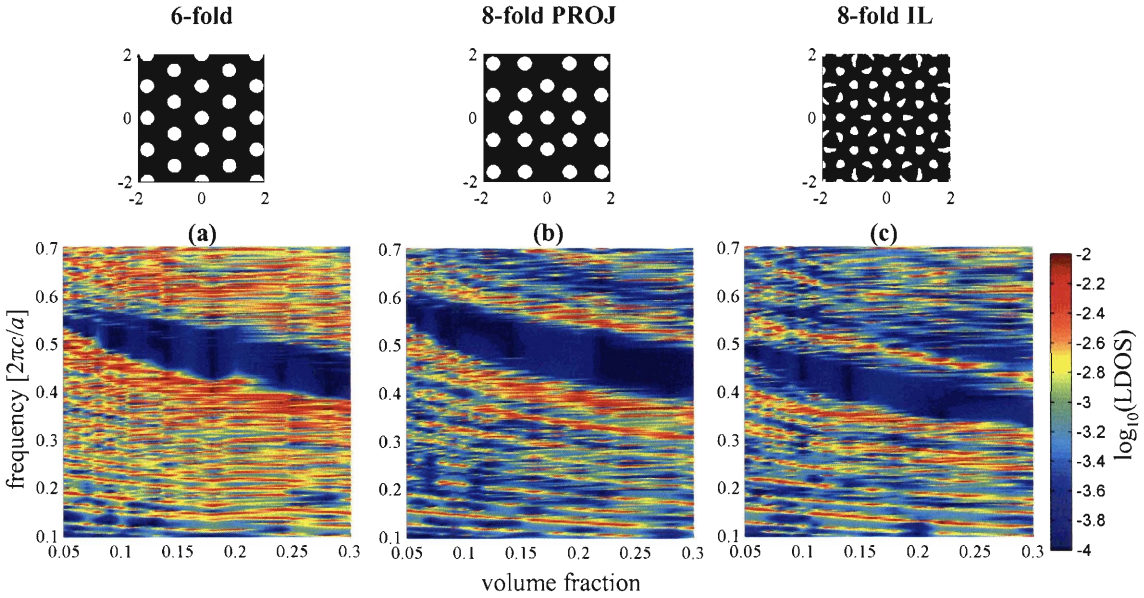

Figure 5-12 - Gap maps from assembling the LDOS curves calculated at the highest point group symmetry location in each structure at various fill fractions for **(a)** 2D triangular photonic crystal, **(b)** octagonal PROJ- PQC and **(c)** octagonal IL-PQC, all with $\varepsilon = 4$ dielectric in air. Small pieces of each PBG structure with 18% dielectric (white regions) are shown above each LDOS plot for emphasizing the structural differences between quasicrystals.

The results in the above figure show that the octagonal PROJ-PQC has a complete TM PBG that is wider and with sharper edges than in the case of the IL-PQC. Nevertheless, with the exception of low fill fractions ($f < 0.10$), it is interesting to note that neither of the two quasicrystals leads to gaps significantly wider than the triangular lattice 2D PC. To further gain insight into this problem we next examine the case of a higher dielectric constant, $\varepsilon = 6$.

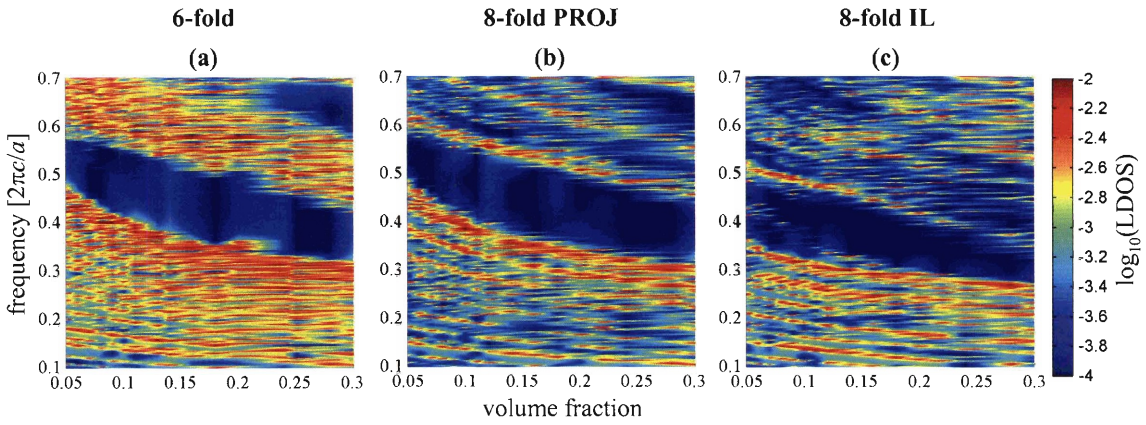

Figure 5-13 - same as Figure 5-12, but for a dielectric with $\varepsilon = 6$.

The results in Figure 5-13 show that for 8mm point group symmetry, PROJ-PQC exhibits larger 2D complete TM PBG than IL-PQC. Nevertheless, as before, the data suggests that increasing the rotational symmetry from 6-fold as in the shown PC to 8-fold as in the two studied PQC structures does not lead to significantly wider PBGs.

Since for the two dielectric contrasts investigated above, the octagonal PROJ-PQC displayed larger 2D TM PBG than the corresponding IL-PQC, we next compare the remaining two types of quasicrystals, decagonal and dodecagonal. Our goal is to understand if there is a systematic difference between TM PBG formation in PROJ-PQC and IL-PQC that is independent of point group symmetry.

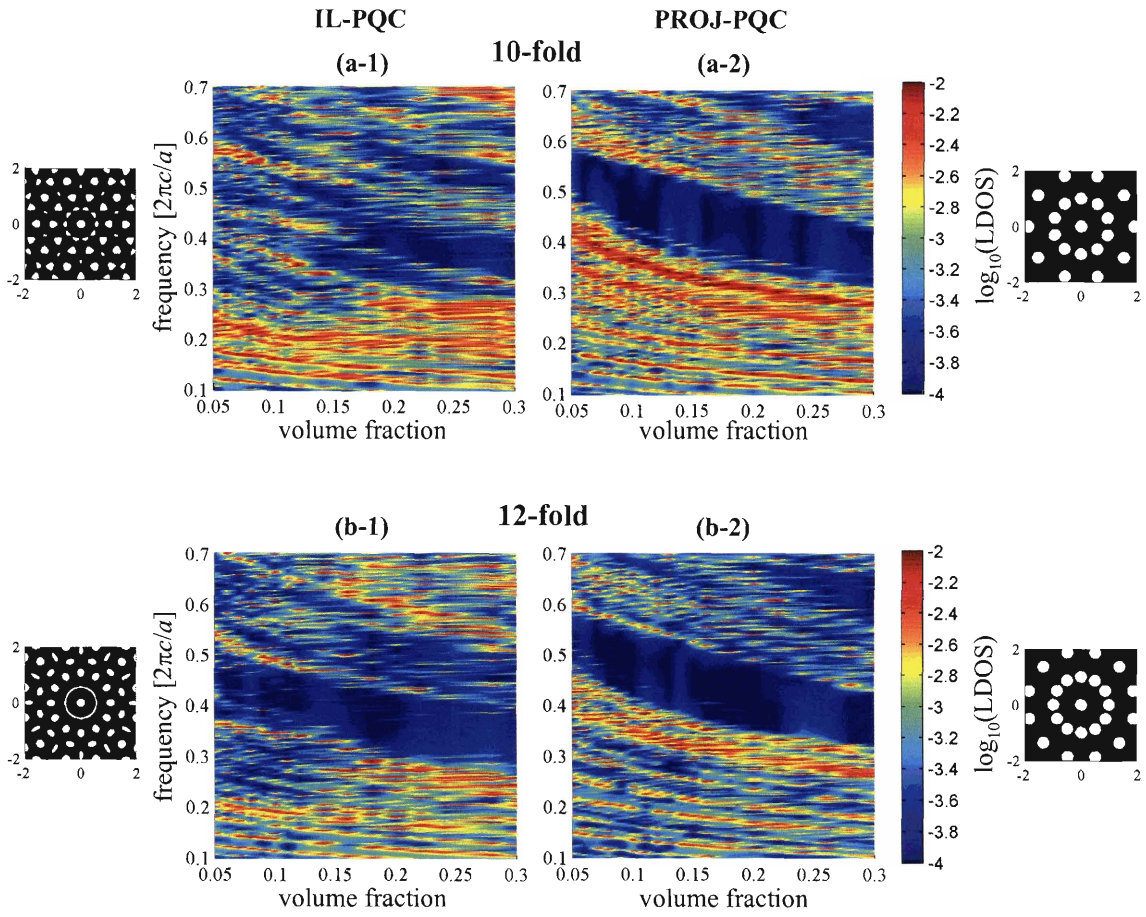

Figure 5-14 - Gap maps from assembling the LDOS curves calculated at various fill fractions for **(a-1)** IL-style and (**a-2**) PROJ-style 2D decagonal quasicrystal, and **(b-1)** IL-style and (**b-2**) PROJ-style 2D dodecagonal quasicrystal, all with $\varepsilon = 6$ dielectric and air. Small pieces of each PQC with 18% dielectric (white regions) are shown next to each LDOS plot for emphasizing the structural differences between quasicrystals.

The results in Figure 5-14 point to a number of interesting facts. First, the importance of the quasiperiodic structure for a given point group symmetry is greatly emphasized in the case of 10-fold rotational symmetry. While the decagonal IL-PQC shown in Figure 5-14(a-1) has multiple narrow TM PBGs, (separated by what could be bands of defect modes) the corresponding PROJ-PQC, where one places cylinders at the vertices of the tiling displays a significant, and well-defined complete 2D TM PBG across the entire range of volume fractions explored in Figure 5-14(a-2). Interestingly, for dodecagonal rotational symmetry, the IL-PQC displays a complete 2D TM band gap,

shown in Figure 5-14(b-1), with a very similar *absolute* width as in the case of the corresponding PROJ-PQC shown next to it. However, since in the case of the dodecagonal IL-PQC the gap is centered at a smaller frequency, in *relative* terms the IL-PQC seems slightly superior to the dodecagonal PROJ- PQC, according to Eq. (5-6).

To gain further insight into the importance of the quasiperiodic motifs at a fixed point group symmetry, we next repeat the calculations using a higher dielectric contrast.

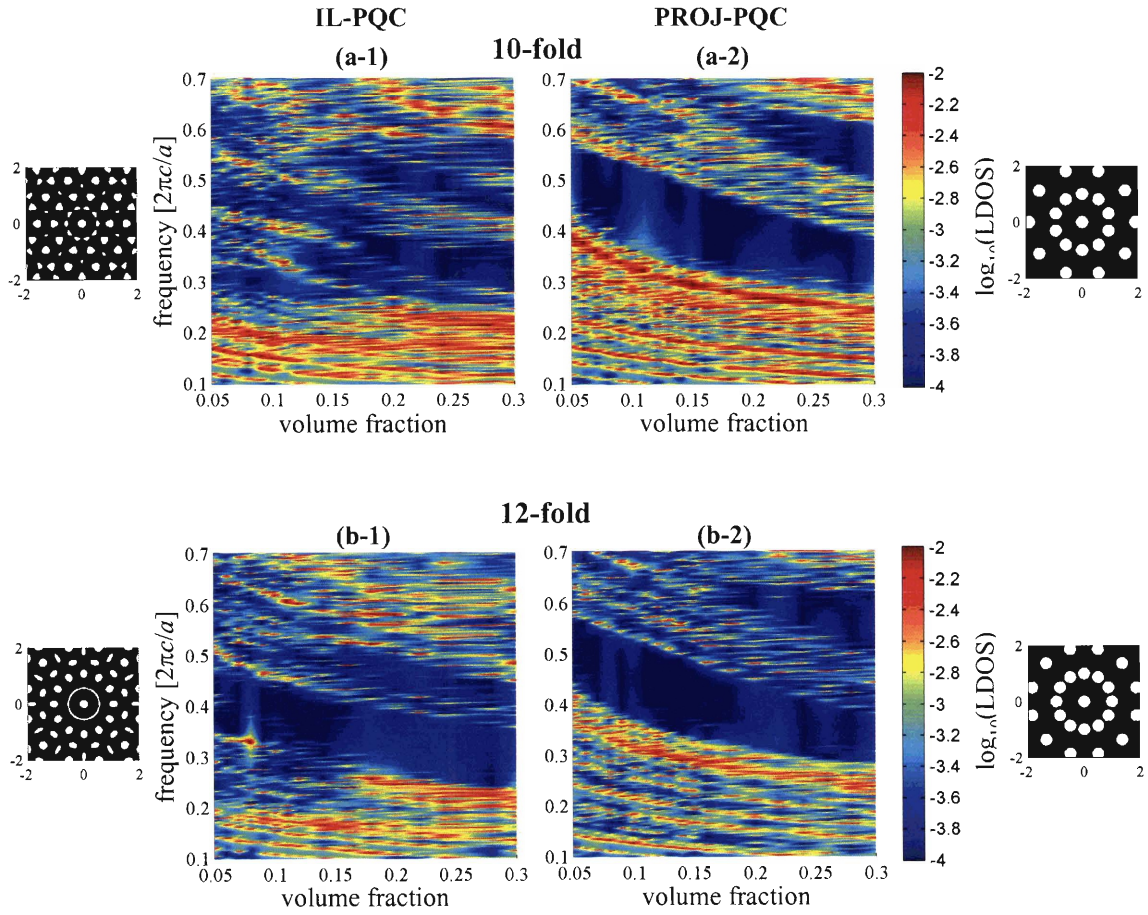

Figure 5-15 - Same as Figure 5-14, with $\varepsilon = 8$ dielectric and air.

The results shown in Figure 5-15 confirm the key observed PBG formation differences between decagonal IL-PQC and PROJ-PQC. For this symmetry, corresponding IL-PQC structures are shown in Figure 5-4(b) at various volume fractions,

and a representative PROJ-PQC structure is shown in Figure 5-7(b). The LDOS calculations at the specific high point group symmetry locations and for a variable dielectric contrast presented in this section support the conclusion that, in the case of decagonal rotational symmetry, the more "fragmented" nature of 2D photonic quasicrystals made via IL leads to inferior PBG properties than a quasiperiodic array of uniformly sized dielectric rods as in a PROJ-PQC.

However, Figure 5-15 also shows that the wider distribution of feature sizes and shapes from an IL-PQC does not always lead to an inferior TM PBG compared to corresponding PROJ-PQC structures with the same point group symmetry. While this was the case for octagonal PQC (small differences, see Figure 5-12 and Figure 5-13), and clearly the case for decagonal PQC as discussed above, we see in Figure 5-15 that the situation is reversed for the dodecagonal case. At low fill fractions ($f < 0.10$), the absolute gap widths are similar for both IL-PQC and PROJ-PQC, but due to its lower center frequency the dodecagonal IL-PQC has a slightly larger relative gap width. At larger fill fractions, e.g. $f > 0.15$, the 12mm IL-PQC displays a wider gap in both absolute and relative terms than the dodecagonal PROJ-PQC. Therefore, no clear correlations between rotational symmetry and PBG width seems to exist across the entire range of dielectric volume fractions explored, when only the formation of complete 2D TM PBG is considered.

5.6. Summary and Conclusions

The focus of this chapter has been to gain insight into the opportunities for employing quasiperiodicity in the design of photonic band gap materials. Due to the

fundamental physics of wave propagation in periodic media developed over the past century that enabled analogies with atomic crystals, photonic crystals represent today the main approach for designing materials with photonic band gaps. Materials with quasicrystalline atomic packing have been known for a relatively short time (discovered in 1984), and their photonic analogs have only been introduced in 1998. The absence of translational periodicity in quasicrystals prohibits predicting their optical properties using the well-developed theoretical tools of solid state physics that enabled rapid progress in photonic crystals. While, by comparison, the field of photonic quasicrystals is largely undeveloped, recent results have stimulated an increasing attention towards this class of structures. By not being subject to the rotational symmetry limitations of crystals, quasicrystals may offer a path towards the rational design of structures with higher symmetries and thus the potential to enable larger photonic band gaps in known material platforms.

In the current chapter, we have focused on two basic, and previously unexplored problems. First, we have analyzed the importance of point group symmetry on photonic band gap formation in 2D in quasiperiodic structures produced by interference lithography using an approach based on multiple exposures of line gratings. As it will be shown in the next chapter (experimental study), this type of photonic quasicrystal has great fabrication advantages for large area devices as compared to quasicrystals based on tiling patterns, and to date there is only one theoretical investigation published earlier in this year (2005) for the case of 12-mm IL-PQC [14]. We first examined the cases of 4- and 6-fold rotationally symmetric photonic crystals (i.e. placing a dielectric cylinder at site *1a* in *p4mm* and *p6mm* lattices), by calculating photonic band structures for TM

polarization in arrays of dielectric rods in air. We showed quantitatively that increased rotational symmetry does indeed lead to wider complete TM photonic band gaps, but this effect is weaker as the refractive index contrast increases. We attribute this observation to a competition between dielectric contrast and point group symmetry towards rounding the dispersion surface in reciprocal space - if either of the two factors is very strong, and the dispersion surface has already been substantially rounded, increasing the other factor will not lead to as great of an increase of the PBG width. We have then conducted numerical FDTD simulations to calculate the 2D LDOS for 8-, 10- and 12-fold rotationally symmetric quasicrystals at the highest global point group symmetry location in the structure, at varying dielectric contrasts and fill fractions. We have focused on TM polarized eigenmodes, and examined the LDOS for the case of the center of high rotational symmetry residing in the dielectric material (e.g. similar to the photonic crystal case, with dielectric rods in air rather than a dielectric matrix with air holes type of structures). Our findings indicate that in this case, there is no clear correlation between point group symmetry and the width of the complete 2D TM PBG in the PQC structures produced by interference lithography. We found that decagonal IL-PQC have significantly inferior PBG properties than octa- and dodecagonal IL-PQC. We have attributed this finding to a combination of structural features in the decagonal case that is unfavorable towards localizing TM modes (size of decagonal clusters, intercluster distance, and size&shape distribution of the dielectric domains spanning the distance between such clusters). The octagonal IL-PQC proved to display slightly larger gaps than in the dodecagonal IL-PQC at small fill fractions ($f < 0.10$), with the situation reversed at high fill fractions ($f > 0.2$).

The second problem we investigated was the comparison of TM PBG properties of 2D IL-PQC to PROJ-PQC, obtained by placing equal diameter cylinders at the vertices of 2D quasiperiodic tilings. This comparison is important because it allows a better understanding of the potential impact of PQC as photonic band gap materials, by separating the effects of point group symmetry from the effect of the choice of quasiperiodic motifs. We again conducted FDTD numerical simulations of the 2D TM LDOS, and included in our comparisons the two types of PQC and also finite 2D triangular PC structures (which are known to have some of the largest TM PBG in 2D for crystals [9]). We found that for both 8mm and 10mm point group symmetries, the PROJ-PQC displayed wider gaps than the corresponding IL-PQC, regardless of the dielectric contrast or fill fraction. This was attributed to a better ability of the PROJ-PQC lattice to localize light as resulting from the use of equal diameter dielectric cylinders (contrasting with IL-PQC, which consists of dielectric domains with a variety of sizes and shapes at a given fill fraction). However, in the case of dodecagonal rotational symmetry it was found that the situation is reversed, with the IL-PQC and PROJ-PQC displaying similar gap widths in absolute terms, but with the IL-PQC offering a wider gap in relative terms, due to its lower gap center frequency.

Although not conclusive, in order to allow a future reference point, we summarize the above results for a representative case of a dielectric contrast 8:1, choosing a dielectric fill fraction of 15%, for which the TM PBG in 2D PC with 4mm and 6mm symmetries is maximum (see Figure 5-9), a "worse case scenario" for the investigated PQC.

Table 5-3 - 2D TM PBG results from LDOS calculations at the center of high point group symmetry, for 2D square (4mm) and triangular (6mm) PC, and 2D 8mm, 10mm, and 12mm IL-PQC and, respectively, PROJ-PQC. The results correspond to a dielectric contrast of 8:1, at the fill fraction of 15%, where the 2D PC have maximum PBG widths.

Structure	complete TM PBG?	ω_{lower} [2πc/a]	ω_{upper} [2πc/a]	ω_{center} [2πc/a]	$\Delta\omega/\omega_{center}$	definition of a
2D square PC	yes	0.303	0.397	0.350	27.0%	PC period
2D triangular PC	yes	0.310	0.457	0.383	38.3%	PC period
8mm IL-PQC	yes	0.288	0.395	0.342	31.3%	grating period*
10mm IL-PQC	no (?)	-	-	-	-	grating period*
12mm IL-PQC	yes	0.303	0.407	0.355	29.3%	grating period*
8mm PROJ-PQC	yes	0.345	0.495	0.420	35.7%	side of tile**
10mm PROJ-PQC	yes	0.344	0.487	0.416	34.4%	side of tile**
12mm IL-PQC	yes	0.335	0.485	0.410	36.6%	side of tile**

* for IL-PQC, a is chosen to be equal to the period of the line grating written in each exposure (multiple exposure approach is assumed). Thus $a = \lambda/2$, where λ is the wavelength of the interfering laser beams (See Eq. 5.2, and Figure 5-10). This choice insures that in the case of two exposures at 90°, producing a 2D square lattice, with a period equal to a.

** for PROJ-PQC, a is chosen to be equal to the side of the tiles composing the quasiperiodic tiling pattern (for all 8mm, 10mm, and 12mm symmetries, the tiles are regular polygons).

Even if the results presented in this chapter are based on LDOS calculations at a single location of high point group symmetry, and should thus be improved in the future by averaging LDOS over many locations in 2D PQCs, they still contribute significantly towards our current understanding of the basic effects of point group symmetries on PBG formation and width in 2D quasicrystalline structures obtained from interference lithography and from mathematical quasiperiodic tilings.

5.7. Future Directions

Given the long duration of the FDTD simulations conducted during the studies presented in Chapter 5, we have restricted our numerical investigations to TM polarized PBG. It is of great interest to continue the analysis for TE polarizations as well, and then to determine if there are overlaps between the TM and TE photonic gaps. Studying the formation of complete PBG for both polarizations is very important, because photonic quasicrystals from IL can be fabricated over ultra-large areas with reasonable costs and thus, if they would also offer complete 2D PBG at low refractive index contrasts, they could significantly impact practical applications (e.g. integrated photonics, light emission management in organic or inorganic semiconductor LEDs, etc.). In the case of 12-fold rotational symmetry, PQC obtained from quasiperiodic tilings have already be shown in the literature to exhibit complete gaps for both polarizations that are larger than in photonic crystals [13]. However, the impact of this result is greatly limited in practice due to the need to use electron-beam lithography for sample fabrication.

Another direction of future research should include an investigation of the more subtle problem of quasiperiodic tiling uniqueness. Photonic quasicrystals based on such tilings represent the subject for the majority of the few existing investigations in the PQC area. Nevertheless, we have been unable to determine exactly from these articles the recipes used to generate a particular 2D tiling pattern, onto which dielectric cylinders are then placed. This is a concern, since none of the papers we have seen [6, 12, 13, 29] mentions the fact that a family of quasiperiodic structures can be obtained for a given rotational symmetry when using most quasiperiodic generation methods [11]. For

example, using the projection method to generate a decagonal quasiperiodic tiling can lead to a variety of structures, out of which only a few (but not only one) can be rigorously identified as Penrose (as opposed to Penrose-like) tilings [11]. To show this, we have used the projection method and have varied the position of the plane in high dimensional space along its normal direction, onto which the high dimensional lattice is projected. This concept can more easily be understood by examining Figure 5-5, where a variety of 1D quasicrystals will be generated by moving the line ***E*** along its normal, and then projecting the appropriate points from the 2D plane.

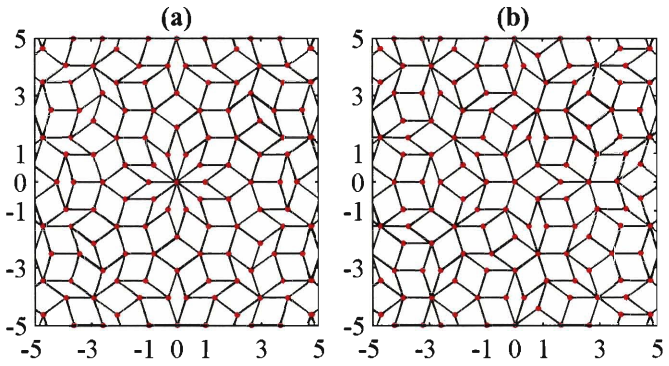

Figure 5-16 - Effect of a shift of the projecting plane in high dimensions. The projected Penrose-family 2D quasicrystalline structural changes. **(a)** projection plane going the origin of the higher dimensional space, **(b)** shift with half a period in the hyperspace. See [11].

The importance of the location of the plane onto which the high dimensional lattice is projected, is depicted in Figure 5-16. While the two quasicrystal tilings shown in Figure 5-16 are composed of the same two tiles of the Penrose lattice, and both structures exhibit a 10-fold rotational symmetry in reciprocal space, local environments differ significantly. This problem should be investigated in the future, in order to determine which factor has a greater influence on photonic band gap properties - long-range quasiperiodicity, and/or the variety of possible local environments in a given QC

pattern. Especially relevant for the studies reported in this chapter, it would be useful to compare LDOS calculated at the centers of maximum point group symmetry with an estimate of the total DOS based on averaging LDOS over many locations in the PQC structure.

Another problem that warrants further investigation is related to the location of the dielectric cylinders on PQC based on tilings. We have investigated in the current chapter the case of placing cylinders at the vertices of patterns such as shown in Figure 5-16(a), but one could envision placing the rods in the center of the tiles, of substituting air or dielectric for the two types of tiles, etc.

5.8. References

1. Janot, C. *Quasicrystals: a primer*, 2nd Edition, Clarendon Press (New York, 1994).

2. Shechtman, D., Blech, I., Gratias, D., and Cahn, J. W. "Metallic Phase with Long-Range Orientational Order and No Translational Symmetry," *Physical Review Letters*, **53**, 1951 (1984).

3. Levine, D., and Steinhardt, P. J. "Quasicrystals - a New Class of Ordered Structures," *Physical Review Letters*, **53**, 2477 (1984).

4. Yablonovitch, E. "Inhibited Spontaneous Emission in Solid-State Physics and Electronics," *Physical Review Letters*, **58**, 2059 (1987).

5. John, S. "Strong Localization of Photons in Certain Disordered Dielectric Superlattices," *Physical Review Letters*, **58**, 2486 (1987).

6. Chan, Y. S., Chan, C. T., and Liu, Z. Y. "Photonic band gaps in two dimensional photonic quasicrystals," *Physical Review Letters*, **80**, 956 (1998).

7. Cheng, S. S. M., Li, L.-M., Chan, C. T., and Zhang, Z. Q. "Defect and transmission properties of two-dimensional quasiperiodic photonic band-gap systems," *Physical Review B*, **59**, 4091 (1999).

8. Ashcroft, N. W., and Mermin, N. D. *Solid state physics*, Saunders College (Philadelphia, 1976).

9. Joannopoulos, J. D., Meade, R. D., and Winn, J. N. *Photonic crystals: molding the flow of light*, Princeton University Press (Princeton, N.J., 1995).

10. Allen, S. M., and Thomas, E. L. *The structure of materials*, John Wiley (New York, 1999).

11. Senechal, M. *Quasicrystals and geometry*, Cambridge University Press (New York, 1995).

12. Notomi, M., Suzuki, H., Tamamura, T., and Edagawa, K. "Lasing action due to the two-dimensional quasiperiodicity of photonic quasicrystals with a Penrose lattice," *Physical Review Letters*, **92**, (2004).

13. Zoorob, M. E., Charlton, M. D. B., Parker, G. J., Baumberg, J. J., and Netti, M. C. "Complete photonic bandgaps in 12-fold symmetric quasicrystals," *Nature*, **404**, 740 (2000).

14. Gauthier, R. C., and Mnaymneh, K. "Photonic band gap properties of 12-fold quasi-crystal determined through FDTD analysis," *Optics Express*, **13**, 1985 (2005).

15. Villeneuve, P. R., and Piché, M. "Photonic band gaps in two-dimensional square and hexagonal lattices," *Physical Review B*, **46**, 4969 (1992).

16. Yariv, A. *Optical electronics in modern communications*, 5th, Oxford University Press (New York, 1997).

17. Burns, M. M., Fournier, J. M., and Golovchenko, J. A. "Optical Matter - Crystallization and Binding in Intense Optical-Fields," *Science*, **249**, 749 (1990).

18. Wang, X., Ng, C. Y., Tam, W. Y., Chan, C. T., and Sheng, P. "Large-area two-dimensional mesoscale quasi-crystals," *Advanced Materials*, **15**, 1526 (2003).

19. Gauthier, R. C., and Ivanov, A. "Production of quasi-crystal template patterns using a dual beam multiple exposure technique," *Optics Express*, **12**, 990 (2004).

20. Della Villa, A., Enoch, S., Tayeb, G., Pierro, V., Galdi, V., and Capolino, F. "Band gap formation and multiple scattering in photonic quasicrystals with a Penrose-type lattice," *Physical Review Letters*, **94**, (2005).

21. Socolar, J. E. S. "Simple Octagonal And Dodecagonal Quasicrystals," *Physical Review B*, **39**, 10519 (1989).

22. Sakoda, K. *Optical properties of photonic crystals*, Springer (Berlin, 2001).

23. Taflove, A., and Hagness, S. C. *Computational electrodynamics: the finite-difference time-domain method*, 2nd Edition, Artech House (Boston, 2000).

24. http://ab-initio.mit.edu/wiki/index.php/Meep

25. Allan, D. C., and Joannopoulos, J. D. "Theory of Electronic Structure" in *The Physics of Hydrogenated Amorphous Silicon II. Electronic and Vibrational Properties* (eds. Joannopoulos, J. D. & Lucovsky, G.), p. 5 (Springer-Verlag, New York, 1984).

26. Yndurain, F., and Joannopoulos, J. D. "Study of the electronic local density of states using the cluster-Bethe-lattice method: Application to amorphous III-V semiconductors," *Physical Review B*, **14**, 3569 (1976).

27. Wang, Y. Q., Cheng, B. Y., and Zhang, D. Z. "The density of states in quasiperiodic photonic crystals," *Journal of Physics-Condensed Matter*, **15**, 7675 (2003).

28. http://ab-initio.mit.edu/wiki/index.php/MIT_Photonic_Bands

29. Nozaki, K., and Baba, T. "Quasiperiodic photonic crystal microcavity lasers," *Applied Physics Letters*, **84**, 4875 (2004).

Chapter 6.
Fabrication and applications of 2D and 3D quasiperiodic sub-micron structured materials from interference lithography

As discussed in the previous chapter, quasiperiodically structured materials represent a novel class of photonic band gap (PBG) materials. By comparison with photonic crystals (PC), the progress in the area photonic quasicrystals (PQC) has been much slower. While PC enjoyed an explosive growth after their introduction in 1987 by Yablonovitch [1] and John [2], the first report of PBG formation in a quasiperiodic material structure, by Chan and coworkers in 1998 [3], has been followed by a much smaller number of investigations to date. This slower growth rate is arguably the result of two key problems specific to PQC. The first problem has been discussed in the previous chapter, and it is related to difficulties in developing a fundamental theoretical framework for understanding and predicting light propagation in PQC (e.g. the lack of translational periodicity forbids the use of Bloch's theorem, band structure calculations, etc). The second problem is experimental, and arguably related to an insufficient understanding of the available choices of quasicrystalline structures and associated fabrication techniques. As an example of the complex choice of PQC structures [4, 5], consider that all 2D crystals can be classified into five distinct Bravais lattices [6], while 2D quasicrystals with N-fold rotational symmetry can be defined for arbitrarily large N,

and that for certain values of N more than one quasicrystal lattice has to be considered [7]. The choice of fabrication techniques available for PQC is impacted by their structural complexity (note that by "photonic", we imply that the PQC structures of interest are those with features comparable in size with the wavelength of visible and near-IR light). The few existing studies of optical properties of PQC have employed electron beam lithography (EBL) for fabricating 2D structures [8, 9], because EBL allows writing arbitrary patterns with a very high resolution (enabled by focusing an electron beam to a spot size of a few nanometers). However, the serial nature of EBL, wherein a 2D pattern is built pixel by pixel by exposing a resist to the electron beam at the nanoscale, greatly limits the progress of experimental studies - EBL is not only time consuming and restrictive of sample sizes to sub-millimeter dimensions, but it also requires the use of expensive equipment.

In this chapter, we focus on using a different and more promising approach for the fabrication of PQC structures based on interference lithography (IL), also referred to as holographic lithography in the literature [10-12]. Using a multiple exposure IL approach, we fabricated 2D PQC with 8-, 10-, and 12-fold rotational symmetries similar to those described in Section 5.2.1. What distinguishes our results from those reported in the only two existing publications on quasiperiodic patterning with IL [13, 14], is a ~10x reduction in the feature size to ~100nm, better pattern quality, and a much larger sample size (typical is 1-2 cm^2, but our technique can be easily extended to patterning of up to 12" wafers using other available IL tools, such as the scanning beam interference lithography tool developed at MIT [15]). Thus, we show that IL can be used to produce PQC that are not only comparable in quality with those fabricated via EBL, but that IL

may become the key technique for fabricating PQC samples large enough to impact a wider range of future applications. We end the chapter with a presentation of initial results for two kinds of applications. First, we develop a coherent diffraction lithography (CDL) based approach [16] for the fabrication of novel 3D sub-micron quasiperiodically structured materials by using transparent, conformable polydimethylsiloxane diffraction gratings fabricated by replica molding from 2D PQC silicon oxide substrates. Second, the self-assembly of block copolymer thin films on quasiperiodic topographically patterned substrates is discussed, as a potentially valuable path towards understanding the competition between crystalline and quasicrystalline structure formation in materials.

6.1. Introduction

IL has emerged over the past five years as a highly versatile and capable tool for the fabrication of 2D and 3D PC [11, 17-19], because interfering multiple laser beams can readily produce 2D and 3D periodic light intensity patterns with unit cells comparable in size to the wavelength of visible and infrared light. The rapid acceptance of IL as a potentially complete platform for the fabrication of PC has been catalyzed by the availability of photosensitive materials and corresponding laser sources, and, most importantly, by a well developed knowledgebase of the crystallography of optical lattices produced by laser interference [20]. Indeed, outside the field of photonic crystals, interference of multiple laser beams has been studied for at least two decades as a means of creating periodic electromagnetic energy landscapes for trapping atoms in high vacuum systems [21], or colloidal particles in liquid media [22]. Subsequently, Berger, Gauthier-Lafaye and Costard were first to report in 1997 the use IL for the fabrication of

PBG materials - by interfering 3 laser beams, they produced a 2D triangular lattice PC after transferring the resulting photoresist pattern into gallium arsenide (GaAs) [10, 23]. However, it was not until 2000 when IL truly gained recognition as an important tool for PC fabrication - Campbell *et al.* reported in *Nature* on the use of 4 beam IL for the fabrication of a 3D PC with the desired diamond-like dielectric network, and showed experimental results for a $R\bar{3}m$ structure 3D PC [11]. While the theoretical concept of using 4 beam interference to produce 3D PC with FCC, BCC, etc. lattices was known from as early as 1995 [24], the key merit of the report of Campbell *et al.* is to have experimentally proved the usefulness of IL as a platform for actually *fabricating* PC. First, an appropriately designed 3D light intensity pattern was recorded in a photopolymer to create a sub-micron structured, porous polymeric structure (itself a 3D PC), and then this polymeric template was infiltrated with a titania precursor, and calcined such that 3D PC with higher refractive index contrast (titania vs. air) was obtained [11]. Thus, what makes IL a true platform is the fact that the design and recording of the desired structure can be separated from the processing constraints of the high refractive index materials needed for large PBG (since the polymeric structure can template the deposition of precursors for a number of high index materials, such as titania, silicon, etc., and in the end be replaced by air after removal of the polymer through pyrolysis). The flexibility of IL for controlling the structure of 3D PC was later confirmed quantitatively by Cai *et al.* who showed that all fourteen Bravais lattices in 3D can be obtained by varying the directions of the 4 laser beams [25], and by Ullal *et al.* who introduced a level set based approach for finding the directions, polarizations and

amplitudes of the 4-beams that can lead to 3D PC with any of the 230 space group symmetries [26].

More recently, IL has also attracted attention for the fabrication of photonic quasicrystals. It was known from early work on optical trapping of colloidal particles [22] and from acoustic wave experiments [27] that interference of 5 beams converging to a single point from the corners of a regular pentagon (72° between successive beams) leads to a 10-fold rotationally symmetric, Penrose-like quasiperiodic pattern. However, it was not until 2003 when Wang *et al.* [14] published the first report on recording in a photopolymer a 2D quasiperiodic light intensity pattern produced by interfering 5 laser beams equally spaced at 72° around a central point. One year later, in 2004 Gauthier and Ivanov reported on an alternative approach for using IL to create 2D quasiperiodic photoresist patterns, where multiple line gratings produced by 2-beam IL were recorded with subsequent substrate rotations after each exposure to produce 8-, 10- and 12-fold rotationally symmetric 2D quasicrystalline structures [13]. A third report on using IL for fabricating PQC was published in 2005, where Gorkhali *et al.* [28] used the same multiple beam approach as Wang *et al.* [14] to record a 2D Penrose-like quasicrystalline structure in a liquid crystal containing photosensitive polymer system, yielding an electric field tunable Penrose quasicrystal structure.

In this chapter, we further extend the use of IL for the fabrication of both 2D and 3D PQC. We first theoretically compare the multiple beam and multiple exposure IL approaches for the fabrication of 2D PQC, and quantitatively show that the resulting interference patterns are not equivalent, but they have the same rotational symmetries. Moreover, we theoretically show that at least 3 laser beams (or 3 exposures) are needed

to produce a 2D quasiperiodic structure (i.e. without translational periodicity). This result is important not only for theoretical reasons, but also for experimental reasons since it provides a simple route for the fabrication of translationally aperiodic 2D patterns.

While the reports of Wang *et al.* [14] and Gauthier and Ivanov [13] experimentally prove the concept that IL can produce 2D quasiperiodic structures, their experimental results consist of materials with features on the few-micron scale and thus do not yet enable applications requiring PBG for visible or telecommunication (1.55μm) wavelengths. To scale down the IL process for the fabrication of PQC with smaller feature sizes, one needs to address two important issues, besides e.g. the trivial reduction of the laser wavelength. First, there is the material science problem related to capturing the intensity pattern in a photoresist given the low contrast in the light intensity distribution resulting from the use of multiple beams or of multiple exposures, which becomes an even bigger problem as the desired feature size of the PQC is made smaller. Second, there is an optical design problem that relates to the stability of the interference pattern, which is key for multiple exposures and a requirement for accurate pattern generation in the photoresist at small length scales. We demonstrate a multiple exposure approach to fabricate ultra-large area 2D photonic quasicrystals with 8-, 10-, and 12-fold rotational symmetries and feature sizes as small as 100nm. The accurate fabrication of our samples at this small length scale, was enabled by the use of an ultra stable Lloyd's mirror interferometer (its inherent high stability arises from the fact that there is only one laser beam in the system [29]), the use of an optically absorbing antireflection coating

underneath the photoresist for accurately recording the low contrast interference pattern, and using a short wavelength laser (325nm HeCd UV laser).

6.2. Quasiperiodicity and IL: theoretical problems

In this section we analyze a number of theoretical problems that are relevant for understanding how quasiperiodicity is obtained from interfering light waves (which are by definition, translationally periodic), and for predicting the physical PQC structures that can be obtained from IL. In Section 6.2.1 we quantitatively compare the multiple exposures and the multiple beams approaches for IL. In Section 6.2.2 we present an analysis of the minimum number of beams (or exposures) for 2D quasiperiodicity, which is found to be 3. Finally, in Section 6.2.3 we present a general model for predicting the 3D light intensity pattern produced by interfering an arbitrary number of beams with arbitrary polarizations and directions.

6.2.1. Theoretical comparison of multiple beams IL vs multiple exposures IL for 2D PQC fabrication

It is currently known that quasiperiodicity can be produced in IL with both multiple laser beams (MB-IL) [14, 30] and with multiple exposures of line gratings (ME-IL) [13]. In this section we show quantitatively that the two techniques are not equivalent, but that both can result in 2D quasiperiodic lattices with similar rotational symmetries.

We begin the analysis by assuming that both ME-IL and MB-IL approaches use the same laser wavelength, and that the beams propagate in the sample plane, to simplify

the expressions to be derived. As shown in Chapter 5, Section 5.2, the spatial distribution of the intensity pattern obtained after N exposures of line gratings is equal to the sum of the intensities produced from the interference of 2 beams:

$$I(x,y) = 2I_0 \sum_{j=1}^{N} \left(1 + \cos(\frac{2\pi}{P} \mathbf{P}_j \cdot \mathbf{r} + \Delta\phi_j) \right) \tag{6-1}$$

where $P = \lambda / 2$ is the spatial period of the line gratings (λ = laser wavelength), $\Delta\phi_j$ is the phase difference between the two beams in exposure j, and the vector $\mathbf{P}_j$ is a unit vector along the periodicity direction of each line grating, e.g. $\mathbf{P}_j = \mathbf{x}\cos\theta_j + \mathbf{y}\sin\theta_j$ with the angle θ_j measured from $\mathbf{x}$ towards $\mathbf{y}$ in the sample plane.

In the case of MB-IL, we first need to calculate the total electric field resulting from the superposition in the sample plane of the M beams, and then to derive the expression for the intensity distribution. To simplify the expressions that will be calculated and still capture the effects of interfering M beams, we further assume that all the beams have the same amplitude and out-of-plane polarization. Thus, the total electric field at a position in space is

$$E_{total}(\mathbf{r}) = \sum_{j=1}^{M} \left(E_0 \exp\left(i (\mathbf{k}_j \cdot \mathbf{r} + \phi_j) \right) \right) \tag{6-2}$$

where E_0 is the wave amplitude, and ϕ_j is an arbitrary phase term.

The resulting intensity pattern distribution is proportional to the modulus of the complex electric field

$$I(\mathbf{r}) \propto E_{total}(\mathbf{r}) E^*_{total}(\mathbf{r}) \tag{6-3}$$

Thus, the final intensity pattern I(**r**) is described by

$$I(\mathbf{r}) = \left(\sum_{j=1}^{M} \left(E_0 \exp\left(i \left(\mathbf{k}_j \cdot \mathbf{r} + \phi_j \right) \right) \right) \right) \left(\sum_{l=1}^{M} \left(E_0 \exp\left(-i \left(\mathbf{k}_l \cdot \mathbf{r} + \phi_l \right) \right) \right) \right) \tag{6-4}$$

To be able to more clearly compare the 2D QC from MB-IL and ME-IL, we continue the analysis for the specific case of 10-fold rotationally symmetric QC. This type of 2D QC can be obtained from either $N = 5$ exposures with rotations of 72° (or 36° as it will be shown below), or from the interference of $M = 5$ beams converging to a central point from the corners of a regular pentagon (i.e. the M beams are also separated by 72°).

Thus, continuing the analysis for the case of MB-IL with $M = 5$, Eq. 6-4 leads to the following expression for the total intensity distribution:

$$I(\mathbf{r}) = I_0 \sum_{j=1}^{5} \sum_{l=1}^{5} \exp\left(i \left(\Delta \mathbf{k}_{jl} \cdot \mathbf{r} + \Delta \phi_{jl} \right) \right) \tag{6-5}$$

where I_0 is the intensity of a single beam ($I_0 \propto E_0^2$), and $\Delta \mathbf{k}_{jl} \equiv \mathbf{k}_l - \mathbf{k}_j$ and $\Delta \phi_{jl} \equiv \phi_l - \phi_j$.

Using the properties that $\Delta \mathbf{k}_{jl} = -\Delta \mathbf{k}_{lj}$, $\Delta \phi_{jl} = -\Delta \phi_{lj}$, and noting that $\Delta \mathbf{k}_{jj} = \Delta \phi_{jj} = 0$, the 25 terms in the double sum above are reduced to a constant term plus 20 cosine terms, which, due to symmetry, further reduce to only 10 independent cosine terms.

$$I(\mathbf{r}) = I_0\big(5 + 2\cos(\Delta\mathbf{k}_{12}\cdot\mathbf{r}) + 2\cos(\Delta\mathbf{k}_{13}\cdot\mathbf{r}) + 2\cos(\Delta\mathbf{k}_{14}\cdot\mathbf{r}) + 2\cos(\Delta\mathbf{k}_{15}\cdot\mathbf{r}) + 2\cos(\Delta\mathbf{k}_{23}\cdot\mathbf{r}) + 2\cos(\Delta\mathbf{k}_{24}\cdot\mathbf{r}) + 2\cos(\Delta\mathbf{k}_{25}\cdot\mathbf{r}) + 2\cos(\Delta\mathbf{k}_{34}\cdot\mathbf{r}) + 2\cos(\Delta\mathbf{k}_{35}\cdot\mathbf{r}) + 2\cos(\Delta\mathbf{k}_{45}\cdot\mathbf{r})\big) \tag{6-6}$$

note that the 10 phase differences $\Delta\phi_{jl}$ have been omitted for clarity, as they will not change the conclusions of this analysis (the rigorous result in the above equation would be to use $\cos(\Delta\mathbf{k}_{jl}\cdot\mathbf{r} + \Delta\phi_{jl})$ terms).

We now include in the analysis the fact that the 5 beams that we are considering here are not arbitrarily oriented, but are arranged in a precise fashion.

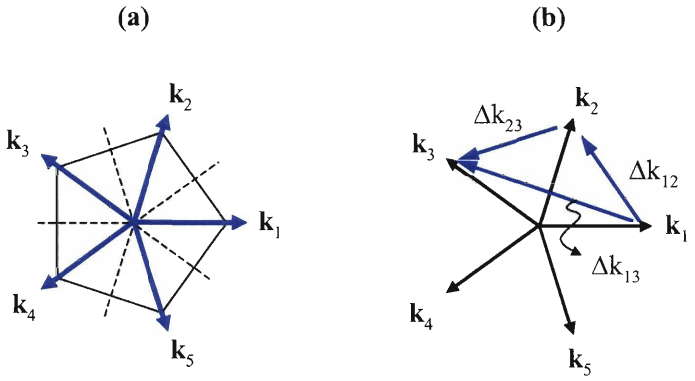

$$\Delta\mathbf{k}_{13} = \Delta\mathbf{k}_{12} + \Delta\mathbf{k}_{23} = \Delta\mathbf{k}_{15} + \Delta\mathbf{k}_{54} + \Delta\mathbf{k}_{43}$$

Figure 6-1 - IL with 5 beams arranged to produce a Penrose-like quasicrystal. **(a)** orientation of the **k** vectors corresponding to each beam; **(b)** orientation and relations between the difference vectors, $\Delta\mathbf{k}_{jl}$, that correspond to the pair-wise interference of any two of the 5 beams shown in (a).

The result of Eq. 6-6 is described graphically by Figure 6-1. The intensity pattern obtained from the interference of any 5 beams shown in Figure 6-1(a) can be described by a superposition of 10 line gratings corresponding to the 10 $\Delta\mathbf{k}_{jl}$ difference vectors. However, by taking into account the special orientation of the beams for the case of a decagonal 2D QC, it can be observed that the lengths of these 10 difference vectors are

equal to either $|\Delta\mathbf{k}_{j,j+1}|$ or to $|\Delta\mathbf{k}_{j,j+2}|$. Moreover, the 5 difference vectors corresponding to each of these two lengths can be arranged such that, put end to end they form a pentagon. This is easiest to see for the case of the $\Delta\mathbf{k}_{j,j+1}$ set, see Figure 6-1(b). To make this point clearer, we summarize this argument in Table 6-1.

Table 6-1 - Analysis of the uniqueness of the 10 general wave vector differences in Eq. (6-6) for the case of an equiangular spacing of the five beams (72° angle). The data in this table relates to Figure 6-1.

wave vector difference, $\Delta\mathbf{k}_{jl}$	equivalent wave vector difference	direction (parallel to)
$\Delta\mathbf{k}_{12}$	$\Delta\mathbf{k}_{12}$	$\Delta\mathbf{k}_{12}$
$\Delta\mathbf{k}_{13}$	$\Delta\mathbf{k}_{12}+\Delta\mathbf{k}_{23}$	$\Delta\mathbf{k}_{45}$
$\Delta\mathbf{k}_{14}$	$\Delta\mathbf{k}_{15}+\Delta\mathbf{k}_{54}$	$\Delta\mathbf{k}_{23}$
$\Delta\mathbf{k}_{15}$	$\Delta\mathbf{k}_{15}$	$\Delta\mathbf{k}_{15}$
$\Delta\mathbf{k}_{23}$	$\Delta\mathbf{k}_{23}$	$\Delta\mathbf{k}_{23}$
$\Delta\mathbf{k}_{24}$	$\Delta\mathbf{k}_{23}+\Delta\mathbf{k}_{34}$	$\Delta\mathbf{k}_{15}$
$\Delta\mathbf{k}_{25}$	$\Delta\mathbf{k}_{21}+\Delta\mathbf{k}_{15}$	$\Delta\mathbf{k}_{34}$
$\Delta\mathbf{k}_{34}$	$\Delta\mathbf{k}_{34}$	$\Delta\mathbf{k}_{34}$
$\Delta\mathbf{k}_{35}$	$\Delta\mathbf{k}_{34}+\Delta\mathbf{k}_{45}$	$\Delta\mathbf{k}_{12}$
$\Delta\mathbf{k}_{45}$	$\Delta\mathbf{k}_{45}$	$\Delta\mathbf{k}_{45}$

Thus, both Figure 6-1 and Table 6-1 show that the interference of 5 laser beams equispaced around a central intersection point with 72° is equivalent to the superposition of two sets of five line gratings, corresponding to two types of difference vectors, $\Delta\mathbf{k}_{j,j+1}$ and $\Delta\mathbf{k}_{j,j+2}$. Each set consists of gratings having the same spatial periodicity ($2\pi/|\Delta\mathbf{k}_{j,j+1}|$ and, respectively, $2\pi/|\Delta\mathbf{k}_{j,j+2}|$), and rotated about a center point by 72°, just as it was described above in the case of ME-IL.

The final expression for the intensity distribution obtained in the interference of 5 laser beams thus becomes

$$I(x,y) = I_0\left(5 + 2\sum_{j=1}^{5}\cos(\frac{2\pi}{P_I}(x\cos\theta_j + y\sin\theta_j)) + \right. \\ \left. + 2\sum_{j=1}^{5}\cos(\frac{2\pi}{P_{II}}(x\cos\theta_j + y\sin\theta_j)) \right) \tag{6-7}$$

where the spatial periods P_I and P_{II} are defined as

$P_I \equiv \frac{2\pi}{|\Delta\mathbf{k}_{j,j+1}|} = \frac{\lambda}{\sqrt{2-2\cos(72^\circ)}} = \lambda * 0.85...$ and

$P_{II} \equiv \frac{2\pi}{|\Delta\mathbf{k}_{j,j+2}|} = \frac{\lambda}{\sqrt{2-2\cos(144^\circ)}} = \lambda * 0.52...$, λ is the laser wavelength, and the angle θ_j, measured from **x** towards **y**, gives the orientation of each of line grating, θ_j = 0, 72, 144, 216, and 288°.

By further noting the special relation between the two spatial periods, $P_I = \tau P_{II}$, where $\tau = (1+\sqrt{5})/2 = 1.61...$ is the golden mean, we conclude on a quantitative basis that the spatial distribution of the intensity of light resulting from interference of five beams can not be equivalent to the intensity distribution obtained from superposing five line gratings, rotated with the same 72°. However, in both cases, the final rotational symmetry of the intensity distribution remains decagonal.

The differences between the structures obtained from ME-IL and MB-IL for decagonal QC are presented graphically in Figure 6-2. The numerical computations assume the same wavelength, and equal amplitude, out-of-plane and in-phase electric field polarizations for all the laser beams. The more expanded aspect of the MB-IL structure shown in Figure 6-2(b) agrees with the fact that the spatial periods P_I and P_{II},

see Eq. (6-7), are larger than the spatial period P of the line gratings written in the ME-IL approach, see Eq. (6-1).

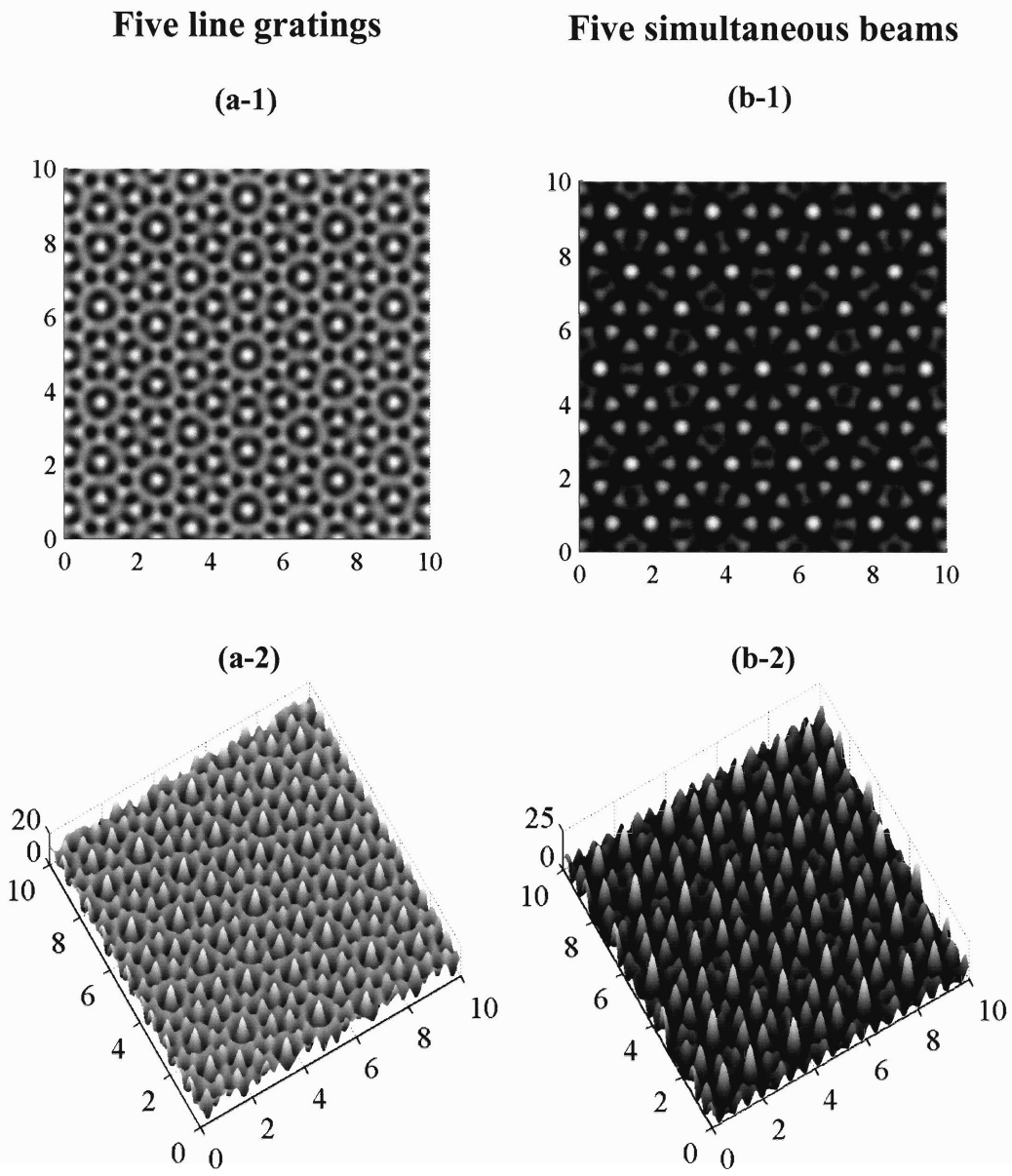

Figure 6-2 - Perspective and top-down views of the 2D decagonal QC intensity distributions obtained from IL with **(a)** 5 exposures with 72° rotations and **(b)** 5 beams separated by 72°. In all cases, the axes are in units of the wavelength, $\lambda = 1$, and the polarizations are out-of-plane and in phase.

The analysis presented in this section can be easily generalized to the case of 2D octagonal and dodecagonal QC. In all cases, the multiple exposures IL approach (with 4

or 6 exposures) produces 2D quasiperiodic patterns that have the same rotational and mirror symmetries but a different lattice compared to the case of multi-beam IL (with 8 or 12 beams).

6.2.2. Minimum number of beams (or exposures) for 2D quasiperiodicity

It is useful to consider now answering the question of what is the simplest IL approach leading to a 2D quasiperiodic pattern. Answering this question will also provide an answer to the more basic question of how is quasiperiodicity obtained from the interference of waves, which by definition are translationally periodic.

The key concept to be considered is that of superposition of incommensurate oscillations. This is easiest understood in 1D, where the sum of, for example, two cosine terms will become a 1D aperiodic function if the ratio of the periods of the two oscillations is an irrational number such as $\sqrt{2}$, $\sqrt{3}$, $\sqrt{5}$ or $\tau = (1+\sqrt{5})/2$, etc.. Thus, two spatial periods are incommensurate if their ratio cannot be expressed as a ratio of two integers.

$$f(x) = \cos(\frac{2\pi}{p}x) + \cos(\frac{2\pi}{p\sqrt{2}}x) \tag{6-8}$$

where $f(x)$ is an 1D aperiodic function, and p is an arbitrary spatial period.

To generalize this concept for generating 2D quasiperiodic variations from IL, it is immediately evident that more than two beams or exposures need to be considered, since any combination of two beams will result in a 2D translationally periodic pattern. As we will show next, three beams (or three exposures) are sufficient to produce a quasiperiodic pattern as long as the third beam is appropriately oriented. If we denote the

wavevectors of each beam with $\mathbf{k}_1$, $\mathbf{k}_2$ and $\mathbf{k}_3$, the following conditions need to be satisfied in order to obtain a 2D quasiperiodic pattern

$$\frac{\mathbf{k}_3 \cdot \mathbf{k}_i}{|\mathbf{k}_i|} = irrational\ number \tag{6-9}$$

where $i = 1, 2$. This result can be understood as insuring that the third beam, $\mathbf{k}_3$, leads to quasiperiodicity along both $\mathbf{k}_1$ and $\mathbf{k}_2$ directions, such that the resulting lattice will become quasiperiodic in 2D. Note that, by analogy, the same consequences are present if, instead of wave vectors $\mathbf{k}_i$, the translation vectors belonging to each exposure in ME-IL are used (e.g. **P** vectors in Eq. (6-1).

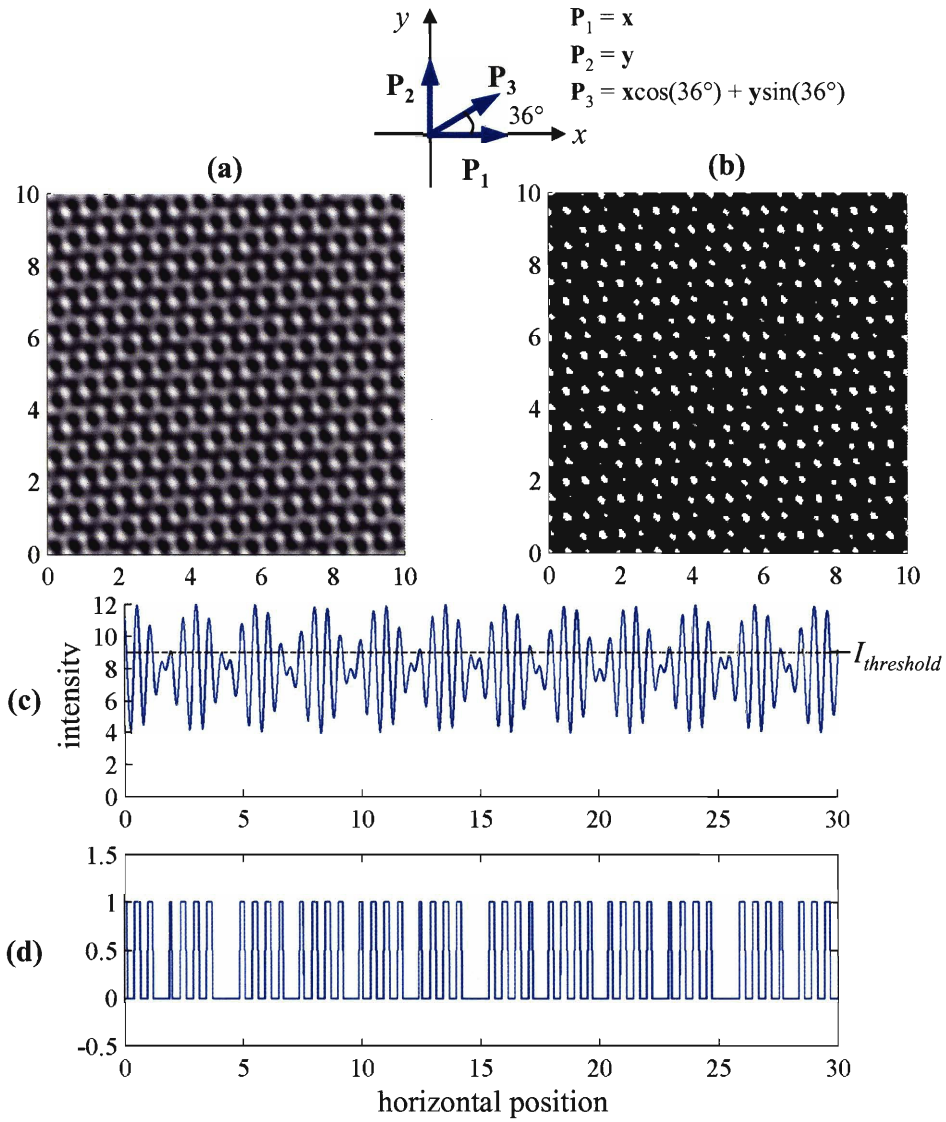

Figure 6-3 - 2D quasiperiodic pattern obtained from 3 exposures of line gratings with equal spatial periods ($P = \lambda/2 = 0.5$, see Eq. 6-1), but oriented as shown in the inset figure (at 0°, 36° and 90° measured from **x** towards **y**). **(a)** Total intensity pattern; **(b)** Binarized intensity pattern obtained by thresholding at $I_{threshold}$ = 75% I_{max} = 9; **(c)** horizontal profile at $y = 0$ for the total intensity pattern shown in (a); **(d)** horizontal profile at $y = 0$ for the binarized intensity pattern shown in (b). All dimensions are in units of λ.

Figure 6-3 shows the example of a 2D quasiperiodic pattern that was obtained from the superposition of 3 line gratings oriented at 0, 36 and 90° from the **x** axis (unit vectors $\mathbf{P}_i$ (i =1,2,3) pointing along the translational periodicity directions are shown in the inset figure). Since the periodicity of total intensity pattern in Figure 6-3(a) is

difficult to assess visually, we have also binarized this intensity landscape by applying a threshold (white pixels if $I(x,y) > I_{threshold} = 75\% I_{maximum}$) and also shown in Figure 6-3(c) and (d) corresponding total and binarized profiles along the **x** axis for $y = 0$. Although these intensity profiles show repeating patterns, a more careful examination should reveal that translational periodicity is absent along **x**. The quasiperiodicity of the profile along **x** can also be quantitatively understood by first observing that, along this direction, the intensity profile is a superposition of the intensity oscillations produced by $\mathbf{P_1}$ and $\mathbf{P_3}$ (since $\mathbf{P_2}$ is normal to **x**). The ratio of the periods of these two oscillations can be shown to be an irrational number related to the golden mean, τ:

$$\frac{\mathbf{x}\cdot\mathbf{P}_1}{\mathbf{x}\cdot\mathbf{P}_3} = \frac{1}{\cos(36^\circ)} = \frac{1}{\tau/2} = \frac{4}{1+\sqrt{5}} \tag{6-10}$$

Thus, the intensity profile along the **x** axis (at y =0) shown in Figure 6-3(c) is quasiperiodic because it is produced by the superposition of two oscillations with incommensurate periods. In a similar fashion, it can be proved that the 2D intensity profile shown in Figure 6-3(a) is quasiperiodic along any direction in the xy plane.

In conclusion, we have shown in this section that the smallest number of beams (or exposures) that allows producing 2D quasiperiodic IL patterns is three. This result may prove to be very useful for applications where the only requirement for the IL pattern is to be 2D quasiperiodic, and to use the smallest number of beams.

6.2.3. Theoretical model for interference lithography in 3D

The last theoretical problem that we consider is the prediction of the 3D light intensity distribution obtained from the interference of an arbitrary number of beams,

with arbitrary directions and polarizations. This model will be extremely useful when exploring for 3D structures with particular features (e.g. connectivity, volume fraction, etc.) or when trying to model an experimental situation, where many beams are interfering simultaneously.

We assume that N beams are interfering in a 3D volume. Each beam j has an arbitrary orientation, $\mathbf{k}_j$, polarization and amplitude $\mathbf{E}_j$ and phase ϕ_j, and we further assume that the interference medium is isotropic such that $\mathbf{E} \perp \mathbf{k}$. The total electric field becomes

$$\mathbf{E}_{total}(\mathbf{r}) = \sum_{j=1}^{N} \left(\mathbf{E}_j \exp\left(i \left(\mathbf{k}_j \cdot \mathbf{r} + \phi_j \right) \right) \right) \tag{6-11}$$

The resulting intensity pattern is simply given by

$$I(\mathbf{r}) \propto \mathbf{E}_{total}(\mathbf{r}) \bullet \mathbf{E}^*_{total}(\mathbf{r}) \tag{6-12}$$

The difficulty arises when actually trying to evaluate the above expression, since the vectors $\mathbf{E}_j$, while perpendicular to their respective $\mathbf{k}_j$ vectors, point in arbitrary directions. Thus, to calculate the intensity $I(x,y,z)$, the x, y and z components of all $\mathbf{E}_j$ and $\mathbf{k}_j$ vectors need to be first determined. To simplify this task, it would be beneficial to implement in this 3D IL model of a straightforward way for describing the polarization of each beam.

A advantageous solution we adopted to deal with this relative difficulty was to borrow from the solution of Maxwell's equations in the *kDB* system [31]. This solution simplifies the problem of solving the system of differential equations in the *xyz* (lab) coordinate system, by expressing all the electromagnetic quantities in a new coordinate

system formed by the **k**, **D** and **B** vectors, called the *kDB* system, in order to reduce the number of differential equations that need to be solved. In a similar fashion, we adopt a right handed coordinate system for each laser beam in our 3D IL problem, with unit vectors $\mathbf{e}_1$, $\mathbf{e}_2$ and $\mathbf{e}_3$ chosen such that:

$$\begin{aligned} \mathbf{e}_1 &\| \mathbf{E}_1 \\ \mathbf{e}_2 &\| \mathbf{E}_2 \\ \mathbf{e}_3 &\| \mathbf{k} \end{aligned} \tag{6-13}$$

where $\mathbf{E}_1$ and $\mathbf{E}_2$ are the two electric field eigenvectors that describe the polarization state of the considered beam *in the $e_1e_2e_3$ system*. Thus, it becomes very easy now to define arbitrary polarizations, since $\mathbf{E}_1$ and $\mathbf{E}_2$ are orthogonal to each other and both are orthogonal to **k** (optically isotropic interference medium). To make this coordinate system unique, the unit vector $\mathbf{e}_2$ is assumed to lie in the plane formed by the unit vectors **z** and $\mathbf{e}_3$, from the *xyz* and, respectively, $e_1e_2e_3$ coordinate systems.

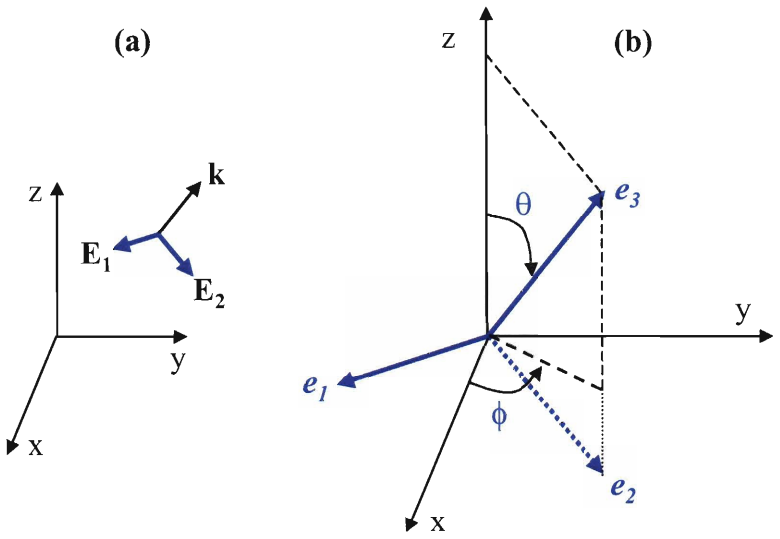

Figure 6-4 - **(a)** A laser beam propagating in the *xyz* lab coordinate frame in an arbitrary direction **k**, with arbitrary amplitude and polarization given by $\mathbf{E}_1$ and $\mathbf{E}_2$; **(b)** Definition the $e_1e_2e_3$ coordinate system in relation with the *xyz* coordinate system.

To calculate the total intensity pattern, we start by assigning $\mathbf{E}_1=E_1\mathbf{e}_1$, $\mathbf{E}_2=E_2\mathbf{e}_2$ and $\mathbf{k} = k\mathbf{e}_3$ for each beam in the $e_1e_2e_3$ coordinate system based on the desired polarizations and wavelength. We then use the polar (θ) and azimuthal (ϕ) angles to describe the propagation direction of each wave in the *xyz* coordinate system, as shown in Figure 6-4. At this point, we can solve for the *xyz* components of the electric field vector corresponding to each beam:

$$\mathbf{E}_{xyz} = \begin{pmatrix} E_x \\ E_y \\ E_z \end{pmatrix} = \underline{\underline{T}} \begin{pmatrix} E_1 \\ E_2 \\ 0 \end{pmatrix} \tag{6-14}$$

where $\underline{\underline{T}}$ is a coordinate transformation matrix having the following elements [31]

$$\underline{\underline{T}} = \begin{pmatrix} \sin\phi & \cos\theta\cos\phi & \sin\theta\cos\phi \\ -\cos\phi & \cos\theta\sin\phi & \sin\theta\sin\phi \\ 0 & -\sin\theta & \cos\theta \end{pmatrix} \tag{6-15}$$

Finally, using Eq. (6-11) and Eq. (6-12), we arrive at the total intensity distribution in the *xyz* coordinate system. The actual computation can be very easily implemented in MATLAB®, which then allows plotting of the 3D data in a variety of useful ways.

The advantage of this model stems from its ability to allow a very clear definition of the polarization state of arbitrary oriented beams, which then allows complete flexibility for modeling 3D IL with an arbitrary number, orientations, polarizations and amplitudes of beams propagating in 3D. Multiple exposures can be readily simulated using this approach by summing the individual intensity distributions produced for each exposure.

6.3. Fabrication of large area 2D quasicrystals by multiple exposure interference lithography

6.3.1. Introduction

As discussed in the previous section, 2D quasiperiodic structures can be obtained from both the interference of multiple laser beams, and from multiple exposures with subsequent rotations of line gratings produced by IL with 2 beams.

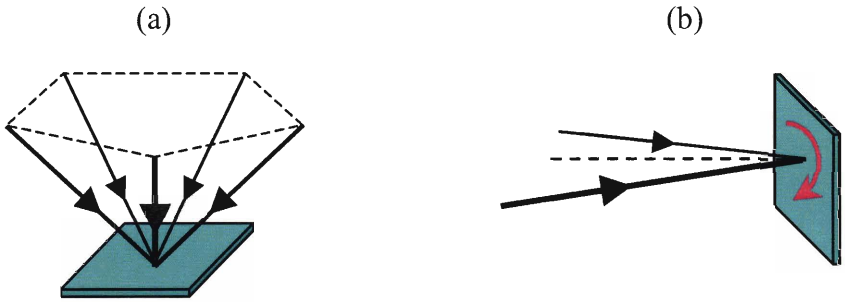

Figure 6-5 - IL configuration for fabricating Penrose-like 2D PQC **(a)** interference of five laser beams converging to a central point from the corners of a regular pentagon (i.e. the projections of the five **k** vectors in the sample plane are separated by 72°); **(b)** Five exposures of line gratings formed by IL with 2 beams, where the sample substrate is rotated with 72° after each exposure.

Although we have successfully implemented in our laboratory both MB-IL and ME-IL methods for fabricating 2D PQC samples, we focused on ME-IL due to a number of advantages over MB-IL, related to sample size and easy reconfiguration for fabricating quasiperiodic structures with different rotational symmetries. While MB-IL offers the greatest flexibility for creating structured materials with IL (the number, directions, intensities, and polarizations of the interfering beams can be independently controlled), its practical uses as typically implemented [11, 14] are limited because of the time-consuming setup step required when the number of beams or the sample periodicity need to be changed. In our laboratory, we used a continuous wave 532nm Coherent Verdi laser to generate 5 beams, which were then overlapped into the photoresist layer to

produce decagonal 2D quasicrystalline samples. Since at least N-1 half wave plates and polarizing cube beam splitters are needed to generate and adjust the power for N beams, and then at least one more wave plate is needed for controlling the polarization of each of the interfering beams, the cost of the optical components and the experimental setup time become limiting for implementation of 8 or 12 MB-IL and the fabrication of octagonal and dodecagonal 2D quasicrystals. Another optics related problem we had to deal with was related to the small diameter (4-5mm) and the Gaussian profile of the output beam of our laser, which produced samples with limited sizes and radial gradients of the volume fraction in the recorded structures. Additional difficulties we encountered were related to the need to prepare in-house a photoresist mixture sensitive to 532nm, since no commercial resists were found (most are designed for UV). We followed the method of Yang *et al.* [19] to prepare a 532nm resist, by mixing appropriate amounts of SU-8 epoxy with a photoacid generator and a photosensitizer that has a strong absorption at 532nm (rubrene from Sigma-Aldrich Inc., or H-NU 535 from Spectra Group Limited), all dissolved in cyclopentanone. Although we were successful in obtaining decagonal quasiperiodic structures from our 5-beam IL setup, the difficulties related to the optical setup constraints, and to the un-optimized, experimental photoresist mixture lead us to focus our efforts on ME-IL.

In this section we present our work on the implementation of ME-IL for the fabrication of 2D PQC structures with 8-, 10-, and 12-fold rotational symmetries. While the proof of concept for this ME-IL approach has been published in 2004 by Gauthier *et al.* [13], our results show for the first time that IL can produce 2D-PQC of similar quality and small feature sizes as those made by electron-beam lithography (EBL) [8, 9, 32]. We

have been able to fabricate 2D PQC samples with feature sizes as small as 100nm (a ~10x reduction factor compared to Gauthier *et al.*) over areas as large as ~2cm^2. Scaling down the feature size in the IL process was possible by using a Lloyd's mirror interferometer with a 325nm HeCd laser, which offers by design highly stable interference fringes (only one laser beam is present in the system, unlike typical 2 beam setups such as that shown in Figure 6-5(b) and used in [13]). The stability of the Lloyd's mirror IL, together with using a specially designed antireflection coating underneath the photoresist layer, allowed a very accurate recording of the low contrast intensity patterns produced by ME-IL. Our approach can be extended for the fabrication of 2D PQC patterns over entire 12" wafers, by using other lithographic interferometer systems currently available at MIT [15].

These results show that IL is a key technique for fabricating 2D PQC large enough to impact practical applications, unlike EBL which produces samples < 1mm^2. The successful production of large area 2D PQC samples enabled us to further develop a coherent diffraction lithography method that uses transparent 2D PQC as diffraction gratings to produce novel quasiperiodic 3D sub-micron structured polymeric templates (by recording the near field intensity pattern produced by the 2D PQC gratings, as it will be presented in the next section). This is a significant achievement, since 3D PQC have been yet to be fabricated at optical length scales - a first experimental study of the properties of 3D PQC has been reported only this year by Man *et al.* [33], who found large band gaps in the microwave regime for macroscopic 3D quasiperiodic polymeric networks with millimeter size features, fabricated with stereolithography.

6.3.2. The Lloyd's mirror lithographic interferometer

Introduced in the 1830's by Humphrey Lloyd, the presently called Lloyd's mirror interferometer consists of a very simple physical setup - a mirror is used to deflect a portion of a single light beam such that interference fringes are produced on a sample plane due to the interference between the mirror-deflected and the non-deflected rays, respectively.

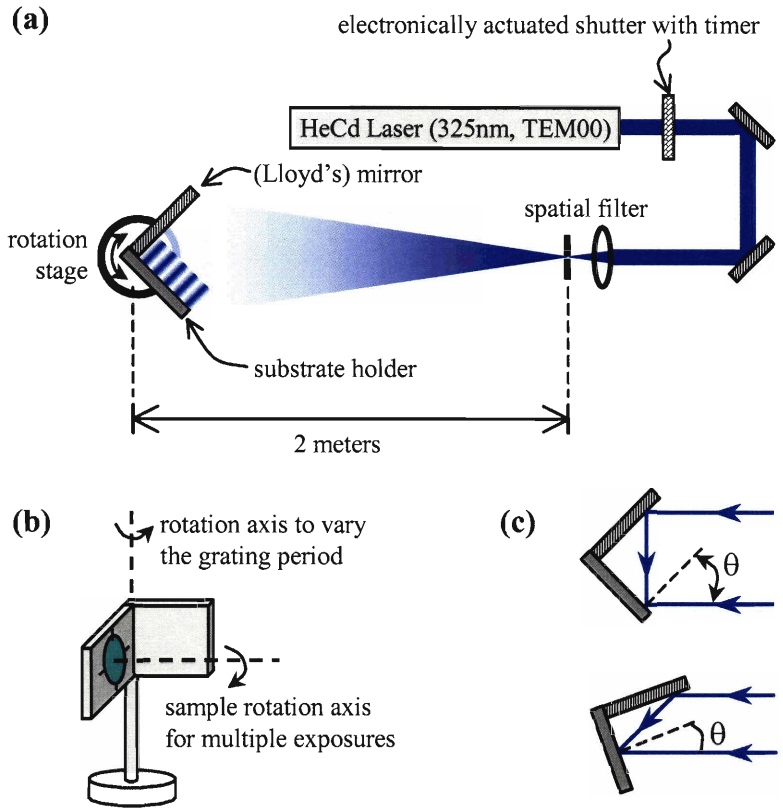

Figure 6-6 - **(a)** Configuration of the Lloyd's mirror IL system built and shared by the MIT Nanostructures Laboratory; **(b)** Sample holder assembly, showing the rotation axis for changing the grating periodicity, and the axis around which the substrate is rotated during ME-IL; **(c)** Rotating the entire stage assembly changes the incidence angle and thus the periodicity of the recorded gratings. Adapted from [29].

The Lloyd's mirror IL setup that was used in our research was built by Dr. Michael Walsh of the MIT Nanostructures Laboratory (NSL) as part of his M.Sc. thesis research [29] under the guidance of Prof. Henry (Hank) Smith, director of the NSL. This

IL system has been originally designed as a versatile IL tool for the fabrication of line gratings with periods varying from ~170nm to ~2000nm, and its quality has made it an important tool in the NSL. The beam source is a 40mW 325nm HeCd laser outputting a single TEM00 mode (i.e. a 2D Gaussian profile). As shown in Figure 6-6, the laser beam is passed through a spatial filter, and expanded over a distance of 2m. Although the phase fronts are in fact spherical, their large radius of curvature (2m) allows a very uniform interference pattern at the sample plane. The output of the laser is linearly polarized, and the optical setup in Figure 6-6 is designed such that the polarization is TE at the sample plane (for a maximum contrast of the exposed line gratings). The sample stage assembly is placed on a high accuracy rotation stage, in order to change the periodicity of the recorded line gratings. By rotating this stage, and thus changing the incidence angle θ, see Figure 6-6(c), it is easy to vary the period P of the recorded line gratings

$$P = \frac{\lambda}{2\sin(\theta)} \tag{6-16}$$

Another key component of the sample stage assembly is the ultra-flat aluminum mirror, which is positioned perpendicular to the sample plane. The sample holder can accommodate entire 4" wafers, and a rotation stage has been added to it so that samples can be rotated between exposures. We have also added to the original setup an electronic shutter with a timer, for an accurate control of the exposure time (the original setup uses a manually actuated shutter).

The Lloyd's mirror IL setup has a number of strengths that make it especially suitable for the fabrication of 2D PQC via ME-IL. Its most important feature is the high

stability of the interference fringes produced at the sample plane. Since only one laser beam is present in the system, any fluctuations caused by air currents, temperature variations, etc. encountered along the propagation direction affect equally the interfering rays (consider than in a typical two beam IL setup (also called Mach-Zender) any differences between the 2 arms leads to translations of the interference pattern on the sample plane, reducing the achievable contrast). The Lloyd's mirror IL setup is only sensitive to air currents in the small space between the mirror and the substrate, and to vibrations of the entire stage assembly. To eliminate these problems, the entire setup is housed on an optical table covered completely with a plastic enclosure.

6.3.3. 2D QPC fabrication issues: contrast in Multiple Exposure IL

As it was shown in Figure 6-2, the quasiperiodic intensity distributions produced by IL consist of fairly complex landscapes having moderate contrast levels. To gain a better understanding of the practical consequences of this reduced contrast, we investigated the dependence of 2D QC volume (area) fraction on an intensity cutoff level applied to the computed intensity pattern (directly related to the exposure dose in experiments) for ME-IL with 4, 5 and 6 exposures (corresponding to 8-, 10-, and 12-fold rotationally symmetric 2D QC patterns). The volume fractions were calculated by evaluating $I(x,y)$ using Eq. (6-1) across a 2D computation domain of size 20x20λ with 40 points per λ, and then finding the fraction of pixels in this 800x800 grid that have intensities greater than a particular threshold level.

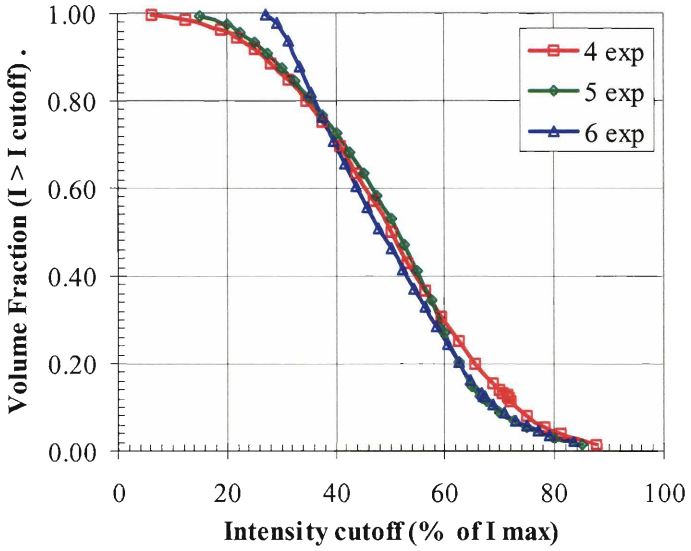

Figure 6-7 - Dependence of volume fractions on the intensity cutoff level for 2D quasiperiodic patterns obtained from 4, 5, and 6 exposure IL. Representative pictures of the three types of 2D PQC structures at a few fill fractions are also shown in Figure 5.4.

The above figure shows that the larger the number of exposures, the more rapidly changing the volume fraction of the 2D QC structure becomes as the exposure dose is increased. For example, while in the case of 4 exposures all the volume fractions could be generated by varying I_{cutoff}/I_{max} between 5 and 88%, in the case of 6 exposures these volume fractions are generated in a significantly narrower range of I_{cutoff}/I_{max} values, from ~28% to 85%.

Thus, it is expected that small changes of the experimental exposure dose will cause larger variations of the 2D QC fill fractions the larger the number of exposures. In order to more accurately capture the complex, feature rich QC patterns expected from ME-IL in the photoresist, we have designed an antireflection coating to minimize the reflection from the bottom interface of the photoresist, since even small changes of the laser intensity inside the resist are expected to significantly affect the resulting 2D QC patterns.

6.3.4. Fabrication process: the tri-layer resist process and materials

Given the sensitivity of the quasiperiodic patterns produced by ME-IL to exposure doses, we have implemented in our experiments the so-called tri-layer resist process [34]. In this process, two specially designed layers are added between photoresist and substrate in order to increase the nanoscale fidelity of the recorded structure.

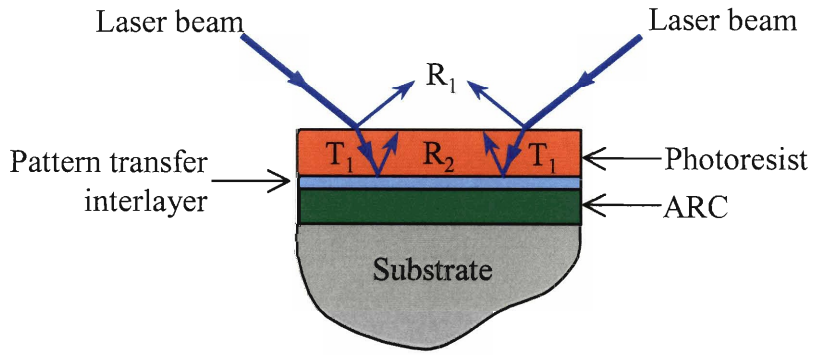

Figure 6-8 - Tri-layer resist stack. An optically absorbing antireflection coating (ARC) placed on top of the substrate is used to eliminate the reflection R_2 from the bottom of the photoresist layer, such that only the interference between the T_1 rays is recorded. An optically thin interlayer (e.g. 20nm SiO_2) is placed between the photoresist and ARC layers for accurately capturing the photoresist pattern before transfer into the substrate.

The two layers added between the photoresist and the substrate are an antireflection coating (ARC) and a pattern transfer layer. The function of the ARC is to minimize the reflection R_2 at the bottom interface of the photoresist layer, as shown in Figure 6-8 (this kind of ARC should not be confused with typical ARCs that are designed to minimize the top reflection, R_1). The second layer is an optically thin pattern transfer interlayer that is placed between the ARC and the photoresist layers in order to improve the fidelity with which the quasiperiodic pattern is transferred into the substrate. This is achieved by choosing an interlayer material that is not affected by typical etching processes used for structuring both the photoresist and the ARC layers. The most

common choice, also used by us, is a silica (SiO_2) interlayer [29, 34] - dry etching is used to "project" the photoresist structure into the ~20nm thin SiO_2 layer (e.g. RIE with CHF_3 or CF_4 gases), and then this structure is transferred into an organic-material based ARC layer using RIE with O_2 plasma. Thus, the photoresist acts as a dry etch mask for the SiO_2 interlayer, which then becomes the etch mask for the organic ARC, which in the end is the mask used to etch the quasiperiodic pattern into the substrate.

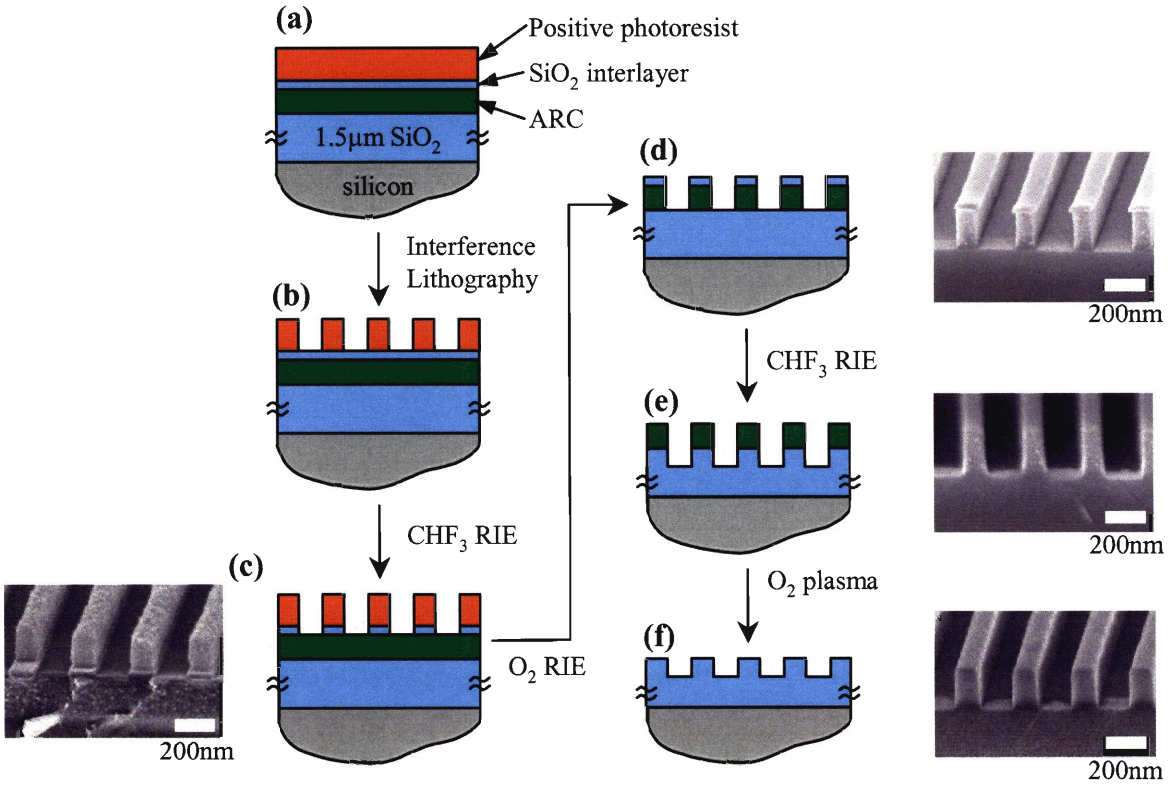

Figure 6-9 - Process flow for using ME-IL to fabricate 2D PQC samples, with SEM images of actual samples produced in the case of line gratings (one exposure). **(a)** the initial tri-layer resist stack is composed of 200nm photoresist, 20nm SiO_2 and 200nm organic ARC material, on a 1.5μm thermal oxide coated silicon wafer substrate; **(b)** the developed photoresist structure; **(c)** the SiO_2 interlayer is etched with CHF_3 RIE using the photoresist as a mask; **(d)** the pattern is further transferred into ARC by etching with O_2 RIE using the thin SiO_2 caps as a mask; **(e)** the 2D quasiperiodic pattern is finally transferred to the SiO_2 substrate by CHF_3 etching using the ARC as a mask; **(f)** the final 2D PQC sample is obtained by stripping the ARC mask with O_2 plasma.

The clean room fabrication process we used to prepare 2D PQC samples with various rotational symmetries is shown above. The materials and deposition details are

summarized in Table 6-2. Please note that a positive rather than a negative photoresist was chosen, in order to be able to more accurately capture the smaller features recorded in the photoresist as the exposure dose is increased, as shown in Figure 5.4 (negative resists are a better choice for recording holes-in-resist types of patterns).

Table 6-2 - Materials, deposition techniques and their refractive indices used in the tri-layer process outlined in Figure 6-9 (list in order of deposition).

Label	Material	Deposition	Refractive index at 325nm*
substrate	1.5μm thermal oxide on silicon, from WaferNet Inc.	n/a	Si: 4.68-2.03*i* SiO_2: 1.48
ARC	AZ BARLi Coating, from Clariant Corporation.	- spin coat, 6500rpm (thickness ~200nm**) - bake 90sec at 175°C	1.55-0.14*i*
interlayer	silicon oxide, SiO_2	- e-beam evaporation (thickness 15-20nm)	1.48
photoresist***	PFI-88 A2 (positive resist) from Sumitomo Chemical Co. Inc.	- spin coat****, 4000rpm (thickness ~200nm) - bake 90sec at 90°C	1.79-0.02*i*

* measured using spectroscopic ellipsometry by Dr. Michael Walsh, from [29].

** ARC thickness is changed according to the period to be recorded, such that the reflection at the bottom interface of the photoresist is minimized (see Figure 6-10). The reported thickness value corresponds to 300nm period lines.

*** a photoresist adhesion promoter is first spun on the SiO_2 interlayer (hexamethyl disilazane, HMDS, which forms a hydrophobic trimethyl-siloxane self-assembled monolayer coating on SiO_2). Without this adhesion promoter the photoresist pattern dewets in the developer solution.

**** the photoresist is developed with a tetramethyl ammonium hydroxide aqueous-based solvent, Microposit CD-26 from Rohm&Haas.

The refractive index data shown in Table 6-2 is used to calculate the thickness of the ARC layer for a desired line grating periodicity. The incidence angle can be determined using Eq. (6-16), and then a simple transfer matrix technique [29, 35] can be used to calculate the reflectivity at the bottom interface of the photoresist (R_2, shown in Figure 6-8) from the upper propagating component of the electric field inside the photoresist layer. ARC thicknesses for which $R_2 < 5\%$ should be used for obtaining line gratings with good vertical profiles.

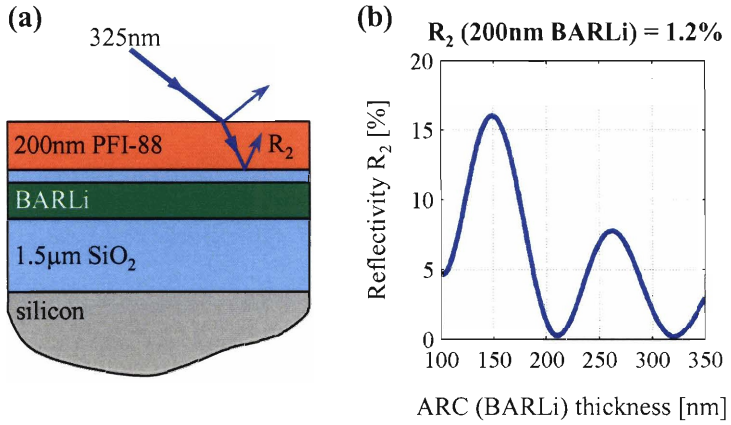

Figure 6-10 - (a) Tri-layer resist stack structure: (from the top) photoresist, SiO_2 interlayer, ARC layer and substrate (1.5μm thermal oxide on silicon); **(b)** Effect of varying the thickness of the ARC layer on the reflectivity R_2 from the bottom interface of the photoresist layer in the case of a 300nm period grating. The simulations used the refractive index data provided in Table 6-2.

The RIE dry etching steps shown in Figure 6-9(b)-(f) were performed in the Nanostructures Laboratory class 100 clean room using a PlasmaTherm 790 Series System VII (13.56MHz RF source) with the following process parameters.

Table 6-3 - Reactive Ion Etching (RIE) process parameters. For all gases, the total flow rate was 15sccm.

Material to be etched	Gas	Pressure	DC Bias / Power	Etch rate
SiO_2	CHF_3	10 mTorr	300V / 150W	~27nm/min
ARC	O_2/He (1:2)	7 mTorr	250V / 130W	~60nm/min
ARC removal	O_2/He (3:1)	25 mTorr	160V / 75W	~100nm/min

6.3.5. Results

The processes and materials described in the previous section were used to fabricate a variety of 1D and 2D structured samples on both silicon and silica substrates.

To showcase the stability of the Lloyd's mirror IL setup, we first report the results of an experiment where line gratings were written in two ways - one shot exposures of a particular dose, and, secondly, by delivering the same dose over multiple exposures with

delays introduced between each successive exposure in order to increase the time elapsed between the beginning and the end of the recording step.

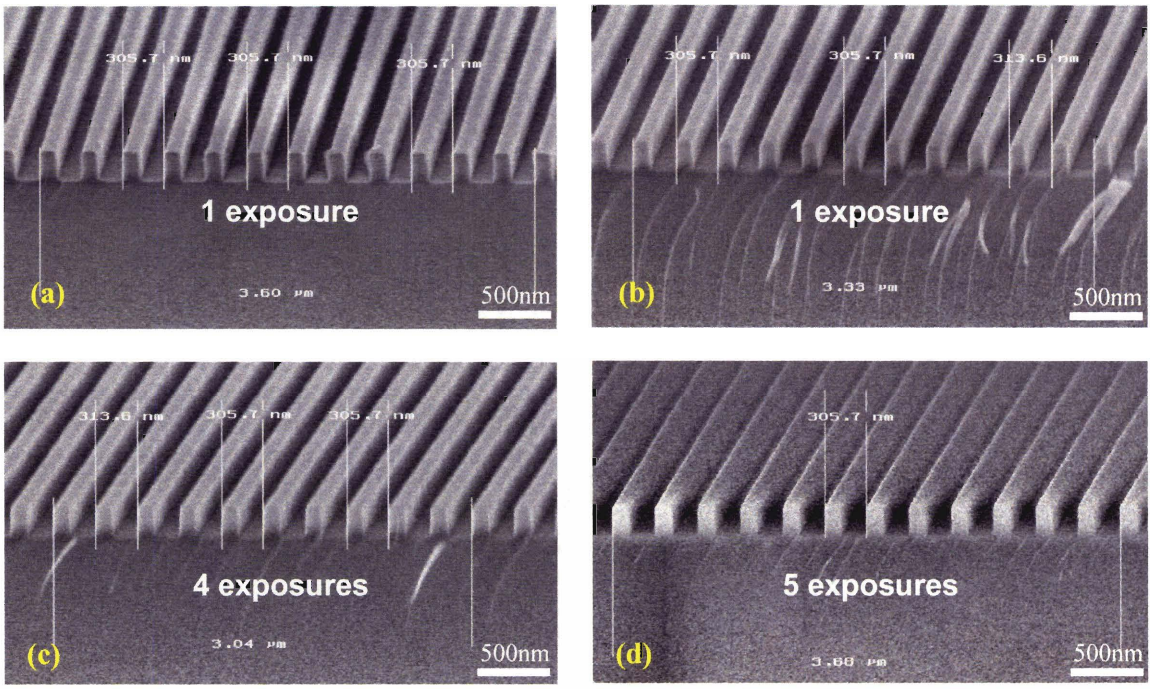

Figure 6-11 - Scanning electron microscope images at 30k magnification of SiO_2 line gratings obtained from photoresist patterns produced using two IL approaches. In **(a)** and **(b)** a single exposure of 11.75min (115nW laser power delivered at the sample plane) is performed. The same total dose is delivered in **(c)** as 4 exposures and in **(d)** as 5 exposures, but additional 1min delays are introduced between each exposure. It can be seen that the resulting gratings are virtually identical within the error limit of the SEM measurement. Measured duty cycles are 43% in (a), and 41% in (b), 39% in (c), and 41% in (d).

In the Lloyd's mirror setup, the laser power delivered to the sample is very low, due to the long expansion length (2m) of an already low power output (~35-40mW typically). It should be mentioned that this laser has no output power adjustment, so the recording dose is controlled by varying the exposure time. Using a Newport Optical Power Meter 1830C calibrated for 325nm, we typically measured about 200nW at the sample plane, but, probably due to the age of the HeCd laser, the delivered power tends to fluctuate between experiments (the highest power in our experience at the sample was about 280nW). In the experiment shown in Figure 6-11 the power was 115nW and one

exposure of 11.75min was used to produce the SiO_2 line gratings shown in (a) and (b). Two more samples were prepared by allowing one minute between successive exposures, while maintaining the same total dose of 11.75*115(min*nW), for the cases of 4 and 5 exposures. For all samples, the periods of the line gratings transferred into the SiO_2 substrate were measured to be almost identical, fluctuating around 307nm, from SEM images at 100k magnification. Similarly, the duty cycles (ratio of linewidth to period) were measured to be 43% and 41% for the single exposure experiments shown in Figure 6-11(a) and (b), and 39% (c) and 41% in (d). Since instability of the fringes would have resulted in an increase of the measured linewidth, we can conclude that the MIT implementation of the Lloyd's mirror IL system is highly stable. No significant drift on the few nanometer scale could be detected even for the longest experiment of ~16min, in the case of 5 exposures shown in Figure 6-11(d).

We now proceed to present our results for the fabrication of 2D quasiperiodic structures using ME-IL. As previously mentioned, N = 4, 5, and 6 exposures with π/N rotation angles produces a $2N$-fold rotationally symmetric 2D quasiperiodic structure (the factor of 2 is due to the mirror symmetry of the line gratings). The photoresist patterns are transferred into the substrate, typically SiO_2, using the process described in Figure 6-9. In Figure 6-12 we first show perhaps the most recognizable 2D quasiperiodic structure, the Penrose-like lattice with 10-fold rotational symmetry, obtained by 5 exposures with rotations of 300nm period line gratings.

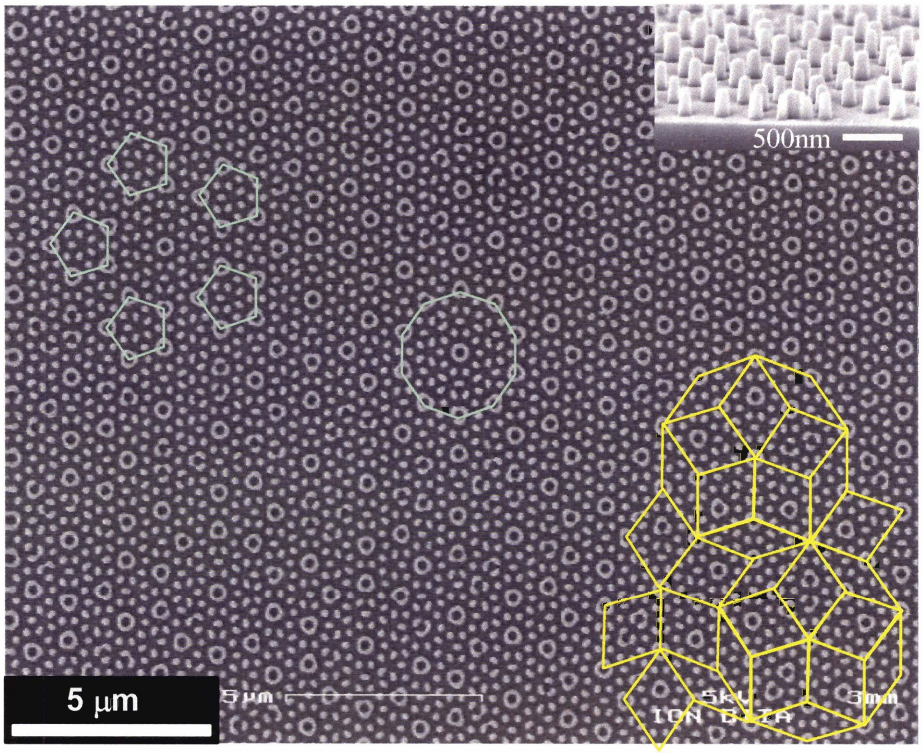

Figure 6-12 - Top-down view SEM image of a Penrose-like decagonal 2D quasiperiodic pattern etched in SiO_2. Areas with local 5 and 10 fold rotational symmetries are emphasized, and a portion of a Penrose tiling pattern is overlayed on the sample image. The inset figure shows an edge-on SEM image of the same sample, where the height of the posts is 240nm. The structure was obtained by 5 exposures with 36° rotations of 300nm period line gratings.

The above figure experimentally proves the remarkable correspondence of the 2D decagonal quasiperiodic structure produced by IL and a mathematical Penrose tiling, comprising two rhomboidal motifs (acute angles of 36° and 72°). Structural defects can also be seen throughout the pattern, e.g. as occasional, incompletely closed circular features. This is an inevitable result of capturing in the photoresist a low contrast interference pattern. Insufficient contrast causes photoresist traces to be left on the substrate after developing (e.g. the dose delivered at certain locations is not high enough to complete the photochemistry leading to solubilization in developer solution). Any such defects are unfortunately projected into the SiO_2 interlayer, and maintained with high fidelity throughout the entire fabrication process shown in Figure 6-9.

Nevertheless, the uniformity of the structure is remarkably high. The advantage of ME-IL over MB-IL for fabricating 2D QPC with various rotational symmetries is presented in the next figure, where three kinds of quasicrystals were readily fabricated just by changing the number and corresponding angles of rotations. In all three cases, line gratings with 300nm periods were recorded in each exposure.

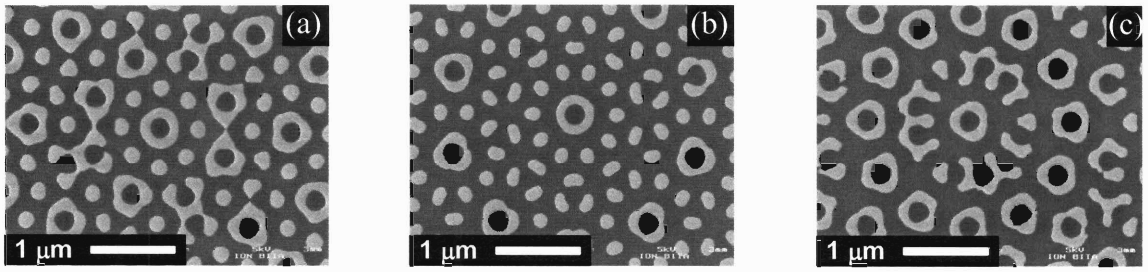

Figure 6-13 - Top-down SEM images of 2D **(a)** octagonal, **(b)** decagonal, and **(c)** dodecagonal quasiperiodic structures in silica produced by ME-IL with N = 4, 5, and 6, respectively, exposures and rotations with 180°/N angles. Views of the central axis showing 8mm, 10mm, and 12mm point symmetry.

As expected, changing the exposure dose allows to readily vary the volume (fill) fraction of the resulting 2D quasiperiodic structures.

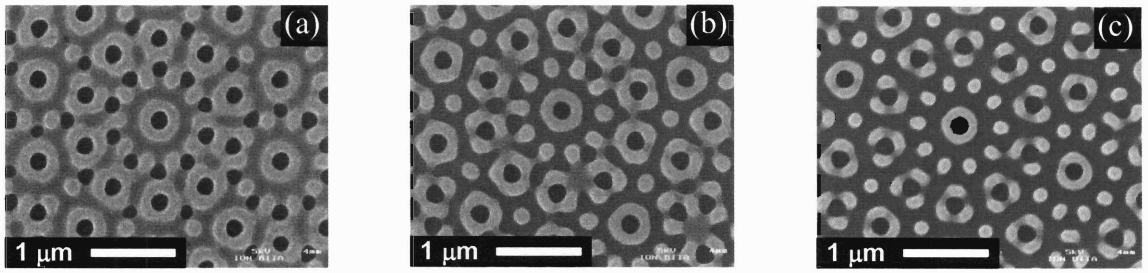

Figure 6-14 - Effect of exposure dose on the recorded photoresist pattern for the case of a 2D decagonal quasicrystal from ME-IL with 5 exposures and rotations with 36°. The fraction of substrate area covered with photoresist (light gray areas in the figures) is 66% in **(a)**, 44% in **(b)**, and 30% in **(c)**.

A comparison between the photoresist patterns produced by IL and simulated intensity patterns is shown next. A good correspondence between the experimental and

predicted structures is obtained by varying the intensity threshold applied to the total intensity distribution predicted by Eq. (6-1), and plotting $I(x,y) - I_{threshold}$.

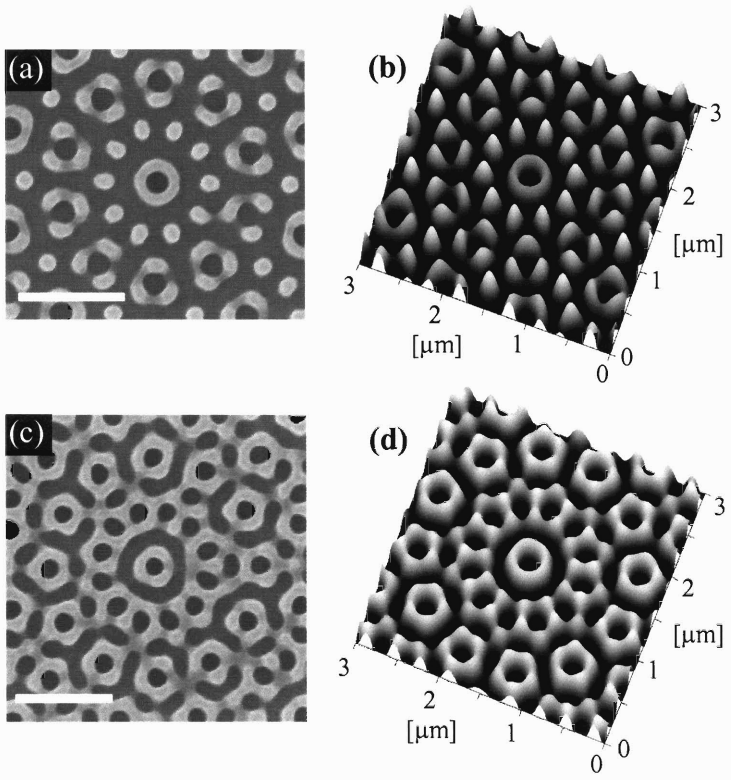

Figure 6-15 - Comparison between SEM images of experimental photoresist patterns produced by ME-IL with **(a)** 5 exposures and 36° rotations, or **(c)** 6 exposures and 30° rotations, with computed intensity patterns approximating the experimental conditions, as **(b)** and **(d)**. 300nm period line gratings were recorded in each exposure.

Perhaps the greatest advantage of ME-IL stems from its ability to allow fabrication of 2D quasiperiodic structures over very large areas. While, for practical reasons, our typical samples were square pieces of silicon wafers with ~1-2cm sides, IL tools have been developed at MIT that can pattern entire 12" wafers [15]. As an example, we next show a large area SEM image of a 2D octagonal quasicrystal fabricated by 4 exposures with 45° rotations.

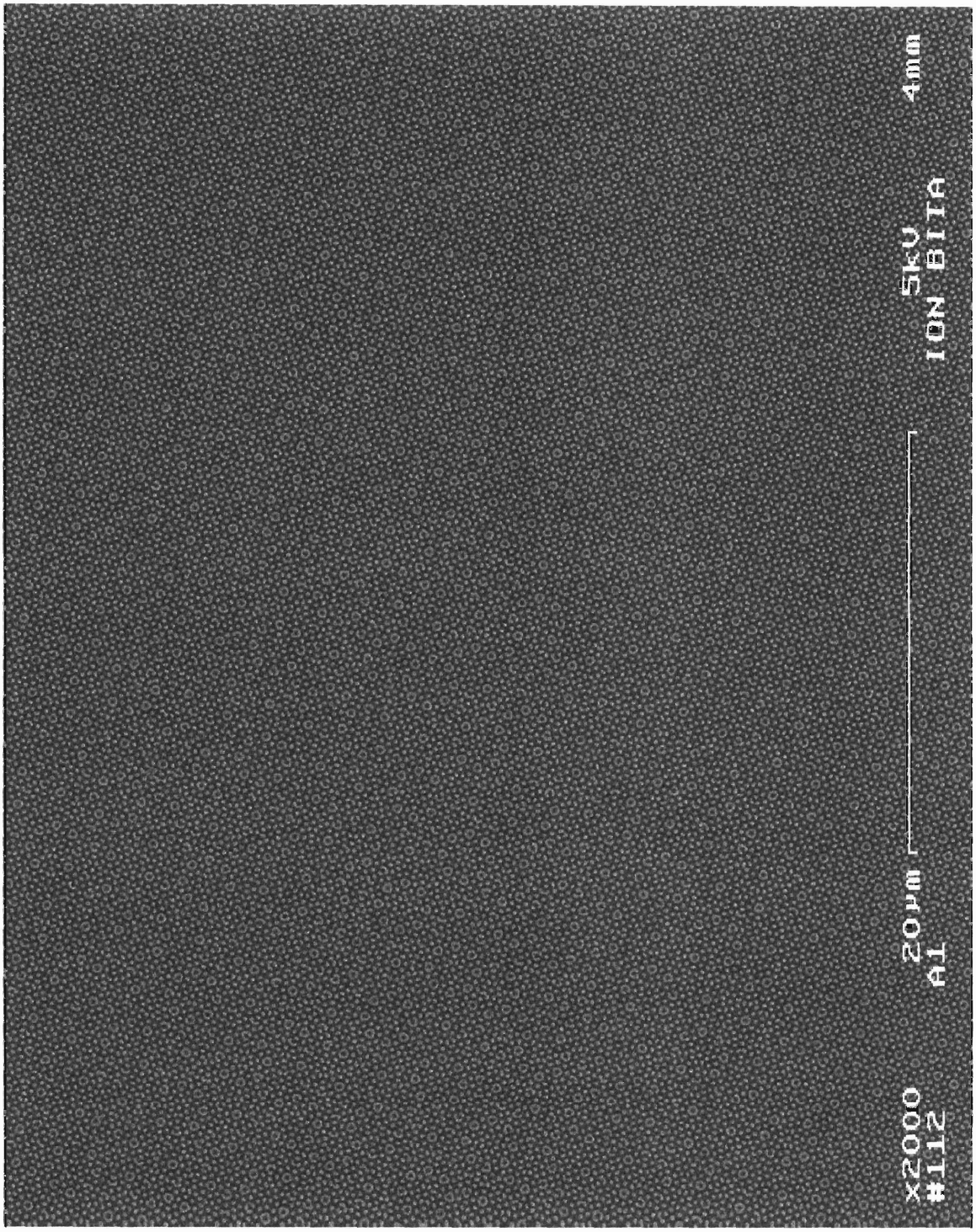

Figure 6-16 - Large area, plan view SEM image of an octagonal 2D quasiperiodic silica structure obtained by 4 exposures of line gratings with 300nm periodicity, and subsequent rotations with 45°.

6.4. Towards Applications

Having considered opportunities related to further studying issues such as the optical properties of 2D quasiperiodic materials, the influence of controlling the spatial coherence between successive exposures, the fabrication of samples with rotational symmetries larger than 12-fold, etc., we decided instead to focus on two other problems with potential for higher impact. As described in this short section, we attempted proof-of-concept experiments and obtained initial success in employing the 2D PQC patterns we fabricated as gratings for the fabrication of 3D sub-micron structured samples. Such quasiperiodic 3D structured materials have not been previously reported. We have also conducted initial experiments on a fascinating problem, related to frustrating a self-assembling block copolymer system forming a translationally periodic morphology with p6mm symmetry by causing the self-assembly of a monolayer of the spherical microdomains to occur on a quasiperiodic topographically patterned substrate (see Figure 6-21). This line of research has also put us in a position to recognize that a properly chosen 2D array of posts could facilitate not only local ordering, but also help impose a unique global orientation of the block copolymer morphology over entire wafers up to 12" in size, a highly sought goal in the field of block copolymer nanolithography [36-39].

6.4.1. Fabrication of quasiperiodically structured 3D materials by coherent diffraction lithography with 2D quasiperiodic transparent phase masks

As mentioned in the introduction of this chapter, photonic quasicrystals still represent a very young class of photonic band gap materials. Only recently, some quasicrystals have been shown to exhibit PBG properties superior to photonic crystals and to exhibit other interesting optical properties in 2D [8, 9, 32]. It is thus believed that

3D PQC may become very important candidates as 3D PBG materials [33]. However, theoretical investigations of the properties of PQC in 3D are very difficult due to the absence of translational symmetry (as a consequence, computationally prohibitive studies of large enough 3D structures are required to gain quantitative insight into the properties of this class of PBG materials). Offering an experimental solution to these difficulties, only a few months ago, Man *et al.* published an experimental investigation of PBG properties in 3D quasicrystalline materials [33] arguing that an easier path forward is to fabricate actual samples on the millimeter scale and probe them with microwaves. While this study represents a significant step forward towards developing an understanding of the potential optical properties of 3D photonic quasicrystals, the connected-rods structure investigated is close to impossible to fabricate at the optical length scale.

In this section we present a natural extension of our fabrication of 2D PQC samples, which allows access to novel quasiperiodic 3D structured materials with feature sizes on the scale of the wavelength of light. The significance of this path is related to the fact that by varying the structure of the 2D PQC (easily achieved with IL and planar processing), a wide variety of 3D quasiperiodic structures could be rationally designed. Since the resulting structures can be accurately predicted by modeling the IL process, it is conceivable that they could be then optimized for particular applications, such as e.g. enabling a complete 3D PBG at optical wavelengths.

The general approach we took is known in the literature as coherent diffraction lithography (CDL) [16], phase mask lithography [40], or as near-field nanolithography [41]. While we prefer to refer to this method as CDL, regardless of the name used to describe it, its essence remains the same - a transparent 2D diffraction grating is

illuminated from behind, and the near field light intensity pattern produced in the vicinity of the topographically structured side is captured in a photoresist layer. By using thin or thick resist layers, both 2D [16] and 3D samples [40] can be fabricated.

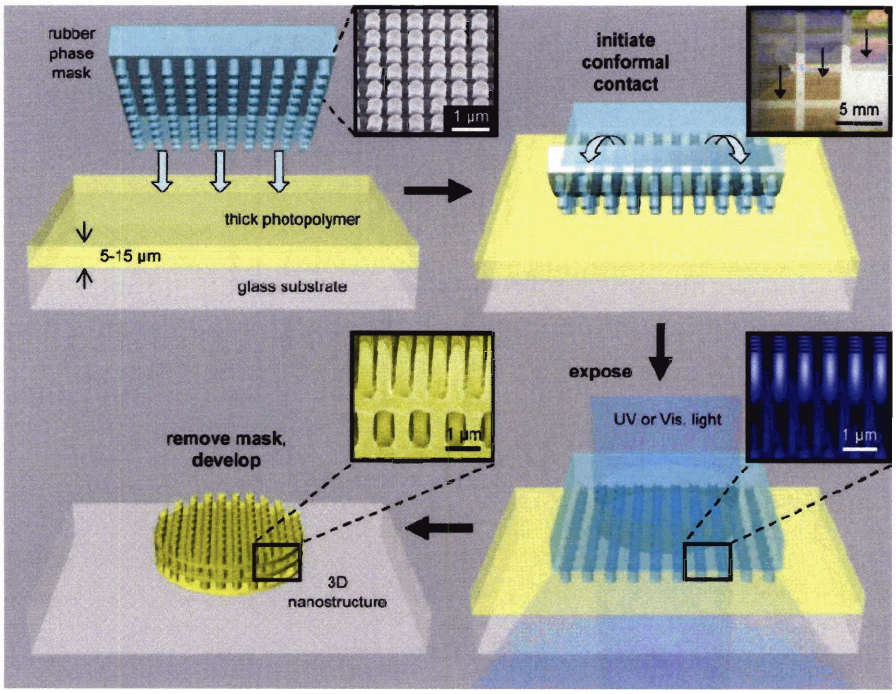

Figure 6-17 - Coherent diffraction lithography (also known as phase mask lithography). The schematic shows an implementation for creating 3D nanostructured polymeric templates by recording the near field intensity pattern generated by an elastomeric, transparent, 2D periodic diffraction grating into a photoresist. From [40].

While, as a technique, CDL is limited to only producing select families of 3D structures, it has significant practical advantages as a low cost patterning tool that can employ light sources with low coherence (e.g. UV lamps), and cheap, elastomeric diffraction gratings (e.g. polydimethylsiloxane, PDMS, borrowing from the nanostructured stamp-making expertise developed in the field of soft-lithography [42]).

Our goal is to employ transparent, 2D quasiperiodic diffraction gratings to create 3D structured materials with quasiperiodicity, by recording the near field intensity pattern produced when a laser beam passes through the diffraction grating. The actual

implementation of CDL for our case is relatively simple. 2D PQC gratings are patterned into a thick thermal oxide layer on silicon wafers using the multiple exposure with sample rotation IL approach described in the previous section. Following typical procedures for creating PDMS stamps from nanostructured master patterns for soft-lithography [42], we use the resulting hard material 2D quasiperiodic diffraction gratings as molds for creating an elastomeric replica in PDMS (prepared by casting a liquid precursor, Sylgard 184 from Dow-Corning). The silica surfaces of the 2D PQC gratings are first treated with a vapor-deposited perfluroro alkyl trichlorosilane to lower the mold surface energy and to thus facilitate the release of cured PDMS gratings (i.e. we fabricate more than one PDMS grating from a given master). PDMS is a very useful material for CDL, because of its excellent transparency across the visible and into the UV region, and because PDMS diffraction gratings easily conform on resist coated substrates to create a good optical contact and thus allow recording the near field intensity pattern onto large area substrates.

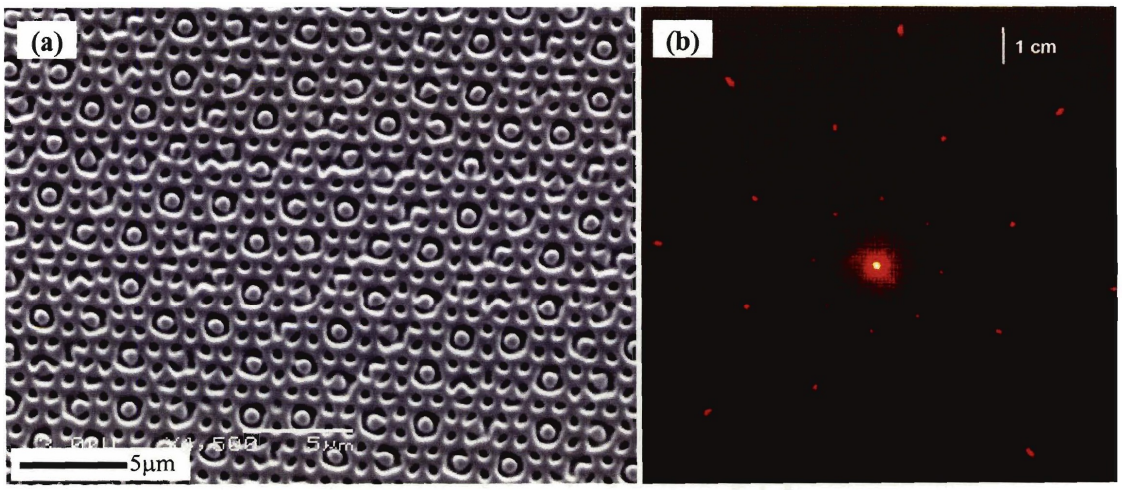

Figure 6-18 - (a) Elastomeric replica in PDMS of an octagonal 2D quasiperiodic silica grating. The depth of the topographical features is 450nm; **(b)** the diffraction spectrum obtained for a 632nm HeNe laser - imaged by projection on a paper screen placed at 5.2cm away from the PDMS grating (digital photograph captured by Mr. Marcus Dahlem, MIT EECS).

To test the CDL approach for fabricating 3D quasiperiodic structures, a 361nm line of an Ar-ion laser was used to expose 5 micron thick films of a commercial SU-8 2005 photoresist (from MicroChem Inc.) through a series of 2D octagonal quasiperiodic PDMS gratings with varying volume fractions. A representative SEM image of the surface of a PDMS diffraction grating, and a photograph of its diffraction spectrum obtained with a HeNe laser are shown in Figure 6-18. While all the SU-8 structures we recorded with CDL from PDMS stamps also produced diffraction spectra with the same octagonal symmetry (indicative of the fact that the quasiperiodic structure has been recorded in the volume of the epoxy resist), it has been a challenge to find the right combination of the exposure dose, post exposure bake and development times that would produce high quality bicontinuous air-epoxy 3D structures.

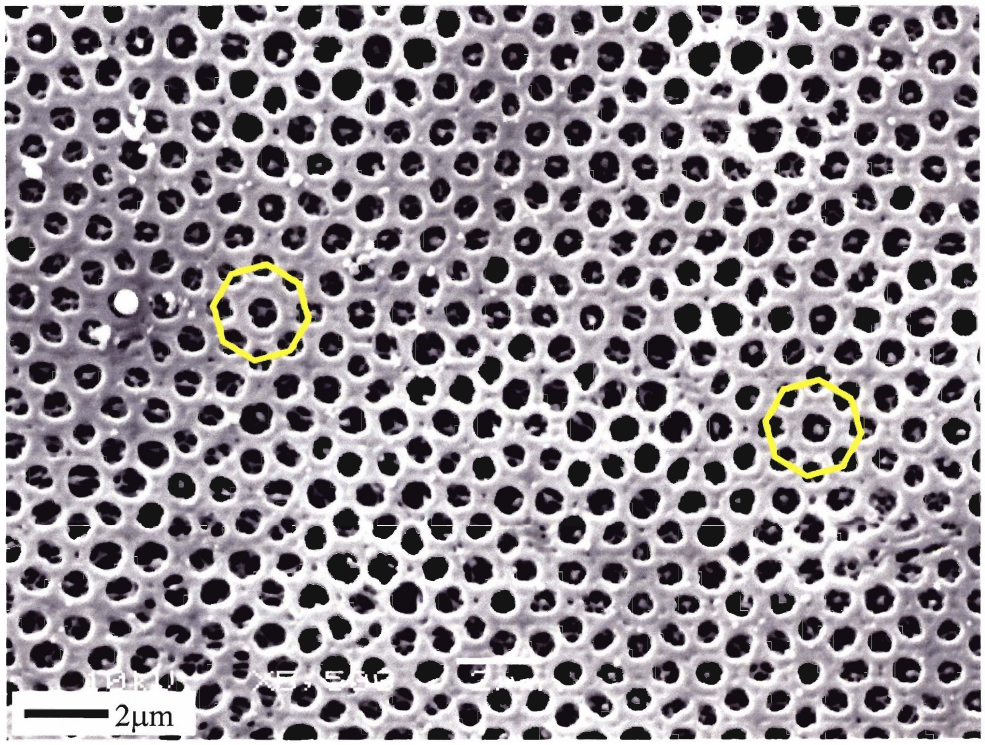

Figure 6-19 - A sub-micron structured, 3D epoxy polymeric network with quasiperiodicy obtained by CDL with a transparent octagonal 2D quasiperiodic PDMS grating, exposed with the 361nm line of an Ar-ion laser. Representative local octagonally symmetric regions are indicated with green octagons.

While currently this project remains a work in progress, by exploring this large experimental parameter space in collaboration with Ms. Taeyi Choi (MIT DMSE), we have already been able to obtain open 3D quasiperiodic structures with octagonal symmetry, proving our initial hypothesis that a 2D quasiperiodic structure can be used to fabricate quasiperiodic 3D structured materials by CDL. Such a 3D structure is shown in Figure 6-19, and it was obtained for a 361nm exposure through the PDMS stamp shown in Figure 6-18(a) for 23sec at a power level of 8.5μW, followed by a 7min postbake step in a 65°C oven, 3min cool-down, and 1.5min development in cyclopentanone at room temperature.

While CDL should clearly allow the fabrication of a wide range of 3D quasiperiodically structured materials provided their respective 2D PQC gratings are available, the practical implementations will require a tedious optimization. Based on our experience with the fabrication of 2D PQC structures, and the difficulty of low contrast in interference patterns, it is predictable that CDL-based methods may end up requiring processing in a very narrow window of experimental parameters in order to obtain a desired 3D air/polymer bicontinuous structure. Too better understand the contrast issue, consider that the near field light intensity distribution that is used in CDL to pattern the photoresist, could be treated as a superposition of all the far field diffracted orders - since each order consists of 8, 10, or 12 beams depending on the quasicrystal (e.g. see Figure 6-18), the large number of total beams simultaneously interfering in the near field will lead to a reduced contrast in the final 3D intensity pattern. A last observation we make is related to the fact that there appears to be no theoretical tools for predicting the intensities of each diffracted order for a given transparent 2D quasiperiodic stamp. This precludes

using simple models for predicting the 3D intensity pattern, such as that presented in Section 6.2.3, which is a big disadvantage for experiments, given the large sensitivity of quasicrystal volume fraction on exposure dose previously observed for the 2D case.

However, as previously mentioned, this work is still in progress. We have also been collaborating with Mr. Marcus Dahlem and Prof. Erich Ippen of the MIT EECS department to image the 3D near field intensity pattern in the vicinity of the PDMS stamps using a home built near field optical microscope (NSOM). This kind of measurement may become the experimental answer to the hard problem of theoretically predicting the resulting structure from a phase mask a function of exposure dose. In principle, one could pass through the PDMS a laser wavelength that produces the same number of diffracted orders in air as the experimental recording wavelength produces in the photoresist. By scanning a *xyz* volume in the near field, one could quickly gain an understanding of the connectivity of the resulting 3D intensity patterns as a function of PDMS stamp structural features (fill fraction and height of the 2D quasiperiodic topographical features). Ultimately, one would still need to optimize the exposure and postexposure processing steps, but NSOM seems the right tool for channeling these efforts towards only the more promising samples.

6.4.2. Self-Assembly of block copolymers thin films on 2D quasiperiodic topographically patterned substrates

A second line of investigation we pursued, that was enabled by the 2D quasiperiodic samples we fabricated, is related to the problem of constraining a material that prefers to adopt a translationally periodic structure to self-assemble on a substrate with topographical features arranged in 2D quasiperiodically.

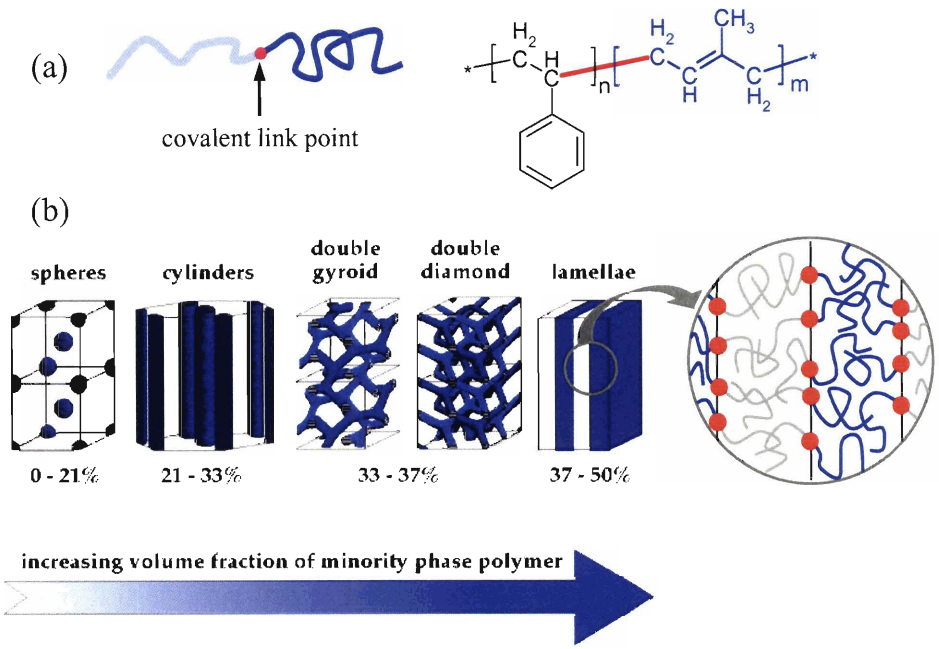

Figure 6-20 - (a) Schematic of a diblock copolymer molecule, formed by two chemically distinct polymer chains joined covalently. Polystyrene-*b*-polyisoprene is shown as an examle; **(b)** Bulk morphologies obtained in diblock copolymers as the volume fraction of a component is increased from 0 to 50%.

One particular application for which block copolymers (BCP) have been widely investigated in the recent past is nanopatterning. BCP nanolithography refers to the use of block copolymers composed of blocks with different etch properties (i.e. one block can be selectively removed), to pattern substrates with the structure formed by a BCP self-assembling in thin films [36-39].

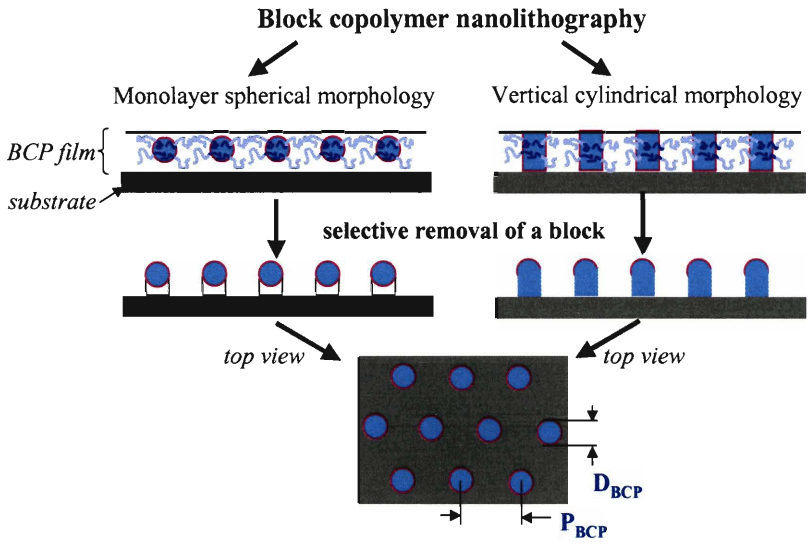

Figure 6-21 - Block copolymer nanolithography. Formation of a nanopatterning mask after selectively removing a component from a self-assembled block copolymer thin film with either spherical or cylindrical morphology.

Thus, there is currently a large interest for understanding and controlling the process of self-assembly of BCP in thin films. Nevertheless, our initial motivation to study self-assembly on quasiperiodic topographically patterned substrates was a different one - we were fascinated with the problem of how would a material that normally adopts a translationally periodic structure organize when constrained with quasiperiodic boundary conditions. Furthermore, we had hoped that using 2D quasicrystals with different rotational symmetries, particularly 12-fold, may allow for interesting consequences given the 6mm symmetry of a BCP thin film with a monolayer spherical microstructure.

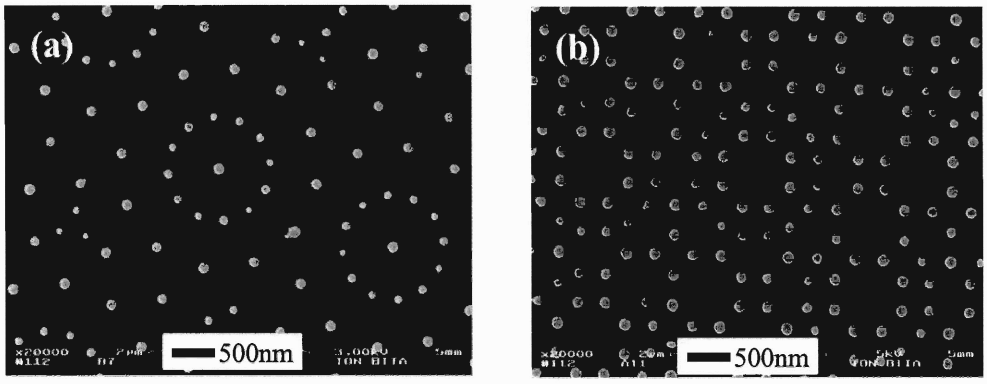

Figure 6-22 - Plan view SEM images of representative 2D quasiperiodic array of posts used as templates for BCP self-assembly studies **(a)** 2D dodecagonal QC; **(b)** 2D octagonal QC.

Typical quasiperiodic structures that were used for BCP self-assembly studies are shown in Figure 6-22, and were fabricated by exposing a positive photoresist with large enough doses to produce small diameter posts. These are further transferred into the 1.5micron thick thermal oxide layer of a silicon wafer. The height of the posts is chosen to correspond to a BCP sphere monolayer thickness (see Figure 6-21). In our studies, we have used a polystyrene-*b*-polyferrocenyldimethylsilane (PFS, 47:15 kg/mol), whose self-assembly and processing were extensively investigated at MIT [37-39]. BCP films with thickness of 55nm were deposited by spin coating from 1.5wt% toluene solutions onto quasiperiodic substrates comprised of 55nm tall posts, such as those shown in Figure 6-22. These films were annealed for at least 72hrs at 140°C under vacuum, and then O_2 plasma treated for 45sec (6mTorr O_2, 90W) to selectively remove the PS block and provide good contrast in SEM.

Unfortunately, our investigations of this material system have only produced typical hexagonal packings of the BCP spheres. Given the small sphere size of the BCP (~28nm diameter spheres, ~45nm center to center distance), it is conceivable that the

quasiperiodic features that are just too far apart to properly interact with the BCP nanostructure (i.e. the posts on the quasiperiodic lattice are decoupled).

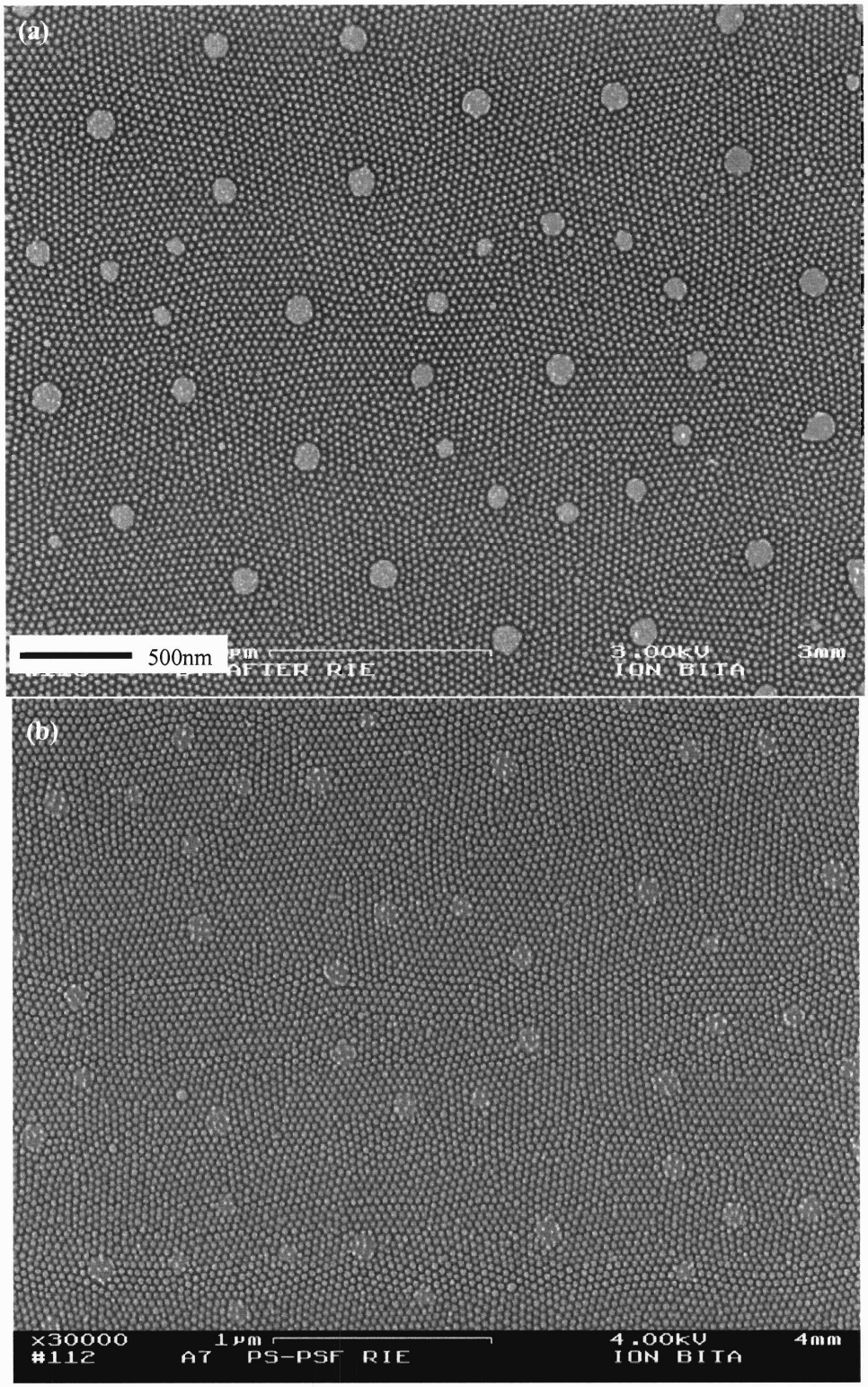

Figure 6-23 - SEM images of a monolayer of PS-PFS spherical morphology BCP, after O_2 RIE, self-assembled on 2D quasiperiodic topographically patterned substrates with **(a)** 12-fold rotationally symmetric QC and **(b)** 8-fold rotationally symmetric QC.

This project, however, is still work in progress. Since scaling down the 2D quasiperiodic structures in ME-IL is limited by the 325nm HeCd laser wavelength employed by the Lloyd's mirror interferometer, a higher molecular weight block copolymer would offer a solution to producing samples where the posts and the polymer spheres are comparable in size. In this case, only a few spheres can fit in the spaces between the quasiperiodically distributed posts, maximizing the effect of the template on the self-assembling BCP.

An unexpected and very fortunate result of this study has been the realization that properly configured 2D arrays of posts offer a logical path towards guiding the self-assembly of spherical and standing-up cylindrical morphology BCPs in thin films over entire wafers, when the 2D post array is formed by interference lithography. Given the early stage of this project, and the IP issues, it will not be further pursued in the thesis.

6.5. Conclusions

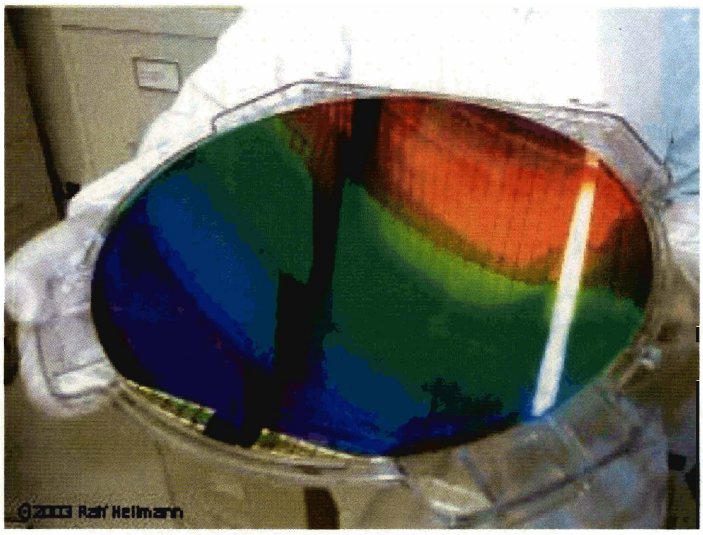

Figure 6-24 - MIT Nanoruler Project: 12" wafer patterned with 400nm period line gratings (*http://web.mit.edu/newsoffice/2004/nanoruler-0128.html*)

Interference lithography was explored in this chapter as a highly versatile tool for the fabrication of 2D quasiperiodic structures. We have first considered a number of theoretical issues associated with understanding the quasicrystalline structures that can be produced by interfering multiple beams or by multiple exposures with substrate rotations. It was shown that these two situations are not equivalent, and that the interference of multiple beams leads to a superposition of multiple and incommensurate quasiperiodic lattices, while maintaining the same overall rotational symmetry of the structure. The generation of 2D quasiperiodicity in IL was explained on the basis of incommensuration of translationally periodic intensity variations produced in the interference of light. A class of 2D quasiperiodic structures produced from a minimal number of beams or exposures was explored, and shown to require at least 3 beams or 3 exposures.

Experimentally, we have focused on interference lithography with multiple exposures and rotations of the sample and showed that this technique represents a very powerful tool for the fabrication of 2D quasiperiodic structures. We were able to fabricate 2D quasicrystals with 8-, 10-, and 12-fold rotational symmetries having feature sizes as small as 100nm, with overall sample sizes of a few square centimeters. For the first time we show that IL can be used to fabricate 2D photonic quasicrystals with features sizes and quality comparable to those obtained from electron beam lithography.

Building on the successful fabrication of 2D quasiperiodic structures, we pursued novel 3D sub-micron structured quasiperiodic materials fabricated by coherent diffraction lithography (capturing the near field intensity pattern produced by a transparent 2D grating into a thick resist layer). This class of materials is currently of high interest, since the remarkable properties of quasicrystals are yet to be measured in 3D due the lack of

available materials - fabricating 3D quasiperiodic materials with sub-micron features has not yet been reported in the literature. While our preliminary results still require optimization, they prove the feasibility of this experimental approach.

Much remains to be done in the area of quasicrystals. A particularly important need exists in understanding the symmetries of the structures that are available experimentally. Many types of quasicrystals can be fabricated, and theoretical guidance is needed for focusing the experimental efforts at this early stage of the field. Great opportunities must lie ahead, and introducing experimental methods for the fabrication of a variety of quasicrystals is a first step forward taken in this thesis.

6.6. References

1. Yablonovitch, E. "Inhibited Spontaneous Emission in Solid-State Physics and Electronics," *Physical Review Letters*, **58**, 2059 (1987).

2. John, S. "Strong Localization of Photons in Certain Disordered Dielectric Superlattices," *Physical Review Letters*, **58**, 2486 (1987).

3. Chan, Y. S., Chan, C. T., and Liu, Z. Y. "Photonic band gaps in two dimensional photonic quasicrystals," *Physical Review Letters*, **80**, 956 (1998).

4. Senechal, M. *Quasicrystals and geometry*, Cambridge University Press (New York, 1995).

5. Janot, C. *Quasicrystals: a primer*, 2nd Edition, Clarendon Press (New York, 1994).

6. Allen, S. M., and Thomas, E. L. *The structure of materials*, John Wiley (New York, 1999).

7. Mermin, N. D., Rokhsar, D. S., and Wright, D. C. "Beware of 46-Fold Symmetry - the Classification of Two-Dimensional Quasicrystallographic Lattices," *Physical Review Letters*, **58**, 2099 (1987).

8. Notomi, M., Suzuki, H., Tamamura, T., and Edagawa, K. "Lasing action due to the two-dimensional quasiperiodicity of photonic quasicrystals with a Penrose lattice," *Physical Review Letters*, **92**, (2004).

9. Nozaki, K., and Baba, T. "Quasiperiodic photonic crystal microcavity lasers," *Applied Physics Letters*, **84**, 4875 (2004).

10. Berger, V., Gauthier Lafaye, O., and Costard, E. "Photonic band gaps and holography," *Journal of Applied Physics*, **82**, 60 (1997).

11. Campbell, M., Sharp, D. N., Harrison, M. T., Denning, R. G., and Turberfield, A. J. "Fabrication of photonic crystals for the visible spectrum by holographic lithography," *Nature*, **404**, 53 (2000).

12. Escuti, M. J., and Crawford, G. P. "Holographic photonic crystals," *Optical Engineering*, **43**, 1973 (2004).

13. Gauthier, R. C., and Ivanov, A. "Production of quasi-crystal template patterns using a dual beam multiple exposure technique," *Optics Express*, **12**, 990 (2004).

14. Wang, X., Ng, C. Y., Tam, W. Y., Chan, C. T., and Sheng, P. "Large-area two-dimensional mesoscale quasi-crystals," *Advanced Materials*, **15**, 1526 (2003).

15. Chen, C. G. *Beam Alignment and Image Metrology for Scanning Beam Interference Lithography – Fabricating Gratings with Nanometer Phase Accuracy*, PhD thesis, Department of Electrical Engineering and Computer Science, Massachusetts Institute of Technology (Cambridge, MA, 2003).

16. Zanke, C., Qi, M. H., and Smith, H. I. "Large-area patterning for photonic crystals via coherent diffraction lithography," *Journal of Vacuum Science & Technology B*, **22**, 3352 (2004).

17. Toader, O., Chan, T. Y. M., and John, S. "Photonic band gap architectures for holographic lithography," *Physical Review Letters*, **92**, (2004).

18. Ullal, C. K., Maldovan, M., Thomas, E. L., Chen, G., Han, Y. J., and Yang, S. "Photonic crystals through holographic lithography: Simple cubic, diamond-like, and gyroid-like structures," *Applied Physics Letters*, **84**, 5434 (2004).

19. Yang, S., Megens, M., Aizenberg, J., Wiltzius, P., Chaikin, P. M., and Russel, W. B. "Creating periodic three-dimensional structures by multibeam interference of visible laser," *Chemistry of Materials*, **14**, 2831 (2002).

20. Petsas, K. I., Coates, A. B., and Grynberg, G. "Crystallography of Optical Lattices," *Physical Review A*, **50**, 5173 (1994).

21. Grynberg, G., Lounis, B., Verkerk, P., Courtois, J. Y., and Salomon, C. "Quantized Motion of Cold Cesium Atoms in 2-Dimensional and 3-Dimensional Optical Potentials," *Physical Review Letters*, **70**, 2249 (1993).

22. Burns, M. M., Fournier, J. M., and Golovchenko, J. A. "Optical Matter - Crystallization and Binding in Intense Optical-Fields," *Science*, **249**, 749 (1990).

23. Berger, V., Gauthier Lafaye, O., and Costard, E. "Fabrication of a 2D photonic bandgap by a holographic method," *Electronics Letters*, **33**, 425 (1997).

24. Mei, D. B., Cheng, B. Y., Hu, W., Li, Z. L., and Zhan, D. H. "3-Dimensional Ordered Patterns by Light Interference," *Optics Letters*, **20**, 429 (1995).

25. Cai, L. Z., Yang, X. L., and Wang, Y. R. "All fourteen Bravais lattices can be formed by interference of four noncoplanar beams," *Optics Letters*, **27**, 900 (2002).

26. Ullal, C. K., Maldovan, M., Wohlgemuth, M., and Thomas, E. L. "Triply periodic bicontinuous structures through interference lithography: a level-set approach," *Journal of the Optical Society of America a-Optics Image Science and Vision*, **20**, 948 (2003).

27. Deespinosa, F. M., Torres, M., Pastor, G., Muriel, M. A., and Mackay, A. L. "Acoustic Quasi-Crystals," *Europhysics Letters*, **21**, 915 (1993).

28. Gorkhali, S. P., Qi, J., and Crawford, G. P. "Electrically switchable mesoscale Penrose quasicrystal structure," *Applied Physics Letters*, **86**, 011110 (2005).

29. Walsh, M. E. *Nanostructuring magnetic thin films using interference lithography*, S.M. thesis, Department of Electrical Engineering and Computer Science, Massachusetts Institute of Technology (Cambridge, MA, 2000).

30. Guidoni, L., Triche, C., Verkerk, P., and Grynberg, G. "Quasiperiodic optical lattices," *Physical Review Letters*, **79**, 3363 (1997).

31. Kong, J. A. *Electromagnetic wave theory*, EMW Publishing (Cambridge, Mass., 2000).

32. Zoorob, M. E., Charlton, M. D. B., Parker, G. J., Baumberg, J. J., and Netti, M. C. "Complete photonic bandgaps in 12-fold symmetric quasicrystals," *Nature*, **404**, 740 (2000).

33. Man, W. N., Megens, M., Steinhardt, P. J., and Chaikin, P. M. "Experimental measurement of the photonic properties of icosahedral quasicrystals," *Nature*, **436**, 993 (2005).

34. Schattenburg, M. L., Aucoin, R. J., and Fleming, R. C. "Optically matched tri-level resist process for nanostructure fabrication," *Journal of Vacuum Science & Technology B*, **13**, 3182 (1995).

35. Yeh, P. *Optical waves in layered media*, Wiley (New York, 1988).

36. Segalman, R. A. "Patterning with block copolymers," *Materials Science & Engineering R*, **48**, 191 (2005).

37. Cheng, J. Y., Ross, C. A., Thomas, E. L., Smith, H. I., and Vancso, G. J. "Templated Self-Assembly of Block Copolymers: Effect of Substrate Topography," *Advanced Materials*, **15**, 1599 (2003).

38. Cheng, J. Y., Ross, C. A., Thomas, E. L., Smith, H. I., and Vancso, G. J. "Fabrication of nanostructures with long-range order using block copolymer lithography," *Applied Physics Letters*, **81**, 3657 (2002).

39. Cheng, J. Y., Mayes, A. M., and Ross, C. A. "Nanostructure engineering by templated self-assembly of block copolymers," *Nature Materials*, **3**, 823 (2004).

40. Jeon, S., Park, J. U., Cirelli, R., Yang, S., Heitzman, C. E., Braun, P. V., Kenis, P. J. A., and Rogers, J. A. "Fabricating complex three-dimensional nanostructures with high-resolution conformable phase masks," *Proceedings of the National Academy of Sciences of the United States of America*, **101**, 12428 (2004).

41. Rumpf, R. C., and Johnson, E. G. "Comprehensive modeling of near-field nano-patterning," *Optics Express*, **13**, 7198 (2005).

42. Xia, Y., and Whitesides, G. M. "Soft Lithography," *Annual Review of Materials Science*, **28**, 153 (1998).

Chapter 7.
Thesis conclusions and future research directions

In this last section, I will outline what I consider to be the main accomplishments presented in this thesis, and finish with a list of future directions of research that should be further explored.

7.1. Overview of research accomplishments

The central theme of this work has been to study structured materials where certain symmetries are absent, with a particular focus on the case when the size of the structural features is comparable to the wavelength of light.

The first part of the thesis examined a class of 1D periodic photonic crystals where both space-inversion and time-reversal symmetries are broken. Space inversion symmetry is absent in non-centrosymmetric photonic crystal structures such as those obtained by either using centrosymmetric materials in a noncentrosymmetric arrangement (e.g. helical, or spiral structures), or by using noncentrosymmetric materials (i.e. optically active materials) in the photonic crystal unit cell. Similarly, time-reversal symmetry is broken by including magneto-optically active material components in the photonic crystal. As described in Chapter 3, a number of remarkable properties were found for the first time for this class of photonic crystals as a direct consequence of the absence of the

two inversion symmetries, properties that are independent of the particular choice of materials, magnitude of their optical constants, etc.. These consequences include formation of indirect photonic band gaps, propagating eigenmodes with negative group velocity (backward waves), negative refraction at the air-photonic crystal interface, unidirectional superprism effects, and bending the path of light by perpendicular magnetic fields (photonic Hall effect).

While seemingly a very abstract theoretical problem, by focusing our analysis only on those properties that arise from symmetry constraints, our results impact a wide range of practical problems. The remarkable set of properties identified for the nonreciprocal photonic crystal system introduced in Chapter 3 are general, and should thus be present in other material systems as well. A notable example, due to the electronic-photonic crystal analogy, is the propagation of spin-polarized electrons in appropriate semiconductors and semiconductor heterostructures. Electronic systems that display both noncentrosymmetry and magnetization include semiconductors with zinc-blende crystal structure (e.g. gallium arsenide, etc.) doped with magnetic atoms (manganese most often), or chiral carbon nanotubes with axial magnetic fields. This class of semiconductors is currently under active research, and results such as those presented in Chapter 4 on tunneling time dynamics offer new perspectives on the underlying physics in these materials.

The results in Chapter 4 may represent the most valuable contribution of this thesis - we show that the nonpropagating modes inside an indirect gap formed at the anticrossing of modes with different group velocities are fundamentally different than the usually assumed evanescent modes. Our analysis, for a noncentrosymmetric, axially

magnetized barrier material, reveals that these gap modes have complex wave vectors that, in addition to the usual imaginary components, also have non-zero real components that change with frequency. This finding is significant because typical quantum mechanical treatments of spin polarized particle tunneling in such barrier materials assume a purely imaginary (evanescent) wave vector (e.g. Ref. 14 in Chapter 4). One particular consequence of the nature of these gap modes was described in the context of the tunneling time of a spin-polarized particle, which was found to not obey the classical Hartman effect. The tunneling time becomes dependent on barrier length, with a group delay that changes sign according to the spin of the tunneling particle.

The remaining part of the thesis focuses on the study of 2D and 3D sub-micron structured quasiperiodic materials, where the symmetry being broken by design is translational symmetry enabling locally higher point group symmetries.

Chapter 5 presents the results of a theoretical analysis of the opportunities offered by quasiperiodicity in the design of photonic band gap materials, motivated by the high rotational symmetries available in quasicrystals. Given the paucity of literature on this problem, particularly the lack of systematic studies that could guide research in this area, we undertook an ambitious task - to understand the effects of symmetry and of 2D quasicrystal type on the formation of photonic band gaps. Two quasicrystal types were investigated, those obtained from interference lithography (IL-PQC) and those obtained by placing dielectric rods on mathematical quasiperiodic lattices (PROJ-PQC). For each quasicrystal type, three point group symmetries were investigated: 8mm, 10mm, and 12mm. Given the computational resource restrictions imposed by the need to simulate large area quasicrystals, we decided to examine only TM photonic band gaps by

calculating the local density of states at a center of high rotational symmetry as a function of dielectric contrast - both low and high contrasts were investigated ($\varepsilon_{dielectric}/\varepsilon_{air}$ of 4:1, 6:1, 8:1, and 10:1). To establish a baseline, we first studied the effect of point group symmetry in 2D photonic crystals (4mm and 6mm: square and hexagonal lattices), for which it was found that a higher symmetry does indeed lead to wider 2D complete TM band gaps, but that this effect becomes weaker as the refractive index contrast increases. In the case of the quasicrystals, the results of this preliminary study did not allow us to extract a similar, clear correlation between point group symmetry and the width of the complete 2D TM photonic band gaps, as determined from LDOS curves at the center of high point group symmetry. In the case of the 2D IL-PQC, while both octagonal and dodecagonal IL-PQC displayed a well defined lowest order PBG gap, the decagonal symmetry was found to display many narrower gaps in the same frequency range. At lower fill fractions ($f < 0.10$) the octagonal IL-PQC displayed slightly wider gap than the dodecagonal PQC, with the situation reversed at higher fill fractions ($f > 0.20$). Furthermore, when comparing IL-PQC with PROJ-PQC, it was found that both 8mm and 10mm PROJ-PQC displayed wider gaps than the corresponding IL-PQC, with the situation reversed for the case of 12mm symmetry. However, all these differences are small enough (5-10%) to not allow us to draw definitive conclusions until a later time when data for a total DOS will be obtained by averaging the LDOS over multiple locations in the PQC structures.

Our studies of quasicrystals continued in Chapter 6, where interference lithography methods for fabricating 2D quasicrystals are quantitatively analyzed and experimentally implemented. We first considered a number of theoretical issues

associated with understanding the physical quasicrystalline structures that can be produced by interfering multiple beams or by multiple exposures with substrate rotations. It was shown that these two situations are not equivalent, and that the interference of multiple beams leads to a superposition of multiple and incommensurate quasiperiodic lattices, while maintaining the same overall rotational symmetry as also obtained from multiple exposures. A class of 2D quasiperiodic structures produced from a minimal number of beams or exposures was explored, and shown to require at least 3 beams or 3 exposures. Experimentally, we used interference lithography with multiple exposures and rotations of the sample substrate to fabricate 2D quasicrystals with 8-, 10-, and 12-fold rotational symmetries having feature sizes as small as 100nm and overall sample sizes of a few square centimeters. For the first time we show that IL can be used to fabricate 2D photonic quasicrystals with features sizes and quality comparable to those obtained from electron beam lithography.

Building on the successful fabrication of 2D quasiperiodic structures, we pursued the fabrication of novel 3D sub-micron structured quasiperiodic materials by coherent diffraction lithography (recording the near field intensity pattern produced by a transparent 2D grating into a thick resist layer). This class of materials is currently of high interest, since the remarkable optical properties of quasicrystals are yet to be explored in 3D due the lack of available materials - fabricating 3D quasiperiodic materials with sub-micron features has not yet been reported in the literature. While our preliminary results still require optimization, they prove the feasibility of this experimental approach. Another proof-of-concept experimental study that was attempted and reported in Section 6.4.2., was related to a very interesting scientific problem related

to the effect of a quasiperiodic topographically patterned template (obtained from 2D IL-PQC) guiding the self-assembly of a block copolymer (BCP) in a thin film, when the BCP normally produces a sphere monolayer morphology (2D hexagonally packing, 6mm point group symmetry). In particular, we have investigated the effect of the point group symmetry of the IL-PQC, choosing 8mm and 12mm in particular. Although the experimentally available diblock copolymer system, polystyrene-*b*-polyferrocenyldimethylsilane (PS-PFS), had a molecular weight that led to inconclusive conclusions (the IL laser constrained, smallest achievable average distance between the topographical features of the IL-PQC was too large compared to the BCP period), this study has put us in an unique position to realize that templates with properly designed 2D arrays of topographical features could potentially become key for guiding the self-assembly of BCP over ultra large areas. Controlling the alignment of the BCP microdomains further enables useful applications of the BCP material in nanolithography. This work is in progress, and due to ongoing IP issues, will not be explored further in the thesis.

7.2. Future research directions

The research presented in this thesis has brought us to realize that, while we were able to shed light on a number of important problems, much remains to be done in order to completely explore all the implications of our findings.

In the areas explored by Chapters 3 and 4, we believe that more remains to be learned about the propagation of spin-polarized electrons in semiconductor heterostructures by exploiting the analogies with the photonic crystal case. While we

have only suggested this analogy, we have not rigorously explored the electronic case. Recent studies of analogous electronic systems [1] indicate that some of our predictions are correct (e.g. negative group delay predicted for spin polarized electrons tunneling in magnetized noncentrosymmetric semiconductor heterostructures), and thus that all the other symmetry-related observations presented in Chapters 4 and 5 should also apply in the case of electrons propagating in appropriate semiconductors (e.g. nonreciprocal effect of the magnetic field on the velocity of propagation of electrons, particularly interesting for carbon nanotubes, where an axial magnetic field should allow tuning the conductivity in a forward and backward direction).

In the area of quasicrystals, future opportunities must likely exist for 3D bicontinuous quasicrystalline networks. These opportunities include pursuing photonic band gap properties (still a big computational challenge), and applications that rely on the improved mechanical properties of these materials (in the absence of translational periodicity, there are no crystal planes along which fractures can propagate, etc.). We have showed that coherent diffraction lithography is a very economical method for producing large area, 3D structured quasiperiodic materials. However, the optimization of this method is not trivial, both experimentally and theoretically (i.e. prediction of the near field intensity pattern for a given quasiperiodic transparent mask).

Another promising direction in the area of 3D structures with quasiperiodicity involves creating a hybrid 3D material composed of quasiperiodic 2D slabs. These slabs would be stacked to form a 3D structure with a refractive index changing either periodically or quasiperiodically along the direction normal to the layers. Such a structure would be readily accessible experimentally, because very capable planar

processing solutions can be borrowed from the semiconductor industry toolbox. This approach has been previously used to construct 3D photonic crystals, based on fabrication of 2D photonic crystal slabs and controlling the alignment between individual layers [2]. Due to the absence of translational periodicity, an inviting speculation is that using 2D quasicrystal slabs in this stacking approach may enable 3D photonic band gaps that are *insensitive to the alignment* of individual quasicrystalline layers. This would clearly greatly reduce the costs associated with fabricating the 3D structures, since the typical alignment on the 100nm scale or less used in 3D layered photonic crystals would not be necessary anymore.

Lastly, a problem that was only briefly touched upon in the last section of Chapter 6, was that related to studying basic self-assembly of block copolymers (BCP) that adopt translationally periodic structures (e.g. 2D hexagonally packed spheres or standing-up cylinders), when constrained in thin films on quasiperiodic topographically 2D patterned templates. Future studies along these lines could offer more insight into how atomic quasicrystals form, a problem still poorly understood today in material science. It would be of interest to explore higher molecular weight BCPs, such that the size of the topographical features is comparable to the size of the BCP in order to increase the effect of the template on the self-assembling system. As alluded to in the previous section, other 2D structured templates offer similarly interesting opportunities for controlling BCP self-assembly, with applications in nanofabrication.

7.3. References

1. Guo, Y., Shang, C.-E., and Chen, X.-Y. "Spin-dependent delay time and the Hartman effect in tunneling through diluted-magnetic-semiconductor/semiconductor heterostructures," *Physical Review B*, **72**, 045356 (2005).

2. Qi, M., Lidorikis, E., Rakich, P. T., Johnson, S. G., Joannopoulos, J. D., Ippen, E. P., and Smith, H. I. "A three-dimensional optical photonic crystal with designed point defects," *Nature*, **429**, 538 (2004).